



AIAA Design Build Fly Competition Summary 2020-21

Beechcraft

Cessna

Jawker

TEXTRON AVIATION

Raytheon
Missiles & Defense

AIAA
FOUNDATION

The 2020-21 AIAA/Textron Aviation/Raytheon Missiles & Defense Design/Build/Fly Competition concluded with a scored video presentation in place of the competition fly-off due to the Coronavirus pandemic and the award ceremony on May 14, 2021. This was the 25th year for the competition. Of the 117 proposals submitted and judged, 115 teams were invited to submit a formal report for the next phase of the competition. Ninety-two (92) teams submitted design reports to be judged and were invited to submit a video presentation of their design with demonstrated flight missions for scoring in place of the cancelled fly-off. Sixty-eight (68) teams submitted video presentations that were then scored by the members of the DBF Organizing Committee. The final scores for each team were then computed using both report and video scores.

The contest theme this year was UAV with Sensor Suite. The aircraft was limited to a maximum five foot wing span. Each aircraft was required to transport the sensor deployment system along with multiple sensors in shipping containers and then be configured with the deployment and recovery mechanism and one sensor and deploy the sensor after take-off and recover the sensor before landing. The sensor was required to contain LEDs in a pattern detectable by the Flight Director from the ground and turned on and off from the pilot or observer remotely. The teams were required to complete three flight missions, each with a maximum take-off distance of 100 feet. The first mission was a Staging Flight with no payload for three laps within five minutes. The second mission was a Delivery Flight with the deployment and recovery device and sensors in shipping containers as payload and the score based on the number of sensors in shipping containers carried. The final mission was a Sensor Flight which required deployment, operation and recovery of the sensor during flight with a score based on number of laps flown in 10 minutes plus sensor weight. Teams were also required to complete a timed ground mission demonstrating the requirements for the Delivery and Sensor Flights as well as robustness of the sensor shipping container. More details on the mission requirements can be found at the competition website: <http://www.aiaadbf.org>.

For this year, the teams were invited to submit a video in place of the competition fly-off. The video required a presentation of the teams design and supporting analysis as well as demonstration of the flight and ground missions. The final competition score was a product of the report score and video score. More details on the mission requirements can be found at the competition website: <http://www.aiaadbf.org>.

First Place went to the Dayananda Sagar College of Engineering, Second Place went to the University of Central Florida and Third Place went to Embry-Riddle Aeronautical University Daytona Beach. A full listing of the results is included below. The Best Paper Award, sponsored by the Design Engineering TC for the highest report score, went to the University of Michigan -- Ann Arbor with a score of 91.67.

We owe our thanks for the success of the DBF competition to the efforts of many volunteers from Textron Aviation, Raytheon Missiles & Defense, and the AIAA sponsoring technical committees: Applied Aerodynamics, Aircraft Design, Flight Test, and Design Engineering. These volunteers collectively set the rules for the contest, publicize the event, gather entries, judge the written reports, and organize the flyoff. Thanks also go to the Premier Sponsors: Raytheon Missiles & Defense and



AIAA Design Build Fly Competition Summary 2020-21

Beechcraft

Cessna

Hawker

TEXTRON AVIATION

Raytheon
Missiles & Defense

AIAA
FOUNDATION

Textron Aviation, and also to the AIAA Foundation for their financial support as well as our Gold sponsor this year – Mathworks.

Finally, this event would not be nearly as successful without the hard work and enthusiasm from all the students and advisors. If it weren't for you, we wouldn't keep doing it.

Matt Angiulo
For the DBF Organizing Committee

MACH

2020-2021 AIAA DBF Competition

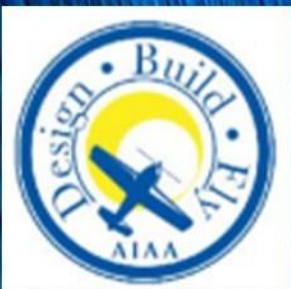
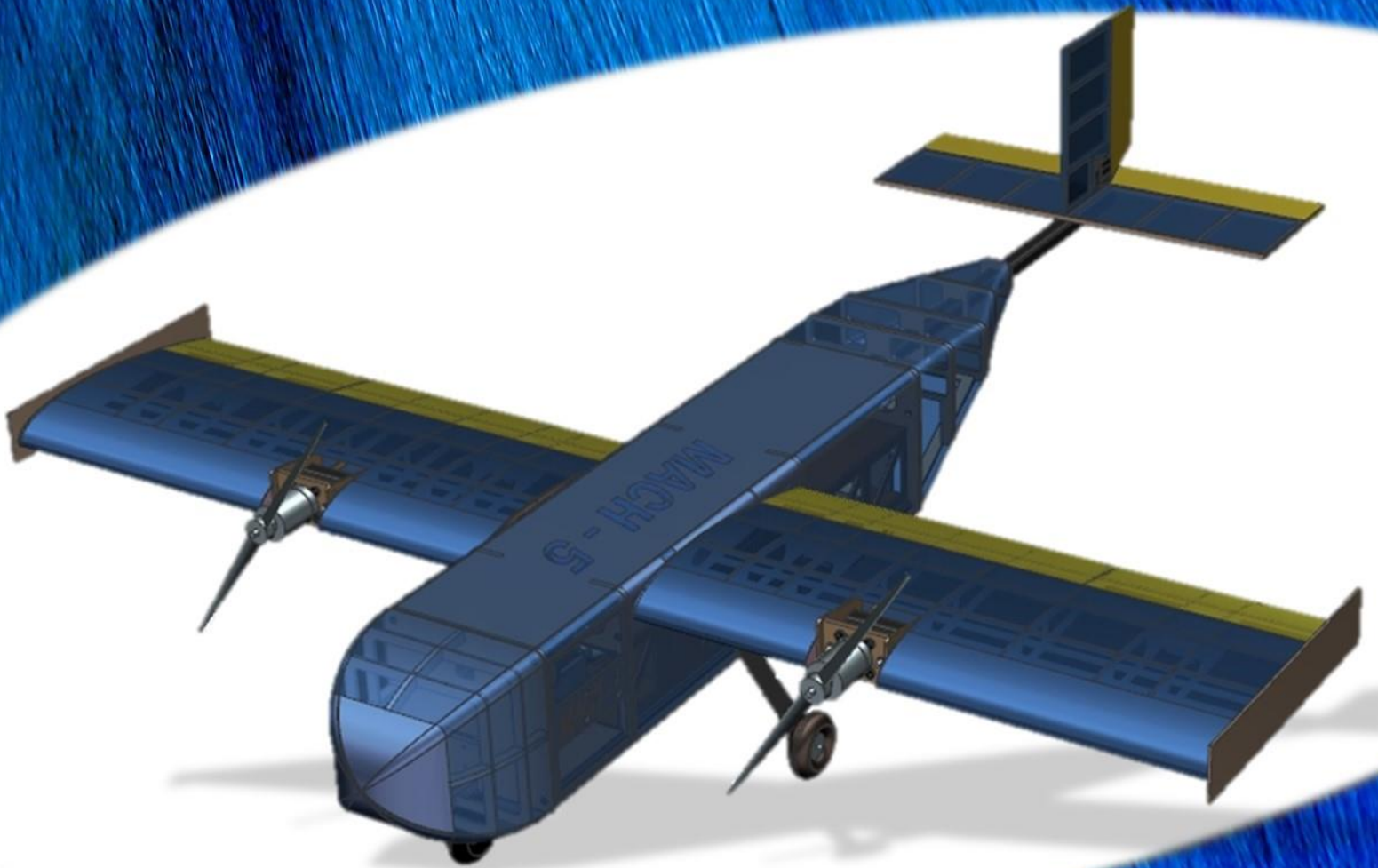




TABLE OF CONTENTS

1	EXECUTIVE SUMMARY	5
2	MANAGEMENT SUMMARY	6
2.1	Team Structure & Organization.....	6
2.2	Milestone Chart	6
3	CONCEPTUAL DESIGN.....	8
3.1	Mission Requirements.....	8
3.1.1	Mission 1 - Staging Flight.....	8
3.1.2	Mission 2 - Delivery Flight	8
3.1.3	Mission 3 – Deployed Sensor Flight.....	8
3.1.4	Ground Mission – Operational Demonstration	9
3.1.5	Total Competition Score.....	9
3.2	Translation into Design Requirements	9
3.3	Sensitivity Analysis.....	10
3.4	Configuration Selection	11
3.5	Subsystem Conceptual Selection	12
3.5.1	Propulsion	12
3.5.2	Landing Gear.....	13
3.5.3	Tail.....	13
3.5.4	Towable Sensor	14
3.6	Conceptual Design Overview.....	14
4	PRELIMINARY DESIGN.....	15
4.1	Design/Analysis Methodology	15
4.2	Sizing Analysis	16
4.2.1	Mission Model	16
4.2.2	Wing Sizing Analysis	17
4.2.3	Tail Sizing Analysis	19
4.2.4	Control Surface Sizing Analysis	20
4.3	Design Trade Studies.....	21
4.3.1	Airfoil Selection.....	21
4.3.2	Wingtip Plates	22
4.3.3	Sensor Design.....	23
4.3.4	Propulsion	25
4.4	Aircraft Stability	27
4.5	Dynamic Stability.....	27
4.6	Sensor Stability	28
4.7	Lift and Drag Estimations	29
4.8	Estimated Mission Performance	30
5	DETAIL DESIGN.....	30
5.1	Preliminary to Final Design Modifications	31
5.2	Structural Layout	31
5.3	System and Subsystem Design	32
5.3.1	Wing Design	32
5.3.2	Tail.....	33
5.3.3	Fuselage Design	33
5.3.4	Sensor Restraint and Deployment System	34
5.3.5	Sensor Container	35
5.3.6	Spool	35
5.3.7	Sensor Design.....	36
5.3.8	Propulsion	37
5.4	Weights and Balance	37
5.5	Structural Performance	38
5.5.1	Wing Structural Analysis	38
5.5.2	Wing Structural Design Trade Study.....	39
5.5.3	Wing Mount Structural Analysis	40

5.5.4	Engine Mount Structural Analysis	41
5.5.5	Landing Gear Structural Analysis.....	42
5.6	Performance Parameters and Expected Mission Performance of Final Design.....	42
5.7	Drawing Package	42
6	MANUFACTURING PLAN	43
6.1	Manufacturing Processes Investigated	43
6.1.1	Laser Cutting	43
6.1.2	3D Printing.....	44
6.1.3	CNC Hot Wire Foam Cutting.....	44
6.1.4	Composites	44
6.1.5	UltraKote Covering	45
6.2	Manufacturing Processes for Major Aircraft Components	45
6.2.1	Wing	45
6.2.2	Tail.....	46
6.2.3	Fuselage.....	46
6.2.4	Sensor Position-Securing Claw Mechanism	46
6.2.5	Sensor Deployment and Retrieval Mechanism	47
6.2	Manufacturing Timeline	47
7	TESTING PLAN.....	48
7.1	Tests and Objectives.....	48
7.1.1	Static Thrust Test	49
7.1.2	LED Brightness Test	49
7.1.3	Wingtip Test	49
7.1.4	Sensor Stability Tests	50
7.1.5	Sensor Container Drop Test	50
7.1.6	Sensor Loading Tests	50
7.1.7	Flight Test Schedule and Plan	51
8	PERFORMANCE RESULTS	54
8.1	Subsystem Testing Results.....	54
8.1.1	Propulsion Testing Results	54
8.1.2	Sensor Performance Results	54
8.1.3	Sensor Container Performance Results.....	54
8.1.4	Predicted Subsystem Performance Results	55
9	BIBLIOGRAPHY	56

Acronyms, Abbreviations, and Symbols

Reduction or Symbol	Definition	Reduction or Symbol	Definition
A_{fus}	Fuselage Cross Sectional Area	M1	Mission 1 Flight Score
AIAA	American Institute of Aeronautics and Astronautics	M2	Mission 2 Flight Score
AR	Aspect Ratio	M3	Mission 3 Flight Score
AVL	Athena Vortex Lattice	MBSE	Model-based Systems Engineering
b_w	Span of Wing	M_{sensor}	Sensor Mass
CA	Cyanoacrylate Adhesive	MTOW	Maximum Takeoff Weight
CFD	Computational Fluid Dynamics	n	Load Factor
CG	Center of Gravity	NiMH	Nickel-Metal-Hydride
c_w	Chord of Wing	RAC	Rated Aircraft Cost
C_D	Coefficient of Drag	Re_c	Reynolds Number (chord)
C_{D_0}	Coefficient of Parasitic Drag	Re_x	Reynolds Number (running)
$C_{D_{wing}}$	Wing Drag Coefficient	s	Ground Roll Distance
$C_{D_{fus}}$	Fuselage Drag Coefficient	S_w	Surface Area of Wing
C_L	Coefficient of Lift	$T_{dynamic}$	Dynamic Thrust
c_{VT}	Vertical Tail Volume Coefficient	T_{lap}	Time of One Lap
c_{HT}	Horizontal Tail Volume Coefficient	T_{static}	Static Thrust
D	Drag	v_{cruise}	Cruise Velocity
$D_{0\alpha}$	Zero Angle of Attack Drag	V_{stall}	Stall Speed
$d_{takeoff}$	Takeoff Distance	V_{TO}	Takeoff Speed
EDF	Electronically Ducted Fan	V_{max}	Max Speed
ESC	Electronic Speed controller	α	Angle of Attack
W_{empty}	Empty Weight	δ	Deflection
FOM	Figure of Merit	λ	Taper Ratio
g	Gravitational Acceleration of 9.81 m/s ²	μ	Ground Roll Coefficient
GM	Ground Mission	τ	Skin Friction
L_{VT}, L_{HT}	Distance from Aerodynamic Center of Wing to Aerodynamic Center of Vertical and Horizontal Tail	θ_{tether}	Tether Angle
L	Lift	ρ	Air Density

1 EXECUTIVE SUMMARY

This report details the design, fabrication, and testing of the University of Michigan's *MACH 5* unmanned aerial vehicle (UAV) designed to compete in the 2020-21 AIAA Design/Build/Fly (DBF) competition. This year's competition requires a UAV with a sensor suite, capable of deploying and retracting an aerodynamically stable sensor midflight as well as transporting it in a protective shipper container. The AIAA requirements state that the wingspan of the UAV may not exceed 5 ft, that the aircraft must take off within 100 ft, and that the sensor must have three external lights fully visible during flight as well as be stored inside the aircraft during flight. *MACH 5* is designed to successfully complete each of the four required missions. The four required missions include:

- Ground Mission: From flight configuration the aircraft will be loaded with the Mission 2 payload, followed by unloading and configuring for Mission 3. Sensor containers are tested for effectiveness.
- Mission 1: Staging Flight: The aircraft must complete three laps of the prescribed flight course within a 5-minute window without any payload.
- Mission 2: Delivery Flight: The aircraft must carry the maximum number of stored sensors plus the deployment/retrieval mechanism for three laps of the flight course within a 5-minute window. The objective is to perform the mission in the shortest possible time with max payload.
- Mission 3: Sensor Flight: The aircraft must complete the maximum possible number of flight course laps possible within a 10-minute window while towing the deployed sensor. The sensor must be deployed and retrieved in-flight.

The *MACH 5* UAV has been designed to satisfy all the mission requirements set forth by the AIAA. *MACH 5* uses a high mounted wing with a 5-ft wingspan to maximize roll stability and lift capabilities while adhering to the design constraints set forth for the DBF competition. The aircraft boasts a thrust to weight ratio of 0.94 which allows the aircraft to take off in an estimated 44-ft and cruise at 64-mph. Cruising at such velocity allows the aircraft to complete one lap of the competition course in approximately 35-seconds, satisfying the speed requirements for both Missions 1 & 2. An in-depth analysis of the aircraft propulsion system estimates that aircraft endurance is over 11-minutes at 60% throttle cruise, exceeding the duration requirements for all three flight missions.

The sensor suite delivered by *MACH 5* also satisfies the AIAA mission requirements. Designed similar to a missile – with a long cylindrical body and stabilizing fins – the sensor has a length to diameter ratio of 14.4, uses three LED diodes controlled via tether connection to the aircraft, and is both statically and dynamically stable. The sensor is stored within the fuselage, deployed following the opening of a bomb-bay door, and retracted using a spool and self-reversing screw mechanism. The sensor is also designed to fit within protective shipping containers made of foam and basswood.

2 MANAGEMENT SUMMARY

MACH is comprised of 20 University of Michigan students ranging from freshmen to graduate students, all united by a shared passion for aircraft design. The team is open to students of all educational disciplines – both technical and non-technical. The team receives generous sponsorships from Lockheed Martin, Raytheon Missiles & Defense, and Ford Motor Company to assist in purchasing materials and travel to competition.

2.1 Team Structure & Organization

To best establish organization within the team, we selected a tiered leadership structure as shown in Figure 1 below. The organization is led by the Team Captain who is responsible for organizing and directing the entire team. The Chief Engineer, Build Manager, and Business Manager are responsible for overseeing the design process, organizing the construction of the aircraft, and managing the budget and sponsor relations, respectively. Under direction of the Chief Engineer, four technical sub-teams are tasked with specific, aircraft related design elements. Each sub-team is led by a sub-team lead, and MBSE interface requirements are used to improve cross-team collaboration and ensure requirements are met.

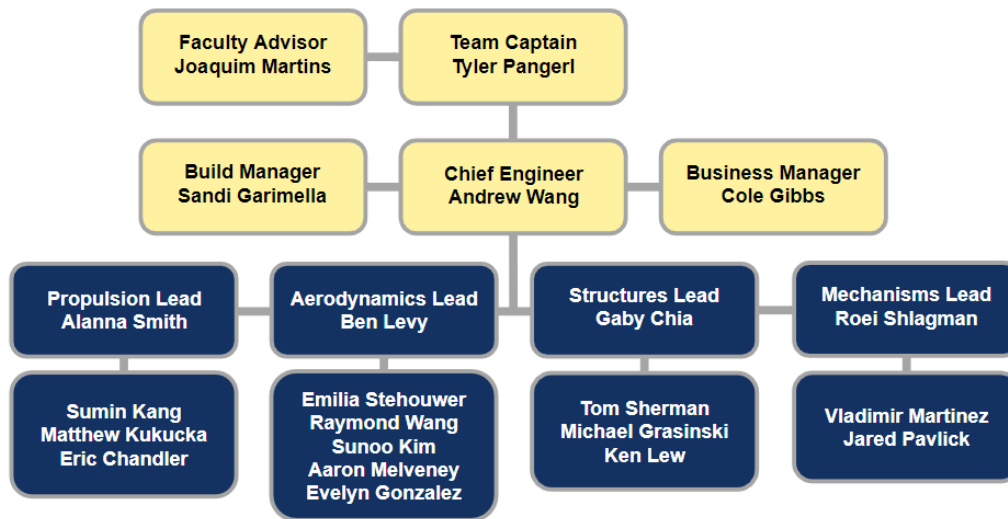


Figure 1: Team Leadership Structure and Membership

2.2 Milestone Chart

MACH utilizes a series of two milestone charts to ensure the team will meet major deadlines and maintain desired progress. The high-level systems chart includes all major designs, tests, and deliverables for the project. The low-level systems chart includes more detailed documentation of subcomponent deadlines. Due to fluctuating state and university regulations related to the COVID-19 pandemic, the team has had to drastically alter their design process for the 2020-2021 competition year. Despite setbacks, cancellations,

and closures due to the restrictions, the team remains on schedule to achieve our goal of a successful flight performance at competition.

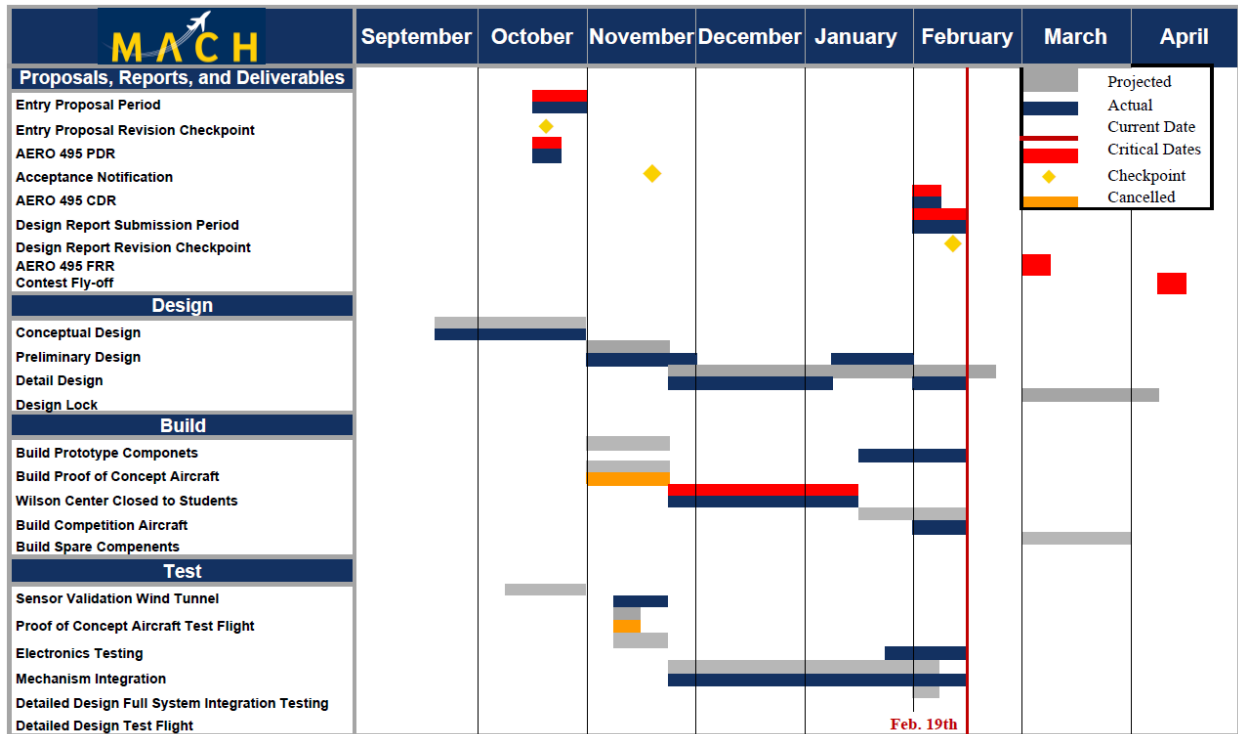


Figure 2: Current Milestone Chart: Projected and Actual Progress of Overall Team

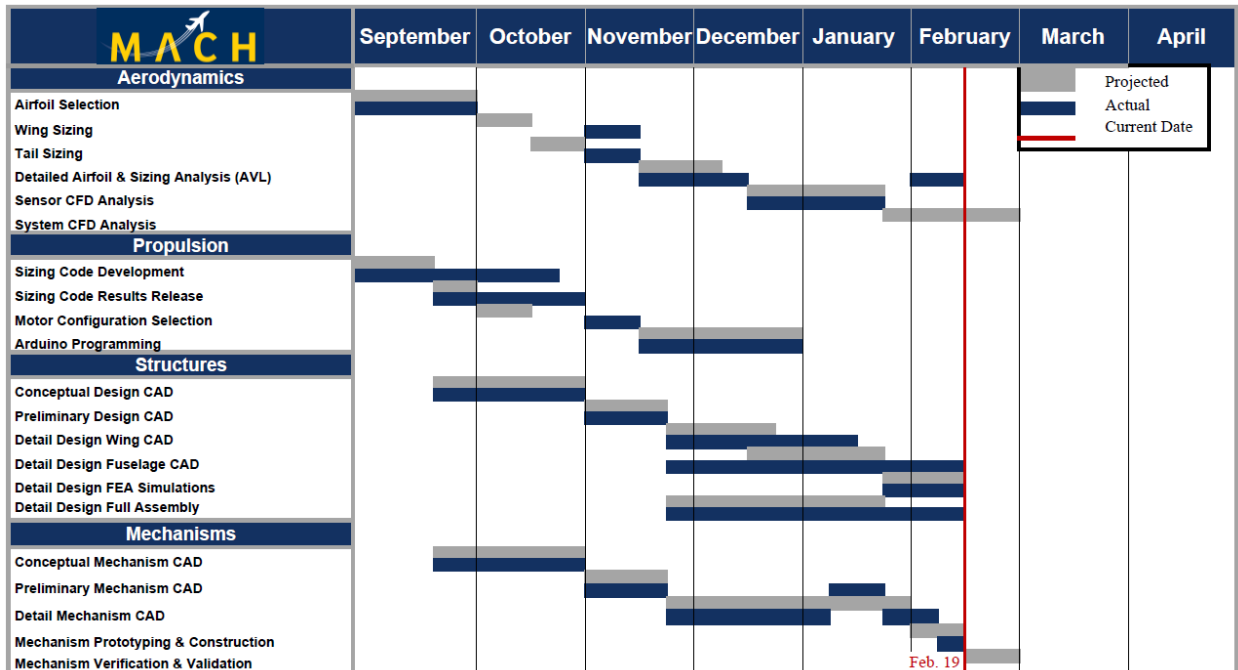


Figure 3: Current Milestone Chart: Projected and Actual Progress of Subcomponents

3 CONCEPTUAL DESIGN

For the 2020-2021 competition season, the AIAA has called for designs of a UAV with a towable sensor suite. This aircraft must be capable of deploying and retrieving an aerodynamically stable, towable sensor mid-flight with visible lights. In addition to towing the sensor, the aircraft must be capable of storing and delivering the sensor(s) in protective shipping containers. This section outlines in detail the processes utilized to develop the team's conceptual design as well as identify all key mission requirements.

3.1 Mission Requirements

This section outlines the detailed system requirements for the four missions taking place at the 2021 AIAA DBF competition.

3.1.1 Mission 1 - Staging Flight

The mission timing begins when the aircraft, containing no payload, advances the throttle for the first take-off attempt. There is a 100-foot take-off requirement. The aircraft must complete 3 laps within a 5-minute flight window followed by a successful landing to receive a score. The time stops when the aircraft passes over the finish line in the air following the third lap. The mission score (M_1) is given below.

$$M_1 = 1 \text{ (for successful completion)} \quad (3.1)$$

3.1.2 Mission 2 - Delivery Flight

The mission timing begins when the aircraft throttle is advanced for the first take-off attempt, with a 100-foot take-off length requirement. The aircraft must be outfitted with an internal payload consisting of sensors and sensor simulators in protective shipping containers, as well as all mechanisms necessary for sensor deployment and retraction. Under this configuration, the aircraft must complete 3 laps of the competition course within a 5-minute flight window followed by a successful landing to receive a score. The time stops when the aircraft passes over the finish line in the air at the end of the third lap. The mission score (M_2) is given below, where " $N_{(\#containers/time)}$ " is the number of sensors and sensor simulators in their containers flown during the mission divided the course completion time and " $Max_{(\#containers/time)}$ " is the highest container per time score amongst all teams at competition.

$$M_2 = 1 + [N_{(\#containers/time)} / Max_{(\#containers/time)}] \quad (3.2)$$

3.1.3 Mission 3 – Deployed Sensor Flight

The mission timing begins when the aircraft throttle is advanced for the first take-off attempt, again with a 100-foot takeoff requirement. The aircraft must deploy the sensor before the first 360-degree turn and complete as many laps as possible within a 10-minute flight window. The design of the sensor is determined by the team. A lap is complete when the aircraft passes over the finish line in the air. After the aircraft crosses the finish line of its last lap, the sensor must be remotely retracted within the aircraft and a

successful landing must take place to receive a score. The score received is proportional to the sensor length, sensor mass, and laps completed. Team performance is normalized by the highest scoring team at competition. The mission score (M3) is given below.

$$M3 = 2 + [N_{(\# \text{ laps} \times \text{ sensor length} \times \text{ sensor weight})} / \text{Max}_{(\# \text{ laps} \times \text{ sensor length} \times \text{ sensor weight})}] \quad (3.3)$$

3.1.4 Ground Mission – Operational Demonstration

The mission begins with the aircraft in the flight configuration, sensor, sensor container, simulators and the deployment/retraction mechanism in the 10' by 10' mission box. The ground mission is broken up into four phases. First, the sensor containers must survive a 10-inch drop on each of its 6 faces – or equivalent, for non-rectangular containers – demonstrating no damage to the container or sensor. The sensor will then be placed into the container for the time trial. Time will begin for each phase of the time trials when the ground mission official says “GO” and end when the assembly crew member returns to the finish line. In the first phase the crew member will start from the start line, load the containers and simulators, and return to the finish line. In the second phase, the crew member will start from the start line, remove the containers and simulators, unpack the sensor, configure the sensor and deployment/retraction mechanism, and return to the finish line. At the end of phase one and phase two of the time trials, the pilot will demonstrate the flight controls are active. After the second flight control demonstration, the crew member will hold the aircraft up and the pilot will demonstrate the sensor deployment and retraction mechanisms are functional – partial deployment is enough for the purposes of this mission. The total score of the ground mission is the ratio of the fastest time from all teams and MACH's time.

$$GM = \text{time}_{\text{best}} / \text{time}_{\text{MACH}} \quad (3.4)$$

3.1.5 Total Competition Score

The total competition score is equal to the sum of the total mission score for the team scaled by the written report score. The total mission score in turn will be calculated as the sum of the individual flight mission and ground mission scores. These relations are represented in the following formulas, where M1, M2, M3, and GM represent the individual flight scores and ground mission score, respectively.

$$\text{Score} = \text{Written Report Score} * \text{Total Mission Score} \quad (3.5)$$

$$\text{Total Mission Score} = M1 + M2 + M3 + GM \quad (3.6)$$

3.2 Translation into Design Requirements

By analyzing the competition rules as well as the results of a sensitivity analysis, the team identified the four design drivers shown in Table 1.

Table 1: Driving Design Requirements

Mission/Scoring Requirement	Design Requirement
Sensor Stability & Score	Long, slender sensor with high mass & fins
Short Ground Mission Time	Fewer sensors and quick configuration setup
Short Lap Time	Low drag and high thrust to weight ratio
Complete Each Mission	Minimal Risk Design

Sensor Design: The sensitivity analysis in the following section demonstrates that the length and weight of the sensor both contribute equally to the change in score of the aircraft. To take advantage of this scoring trend, it was determined that a long sensor with a high mass would maximize the score. In addition to the scoring aspect, the size and weight of the sensor will help to improve the stability of the sensor while in flight with the ideal combination determined through CFD and stability analysis. The stability of the sensor is a critical design element, given that an unstable sensor will result in a 0 score for Mission 3.

Configuration Loading: In order to minimize the ground mission time and increase score, the sensor deployment/retraction mechanism must remain affixed to the aircraft at all times to decrease the number of components that must be removed and replaced during the ground mission. In addition, to decrease the amount of time it takes to load and unload the Mission 2 payload, a smaller quantity of larger sensors would be more ideal for maximizing score.

High Thrust to Weight Ratio: The requirement of a 100-foot takeoff and maximum wingspan of 5-ft imposes a major constraint on the design of the aircraft. To provide adequate take-off and cruise performance to maximize score, a high thrust-to-weight ratio is required to decrease takeoff distance and increase cruising speed.

Minimal Risk Design: By analyzing the results and lessons learned from previous competition years – both for MACH and other teams – it was determined that only a fraction of the teams attending the fly off actually complete every flight mission. Consequently, MACH has placed a large degree of importance on the reliability of the aircraft's performance and an overall risk adverse design.

3.3 Sensitivity Analysis

In order to maximize our fly-off competition score, MACH studied the effects of various design parameters on the total score using a detailed sensitivity analysis. To estimate the baseline score, approximate values from previous competition years were used. These approximated values included time to complete certain ground mission exercises, average flight time per lap, and payload size. The average time of flight per lap selected for the baseline design was selected to be 40-seconds, based on the average time for previous aircraft MACH have developed along with a target cruise speed of 64-mph. The top mission parameters were estimated based on aircraft performances given in top reports from previous years.

Table 2: Estimated Top Competition Mission Performance

Top Mission Performance	Assumptions
GM	90 s
Sensor length	18 in
T_{lap}	40 s
$N_{sensors}$	2

The sensitivity analysis shown below revealed that minimizing the ground mission time and time per lap have a larger impact on the score than the number of sensors or sensor length.

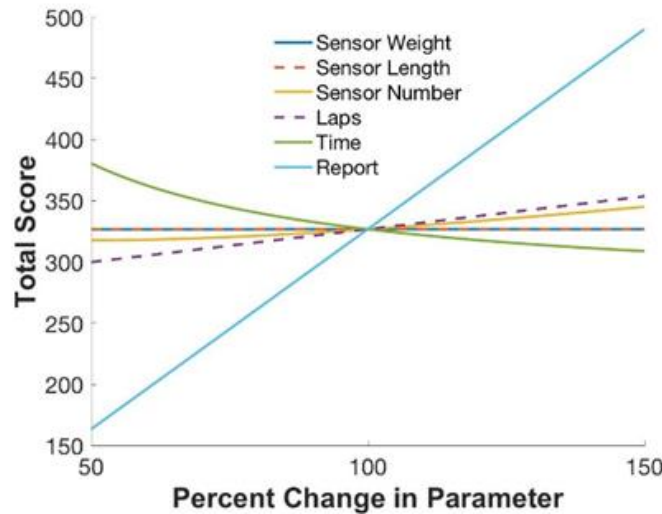


Figure 4: Sensitivity Analysis Showing Change in Total Score

3.4 Configuration Selection

Wing design for 2021 was constrained only by the 5-foot limit placed on wingspan, thus all considerations were centered around this. The scoring indicated that a lower sensor count – using long and heavy sensors – coupled with the fastest speed would lead to the best scoring aircraft design. Therefore, our selection criteria – from highest to lowest weight – are interior volume, controllability, manufacturability, ease of integration, aerodynamics, knowledge base, and cost. Due to the large payload, it was decided that cargo capacity, lift, and stability would be of utmost importance in our configuration selection, followed by speed to aid us in completing the course in a timely fashion. Following these guidelines and using a weighted decision matrix shown in Table 3, the highest scoring design was a high wing single tube configuration. However, after further discussion as a team we decided to use a high wing guppy because it only scored two points lower than the aforementioned configuration and offered a higher interior volume.

Table 3: Aircraft Configuration Decision Matrix

Aircraft Configuration		High Wing Guppy	High Wing Slab-Sided	High Wing Single Tube	High Wing Double Tube
Categories	Weights	Value (1-5)	Value (1-5)	Value (1-5)	Value (1-5)
Aerodynamics	3	3	2	4	2
Manufacturability	4	3	5	4	3
Knowledge Base	2	4	5	5	3
Interior Volume	5	4	3	3	4
Integration	4	5	4	4	3
Controllability	4	5	5	5	5
Cost	2	4	5	5	4
Total		97	97	99	84

3.5 Subsystem Conceptual Selection

Once the overall aircraft configuration was selected, the conceptual design process shifted to the design of the aircraft’s major subsystems.

3.5.1 Propulsion

When selecting propulsion hardware, it was important to weight all considerable options to find which would produce the most efficient results for our aircraft while maintaining the desired thrust-to-weight ratio and maximizing endurance. This began with a decision matrix of single, twin, and triple motor configurations.

Table 4: Propulsion Configuration Decision Matrix

Propeller Configuration		Twin Prop (Wing Mounted)	Pusher	Puller	Pusher / Puller	Tri-Engine
Categories	Weight	Value (1-5)	Value (1-5)	Value (1-5)	Value (1-5)	Value (1-5)
Efficiency	4	5	3	5	2	4
Manufacturability	3	4	2	5	1	3
Cost	4	3	4	5	2	1
Knowledge	3	5	2	5	1	3
Ground Clearance	5	5	5	3	0	2
Total		84	65	85	22	48

The propulsion system configuration was selected using the design matrix shown above in Table 4, with efficiency, manufacturability, cost, knowledge, and ground clearance as the core criteria. The most weight was given to ground clearance and efficiency as those were the main drivers of the fuselage design chosen earlier.

The wing-mounted twin prop and puller configuration had the highest rated totals. They both had high assumed values of efficiency, manufacturability, and previous team knowledge. Although the twin prop had

a slightly lower total, the team opted for a counter-rotating twin engine design to add flight stability. This motor configuration maximizes fuselage capacity, prevents blowback, and decrease the moment due to torque.

3.5.2 Landing Gear

Three options were considered for the landing gear design: a traditional tricycle design with wheels, a tail dragger with front wheels and a rear skid plate, and a millipede design with four total wheels. To determine the best option, the four criteria used were ranked in order of importance. These criteria include ground control, manufacturability, previous knowledge base, cost, and ground clearance. The numerical rankings are found in Table 5 below. Through this ranking system, we determined the optimal solution would be a conventional tricycle configuration due to its increased ground control and manufacturability.

Table 5: Landing Gear Decision Matrix

Landing Gear Configuration		Tricycle Landing Gear	Tail Dragger Landing Gear	Millipede
Categories	Weights	Value (1-5)	Value (1-5)	Value (1-5)
Ground Control	4	5	3	4
Manufacturability	3	3	2	1
Knowledge Base	3	5	4	1
Cost	3	3	4	1
Ground Clearance	5	3	3	4
Total		68	57	45

3.5.3 Tail

The tail configuration of the aircraft was also selected using a decision matrix. The configurations considered were a conventional tail, a twin boom joined with a horizontal stabilizer, a V-tail, an H-tail, and a U-tail. The categories considered for the selection of the tail, in order of importance, were controllability, tow cable clearance and aerodynamic effects, previous knowledge base, structural integrity, manufacturability, and cost. The potential tether interference was weighted the highest as it has the potential to make a design inviable and lead to a total airframe loss. These decisions are summarized in Table 6. Despite the U-tail scoring highest in the trade analysis, we transitioned to the closely scoring conventional tail after determining that our sensor would be towed underneath the aircraft and tether interference would not be as high a risk concern.

Table 6: Tail Configuration Decision Matrix

Tail Configuration		Conventional	Twin Boom	V-Tail	H-Tail	U-Tail
Categories	Weights	Value (1-5)	Value (1-5)	Value (1-5)	Value (1-5)	Value (1-5)
Controllability	5	4	4	1	4	4
Manufacturability	3	5	1	1	4	4
Cost	1	5	2	5	4	4
Knowledge Base	4	5	1	1	3	4
Structural Integrity	3	5	3	2	4	4
Clearance / Aerodynamics	5	2	4	4	2	5
Total		85	58	43	68	89

3.5.4 Towable Sensor

The sensor design was selected using a decision matrix. Prior to the AIAA D.B.F. FAQ release, we considered a straight winged sensor, a delta winged sensor, a finned sensor, and a sensor with strakes. Due to the FAQ release we re-assessed the designs considered, and narrowed down to a triangular finned sensor, a sensor with strakes, a sensor with no external aerodynamic features, a sensor with fins and a shuttlecock end and a sensor with rectangular fins. The categories considered for the selection of the sensor were, in order of importance, aerodynamic stability, sensor drag and ease of manufacturing. We weighted aerodynamic stability the highest as mission completion is determined by the sensor's ability to remain stable in flight. These decisions are summarized in Table 7. Using these results, we decided to focus our efforts on the shuttlecock sensor and the rectangular finned sensor.

Table 7: Sensor Configuration Decision Matrix

Sensor Configuration		Triangular Finned	Straked	Plain	Shuttlecock	Rectangular Finned
Categories	Weight	Value (1-5)	Value (1-5)	Value (1-5)	Value (1-5)	Value (1-5)
Aerodynamic Stability	5	4	4	1	5	4
Aerodynamic Drag	3	4	3	5	2	4
Manufacturability	3	3	2	5	2	3
Sum		36	35	35	37	41

3.6 Conceptual Design Overview

Through the previously mentioned decision matrix selection process, the proposed conceptual design for *MACH 5* became a conventional high-wing monoplane with a traditional tail sporting a “guppy” style

fuselage to maximize payload capacity. This design would also utilize twin, counter-rotating motors mounted to the wings that would reduce the induced torque applied to the fuselage as well as increase the clearance between the ground and the propellers.

The conceptual design of the deployed sensor would include a cylindrical shape with small stabilizing fins on the rear of the towable to improve aerodynamics as well as deployable wings to improve in-flight sensor stability and improve storability within the aircraft and cargo containers.



Figure 5: Orthographic view of the conceptual design showing aircraft configuration

4 PRELIMINARY DESIGN

Once the conceptual design process was completed, the project moved into the preliminary design phase in November 2020. After receiving additional details regarding the competition after the first Q & A on January 8th, 2021, the team revisited the preliminary design phase for three weeks to ensure that the *MACH 5* design met all mission requirements and criteria.

4.1 Design/Analysis Methodology

Beginning with the preliminary design phase, the team divided into sub-teams corresponding to major aircraft systems and areas of expertise. The components of the aircraft were then optimized on a sub-system level until a final configuration was achieved that was predicted to meet all mission requirements. The final phase of the preliminary design process ends with a test flight evaluating the proposed design. When the prototype aircraft successfully completes the test flight, detailed design work begins. If the test flight is unsuccessful, the preliminary design is refined before the next test flight. Due to local and federal restrictions related to the COVID-19 pandemic, this general design/analysis methodology had to be altered to ensure the team's compliance with current guidelines. As a result, the initial prototype test flight prior to moving into the detail design phase was required to be cancelled. Figure 6 outlines the methodology used by *MACH* during the preliminary design phase.

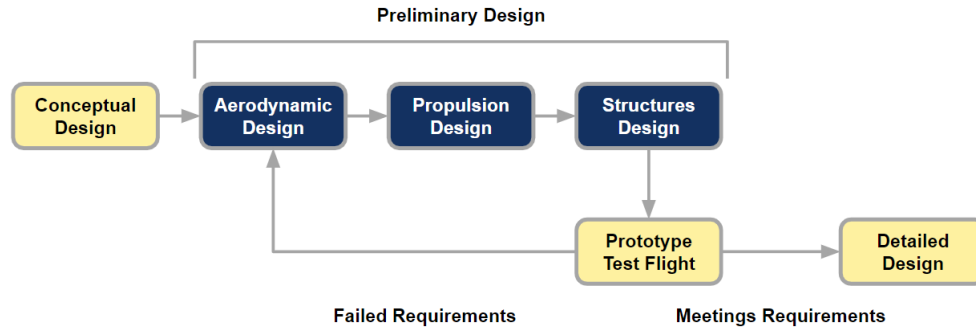


Figure 6: MACH’s Preliminary Iterative Design Methodology

4.2 Sizing Analysis

The first major step in the preliminary design sequence was to size the aircraft. The goal of the sizing analysis performed was to optimize the aircraft’s competition performance and to provide a baseline to aid in the design of the individual subsystems.

4.2.1 Mission Model

A MATLAB program was created to estimate the performance of the aircraft. The program solves for the cruise velocity and for various numbers and dimensions of the aircraft system using an estimated thrust curve and drag profile. The drag acting on the aircraft is calculated using a typical parabolic drag polar, where the coefficient of drag is a function of the parasitic drag and the induced drag. The Oswald efficiency factor that was used in the calculation of induced drag was determined based on Equations 4.1, 4.2, and 4.3 [1]. Similarly, the dynamic thrust is modeled using a quadratic function that has a y-intercept of the predicted static thrust value, which can be seen in Equation 4.4. The estimated cruise velocities of the aircraft are then used to determine the lap time and flight score for each mission.

$$L = W \tag{4.1}$$

$$C_D = C_{D_0} + \frac{C_L^2}{\pi A R e} \tag{4.2}$$

$$e = \frac{0.97 * 0.8}{(0.0524\lambda^4 - 0.15\lambda^3 + 0.1659\lambda^2 - 0.0706\lambda + 0.0119)AR + 1} \tag{4.3}$$

$$T_{dynamic} = -0.015U^2 - 0.060U + T_{static} \tag{4.4}$$

The mission model is broken down into four phases indicated below with the associated assumptions.

1. Takeoff: Takeoff distance is estimated by calculating the ground roll distance as indicated in section 4.2.2. The time associated with takeoff is considered negligible with respect to the overall time of flight.

2. Climb: The aircraft is modeled to climb to an altitude of 50 feet. The density of air is assumed to be 1.14 kilograms per meters cubed, an approximation for air density in Tucson, AZ [2].
3. Cruise: Lift is modeled to equal weight, and the thrust is modeled to equal drag. There are no head or cross winds modeled. The aircraft is assumed to operate at 70% throttle cruise speed throughout the entire flight.
4. Turn: Both turns are modeled with no loss in speed, but there is a drop in altitude of 10 feet. There is assumed to be no loss of speed, however the total arc length of both 180 degree turns and the 360-degree turn is predicted to be 1500 feet, which we believe is an overestimate based on previous competition performance.

4.2.2 Wing Sizing Analysis

To further understand the tradeoffs between competing design-driving parameters, we conducted an analysis using MATLAB to determine the relationship between wing aspect ratio, sensor quantity, and competition score. Figure 7 below describes the process used to determine an estimate of the score for each combination of sensors and wingspan. The outer loop ensures that the estimates made for the sizing and capabilities of the aircraft result in a takeoff that is less than 100 feet. The middle loop sizes the area of the wing to meet the takeoff constraints given an estimated takeoff speed, $C_{L,max}$, and MTOW. To improve takeoff estimates, a simple approximation was used to include the effects of flaps using Equations 4.5 and 4.6. The flaps are assumed to be deflected by 10 degrees and 60% of the wing area is flapped.

$$\Delta C_l = \frac{S_{flap}}{S_{ref}} \cos(\delta_{flap}) \quad (4.5)$$

$$C_{l,TO} = \frac{C_{l,stall}}{1.1^2} + \delta C_l \quad (4.6)$$

Using Equations 4.7 through 4.10, which are presented by Raymer to calculate ground roll distance, the takeoff distance s , is approximated [3].

$$K = \frac{1}{\pi A R e} \quad (4.7)$$

$$K_t = \frac{T}{MTOW} - \mu \quad (4.8)$$

$$K_a = \frac{1}{2} \rho \left(\frac{MTOW}{S_{ref}} \right) \left(\frac{\mu}{C_{l,TO}} - C_{D0} - K C_{l,TO} \right) \quad (4.9)$$

$$s = \frac{\ln \left(\frac{K_t + K_a V_{TO}^2}{K_t} \right)}{2g K_a} \quad (4.10)$$

The inner loop in Figure 8 iteratively determines the size of the propulsion system necessary to meet the desired MTOW for a thrust-to-weight ratio of 0.6. A propulsion system characterization was performed to establish trends between system propulsion and mass. This data was compiled and incorporated into the sizing code to aid in the estimation of the required propulsion system mass for the aircraft. Aircraft performance was estimated by using the mission model described in the Mission Model subsection (4.2.1).

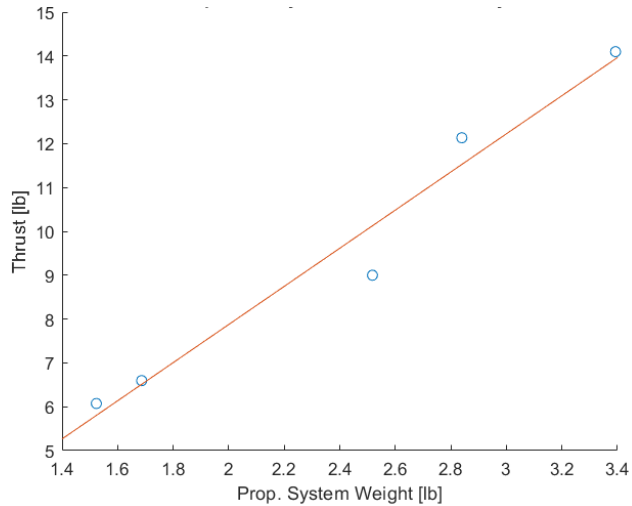


Figure 7: Linear Trend Resulting from Propulsion System Trade Study

Figure 9 shows the normalized score plotted against wing aspect ratio and sensor quantity – two key design parameters for the *MACH 5* aircraft. The area above the red line represents the “feasible” aspect ratio region based on the team’s experience with low aspect ratio aircraft. The black dot indicates the highest scoring configuration, utilizing an aspect ratio of 4 and a payload of 2 sensors. Further analysis indicated that the best sensor length was 18 inches. Therefore, the top scoring aircraft should be designed to deploy one 18-inch-long sensor as well as store two sensors of the same length in cargo containers for another mission. This should include a wing characterized by an aspect ratio of 4 and a total span of 60 inches. The aircraft was sized with a thrust of 10.8 lb-f and MTOW of 18 lbs. The estimated cruise velocity is 64 mph.

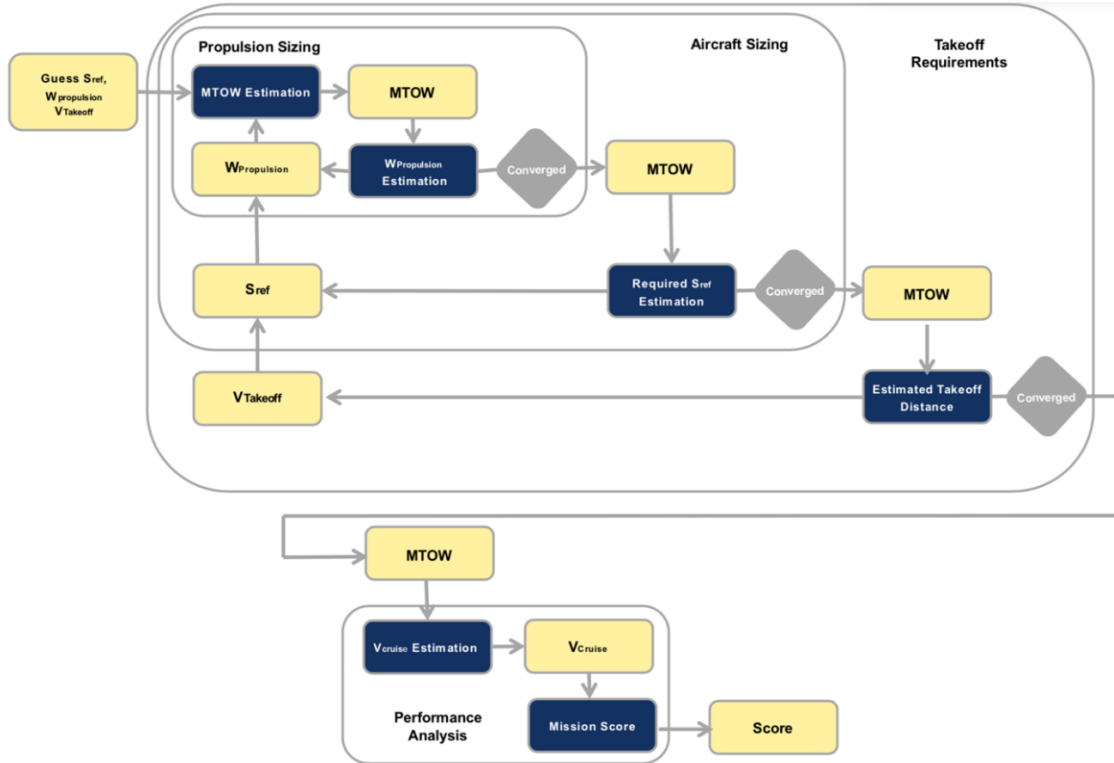


Figure 8: Sizing Analysis Flow Chart

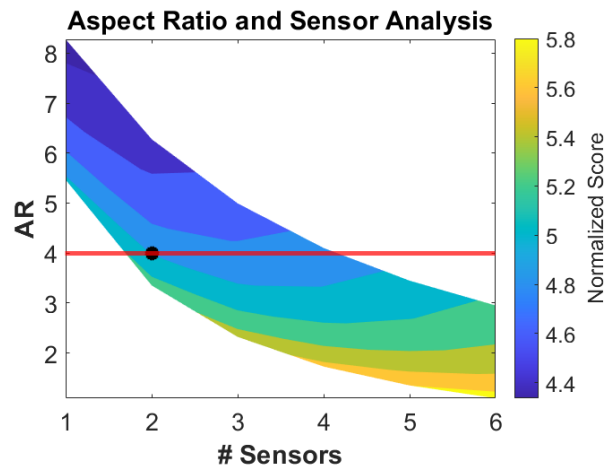


Figure 9: Scoring Analysis Results

4.2.3 Tail Sizing Analysis

The tail of the aircraft was sized using the volume coefficient method (Equations 4.11 and 4.12)

$$S_{VT} = \frac{c_{VT} b_W S_W}{L_{VT}} \quad (4.11)$$

$$S_{HT} = \frac{c_{HT} \bar{c}_w S_w}{L_{HT}} \quad (4.12)$$

Our initial vertical tail volume coefficient (c_{VT}) was 0.07 and our initial horizontal tail volume coefficient (c_{HT}) was 0.8, consistent with the values used for twin-engine, general aviation aircraft from Raymer [3]. Minimization of mass while achieving these specifications was critical for our purposes. We therefore utilized a basic MATLAB script, setting upper and lower bounds for tail length of 60 inches and 20 inches, respectively, from quarter-chord of the wing to the quarter-chord of the tail. Assuming a fixed mass per length for the tail boom and a fixed mass per tail area we constructed a code to optimize our tail size. Assuming Raymer’s recommended vertical and horizontal tail aspect ratios of 1.3 and 3, respectively, the script resulted in an initial tail placement at 45.96 inches behind the wing leading edge, with a horizontal tail area of 167.067 square inches and a vertical tail area of 60.144 square inches [3]. Figure 10 shows the results of the MATLAB tail placement script.

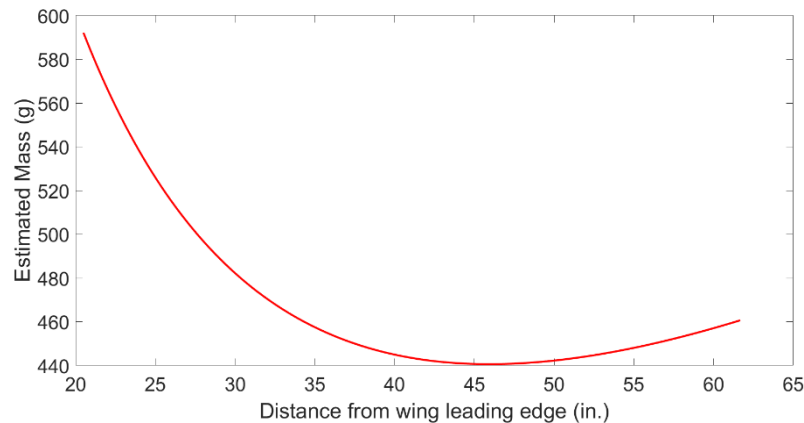


Figure 10: Overall Tail Mass as a Function of Tail Placement

Based on these initial results, we used AVL to confirm the stability of our preliminary design (as detailed in section 4.4). Given that our initial minimum mass estimates satisfied our requirements for stability, we settled on the tail sizing results from our MATLAB script. This included vertical and horizontal tail chords of 6.802-inches and 7.463-inches, and spans of 8.842 and 22.387-inches, respectively.

Although our assumptions about fuselage size changed, decreasing our effective wing area and tail size, given the difficulty of changing a key component of our detailed design, as well as our desire to maximize the stability of the aircraft, we decided to keep our initial tail sizing estimations.

4.2.4 Control Surface Sizing Analysis

Control surface sizing was based on Raymer’s recommendations for sizing [3]. This aileron sizing was chosen to be 25% of the chord and 40% of the span. Using Raymer’s exact recommendations, our tail control surfaces were sized to be 33% of the chord and 100% of span.

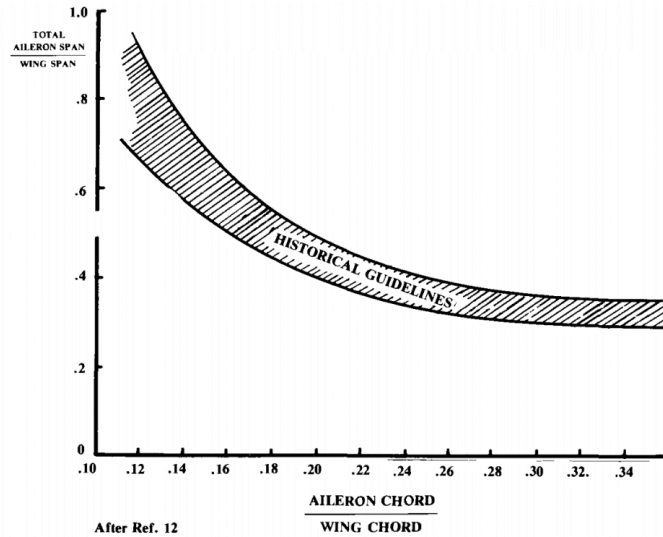


Figure 11: Historical Sizing Guidelines from Raymer [3]

4.3 Design Trade Studies

Preliminary trade studies were conducted to determine the ideal aircraft configuration, aerodynamic performance, and sensor configuration to move into detailed design. These are summarized below and draw on the aircraft sizing calculations discussed in Section 4.2.

4.3.1 Airfoil Selection

Due to the high-load characteristics of our mission specifications, airfoil selection is critical in achieving our desired payload capacity. To achieve this high-lift requirement, we prioritized maximum lift, creating a lower lift coefficient bound for candidate airfoils of 1.4. We then began a detailed search of high-lift airfoils, simultaneously considering the drag characteristics and manufacturability of candidate airfoils. Overall, our criteria for the selection of candidate airfoils were (in order of importance) maximum lift, low drag, and ease of manufacturability.

Our search from data on *airfoiltools.com* yielded three candidate airfoils: the Boeing 103, the NACA 4412, and the Clark Z [4]. Each of these were selected due to their high lift capabilities, high stall angles of attack, and ideal shapes for manufacturing. We used data from XFOil viscous analysis for our more detailed analysis of these candidate airfoils. First, examining the lift characteristics of the candidate airfoils, we found them to have maximum lift coefficients of 1.473 at 16.5-degree angle of attack, 1.445 at 15.3 degrees angle of attack, 1.385 at 13.5-degree angle of attack, respectively, at our takeoff Reynold's number of 200,000. Using our preliminary design wing area of 708.75 square inches and our desired cruise speed of 28.61 meters per second, we arrived at a cruise lift coefficient of 0.363. At this lift coefficient and a cruise Reynold's number of 600,000, our candidate airfoils had drag coefficients of 0.00715, 0.00776, and 0.00877, respectively. Based on the results from XFOil, we selected the Boeing 103 airfoil due to its superior lift characteristics, low drag at cruise, and its simple geometry.

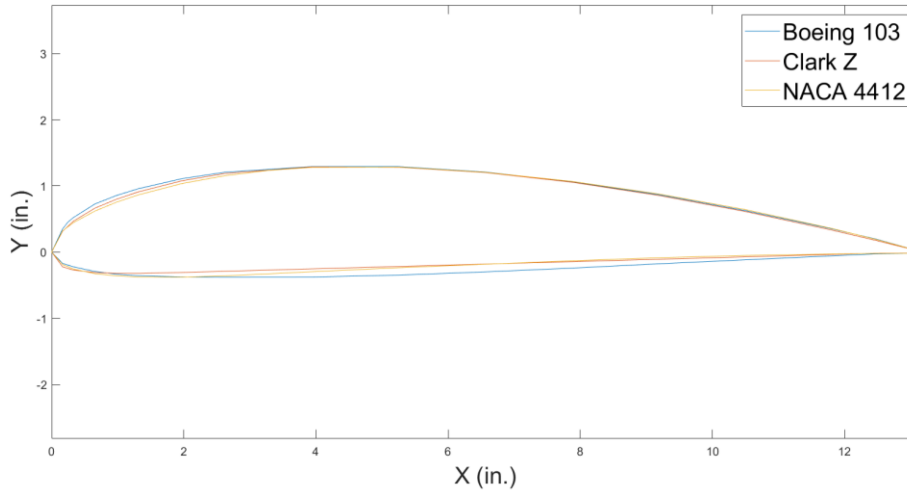


Figure 12: Candidate Airfoil Geometries

4.3.2 Wingtip Plates

A small yet significant trade study conducted was the investigation into the effects of wingtip devices on *MACH 5*. To examine these effects, Mark Drela’s Athena Vortex Lattice program was used. Because AVL cannot properly model wingtip plates due to its simple geometry input method, 1.25-inch winglets were used to model the effects of general wingtip devices. Figures 13 and 14 show AVL geometries with and without the winglets.

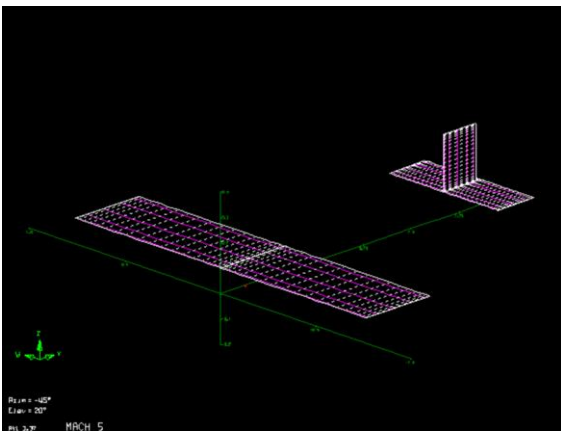


Figure 13: AVL Geometry without Winglets

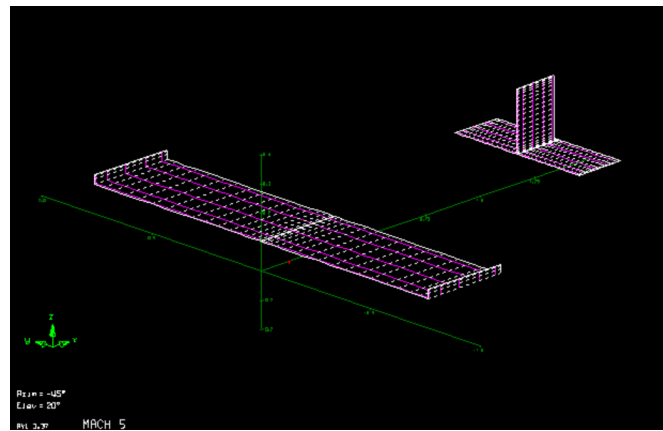


Figure 14: AVL Geometry with Winglets

Using AVL, lift and drag analysis was conducted on the two designs. Overall, the geometry with winglets was found to produce more lift at takeoff and slightly less drag at cruise than the geometry without winglets. Because of the improvement in lift and drag characteristics, it was decided to add wingtip plates to the ends of the wings of *MACH 5*, due to their extremely simple design and similar conceptual effects to the modeled winglets. The lift and drag results from AVL are shown in Table 8.

Table 8: Effect of Wingtip Devices on Lift and Drag

Design	C_L at takeoff	C_D at steady level flight
Without Winglets	1.715	0.01010
With Winglets	1.761	0.00970

4.3.3 Sensor Design

A significant component of MACH’s design requirements is the creation of an aerodynamically stable towable sensor. As a result, quantitative and qualitative analysis was performed on several preliminary sensor designs.

In order to maintain aerodynamic equilibrium, the sensor requires stabilization surfaces, such as fins. Conceptually, aerodynamic stability is the effect of a restoring moment exerted on the sensor. This restoring moment is created by a force exerted aft of the tether attachment point (chosen specifically to be the center of gravity for ease of deployment and retraction), causing the sensor to move back to its equilibrium position. In order to maximize this moment, it was decided to place all aerodynamic surfaces at the rear of the sensor, shifting the center of this restoring moment (the neutral point) towards the rear of the sensor, subsequently increasing the sensor’s static margin.

To optimize the performance of the sensor, a trade study was performed that examined the drag and stability characteristics of two potential sensor designs with different stabilization surfaces. Design 1 exhibited rectangular fins mounted on the rear portion of the sensor, and design 2 exhibited the same fins as design 1, but with an added, shuttlecock-inspired cone mounted on the rear of the sensor to provide additional drag and stabilization.

In order to obtain the drag characteristics of each design, CFD analysis using ANSYS Fluent was performed with each of the configurations. For angle of attack values from 0 to 24 degrees and at the design cruise speed, 64 mph, the drag force on the sensor was found. As shown in Figure 15, the shuttlecock cone on sensor design 2 resulted in it producing significantly more drag than design 1.

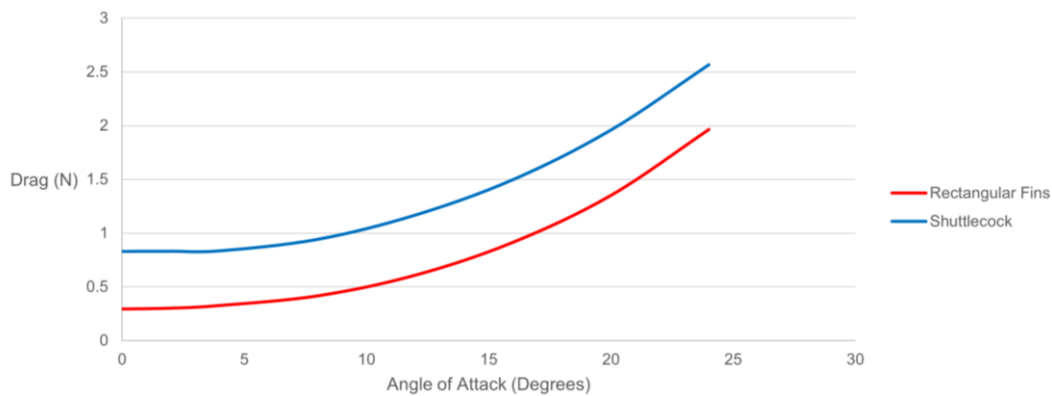


Figure 15: Sensor Drag vs. Angle of Attack

Because it was chosen to attach the tether to the sensor’s center of gravity, a crucial parameter in the drag analysis of the sensor is its drag at zero angle of attack, as this is the extra drag force exerted on the system when the sensor is in its equilibrium position (neglecting tether effects). In addition to the impact on the aerodynamic performance of the aircraft, this drag force will create an equilibrium tether angle relative to the vertical direction. Because of the bomb-bay nature of the sensor deployment mechanism, minimizing drag, and therefore minimizing this tether angle, was placed at high priority. The zero angle of attack drag values of each potential sensor design as well as their equilibrium tether angles are shown in Table 9. These tether angles were obtained using a simple force balance, assuming zero lift and the estimated sensor weight, as shown in equation 4.13.

$$\theta_{tether} = \arctan\left(\frac{D_{0\alpha}}{M_{sensor}g}\right) \tag{4.13}$$

Table 9: Zero Angle of Attack Drag and Equilibrium Tether Angle

Sensor Design	$D_{0\alpha}$ (N)	θ_{tether} (degrees)
Design 1 (Rectangular Fins)	0.292	2.663
Design 2 (Shuttlecock)	0.832	7.549

Also influential in the choice of a sensor design point was the stability of each potential design. To examine this stability, CFD analysis was used to obtain the pitching moment of each sensor design around the desired center of mass, at the design cruise speed, and for angle of attack values from 0 to 24 degrees. As shown in Figure 16, and by the negative $C_{m\alpha}$ values shown in Table 10, both sensor designs are statically stable around the predicted sensor CG, with design 2 (the shuttlecock design) yielding a slightly stronger restoring moment than design 1.

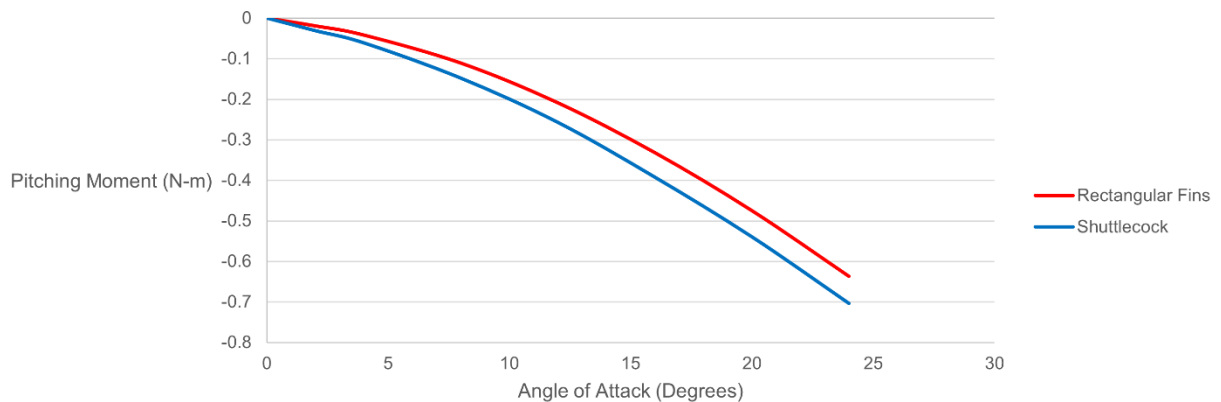


Figure 16: Sensor Pitching Moment vs. Angle of Attack

Table 10: Sensor Design $C_{m\alpha}$ Values

Sensor Design	$C_{m\alpha}$ (deg ⁻¹)
Design 1 (Rectangular Fins)	-0.0097
Design 2 (Shuttlecock)	-0.0155

While static stability is an indicator of the overall aerodynamic stability of the sensor in flight, dynamic stability analysis is necessary to examine whether the restoring forces and moments created by static stability will cause the sensor to tend towards an equilibrium position. Due to the lack of access to resources for physical testing, a MATLAB script was produced that took in lift, drag, and moment data obtained from CFD analysis and used forward Euler time integration to predict the motion of the sensor versus time. As shown in Figure 17, when offset from an equilibrium position, both designs tend towards an equilibrium position as time increases, indicating dynamic stability. While the shuttlecock design approaches the equilibrium point more quickly, the rectangular finned design has a lower tendency to deviate from its equilibrium position.

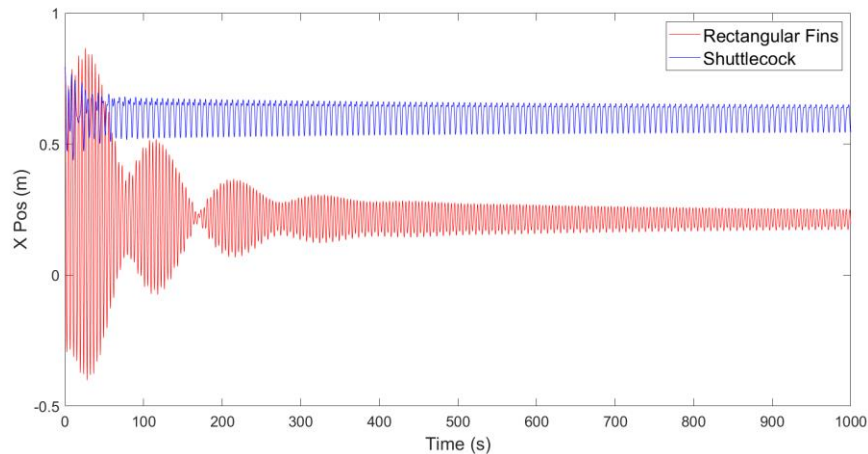


Figure 17: Sensor X Position vs. Time

Having analyzed the stability and drag characteristics of each potential sensor design, a decision was made to proceed forward with design 1, a sensor with rear mounted, rectangular fins. Although exhibiting slightly weaker stability than the shuttlecock-inspired design, design 1 has significantly lower drag, resulting in a lower tether angle and less risk upon deployment and retraction. This reduced risk ultimately results in it being the superior design choice.

4.3.4 Propulsion

Using the sizing code's estimate for system weight, thrust, and wing area accompanied with desired propeller and battery properties, ECalc, an open-source R.C. aircraft performance calculator, was used to sift through a database of common manufacturers to obtain system characteristics and projected

performance data. During this stage, the competition stipulated that one propulsion system setup would be flown in all missions; this was updated in the competition Q&A #1 where different configurations were allowed. When selecting components, two different sets of two 5-cell battery packs are exchanged between missions to switch between the desired flight endurance with the lighter system weight.

Table 11: ECalc Simulation Results: 5S 10000-mAh Battery

Motor Model	kV	Prop Size	Max Current (A)	Max Elec. Power (W)	Max Mech. Power (W)	Max Thrust (oz)	Stall Speed (mph)	Specific Thrust (oz/W)	System Weight (oz)
Turnigy PropDrive v2 4258	500	15x8	49.70	884.0	771.7	144.3	42	0.16	85.6
Dualsky ECO 4120C	430	15x10	40.95	733.2	656.2	139.5	42	0.17	84.0

Once the list of configurations was populated, the propulsion team narrowed the field by using additional criteria to optimize the top contenders. Next, the system weight was generally higher because of the motor configuration, so we looked at the overall system mass of the battery and motor combinations. These values were then normalized and only the top 25% of choices were kept. From this, the team obtained the top three systems that would theoretically produce the best results. Shown in Table 11 above, the first two were the most versatile since we could purchase the motor and exchange the propeller to collect empirical data.

Analyzing these results, we see that the Turnigy PropDrive v2 4558-500 motor coupled with a 5-cell battery and 15x8 propeller produces the most promising results with a stall speed of 42-miles per hour. Using an estimate for the maximum aircraft weight of 18- pounds or 288- ounces, this system is projected to result in a thrust-to-weight ratio of approximately 1.0. This was higher than the desired system, however it was selected as it was closest to the estimated propulsion system weight given in by the preliminary sizing study. The team chose to stay with the additional available thrust as it could provide additional acceleration in takeoff to compensate for any inaccuracies presented by ECalc.

It was very quickly seen that LiPo batteries were the most optimal as they have a twice the energy density with respect to mass and velocity compared to Nickel based batteries allowing for battery packs with the same amount of capacity and discharge rate at a much lower mass [5]. The two 5-cell LiPo batteries used for each mission will have different mAh ratings to accommodate for different mission endurances and thrusts. The cargo mission requires an endurance of 6-minutes, thus the system benefits by using an 8000 mAh system and having a lighter propulsion weight. The sensor mission is longer and will require 11 minutes of reliable flight time, thus the 10000-mAh configuration will be suitable for increased flight endurance. The ECalc-simulated trade study can be found below in Figure 18.

Our preferred motor draws a maximum of 49.7 amps, but because we were unsure of possible alterations to the configuration and overheating with a lower rated ESC, we selected 80-amp ESCs.

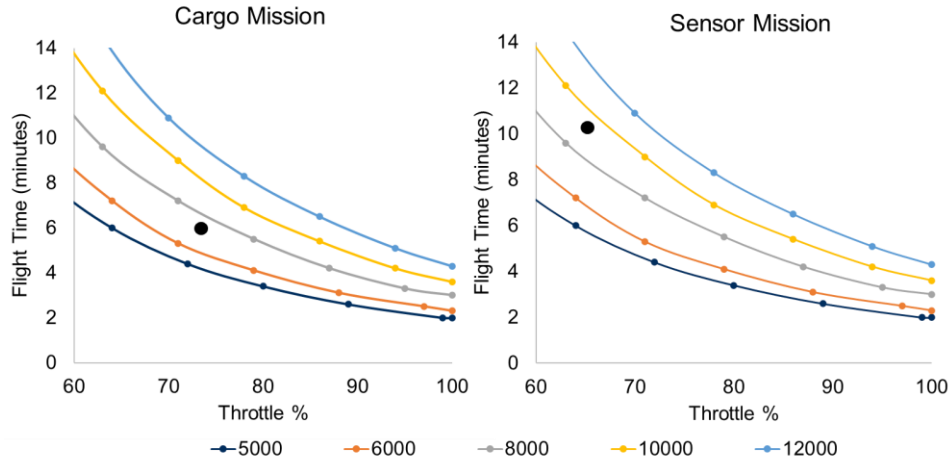


Figure 18: ECalc Battery Endurance Trade Study

4.4 Aircraft Stability

Our stability analysis used the vortex lattice method based AVL by Mark Drela to find our stability derivatives as well as to find our neutral point. We found our neutral point to be 7.02 in behind the leading edge of the wing. Our stability derivatives are below and were found to all have the correct sign. Since AVL produces relatively basic simulation of the aircraft, we did not consider the magnitudes, only the sign. These were calculated at our cruise conditions of 28.61 meters per second and an angle of attack of 0.8824°.

Table 12: Stability Derivatives during Cruise

$C_{L\alpha}$	5.05	$C_{m\alpha}$	-0.80	$C_{Y\beta}$	-0.18	$C_{Y\delta r}$	0.00	C_{Yp}	0.06	C_{Yr}	0.31
$C_{L\delta e}$	0.01	$C_{m\delta e}$	-0.03	$C_{l\beta}$	-0.09	$C_{l\delta r}$	0.00	C_{lp}	-0.65	C_{lr}	0.19
C_{Lq}	8.54	C_{mq}	-17.44	$C_{n\beta}$	0.14	$C_{n\delta r}$	-0.00	C_{np}	-0.03	C_{nr}	-0.25

Table 13: Stability parameters of *MACH 5*

Static Margin	15 %
Elevator Deflection During Cruise	0.00003°

4.5 Dynamic Stability

AVL was also used to analyze the dynamic stability of *MACH 5*. Overall, three run cases were executed on the aircraft, composed of the cases of steady level flight (run case 1), a banked turn (run case 2), and takeoff (run case 3). For each run case, an Eigen mode calculation was performed, and the dynamic stability eigenvalues were recorded. The real and imaginary components of each eigenvalue for run cases one, two, and three are shown in Figure 19. As shown in the figure, all but two of these eigenvalues are

composed of a real component less than zero, indicating the tendency for inflight oscillations to diminish, and the tendency for the aircraft to approach stable flight in most cases. Both positive eigenvalues characterize the aircraft's spiral instability. As most aircraft exhibit spiral divergence to some extent, these positive eigenvalues do not take away from the overall dynamic stability of the aircraft.

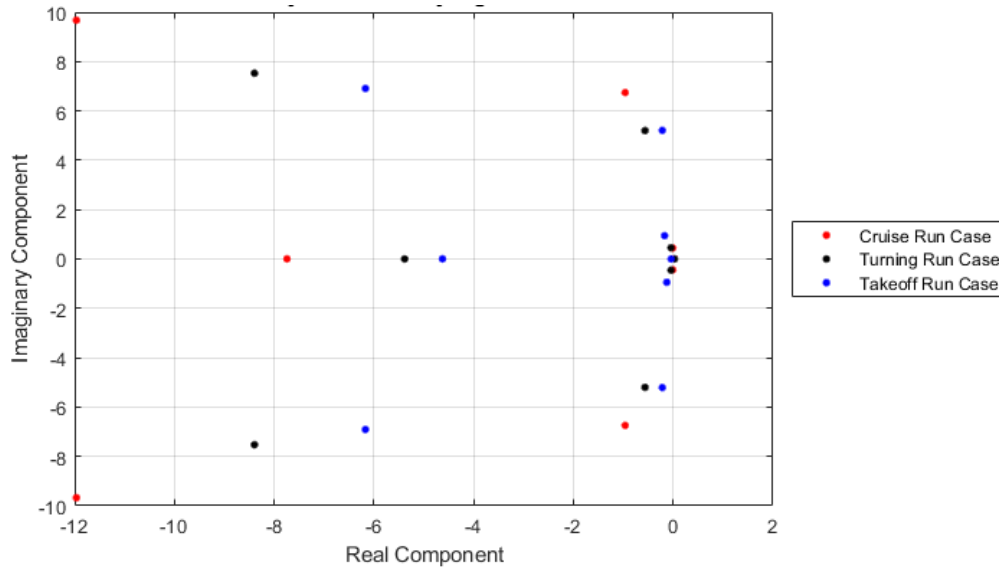


Figure 19: Dynamic Stability Eigenvalues

4.6 Sensor Stability

Due to the inability of AVL to analyze viscous flow, and the unique effects of a tether on the motion of the sensor body, the drag characteristics and stability of the towed sensor was analyzed through CFD simulation with ANSYS Fluent. As discussed in section 4.3.3, lift, drag, and pitching moment data was collected at cruise conditions for angles of attack from 0 to 24-degrees. The critical component of the sensor drag analysis is the drag force produced by the sensor at its equilibrium position, or at an angle of attack of zero. A small equilibrium drag force of 0.292-N indicates that the system is not significantly affected by the added drag of the sensor, and that the sensor will maintain a low tether angle of 2.663 degrees with respect to the horizontal, allowing for ease of deployment and retraction. Furthermore, a C_{m_α} of -0.0097 deg^{-1} , corresponding with a decreasing pitching moment with respect to angle of attack, as shown in Figure 20, indicates that the sensor is statically stable.

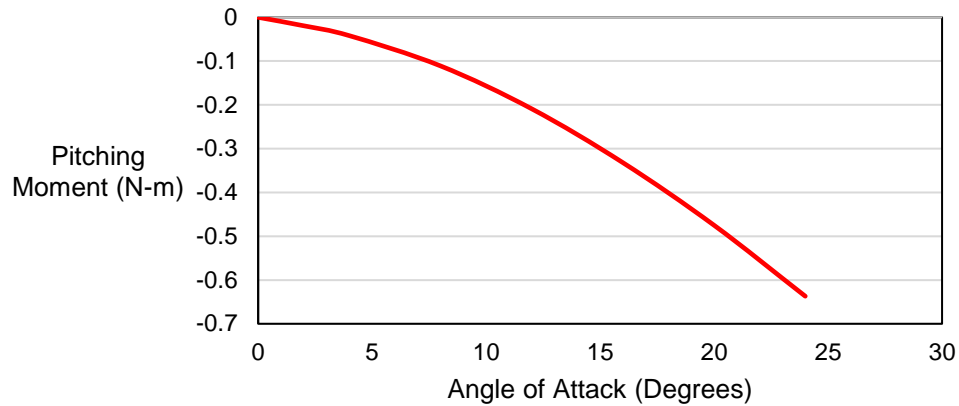


Figure 20: Sensor Pitching Moment vs. Angle of Attack

Although difficult, the lift, drag, and moment data were used in conjunction with a MATLAB program to estimate the dynamic stability characteristics of the sensor. As shown in Figure 21, when offset from equilibrium, the sensor tends towards an equilibrium position, indicating dynamic stability.

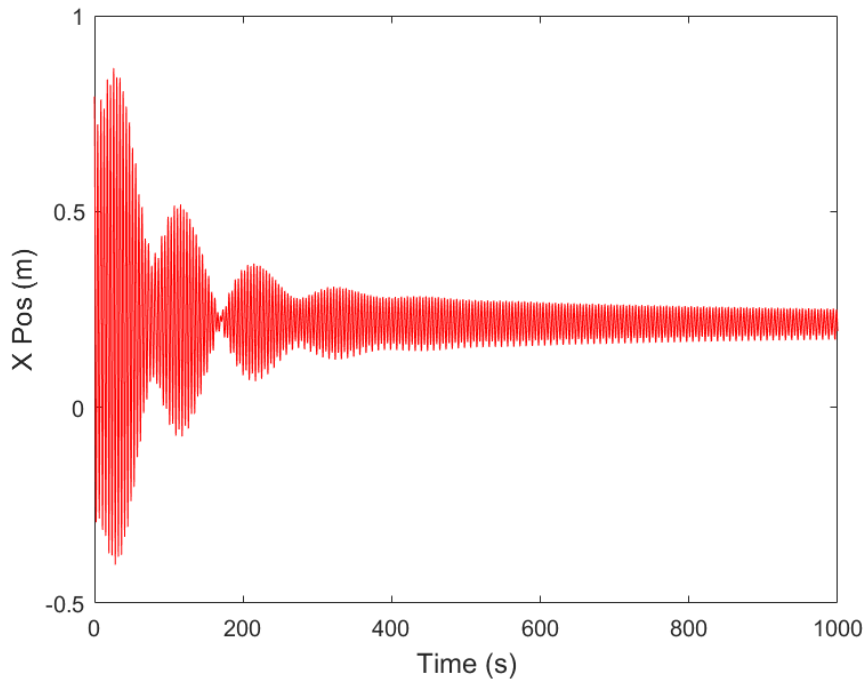


Figure 21: Sensor Position vs. Time

4.7 Lift and Drag Estimations

Using physical constants, as well as the dimensions and cruise speed of *MACH 5*, it was possible to estimate a necessary cruise lift coefficient with the rearranged lift equation, equation 4.14.

$$C_{Lcruise} = \frac{MTOW}{\frac{1}{2}\rho v_{cruise}^2 S_W} \quad (4.14)$$

Using this cruise lift coefficient of 0.3936, AVL was used to determine a cruise angle of attack of 0.882 degrees, and subsequently a roughly estimated cruise drag coefficient of 0.009700. AVL was also used to perform lift and drag analysis at takeoff, yielding lift and drag coefficients of 1.761 and 0.1961, respectively. Using the design parameters of *MACH 5* and equations 4.15 and 4.16, the lift and drag forces on the aircraft at cruise and takeoff were calculated. In addition to the drag from the wing given by AVL, the fuselage produces a significant amount of drag. Assuming the fuselage is a rectangular prism with a drag coefficient of 2.5, a conservative estimate for total drag was obtained using the following equations. These estimates are shown in Table 14.

$$L = \frac{1}{2}\rho v^2 S_W C_L \quad (4.15)$$

$$D = \frac{1}{2}\rho v^2 S_W C_{Dwing} + \frac{1}{2}\rho v^2 A_{fus} C_{Dfus} \quad (4.16)$$

Table 14: Estimated Lift and Drag Properties of *MACH 5*

Flight Condition	Lift (N)	Drag (N)
Cruise	80.854	50.154
Takeoff	361.776	12.010

4.8 Estimated Mission Performance

Using our estimated cruise speed of 64mph and an estimated course length of 3800-ft, we expect our aircraft to complete the competition course in approximately 40-seconds. Based on this approximation, we expect the aircraft to complete missions 1 & 2 in 140-seconds – a 20-second buffer is included to consider takeoff and climb. Using the same methodology, we expect the aircraft to complete 14 laps during the 10-minute endurance window of mission 3. We also expect our aircraft to score high based on the aircraft payload of 2-18inch sensors. This was chosen to maximize our score as explained in the scoring section. Based on physical testing – which will be discussed later in this report – our aircraft produces enough thrust at 60% throttle to sustain cruise for over 16 minutes, well over the required endurance limit of 10 minutes.

5 DETAIL DESIGN

Detail design was the final step before full-system fabrication and focused on the specificities of each subsystem and their integration. This includes full structural build ups of the wing, fuselage, motor mount configuration, landing gear, and tail as well as the design of all individual mechanisms. The detail design phase continued through initial fabrication and ground testing to adapt to construction challenges as well as testing results.

Table 15: MACH 5 Dimensions

Overall			Wing		
Length	4.957	ft	Span	4.333	ft
Width	5.000	ft	Chord	1.094	ft
Height	1.618	ft	Area	4.740	ft ²
Static Margin	15.0	% Chord	Aspect Ratio	4.0	
Vertical Stabilizer			Horizontal Stabilizer		
Span	0.75	ft	Span	1.875	ft
Chord	0.627	ft	Chord	0.625	ft
Area	0.470	ft ²	Area	1.172	ft ²

5.1 Preliminary to Final Design Modifications

The initial design described in our proposal, with a guppy fuselage instead of a slab-sided fuselage and a sensor towed behind the aircraft required drastic redesigns after the DBF Q&A #1 was released on January 8th, 2021. Our previous sensor design with unfolding wings had to be scrapped in favor of our fixed-fin sensor. This also necessitated a change in deployment strategy, from being deployed from behind the aircraft to being deployed from a bomb-bay style door on the bottom of the aircraft. Due to this redesign, we chose a slab-sided fuselage in order to satisfy our interface requirements, as well as simplify construction and design of the fuselage. The Q&A also resulted in a reconsideration of our battery sizing, seeing that it was clarified that different battery configurations were now permitted for the different missions.

5.2 Structural Layout

The structural layout for each subsystem was designed to ensure that all loads had a proper load path to major load-bearing components. The loads experienced by the aircraft can be broken down into three categories. The propulsive loads include the loads applied to the wing due to thrust and motor torque, which can cause bending, torsion, and vibrations. The ground loads are the loads experienced due to impact during landing. The aerodynamic loads include the lift, drag, and moment loads imparted on the wings and tail, which lead to bending and torsion. The loads are transferred into the major load-bearing components, which include the wing spars, carbon fiber stringers, and the fuselage spar. The wing must withstand at least a 2.5-G load of its maximum weight during flight, as specified by the wing tip test, as all loads traverse to the spar attachment point connected to the main fuselage spar.

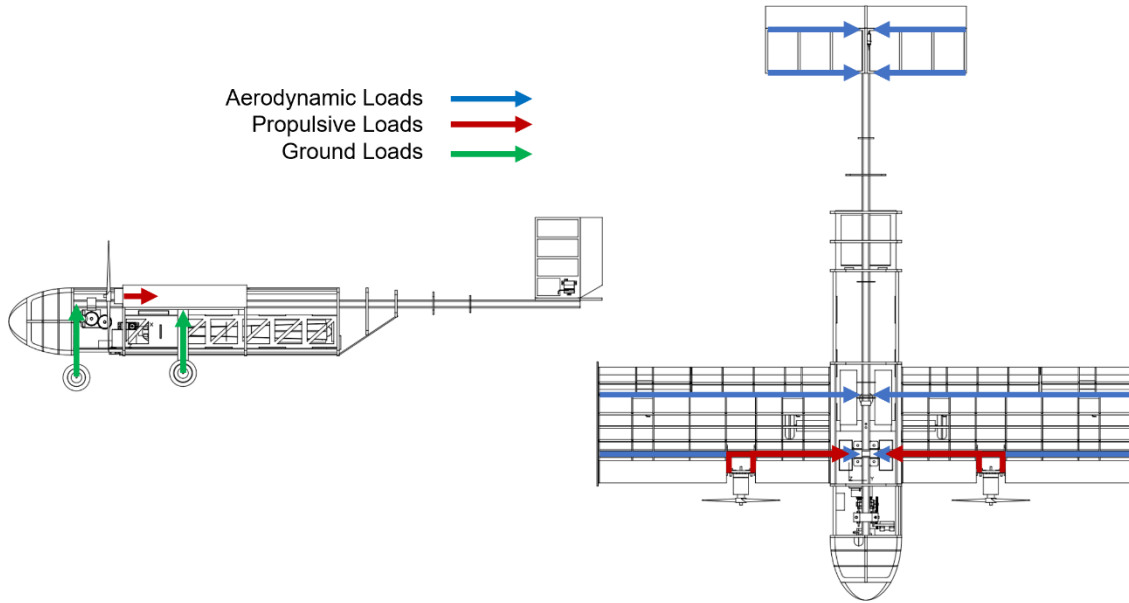


Figure 22: Load Path Diagram

5.3 System and Subsystem Design

5.3.1 Wing Design

The wing has a rib and spar construction covered with UltraKote to provide the most lift while minimizing mass. The wing consists of a 3/4-inch x 3/4-inch (inner diameter) square carbon spar located at the 1/4 chord and a 1/8-inch bass spar located at the 3/4 chord, interspersed with 1/8-inch balsa ribs. Flaps and ailerons each have 1/8-inch balsa spars located at their respective leading edge. Rib placement is based on servo locations, with one servo per control surface. Four stringers are located above and below the wing to help maintain the aerodynamic shape of the wing surface created by the UltraKote wrap. A foam leading edge and a carbon strip trailing edge create accurate aerodynamic surfaces and provide additional strength to the wing structure.

Each motor is mounted to a 1/4-inch bass plate sandwiched between two 1/8-inch bass plates, joined with aluminum L-shaped brackets and steel bolts. The two parallel bass plates are directly mounted to the square carbon spar. Our motor mount design was verified through FEA, performed in Siemens NX.

As shown below in Figure 23, a wing-bracket, located between the two sides of the wing, incorporates the wing structure into the fuselage. The square carbon spar runs through the wing bracket, which secures it to the main boom.

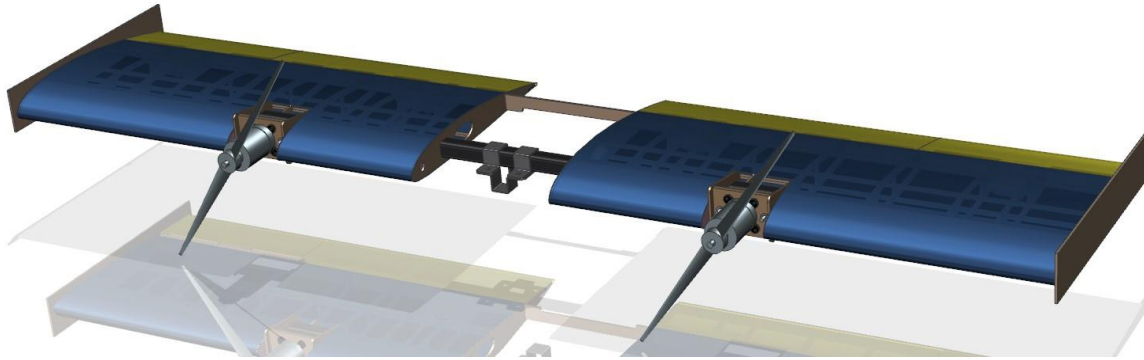


Figure 23: Full Wing Assembly with Wing-Bracket and UltraKote Skin

5.3.2 Tail

The tail is designed to provide sufficient directional stability and control and has been scaled up in size from that of the preliminary design. The final tail is a traditional tail design, consisting of a horizontal and vertical stabilizer. The elevator and rudder occupy roughly the rear one-third of the tail surface area and are movable up to a deflection of 30-degrees in either direction. 1/4 inch by 1/4 inch balsa wood stick build up is being used for the tail and standard elevator stock being used for the deflection surfaces. These will be actuated by metal gear servos as plastic gear servos were found to be stripped due to flight loads on previous aircraft of a similar size and role.

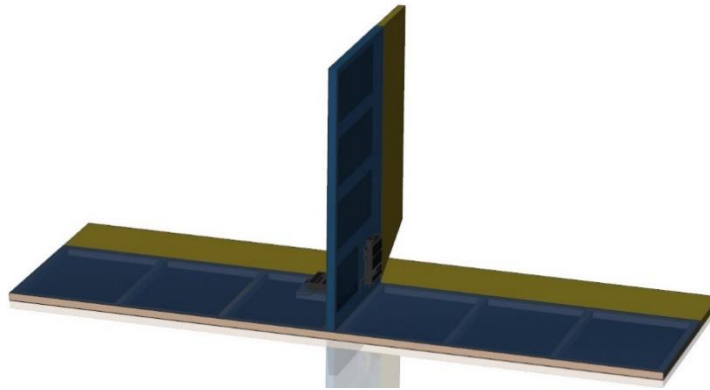


Figure 24: Tail Assembly with 1/4-inch by 1/4-inch Balsa Structure and UltraKote Skin

5.3.3 Fuselage Design

The fuselage is designed to hold all major electronic components and mission specific payloads, as well as to tie all major flight and ground induced loads together. The fuselage is composed of a variety of materials, with a series of wooden ribs and plates to create the shape and allow mounting of components, a main carbon fiber spar to absorb the structural loads, and carbon fiber tubes to increase torsional rigidity. The fuselage also serves to connect the tail boom, wing structure, and landing gear together. The voluminous

fuselage interior allows for the storage of the sensor deployment and retraction mechanism, as well as the max cargo payload of two 18-inch sensors and containers. The final fuselage design is shown below in Figure 25. The fuselage main structure was designed to remain as one piece after construction with the wing being removable. This is accomplished by 1/16-inch-thick aluminum brackets that directly connect the wing spar to the fuselage spar, adequately distributing any critical loads to the carbon fiber. Once all structural members were placed, a tail fairing was added at the rear of the fuselage, attached to the fuselage spar, that will improve aerodynamics of the fuselage by avoiding separation and the associated pressure drag on the aircraft. It also supports the rear fuselage door for cargo access.



Figure 25: Wood Fuselage with Carbon Supports

5.3.4 Sensor Restraint and Deployment System

The sensor restraint and deployment system, which is used in Mission 3, was designed to minimize loading and unloading time, provide an acceptable restraint for the sensor contained within the aircraft, and to enable deployment and retraction of the sensor remotely in flight. The components that make up this system include a sensor gripping claw – which is connected to a gear rack & pinion, a retractable bomb bay door, and a tether winding spool. The claw gear rack is driven by a servo motor, which pushes the claw into the cargo bay to secure the sensor and retracts it out of the cargo bay to release the sensor for mission deployment or removal from aircraft. Installing the sensor for the mission is a simple process consisting of remotely opening the bomb bay door underneath the plane, securing the tether inside the sensor with pins, then implementing the claw via remote control to restrain the sensor. During flight, when it is time to deploy the sensor, the pilot will initiate the process via remote control, opening the servo-controlled bomb bay door and retracting the claw from the sensor. The sensor will then drop out of the aircraft using its own weight and the resulting drag forces to unwind the 15-foot-long tether. To retract the sensor, the motor attached to the spool activates and winds the tether until it is fully wound up and the sensor is enclosed within the aircraft. At this point, the claw activates again and restrains the sensor in the cargo bay. Figure 26 shows

the layout of the claw and the sensor within the cargo bay, as it would be configured for Mission 3. The only changes needed for Mission 2 is replacing the sensor with the two shipping containers. MACH designed the cargo bay in this configuration to minimize the amount of space in the aircraft that we would need to take up for both Missions to succeed.

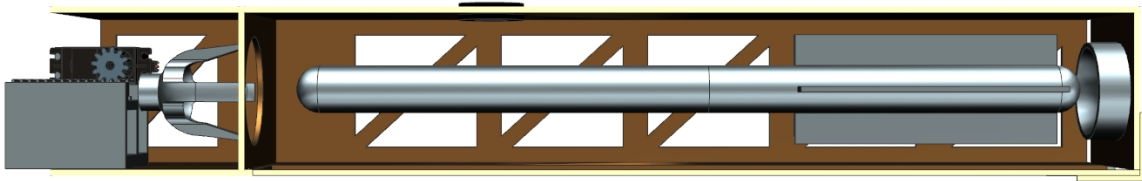


Figure 26: Side View of the Cargo Bay: Claw Mechanism and Sensor

5.3.5 Sensor Container

MACH constructed the sensor container using basswood walls and a sensor-fitting foam interior. These materials ensure that no matter which orientation the container will be dropped during the ground mission, the sensor will be protected from damage. The container is rectangular to best fit our 18-inch-long circular sensor with fins as well as to easily fit into the rectangular fuselage and cargo bay of the airplane during Mission 2. The dimensions of a single container are 18.35 x 3 x 2.75 inches, ensuring the sensor can fit within. The dummy container will also incorporate basswood walls with the same dimensions but will instead be ballasted internally with steel masses to match the weight and CG location of the real container and sensor for proper mass distribution in the cargo bay. MACH has tested these containers in the workshop, with a 3D printed model of the sensor shell and ballasts inside, but with no foam internal support. The containers were dropped from 10-15 inches height on all sides and there was no damage to the container or the sensor. The foam interior will be useful with the real sensor to protect the internal electronics from damage due to the shock of the drop.

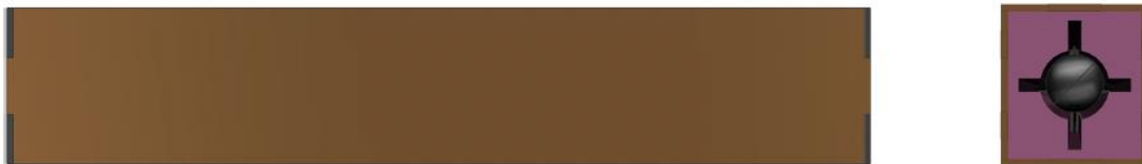


Figure 27: Model of Sensor Container: Removed Cover

5.3.6 Spool

The spool was designed to ensure reliability of the deployment process and to be strong enough to handle all aerodynamic and gravitational loads on the sensor during flight and retraction. The spool is sized with 1.1 inches of traverse length for the tether, 2-inch end diameters and a 0.5-inch inner barrel diameter. Since the spool needs to wind up a combined 20-gauge signal cable (0.036-inch diameter) and a braided Kevlar string (0.015-inch diameter), MACH used a conservative assumption of a 0.1-inch-thick tether to calculate that the spool could carry 18 feet of tether at a 75% perfect wind on the spool [6]. This gives the spool plenty

of margin while flying and retracting the sensor to minimize risk. The spool itself is powered by a DC motor which utilizes a 3-to-1 gear reduction to decrease speed and increase torque. At the front of the spool is a line-guiding mechanism, which helps prevent the tether from tangling and unevenly winding onto the spool during deployment and retraction. This guide is mechanically connected to the spool, to ensure that it is only activated while the spool is activated and to minimize risks and is driven back and forth linearly by a self-reversing screw, as can be seen in Figure 28.

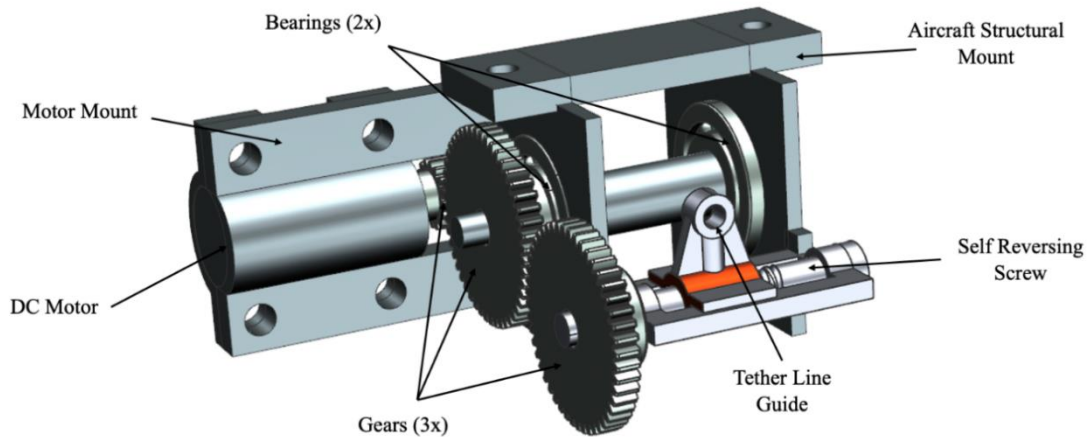


Figure 28: Layout of Spool System

5.3.7 Sensor Design

MACH's sensor is 18 inches long with a circular diameter of 1.1 inches. To comply with mission requirements, we determined that the electronics our sensor will carry are an Arduino mini to control the LEDs, 3 LEDs and 2 batteries. The sensor will also carry a 0.9-lb ballast to meet our final sensor weight of 1.41 lbs. The sensor is split up into 3 parts: the front half of the external shell, the back half of the shell, and an electronics tray that connects the two halves. These 3 components are 3D printed and are secured together with 4 pins from underneath. 3 of the pins have holes to fit the LEDs within them, and the pins have a rectangular head that locks the sensor when rotated. The electronics tray has a compartment for the batteries and Arduino, enabling easy access to the important components. The tether will be attached 5.6 inches from the nose of the sensor, which is the CG of the sensor. The tether is secured with two perpendicular pins that run through a loop in the end of the tether.



Figure 29: (Left) Sensor Internal Electronics Tray. (Right) First 3D Printed Sensor Model used for Testing

5.3.8 Propulsion

The propulsion system consists of the following main components: two motors, two propellers, two ESCs, two batteries, fuses, and a receiver. As stated in the preliminary design section, the Turnigy PropDrive v2 4258 motors utilize the 15x8 inch propellers, one per motor. The APC brand propeller was selected for its lighter weight, better thrust coefficient, and proven performance with the team. The 15x8 was chosen over the 16x10 propeller for its improved endurance with similar thrust performance. The Predator 80 Amp Brushless ESC was selected as the overall weight is relatively low, and it allowed for some versatility between the two propeller combinations as testing took place. For the batteries, two HRB 5s 18.5-volt LiPos wired in parallel were selected to stay under the 200 watt-hours system capacity and the individual 100 watt-hour per pack requirements set by the competition specifications. Along with another safety measure as stipulated by the specifications, the team will include inline blade-style fuses with each battery. The team will include one 80-amp maxi fuse per battery pack to satisfy this requirement using a fuse holder rated for 80 amps with 8 AWG. The calculations are shown below and are under the calculated maximum.

$$C_{\text{rating}} * \text{Current}_{\text{rating}} = \text{Max Fuse Rating} \tag{5.1}$$

$$50C * 5000\text{mAh} = 250A \tag{5.2}$$

The team will use a Spektrum transmitter in competition, so we will be using a receiver of the same brand to mitigate compatibility issues. The outline of the system is shown below in Figure 30 and depicts the exchange of power and signals between the separate subsystems.

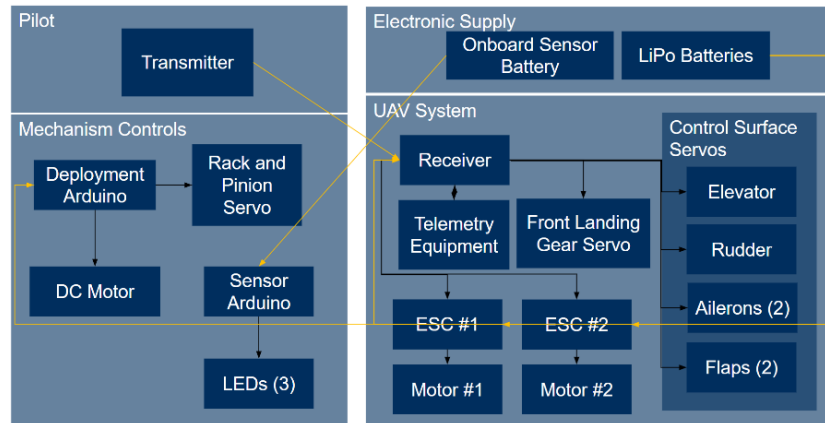


Figure 30: MBSE Outline of Electronics System

5.4 Weights and Balance

Siemens NX CAD software is used to estimate the center of gravity location for each aircraft component. The weights are generated through estimation based on component volumes with known densities, measured component masses, and previous MACH historical averages. Table 16 shows the estimates for each mission. The positive x-axis is measured from the main wing leading edge towards the tail and the positive z-axis is measured up from the center of the main fuselage spar.

Table 16: Weight and Balance Table for All Flight Missions about Quarter Chord

Component	Weight (lb)	CG _x (in)	CG _y (in)	CG _z (in)
Wing	3.41	3.02	0	0.83
Fuselage	1.91	11.66	0	-0.86
Vertical Tail	0.04	51.30	0	5.06
Horizontal Tail	0.09	51.70	0	0.56
Sensor Deployment/Retract Mechanism	0.46	-3.26	0	-1.38
Sensor Claw	0.38	0.36	0	-4.24
Nose Gear	0.31	-5.21	0	-6.40
Main Gear	0.43	7.0	0	-6.03
Arduino	0.02	-0.85	0	-4.91
2x Motors	1.34	0.4633	0	0.88
2x Propellers	0.19	1.35	0	0.88
6x Control Surface Servos	0.32	9.02	0	0.38
Nose Gear Servo	0.08	-3.5	0	-4.41
Bomb Bay Door Servo	0.04	-0.76	0	-5.37
2x Speed Controllers	0.36	3.7	0	-0.97
Receiver	0.04	-1.51	0	-4.50
2x Battery Pack	2.68	10.17	0	-0.42
Empty Total	12.5	6.10	0	0.09
M1				
Total	12.5	6.10	0	0.09
M2				
2x sensor payload	2.82	23.12	0	-3.08
2x sensor container	1.61	26.96	0	-3.08
Total	16.93	11.40	0	-0.84
M3				
Sensor Payload	1.41	23.12	0	-3.08
Total	13.91	7.35	0	-0.14

The table above shows the weight for each mission not including ballast. The vehicle is design such that the position of the CG can be moved using battery placement and ballast, making the aircraft stable in all flight configurations.

5.5 Structural Performance

All aircraft components are designed to withstand all loads expected in flight, during the ground mission, and during takeoff and landing.

5.5.1 Wing Structural Analysis

A model of the structural characteristics of the wing was created in MATLAB to determine the safety factor of the wing design. To accomplish this, we modeled the bending of the spar as the spar carries the bending

loads in the wing. We used a worst-case scenario of a 2.5 G load on the wingtips to analyze our spar using simple Euler-Bernoulli beam bending assumptions.

A diagram of the wing deflection is shown in Figure 31. As shown, we expect the wingtips to deflect about 0.44 in at the 1 G wingtip load. Our calculations also showed that our wing has a factor of safety of approximately 191 at a 1 G wingtip test. The spar's properties were estimated using composites formulas, taking the modulus of elasticity of carbon fiber to be 33 Msi and that of the matrix to be 408 ksi, with a 0.4864 fiber volume fraction, as calculated based on the density listed on our manufacturer's website.

This type of spar has been used in the past with no structural issues and performance matching analysis, thus we are confident in its ability to withstand flight loads.

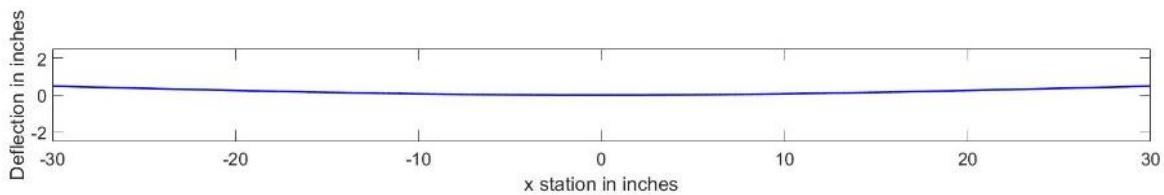


Figure 31: Expected Wing Deflection under Wingtip Loading

5.5.2 Wing Structural Design Trade Study

We conducted a series of linked trade studies to determine the effects of internal rib number, four different leading-edge device, wing stringer numbers, and four different spar design on the weight, structural integrity, manufacturability, and cost of our wing. These trades involved modelling 41 simplified wings with different combinations of these elements, determining their mass, testing their maximum stress and tip deflections using Finite Element Analysis, and estimating overall cost and time to construct. Each category was weighted based on its importance to our craft. Max stress and tip deflection were given the largest weights followed by mass, time to construct, and then cost. Deflection results from the FEA analysis are given in Figure 32 below, as well as an image of the stress concentrations in the leading candidate wing.

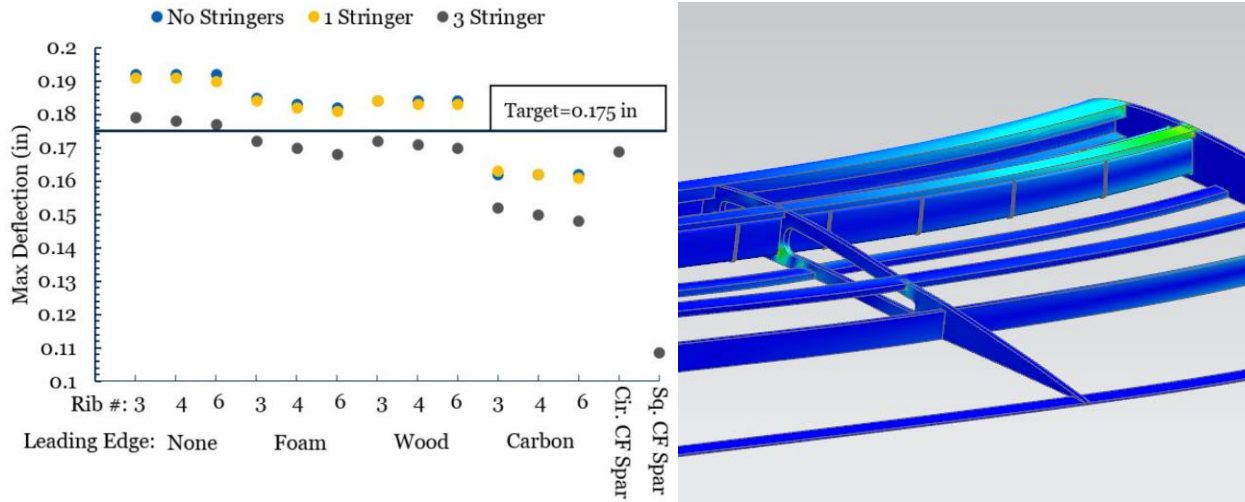


Figure 32: Max Deflection of Different Wing Candidates (Left) and Example Stress FEA (right)

From our analysis we determined that a wing with a square carbon fiber spar, three stringers, minimum number of ribs, and a foam leading edge was the ideal wing candidate out of all tested. This performed the well in the structural testing and time to construct and met our targets for both weight and cost analysis. Based on our cost benefit curve this was the ideal candidate based on our chosen weighting. This wing design was then implemented into the full aircraft wing design and a full design report was written as a guide to future wing design.

5.5.3 Wing Mount Structural Analysis

To mount the wing spar to the main fuselage boom, four bent U brackets made from aluminum were used to allow the wing to be removable with only four bolts. This is a critical structural joint and carries the entirety of the weight of the fuselage, tail, and landing gear in flight, and the weight of the wing when landed. To verify the integrity of this part, FEA was used to determine the maximum stress in this part. This analysis was done by modelling the assembly in NX with proper materials and conducting FEA using NASTRAN. The resulting stress can be seen in Figure 33 below. This figure represents a 2.5 G upward loading case on the wing spar to simulate maximum stress conditions with a fixed fuselage spar. Full spars are not modelled, just those closest to the joint. From this image we see the max stress is only 2,608 psi occurring at the inside corners of the aluminum U brackets. This is much less the aluminum's yield strength of 45,000 psi giving us a safety factor in this joint of 17.25 before non-elastic deformation. This was determined to be more than adequate for our purposes while still providing easy manufacturing and removal and this U bracket design was adopted and added to the full design.

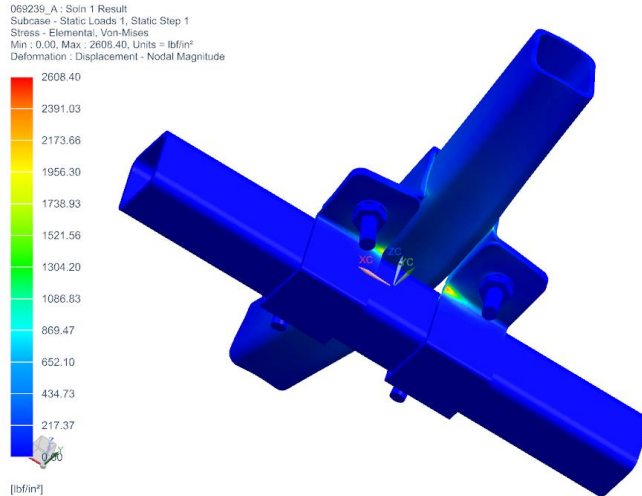


Figure 33: Stress in Wing Mount for 2.5-G Upward Load Case

5.5.4 Engine Mount Structural Analysis

Similar to the wing mount testing, FEA analysis was conducted on the joint to mount the motor to the wing spar to ensure its integrity and determine its safety factor. This was done by modelling the joint in NX and conducting FEA using NASTRAN. To simulate engine loads, the maximum throttle engine load of 8.17 lbs of forces was applied to the washers located in the faceplate that the engine would bolt onto. The locations where the joint would attach to the wing spar were given fixed constraints. All relevant surfaces were then either marked as contact or glued depending on the planned manufacturing. A fine mesh of this simulation results in the stress and deflection given in Figure 34 below.

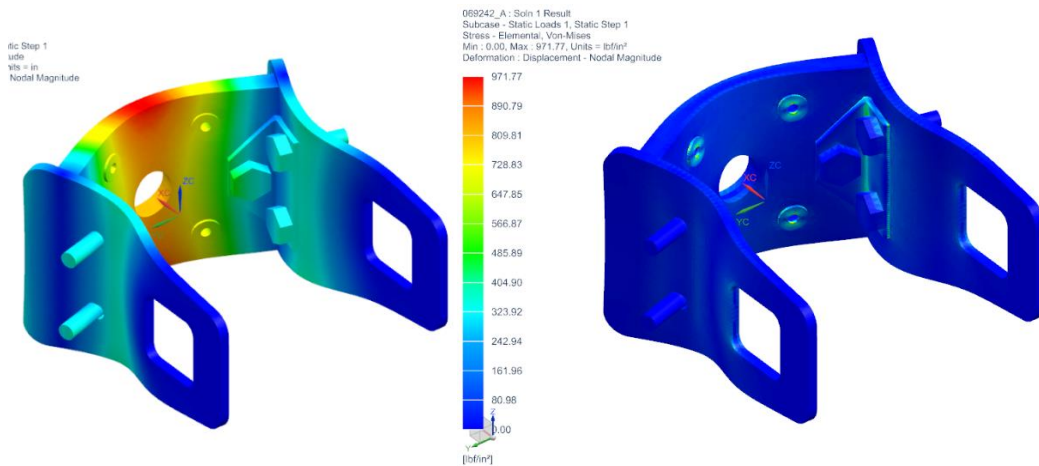


Figure 34: Displacement (Left) and Stress (Right) Results from FEA Analysis of Motor Mount

From this analysis we find the maximum stress occurs in the aluminum corner bracket with 971.77-psi or a safety factor of 46.3 in that region. Additionally, in the rest of the structure we see higher stresses in the steel washers which have a safety factor that is even higher based on a high yield strength. The lowest safety factor we see in the mount occurs in the low stress portion of the bass wood. Here we see stresses

between 0 and 240-psi which is under the worst case perpendicular to grain tensile strength of bass wood of 280. So, our worst-case safety factor at full thrust on this joint is in the bass wood at 1.16 SF. We increase this safety factor during construction by ensuring that the grain of the wood is in line with the thrust vector which gives an along grain ultimate tensile strength of 1710-psi giving a safety factor of 7.125. This safety factor was determined to be adequate and the design was adopted into the full design.

5.5.5 Landing Gear Structural Analysis

The carbon fiber main landing gear has been physically tested both with bench applied forces of up to 18-lbs without any major issues. Landing gears of similar construction have survived hard landings and crashes on several of our aircraft, some heavier than our current aircraft. Based on this, we consider our landing gear to be a low-risk item.

5.6 Performance Parameters and Expected Mission Performance of Final Design

The expected flight performance characteristics for the competition aircraft were calculated for each of the missions and are shown in Table 17 below. The aircraft dimensional and performance characteristics closely align with that produced by our sizing analysis presented in Section 4.2. The mission scores were calculated based on the scoring equation presented in the mission requirement Section 3.1 assuming that MACH scores the highest in all three flights out of all teams.

Table 17: Predicted Aircraft Performance Parameters

Performance Parameter	Mission 1	Mission 2	Mission 3	Ground Mission
W (lbs)	12.5	16.93	13.91	
Max Load Factor	3.39	2.50	3.04	
V_{stall} (ft/s)	39.50	45.98	41.67	
V_{max} (ft/s)	125.5	124.6	125.2	
Mission Score	1	2	3	1
Total Score: 7.0				

5.7 Drawing Package

This section contains a comprehensive drawing package for *MACH 5*. The package consists of a dimensioned 3-View drawing, structural arrangement drawing, system layout and location drawing, and a payload accommodation drawing.

1 2 3 4 5 6

A

B

C

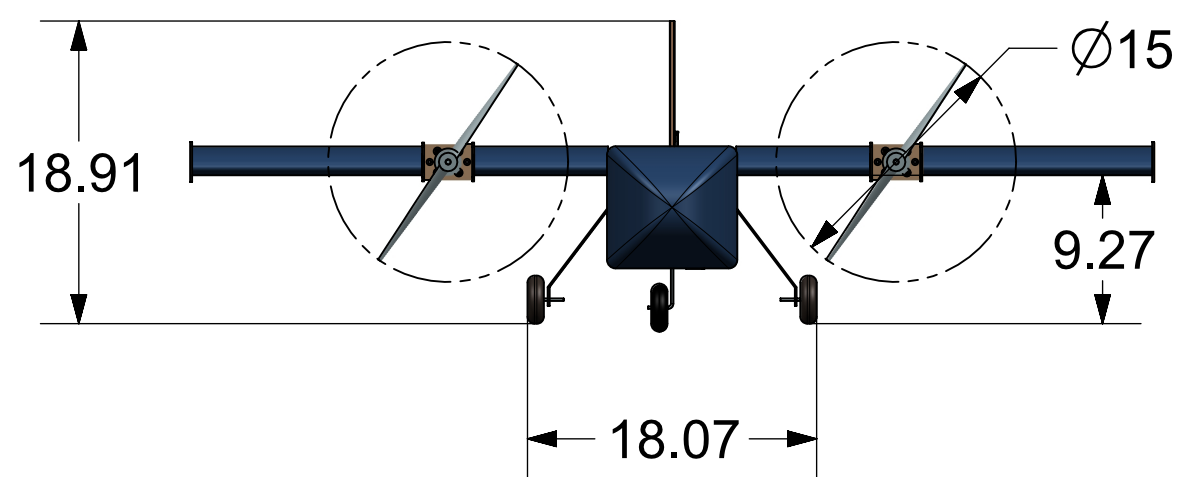
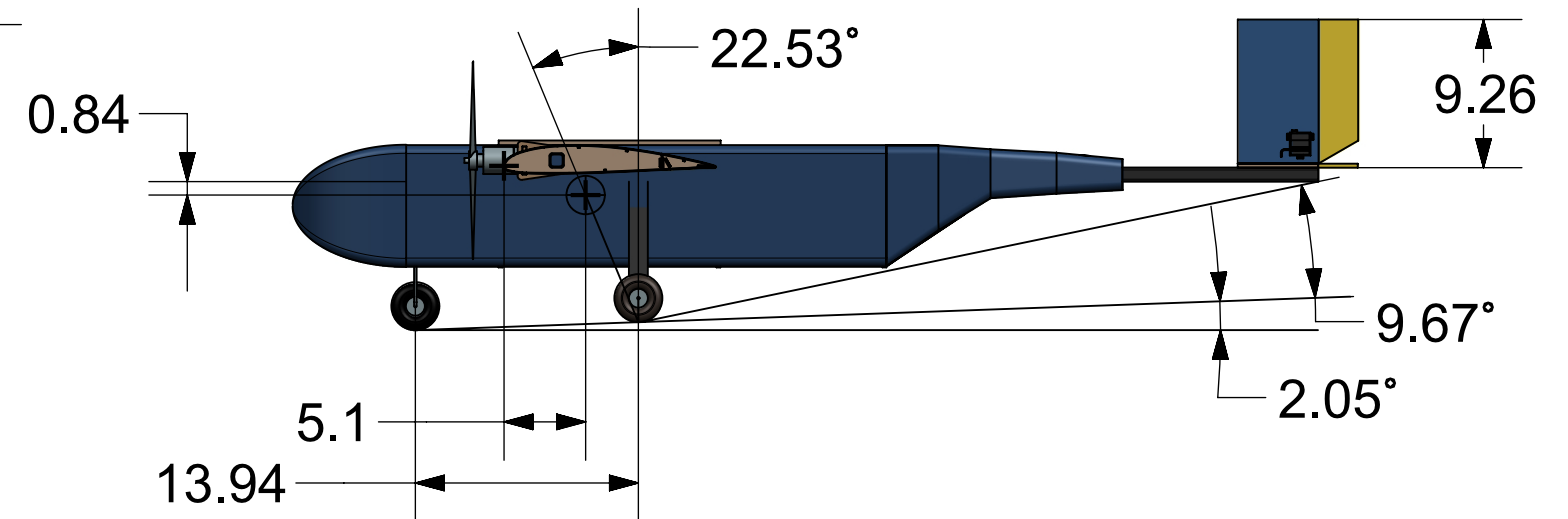
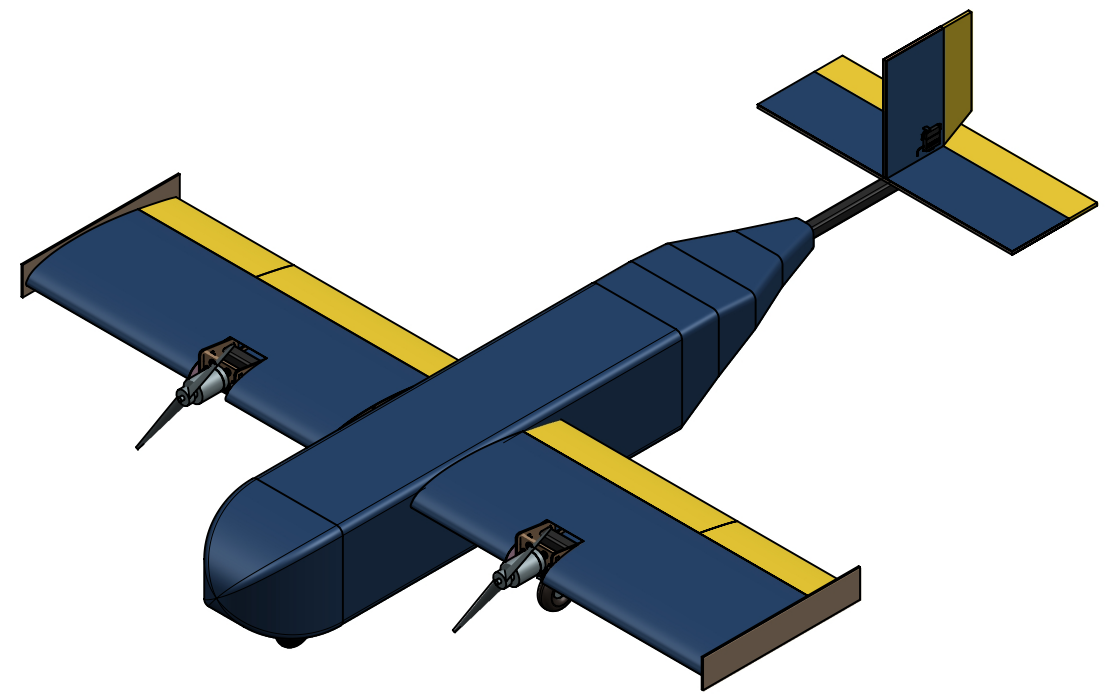
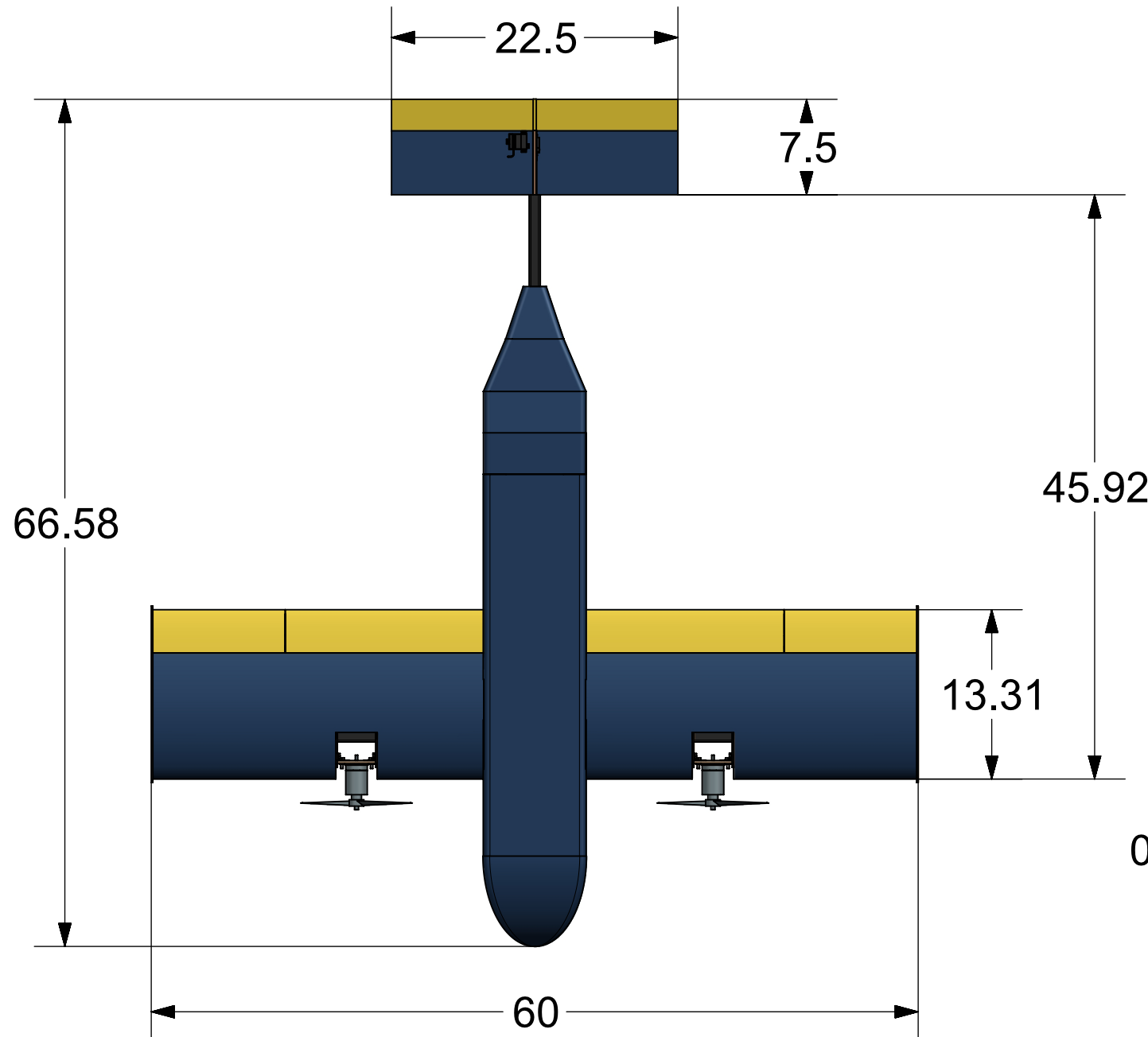
D

A

B

C

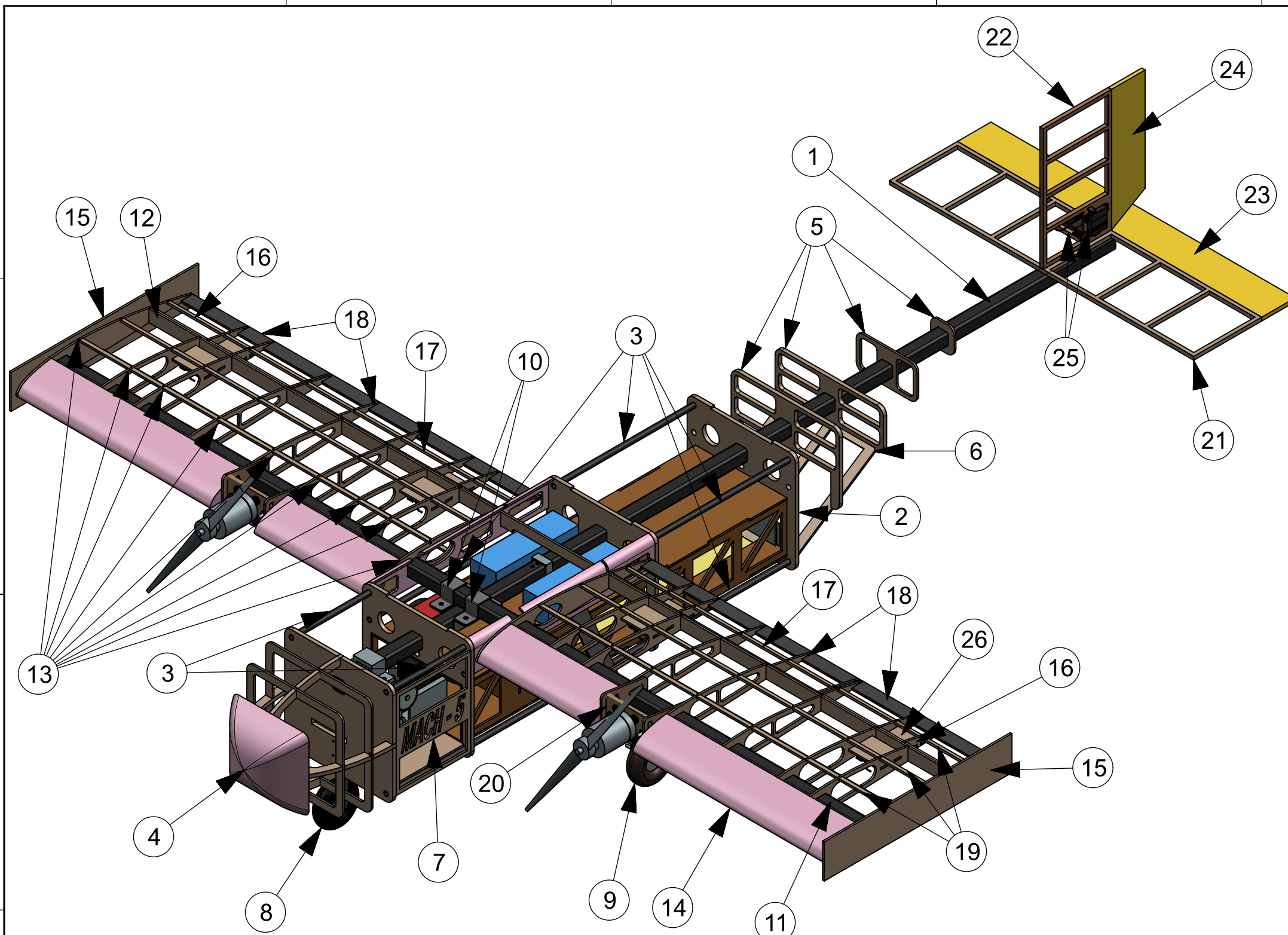
D



ALL DIMENSIONS IN INCHES

SIEMENS		UNIVERSITY OF MICHIGAN MACH		
FIRST ISSUED	G. CHIA	TITLE		
DRAWN BY	G. CHIA	3-VIEW DRAWING		
CHECKED BY	C. GIBBS			
APPROVED BY	T. PANGERL	SIZE	DRG NO.	SHEET REV
DATE	2/19/2021	B	MACH 5, DRAWING PACKAGE	A
		SCALE 1:12		SHEET 1 OF 4

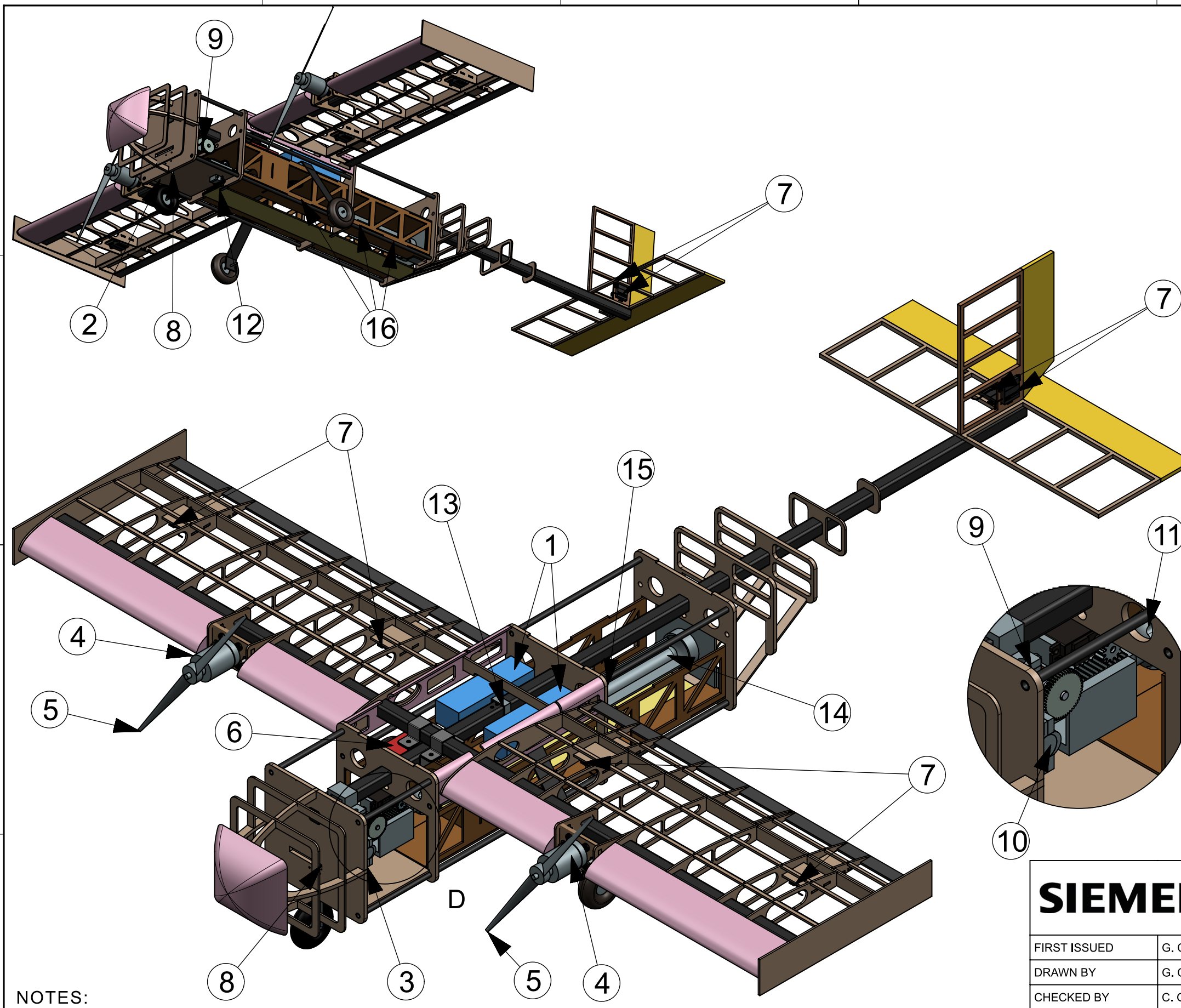
1 2 3 4 5 6



ITEM	Qty.	DESCRIPTION	MATERIAL
1	1	Fuselage Spar	Carbon Fiber
2	1	Fuselage Frame	Balsa and XPS Foam
3	8	Longeron	Carbon Fiber
4	1	Fuselage Nose	Balsa and XPS Foam
5	4	Fuselage Rear Fairing	Balsa
6	1	Fuselage Rear Door	Balsa
7	1	Side Hatch	Balsa
8	1	Nose Landing Gear	Carbon Fiber and ABS
9	1	Main Landing Gear	Carbon Fiber
10	4	Wing Connector Bracket	Aluminum
11	1	Main Wing Spar	Carbon Fiber
12	1	Secondary Wing Spar	Bass
13	18	Wing Rib	Balsa
14	4	Wing Leading Edge	XPS Foam
15	2	Wing Fence	Balsa
16	2	Aileron	Balsa
17	2	Flap	Balsa
18	4	Wing Trailing Edge	Carbon Fiber
19	8	Stringer	Balsa
20	2	Motor Mount	Bass and Aluminum
21	1	Horizontal Tail Frame	Balsa
22	1	Vertical Tail Frame	Balsa
23	1	Elevator	Balsa
24	1	Rudder	Balsa
25	6	Servo Plate	Bass
26	4	Control Horn Plate	Bass

NOTES:
 ALL DIMENSIONS IN INCHES
 ULTRAKOTE SKIN EXCLUDED FOR CLARITY
 TOP HATCH TRANSPARENT TO SHOW DETAIL

SIEMENS		UNIVERSITY OF MICHIGAN MACH	
FIRST ISSUED	G. CHIA	TITLE	
DRAWN BY	G. CHIA	STRUCTURAL ARRANGEMENT DRAWING	
CHECKED BY	C. GIBBS		
APPROVED BY	T. PANGERL	SIZE	DRG NO.
DATE	2/19/2021	B	MACH 5, DRAWING PACKAGE
		SCALE 1:6	SHEET 2 OF 4



ITEM	Qty.	SYSTEM	DESCRIPTION
1	2	Propulsion Battery	HRB 5000mAh 5S LiPo
2	1	Receiver	Spektrum 9-Channel AR9030T
3	2	Microcontroller	Arduino Nano
4	2	Motor	Turnigy PropDrive v2 4258-500
5	2	Propeller	15x8
6	2	ESC	Predator 80A
7	6	Control Surface Servo	HiTec HS-125MG
8	1	Nose Gear Servo	HiTec HS-55MG
9	1	Spool Reeling Mechanism	ABS and Steel
10	1	Spool Motor	
11	1	Sensor Gripping Claw	ABS
12	1	Bomb Bay Door	Balsa
13	1	Tether Pulley	Steel
14	1	Sensor	ABS
15	2	Sensor Battery	Gaonen 450mAh 1S LiPo
16	3	Sensor Light	LED

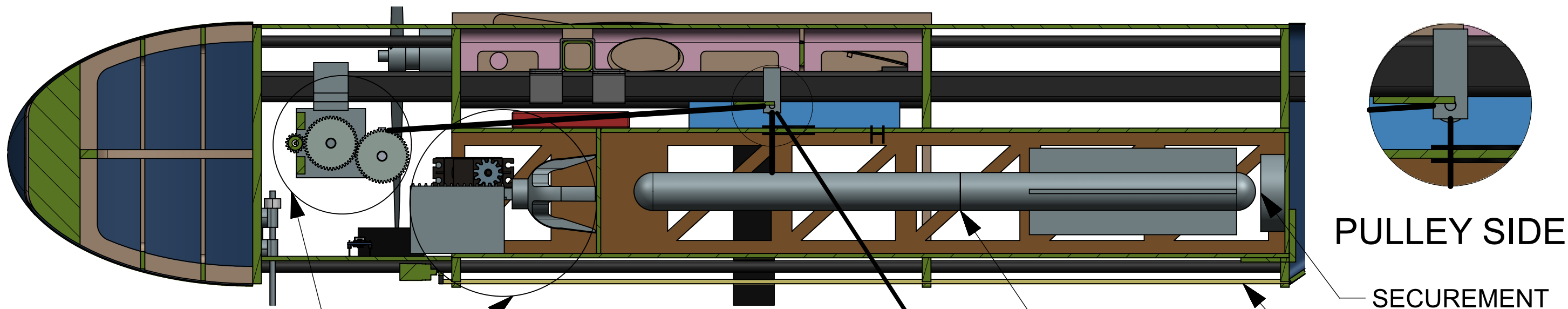
NOTES:
 ALL DIMENSIONS IN INCHES
 ULTRAKOTE SKIN EXCLUDED FOR CLARITY
 SOME BULKHEADS, FLOORS, AND HATCHES TRANSPARENT TO SHOW DETAIL

DETAIL D
 SCALE 1:3

SIEMENS		UNIVERSITY OF MICHIGAN MACH	
FIRST ISSUED	G. CHIA	TITLE	
DRAWN BY	G. CHIA	SYSTEM ARRANGEMENT DRAWING	
CHECKED BY	C. GIBBS		
APPROVED BY	T. PANGERL	SIZE	DRG NO.
DATE	2/19/2021	B	MACH 5, DRAWING PACKAGE
		SCALE 1:6	SHEET 3 OF 4

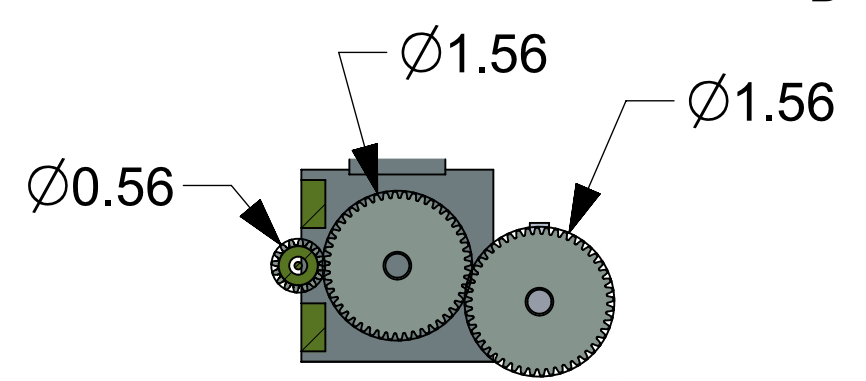
1 2 3 4 5 6

A

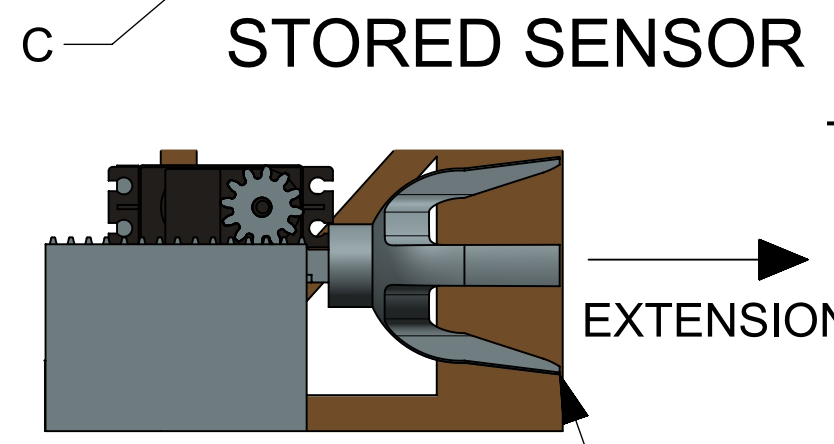


A

B

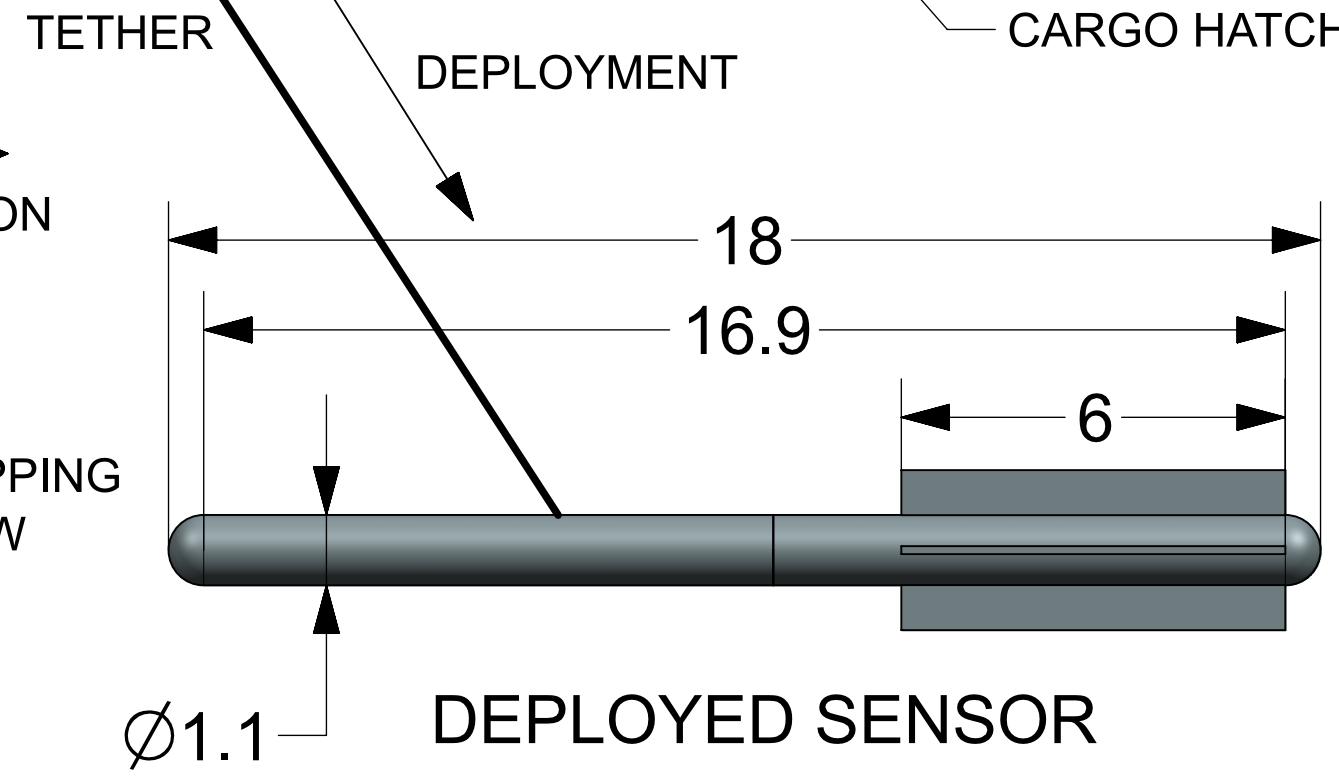
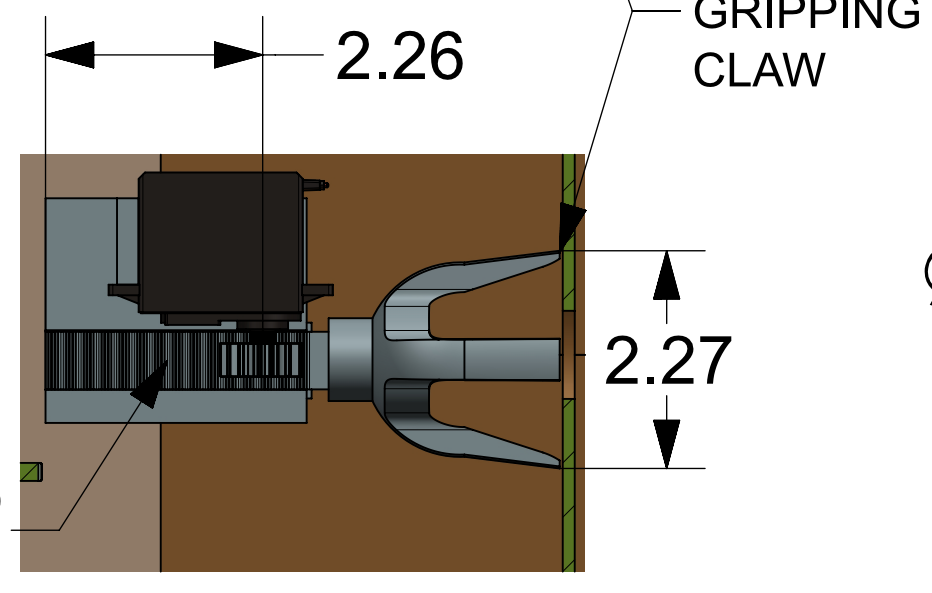
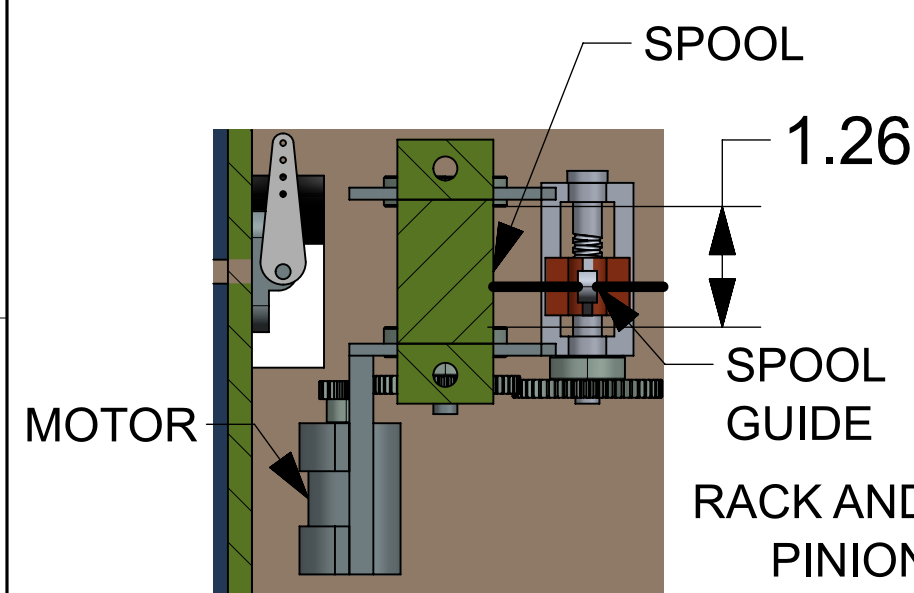


B



C

C



D

D

TOP: TETHER SPOOL TOP: CLAW MECHANISM

ALL DIMENSIONS IN INCHES

SIEMENS		UNIVERSITY OF MICHIGAN MACH		
FIRST ISSUED	G. CHIA	TITLE		
DRAWN BY	G. CHIA	MECHANISMS DRAWING		
CHECKED BY	C. GIBBS	SIZE	DRG NO.	SHEET REV
APPROVED BY	T. PANGERL	B	MACH 5, DRAWING PACKAGE	A
DATE	2/19/2021	SCALE 1:1		SHEET 4 OF 4

1 2 3 4 5 6

6 MANUFACTURING PLAN

Multiple available manufacturing processes were investigated to evaluate the most suitable method of manufacturing the wings, fuselage, tail, and sensor payload mechanisms. The team was able to identify suitable off-the-shelf components that proved more reasonable to purchase than manufacture. The following sections go into further detail regarding the evaluation and selection process.

6.1 Manufacturing Processes Investigated

The team considered five material types and available manufacturing facilities to determine suitable manufacturing methods. Samples can be seen in Figure 35. Each material was assessed for strength, manufacturability, and weight. Construction plans for each component were then developed according to corresponding material properties.

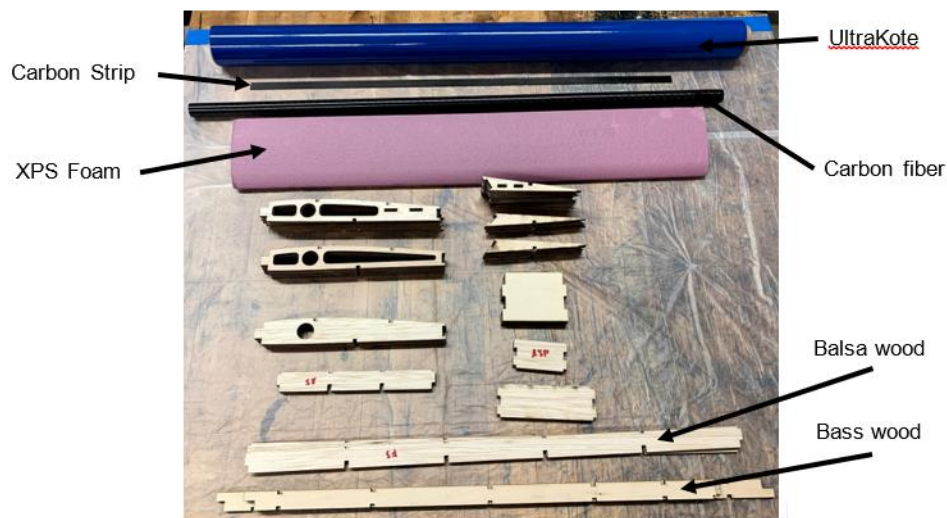


Figure 35: Materials for the Construction of the Aircraft

6.1.1 Laser Cutting

Laser cutting is a resource the team is proficient with. One factor is that a laser cutter is readily available for use to the team. This technique can be used for rapid prototyping of the mechanisms and for fabricating final designs. The dimensional precision on the laser cutter is $\pm 0.0005''$, so we can build interlocking structural components using this method.

Bass and balsa wood are ideal structural materials for RC aircraft due to their low density and rigid structure. The higher density basswood is capable of supporting critical, structural loads in parts such as the fuselage ribs, motor mounting plates, and sensor containers. The lower density balsa is ideal for components that do not experience extreme loads, such as wing ribs, servo trays, and access hatches. Complexity of production is minimal due to their ability to easily cut to precise shapes with a laser cutter.

The team has extensive experience working with these materials, which has translated into a sound understanding of the thickness and number of wooden members used to create a suitable structure of minimum weight. For the 2021 competition, 1/8-inch Balsa and Basswood will again be implemented to construct rib and spar structures for the wing, fuselage, and tail, as well as all non-structural support elements in the fuselage.

6.1.2 3D Printing

Using additive manufacturing for making complex components will be effective due to not having to assemble them out of specific pre-made components. Our team can access an Ultimaker 3 which has a resolution of ± 0.0008 inch. Manufacturing multiple parts simultaneously can help decrease lead times and enable the team to concentrate on more time-consuming parts of the manufacturing process.

ABS Plastics are used extensively in MACH mechanism manufacturing. This material provides the most flexibility in the design of these intricate mechanisms. 3D printing with ABS allows construction of unique shapes such as gears, hinges, and swept fairings that cannot be done easily with other materials. ABS plastic was chosen over other printing plastics and resins as it is a widely available, cheap, and is relatively lightweight. Parts made with this material have the disadvantages of having long lead times for printing and poor strength under significant loads. As a result, this material is only used in components and mechanisms that do not bear significant loads. These include the sensor, sensor deployment and retraction mechanisms, and the sensor claw mechanism.

6.1.3 CNC Hot Wire Foam Cutting

Extruded polystyrene (XPS) foam carved using a CNC hot wire cutter has become a regular tool for MACH. This has been used to rapidly prototype and manufacture verification components such as fuselages, wings, and leading edges in order to validate designs. However, one drawback is its high density. As a result, the amount of XPS foam used on the competition aircraft is kept to a minimum, limited to use on the leading edge to help maintain the desired aerodynamic shape of the airfoil underneath a layer of UltraKote.

6.1.4 Composites

Historically MACH has used composites to manufacture or reinforce major structural elements for various subassemblies because of their high strength-to-weight ratio. Their main use in MACH aircraft is as spars and booms, providing a structural backbone for the aircraft. Carbon fiber has also been used to reinforce structural ribs and spars for previous aircraft wings and fuselages. The major drawback for manufacturing composites is the extensive lead time due to manufacturing molds and fully curing parts. Wax Molds generated by a CNC router have been used in the past, along with foam molds made from a CNC hotwire cutter. Carbon fiber tubes used for spars and booms are readily available as off the shelf parts.

6.1.5 UltraKote Covering

UltraKote is a heat shrinking plastic skin designed for covering rib and spar structures on RC aircraft. This is a thin material that can be wrapped around a rigid wing or fuselage structure and then shrunk with heat to adhere to this structure and become rigid. This is ideal for wings as it will maintain the aerodynamic shape of the ribs across the span with minimal increase in weight. Due to its thin design, it is susceptible to damage in crashes, but easily repaired without a decrease in quality or performance. Carbon fiber was also examined as an alternative covering and was not chosen as it significantly increased weight, build time, cost, and design complexity while providing limited benefits to shape and crash resistance.

6.1.5.1 Adhesives

MACH will utilize three adhesives for construction. These can be seen in Figure 36. Instant cure Cyanoacrylate will be used in the majority of construction. Instant Set and Instant Set Plus epoxies will be used to provide 2 different strengths of hardening epoxy. Instant Set Spar is used to decrease set time. High strength and foam bonds will be done with quick cure epoxy for a more secure hold.



Figure 36: MACH Adhesives

6.2 Manufacturing Processes for Major Aircraft Components

The following subsections lay out the selected manufacturing plans for all major components of the aircraft. These will utilize the materials discussed in Section 6.1 and replicate the detailed design decisions outlined in Section 5.

6.2.1 Wing

Construction of the wing begins by cutting the carbon fiber spar using a band saw. The wooden spar, stringers, and ribs are cut using a laser cutter. The wing ribs slide onto the carbon spar and are placed at specific distances. The rear spar is attached to the back of the ribs with CA adhesive to keep the ribs at required spacing. Next, epoxy is applied to the ribs to secure them to the carbon spar. The reason behind not gluing the ribs to the wing spar first is to ensure correct alignment of the rear spar.

Epoxy is used for the rib and spar joints as its adhesive properties are more compatible with carbon fiber than CA. The stringers are attached using CA adhesive and the leading edge profile is cut from XPS foam using a CNC hot-wire cutter. These sections are then adhered to the wing frame using foam-safe adhesive.

The ailerons and flaps are at the trailing edge of the wing surface and are constructed of laser-cut balsa. The control surface structures are secured using CA adhesive. The trailing edge consists of carbon fiber strip stock, which is adhered to these surfaces after the frames are constructed.

UltraKote heat-shrink film covers the full wing surface, providing a smooth finish, and adding some structural rigidity. The control surfaces will be covered with UltraKote separately. The wing motor mounts are constructed with laser-cut bass wood and glued using epoxy. Extra reinforcement is provided by L brackets.

6.2.2 Tail

The tail will be constructed in two separate parts for the horizontal and vertical stabilizers, in the shape of an inverted T. Balsa sticks will be cut to the required length, and glued together using CA. Small bass sheets will be laser cut and glued using CA to provide a mounting plate for the servos to be bolted in. Once the frame of each is complete, the horizontal and vertical stabilizer will be bolted together using #10 bolts, followed by an UltraKote covering. Following this, the balsa sheets for the elevator and rudder will be cut, sanded, covered using UltraKote, and attached to the tail using nylon hinges. Finally, control horns and control rods will be cut, bent, and installed to trim the tail to the desired deflection angle.

6.2.3 Fuselage

The fuselage consists of bass wood bulkheads and a frame which will be covered in UltraKote. Fuselage bulkheads and framing will be cut using a laser cutter, while the primary longerons are cut using a saw from carbon fiber tubing. All the load bearing components in the fuselage fixed using epoxy for added strength, and then the carbon fiber longerons will be inserted. The tail boom will be cut to length from carbon fiber tube using a saw, and then secured to the fuselage frame using epoxy at multiple locations.

6.2.4 Sensor Position-Securing Claw Mechanism

The claw mechanism serves to constrain the remaining degrees of freedom that are not already taken away by the winding system. To effectively catch the sensor while airborne, the four prongs of the claw themselves have a draft angle outward. This mechanism is actuated by a high-torque servo motor. The entire mechanism is fabricated using 3D printed ABS plastic on an Ultimaker 3. There are only four separate 3D printed parts for this mechanism: the claw, rack, gear, and servo holding frame. G-Code will be generated using 3D models and the claw and rack are glued together using CA. The design ensures that the rack does not raise from the servo frame due to the notches in its cross section. A hard stop will be used to ensure the rack does not move along the linear movement axis further than its length.

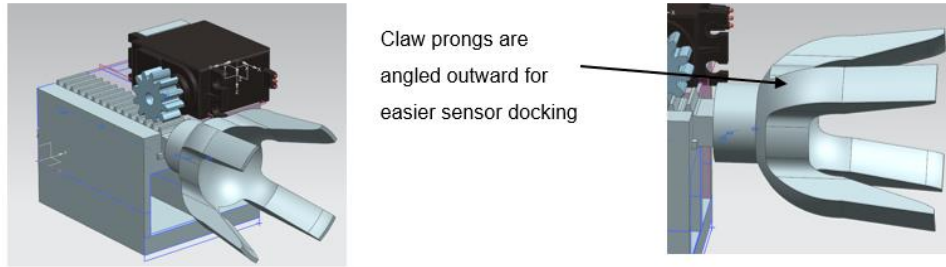


Figure 37: Sensor position securing claw mechanism

6.2.5 Sensor Deployment and Retrieval Mechanism

This part of the sensor mechanism system will be fabricated entirely using 3D printed ABS and fit with ball bearings attached to support the winding spool. Part of the first iteration (shown below) had tolerancing issues which can be remedied by adjusting the CAD model. Epoxy will be used to fix the ball bearings and gears to the 3D printed frame. The gears will be screwed on and secured with epoxy.

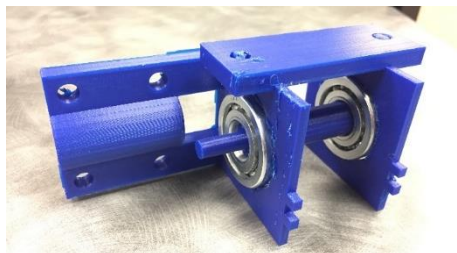


Figure 38: First Iteration of 3D-printed Spool Mechanism

6.2 Manufacturing Timeline

A milestone chart was created to schedule the construction of all aircraft components and mechanism prototypes. Approximately 3 weeks were estimated to construct the aircraft, with expectations that minor schedule modifications will need to be made due to new pandemic restrictions. The learning points from our previous competitions have been incorporated into the timeline. Time will also be allotted to construct backup components in case of a crash during competition.

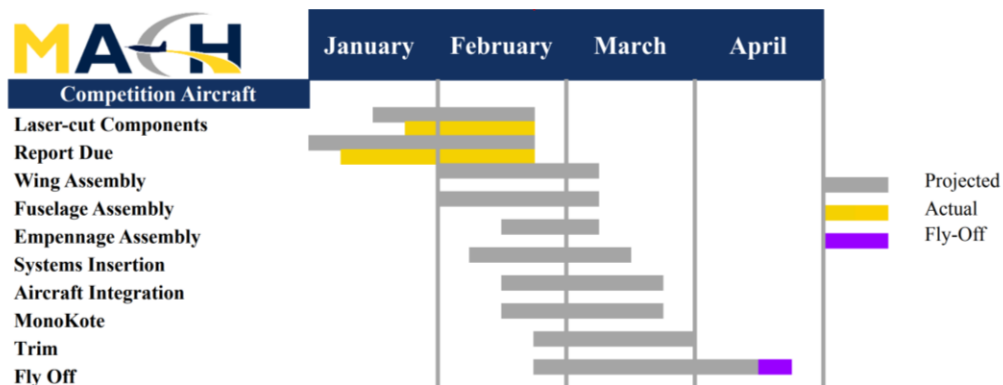


Figure 39: Gantt Chart showing Construction Schedule

7 TESTING PLAN

MACH plans to perform extensive flight and ground testing throughout the design and construction processes. We plan to test each subsystem of the aircraft as they are completed. After ensuring that each part works independently as expected, we will assemble the aircraft and perform additional structural and systems integration testing. Once we are confident in our design, we will begin flight testing. We will test in an iterative manner. When issues are found, we will redesign and retest until we are confident in the results. Our goal in testing is to prove the validity of our design, identify areas of improvement, find the limits of its capabilities, and practice for competition.

7.1 Tests and Objectives

Various tests are conducted to verify specific aircraft characteristics for each sub team and subsystem. Tests are conducted prior to complete integration, where applicable, to minimize risk and prevent system failures that could occur during a test flight. The tests conducted and their primary goals are listed below.

Static Thrust Test

- Verify that the motor and propeller specifications accurately depict performance

LED Brightness Test

- Verify visual distance of LEDs in Mesa, Arizona

Wingtip Test

- Verify that the wing provides sufficient strength
- Simulate pre-flight tech inspection at competition

Sensor Stability Tests

- Verify that the sensor design is aerodynamically stable for flight

Sensor Container Drop Test

- Verify that the sensor cargo container and sensor survive being dropped from a 10-inch height

Sensor Storage, Deployment, and Release Tests

- Verify sensor can be secured within the cargo bay
- Verify sensor can deploy without interference from rest of aircraft

Flight Tests

- Confirm the aerodynamics properties predicted by AVL and Xfoil
- Provide pilot practice for all three flight missions and verify sufficient control
- Performance analysis and telemetry data (Endurance, motor operating temperature, etc.)

wing does not provide enough strength, increasing the thickness of the carbon spar will be considered. The check list for this test in order is shown in the bullets below.

- Check if aircraft contains all internal components
- Ensure fasteners are all secured
- Lift simultaneously from each wing tip slowly until aircraft is not supported on the ground
- Examine for any failures after test

7.1.4 Sensor Stability Tests

To verify that the aerodynamic design of the sensor produced stable results, MACH conducted two tests of the sensor. The first test checked the preliminary sensor design's stability. Due to limited resources, MACH performed this test by carrying a mock sensor made of foam out of the side of a car and qualitatively recorded its performance. These results helped update the design, and most importantly the mass distribution. The second aerodynamic test was conducted with the current sensor design, fully 3D printed, and ran in a wind tunnel. We ballasted the sensor to a CG 2 inches behind the expected CG to give us a bit of margin with our testing and attached the tether at that point.

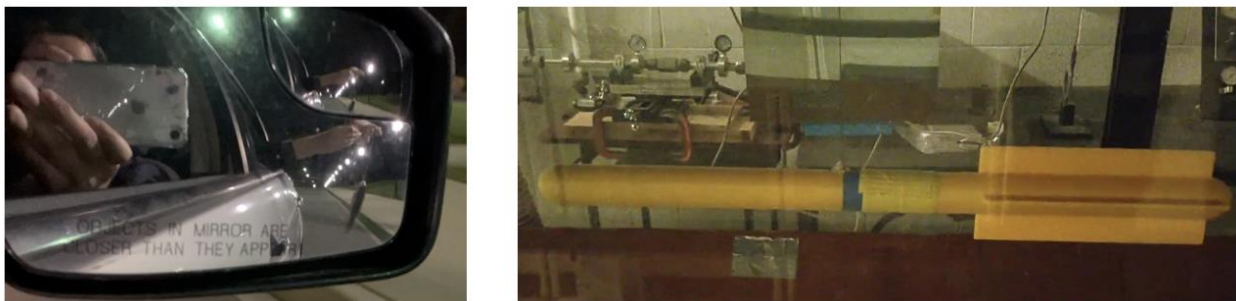


Figure 42: (Left) Preliminary Sensor Vehicle Testing, (Right) Detailed Design Sensor in Wind Tunnel

7.1.5 Sensor Container Drop Test

The sensor container was drop tested several times on all sides with the sensor inside to verify that the design meets the requirements of the Ground Mission: protect the sensor from drops of 10-inch height.



Figure 43: Sensor in Container for Drop Testing

7.1.6 Sensor Loading Tests

The sensor loading test is conducted to verify the sensor can be properly loaded in the two cargo bay configurations. This test is done in two parts in a lab workspace. The first part is representative of the cargo

mission and occurs prior to flight testing. The sensor containers will be slid into the cargo bay through the back hatch of the fuselage. This will be repeated five times to verify there are not abnormalities in construction and decrease installation time.

During the second part of this test, the sensor will be installed using the claw mechanisms and deployed with the use of the claw mechanism and transmitter inputs without the tether attachment. The checklist for this phase is outlined in the bullets below.

- Open bomb bay door and insert sensor body into claws locking onto its ends
- As sensor is being loaded and is in the loaded state, record if any cracking noises is heard as it could indicate a fatal imperfection in a part or mechanism
- In the loaded sensor state, verify that the restraint is flush to the passenger side. If not, alter claw shape to allow for complete contact with the sensor end
- Deploy the sensor, determine if there are any permanent deflection deformations

Prior to the first attempt, a picture will be taken of the setup conditions, so each following test can be reset to the initial state. Once this test is successful five times, the conditions will be run with the tether attached with the same steps.

7.1.7 Flight Test Schedule and Plan

Flight testing is conducted in four stages. First, in the initial stage and maiden flight we determine the airworthiness and handling characteristics of the aircraft by flying a no-payload, basic configuration and a performance flight. Data and pilot feedback from this flight is gathered and reported to the team so design refinements can be made. In the next stage, we will attempt to push the flight envelope to find the performance limits of the aircraft. This includes maximum takeoff weight and endurance flights. This will not only provide valuable data to plan for the missions but will also allow the pilot to gain familiarity with the aircraft. In the third stage, we will fly sensor deployment verification flights with the Mission 3 payload. Finally, in stage four, we will simulate the competition mission conditions to ensure that our aircraft is capable of completing each mission satisfactorily. A test flight schedule can be seen in the table below which provides the date, objective, and results for each test flight.

Table 18: Flight Test Plan

Flight #	Date	Objective	Performance Expectations
Stage 1			
1	3/6/2021	No-Payload Base Configuration	Simple turns (30°), 60% max. cruise throttle, 5 minutes endurance
2	3/6/2021	Performance Evaluation	Tighter turns (60°), limited full throttle
Stage 2			
3	3/13/2021	MTOW Flight	Short takeoff, 3x mission course
4	3/13/2021	Endurance Flight	Mission 3 payload, 10-minute endurance
Stage 3			
5	3/20/2021	Sensor Deployment Verification	Mission 3 payload, verify mechanism operation and sensor stability
Stage 4			
6	3/27/2021	Mission 2 Full Test Flight	Simulate Mission 2
7	3/27/2021	Mission 3 Full Test Flight	Simulate Mission 3

The checklist in Figure 44 shows the checklist used for flight testing. It is designed to prevent mistakes in setting up the aircraft and reduce the chance of in-flight failures by ensuring each system is checked. We plan to use this list during competition runs as well.



Flight Testing Checklist

Date		Time			
Structural					
Wingtip Test	CG Location (Aft of Leading Edge)	Mechanism Locked	Landing Gear Secured	Payload Secured	
Y <input type="checkbox"/> N <input type="checkbox"/>		Y <input type="checkbox"/> N <input type="checkbox"/>	Y <input type="checkbox"/> N <input type="checkbox"/>	Y <input type="checkbox"/> N <input type="checkbox"/> N/A <input type="checkbox"/>	
Electronics					
Battery Voltages Before	Range Check	Ardupilot Powered and Logging		Battery Telemetry	
Receiver:	Y <input type="checkbox"/> N <input type="checkbox"/>	Y <input type="checkbox"/> N <input type="checkbox"/> N/A <input type="checkbox"/>		Y <input type="checkbox"/> N <input type="checkbox"/>	
Propulsion:					
Transmitter:					
Control Surfaces					
Ailerons		Elevator		Rudder	
Direction	Secure	Direction	Secure	Direction	Secure
Y <input type="checkbox"/> N <input type="checkbox"/>	Y <input type="checkbox"/> N <input type="checkbox"/>	Y <input type="checkbox"/> N <input type="checkbox"/>	Y <input type="checkbox"/> N <input type="checkbox"/>	Y <input type="checkbox"/> N <input type="checkbox"/>	Y <input type="checkbox"/> N <input type="checkbox"/>
Propulsion					
Prop Secure	Prop Direction	Throttle-Up Test	Wires Neat/Secure		
Y <input type="checkbox"/> N <input type="checkbox"/>	Y <input type="checkbox"/> N <input type="checkbox"/>	Y <input type="checkbox"/> N <input type="checkbox"/>	Y <input type="checkbox"/> N <input type="checkbox"/>		
Weather					
Wind Speed/Direction		Temperature		Comments	
Pilot Approval _____					
Setup Comments					

Figure 44: Aircraft Flight Test Checklist

8 PERFORMANCE RESULTS

8.1 Subsystem Testing Results

As laid out in the testing plan, each subsystem is individually tested before final assembly.

8.1.1 Propulsion Testing Results

To perform this test, we mounted our system to at Turnigy Power Systems static thrust stand and tested the performance. We recorded current, temperature, and thrust data for each test. First, the team performed thrust testing by varying the throttle from 0 to 100%. Secondly, the team took endurance data by running the system using a fully charged battery. For this test, the different propeller configurations at different throttles were compared. These results are shown below. The 15x8 propeller system has a empirical data to show that the thrust is roughly the same, but with improved endurance after the 16x10 melted internal coils around 6 minutes, the 15x8 system should be more reliable. By decreasing the throttle and altering the propeller, the static thrust test data demonstrate that a 15x8 propeller will satisfy our system requirements.

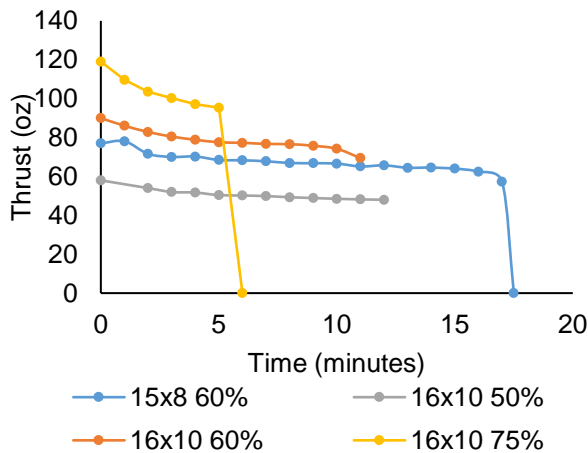


Figure 45: Endurance Thrust Stand Results

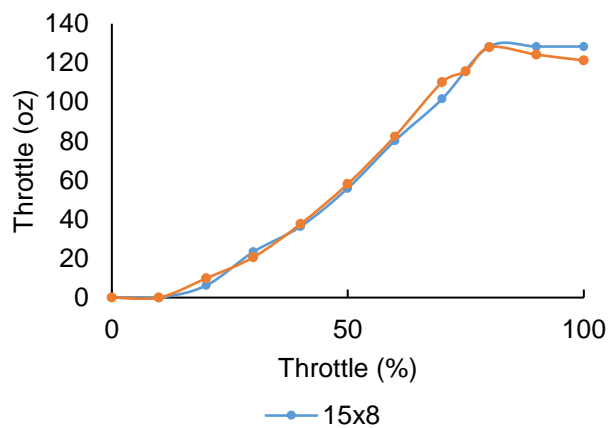


Figure 46: 15x8 and 16x10 Thrust Comparison

8.1.2 Sensor Performance Results

Our wind tunnel based sensor test showed it was stable during tests of up to 82 ft/s (the limit of the wind tunnel). There was a period where the sensor began oscillating from side to side as the wind tunnel was speeding up between 50 to 72 ft/s, however, the sensor did fight back and reduced the oscillations. MACH is confident with the results of these tests.

8.1.3 Sensor Container Performance Results

The sensor container drop tests were successful. We determined both the sensor and the container survived without any non-cosmetic damage thus meeting our requirements.

Table 19: Container Drop Test Results

Test #	Details	Result
1	Container dropped on long side: 3 times from 10", 2 times from 15"	No sensor or container damage, light container scuffing
2	Container dropped on short side 3 times	No sensor or container damage

8.1.4 Predicted Subsystem Performance Results

During our initial sizing and preliminary design of the propulsion system, eCalc predicted that our total system thrust for our chosen motor and 15x8 propeller would be 144.3 ounces with a maximum endurance of approximately 11 minutes. Based on our throttle characterization and 60% throttle endurance test, our tested motor setup yielded a maximum static thrust of 128 ounces and a maximum endurance of 17 minutes. Even though the actual thrust did not meet our expected thrust, it was sufficient to exceed our design point thrust to weight ratio of 0.6 at MTOW. Our verified endurance was more than enough to fulfill the 10-minute endurance requirement of mission 3.

Our sensor stability analysis discussed earlier in this report indicated that theoretically our sensor design was both statically and dynamically stable. Our physical testing did verify those results, showing that as time increased the sensor did tend towards equilibrium, fulfilling the competition requirements of being aerodynamically stable.

9 BIBLIOGRAPHY

- [1] Niță, M., and Scholz, D., “Estimating the Oswald Factor from Basic Aircraft Geometrical Parameters,” German Aerospace Congress, Document 281424, September 2012
- [2] Britannica, The Editors of Encyclopedia. “Tuscon,” *Encyclopedia Britannica*, retrieved 29 September 2020.
- [3] Raymer, D. P., “Aircraft Design, a Conceptual Approach,” *Initial Sizing*, 5th ed., AIAA, 2012, pp. 113-116
Wilk, A., & Skuta, M. (2009). Laboratory tests of the aerodynamic drag coefficient of the flag as a body with low stiffness. *Task Quarterly*, 13(1-2), 5-14
- [4] “Boeing 103 Airfoil,” *Airfoiltools.com*, retrieved 5 September 2020,
<http://airfoiltools.com/airfoil/details?airfoil=boe103-il>
- [5] Winterstein, M., Hernandez, F., Lamirato, T., Vigneau, A., Pringle, R., “Electric Propulsion System Database,” University of Michigan, AERO 405 Paper, May 2019.
- [6] Carris Reels, “Reel Capacity Calculator”, <https://carris.com/reel-capacity-calculator/>



AIAA-DBF
2020-21



ARCIS



**DAYANANDA SAGAR COLLEGE OF
ENGINEERING**

Contents

1	Executive Summary	3
2	Management Summary	4
2.1	Team Organization	4
2.2	Milestone Chart	4
3	Conceptual Design	5
3.1	Technical Requirements	5
3.2	Mission Requirements	6
3.3	Scoring Analysis	8
3.4	Configuration and Component Selection	9
4	Preliminary Design	14
4.1	Design Methodology	14
4.2	Risk Analysis of Uncertainties	15
4.3	Exhaustive Search Analysis (ESA)	16
4.4	Fin Optimization	16
4.5	Propulsion	17
4.6	Airfoil Selection	18
4.7	Sizing	19
4.8	Stability and Control	22
4.9	Aerodynamics [1]	24
4.10	Performance [2]	25
5	Detailed Design	29
5.1	Dimensional Parameters	29
5.2	Structural Characteristics	30
5.3	Subsystem Design	30
5.4	Weight and Balance	38
5.5	Performance	39
5.6	Drawing Package	40
6	Manufacturing Plan	45
6.1	Investigated Processes and Materials	45
6.2	Manufacturing Process	46
6.3	Manufacturing Milestones	48
7	Testing Plan	49
7.1	Test Objectives	49
7.2	Test Milestone	49
7.3	Test Results	50
7.4	Flight Checklists	56
7.5	Flight Tests	57
8	Performance Results	58
8.1	Predicted and Actual Capabilities	58
8.2	Improvements and Advancements	59
	References	60

1 Executive Summary

This report outlines the efforts of Team Arcis from Dayananda Sagar College of Engineering to design, evaluate, and test a radio-controlled aircraft for the 2020-2021 American Institute of Aeronautics and Astronautics (AIAA) Design, Build, Fly (DBF) competition. The objective is to develop an aircraft capable of deploying and retrieving an aerodynamically stable "sensor" mid-flight and carry a substantial number of containers for the sensors while maintaining high speed and safe operation.

The competition requires the aircraft to fly 3 flight missions and one ground mission. The flight missions have a similar path but varying payloads and time constraints - Mission 1 (M1) has no payload and a time constraint of 5 minutes, Mission 2 (M2)'s payload is sensor shipping containers, and Mission 3 (M3)'s payload is a single sensor with its Deployment and Recovery Mechanism (DRM), having a flight time limit of 10 minutes adds to the existing challenge of towing the sensor. A comprehensive practice session for ground mission was employed, which averaged the time taken to be 50s. For M1, which is a 3 lap flight and take off length within 100ft, the climb rate obtained was the highest because of no payload and valued at 11.80ft/s. Our aircraft can lift 12 containers for M2 which is predicted to achieve the highest mission score in the entire competition. The climb rate attained in M2 is 4.95ft/s. The sensor is deployed and recovered in M3, which aims to complete 9 laps within time interval of 8 min 10 sec at a climb rate of 9.16ft/s.



Figure 1.1: Team Arcis 2021 DBF entry

Based on the scoring analysis, trade studies, detailed design, analysis, manufacturing of subcomponents, simulations and testings - a high wing monoplane of rectangular planform with a conventional tail and a tricycle landing gear is designed, manufactured, and tested. The parameters selected were to achieve smooth takeoff, high speed, endurance and payload capacity with the added challenge of stabilising a towed sensor with fin optimization.

A Python program incorporated with MATLAB was named Exhaustive Search Analysis (ESA), was used to maximize the score. ESA heavily influenced the team's design decisions factoring all the constraints of the competition.

The design of the LG gives a 3-degree incline with the thrust line to increase lift, and the use of endplates helps reduce tip vortex formation. The employment of a servo winch system as a DRM ensures smooth deployment and recovery during flight. A dynamic thrust test was conducted in order to observe the variation of thrust with airspeed. X-PLANE was extensively used, and the results were compared to theoretical values.

2 Management Summary

2.1 Team Organization

The team consists of undergraduate students and is entirely student-led. It receives in-kind sponsorships and financial support from corporations, crowdfunding, and other student-led activities such as workshops, community service, and relief, in conjunction with the marketing team. The faculty advisor provides regular guidance to the team and its activities. He has a supervisory role and is the intermediary between the college management and the team.

The Captain is the head of the team and extends oversight to all aspects, including technical, marketing, and logistics. His responsibilities also include schedule planning, material extraction, and supervision. The Vice-Captain and Team Manager have more day-to-day accountability, oversee the technical team, the work in progress, and schedule deadlines. They ensure there is unbroken co-ordination between the technical sub-teams, ensuring easy workflow.

Designers strategize and model the various components using the appropriate CAD software. Aerodynamics is concerned with sizing, trade studies, and fabrication methodology. The Marketing division deals with the public relations and media presence. Furthermore, it is responsible for fundraising and ensures that the team collaborates with established organizations for greater exposure for all the members. Performance and Avionics are accountable for the deliberation, testing, assembly, and maintenance of electronic components. Manufacturing division handle the various components' production and assembly and inspect and repair the aircraft when needed.

All the roles mentioned above comprise individuals with heightened interests who use various tools and their skillsets to fulfill their responsibilities.

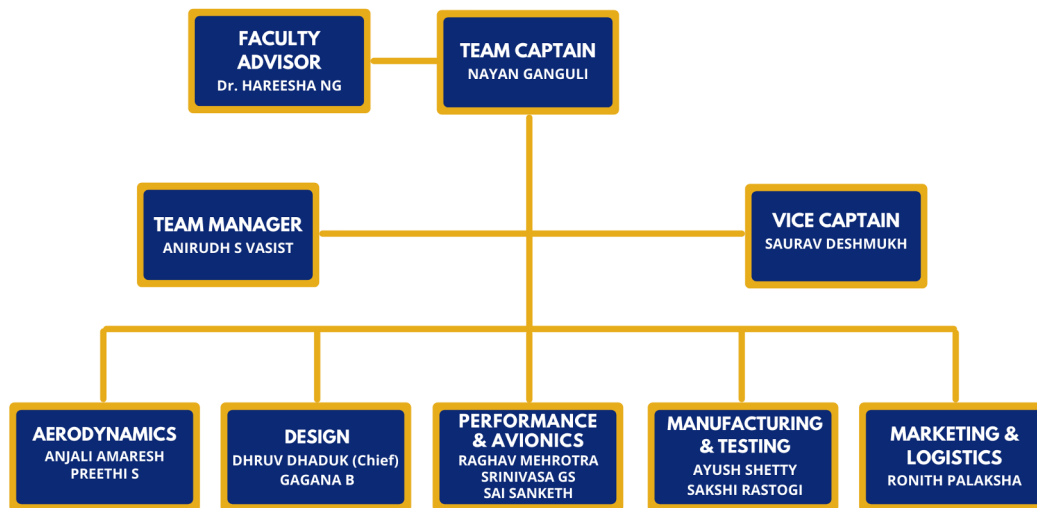


Figure 2.1: Team Organization

2.2 Milestone Chart

The milestone chart was plotted during the first week of meetings, highlighting the principal elements and initializing a smoother workflow. It was done keeping in mind lockdowns due to the pandemic and productivity influenced by online working culture. Its primary purpose was to show essential deadlines and the design and fabrication goals planned, which were enforced by the Vice-Captain and Team Manager. All of the preliminary and

detailed design was done virtually using online tools like Discord due to the university’s restrictions. After relaxation of lockdowns, the team was allowed to gather physically to manufacture and test the aircraft. The milestone plan was adjusted accordingly once the restrictions were lifted, allowing for a smoother workflow shown by the actual progress. The planned progress is shown in yellow, while the actual progress for completed items is in blue. The planned progress includes cushion, which accounts for unexpected delays by material and component extraction, shipping delays, and unforeseen events, planned at the beginning of the year.

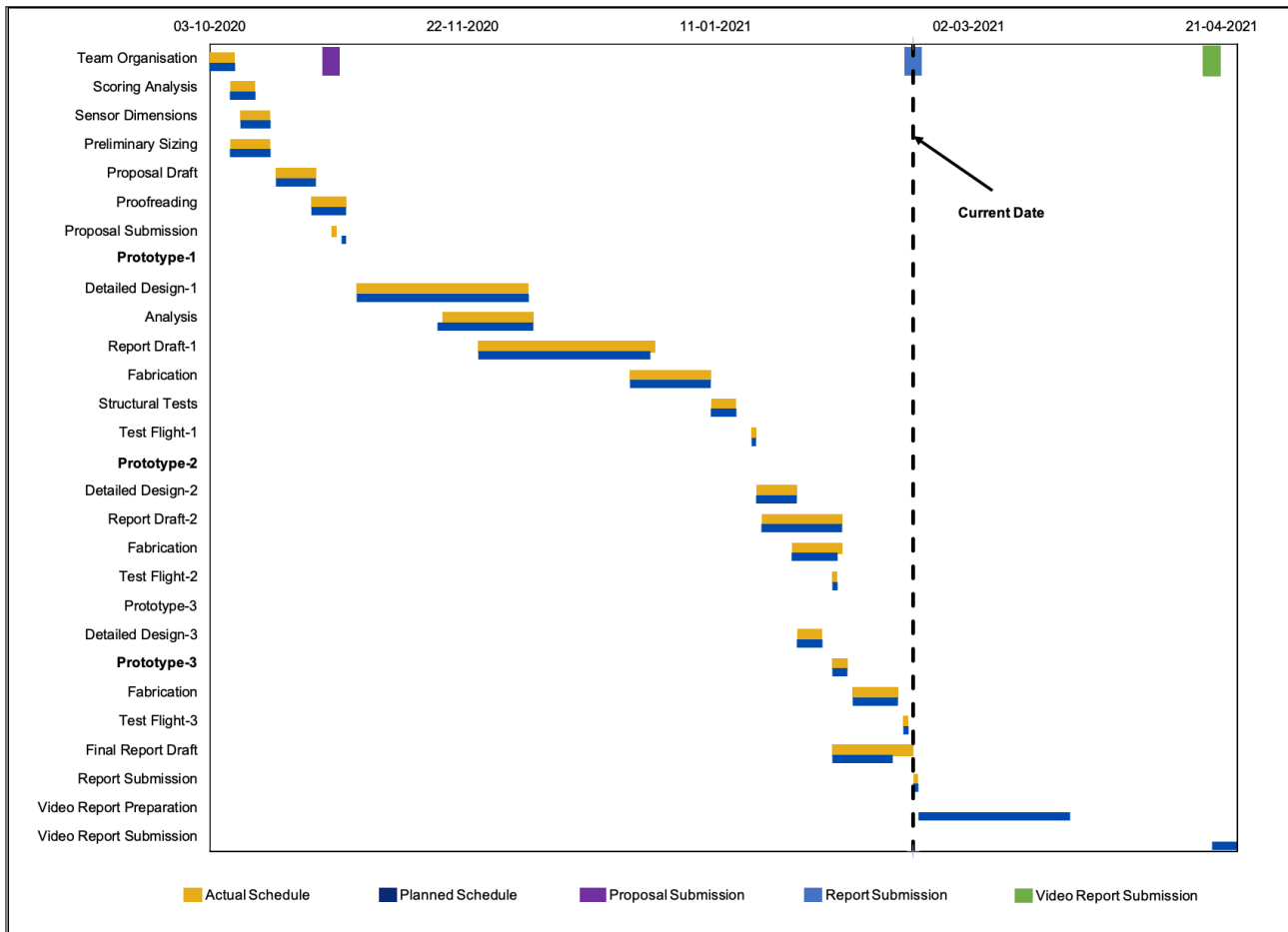


Figure 2.2: Gantt Chart depicting the Plan of Work

3 Conceptual Design

The conceptual design phase began with an in-depth breakdown of the mission requirements, rules, and scoring equations. This was followed by the scoring sensitivity analysis, which allowed us to optimize and help select the aircraft’s configuration.

3.1 Technical Requirements

3.1.1 Aircraft Requirements

1. The aircraft’s wingspan must not exceed 60in.

2. The aircraft's Takeoff Gross Weight (TOGW) must not exceed 55lbs.
3. Aircraft will use ground rolling takeoff and landing.

3.1.2 Sensor Requirements

1. The sensor must have a minimum diameter of 1.00in with a minimum length to diameter ratio of 4.
2. It must be aerodynamically stable while deploying, operating and recovering.
3. It must have a minimum of 3 external lights that can be viewed while in flight in the deployed position.
4. The lights must operate one at a time in the deployed position in a pattern to be determined by each team.
The lights must be bright enough to be viewed in broad daylight.
5. The sensor must contain its own battery power supply.
6. The sensor must be carried internally to the airplane.
7. The DRM for the sensor must be internal to the airplane.
8. The DRM must deploy the sensor a minimum of 10x the total length of the sensor from the exit location of the airplane. The tow line must include a marker such that the Flight Line Director can verify if it is fully deployed in flight.

3.1.3 Shipping Container Requirements

1. The sensor shipping container must fully enclose the sensor and protect it from drop shock event during the Ground Mission (GM).
2. All shipping container simulators must be the same size and weight as the sensor shipping container with the sensor.

3.1.4 Power & Propulsion Limitations

1. Total energy stored cannot exceed 200Wh.
2. LiPo battery packs must be un-altered and commercially procured.
3. In case of multiple battery packs, battery packs must be installed and secured with a minimum air gap of 0.25in between it and any other battery pack.

3.2 Mission Requirements

The missions consist of a ground mission and 3 flight missions. The flight missions must be flown in order with the ground mission attempted at any time between the 2nd and 3rd missions.

3.2.1 Flight Path

The take-off field length is 100ft for all Flight Missions. Upon taking off, the aircraft will fly a specified number of 'laps' which consists of two 180° turns and a 360° turn as depicted in Figure 3.1

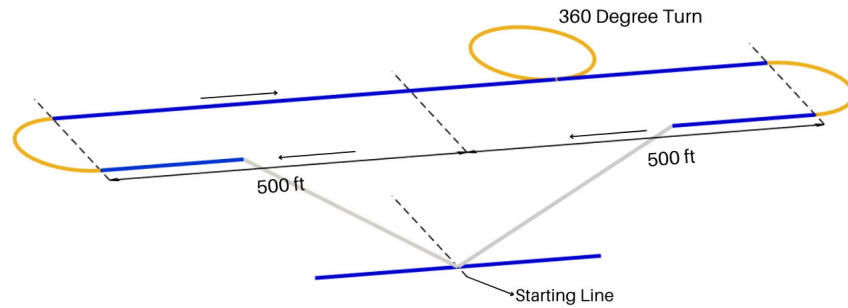


Figure 3.1: Flight Path

3.2.2 Ground Mission

The GM is a timed mission conducted to verify the sensor and its container's integrity. Prior to the mission, a team member shall drop the container (housing the sensor) on all 6 sides, then remove the sensor from its container and demonstrate that it is fully functional and replace it. The timed mission itself is where a team member assembles the entire M2 payload (i.e. shipping container, shipping container simulators and DRM) within the aircraft.

$$M_G = \frac{Min_{Time}}{N_{Time}} \quad (1)$$

Where, Min_{Time} is the fastest time for all teams.

3.2.3 Mission 1

M1 is a staging flight without any payload. The permitted takeoff field length is 100ft. The aircraft must complete 3 laps within a flight window of 5mins. A successful landing is necessary but is not subject to the time constraint.

$$M_1 = 1 \quad (2)$$

3.2.4 Mission 2

M2 is a delivery flight where the payload includes the shipping container, shipping container simulators and DRM. The permitted takeoff field length is 100ft. The aircraft must complete 3 laps within a flight window of 5mins. A successful landing is necessary but is not subject to the time constraint.

$$M_2 = 1 + \frac{N_{Containers}}{Max_{Containers}} \quad (3)$$

Where, $Max_{Containers}$ is the highest containers/time score for all teams

3.2.5 Mission 3

M3 is the sensor flight where the payload is the sensor and DRM. The sensor must be fully extended before the first 360° turn. In a flight window of 10mins the aircraft is required to make the maximum number of laps. The permitted takeoff field length is 100ft. A successful landing is necessary but is not subject to the time constraint.

$$M_3 = 2 + \frac{N_{Laps} \times l_S \times W_S}{Max_{Laps} \times l_S \times W_S} \tag{4}$$

Where, $Max_{Laps} \times l_S \times W_S$ is the highest product of laps, sensor length and sensor weight

3.2.6 Total Score

The total score for AIAA DBF 2021 is calculated using the formula

$$Score = Written\ Report\ Score \times Total\ Mission\ Score \tag{5}$$

Where, Total Mission Score is computed from individual flight scores and the ground mission score

$$Total\ Mission\ Score = M_1 + M_2 + M_3 + M_G \tag{6}$$

3.3 Scoring Analysis

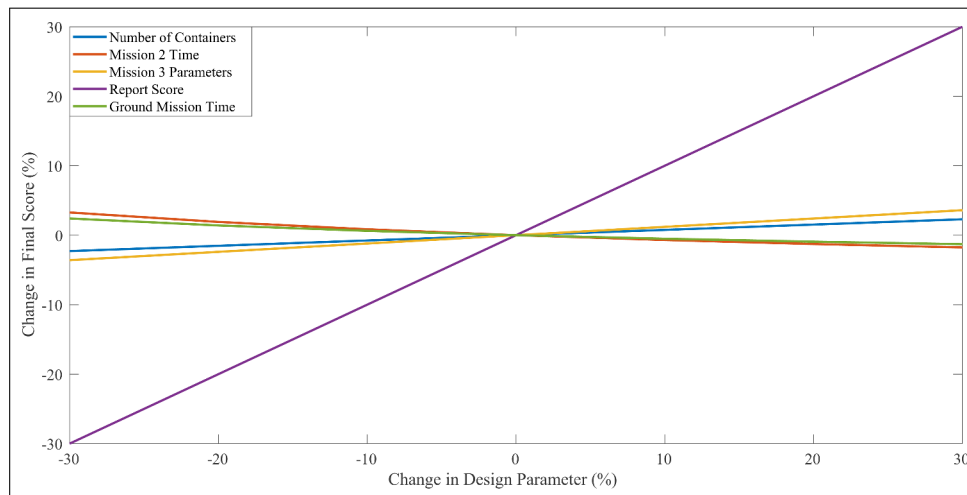


Figure 3.2: Sensitivity Plot

The design centralizes on acquiring a maximum score in the three flying missions and the ground mission. The design has been derived from the factors based on the scoring equations, i.e., the number of containers, report score, time taken for M2, M3 parameters, and GM score. The study of the scoring equations allowed us to gauge our preferences. The sensitivity analysis plot from MATLAB of the parameters mentioned earlier, enables us to examine that the report has the highest consequence. The aircraft's design and its components have been based on the requirements to maximize the score in all the rounds.

3.4 Configuration and Component Selection

A Figure of Merit (FoM) was assigned to each factor based on the efficiency of the parameter, thereby assessing importance of each factor relative to each other. The minimum score for the FoM scale is 1, deems most unsuitable for the efficiency of mission requirements. The maximum score depends on the number of configurations considered for the respective trade studies and stands for the highest score for that parameter. The configuration with the highest total is chosen for the final design. The scoring is based on intensive research, and analysis of historical data generated by the previous year’s aircraft configuration. As an example, a trade study for the number of wings is taken. We have considered 3 configurations; hence, the Merit scale runs on a scale of 1 to 3. Each configuration is then scored based on its performance and efficacy, and then summed.

3.4.1 Wing Configuration

(a) Type of Wing

Three configurations, namely monoplane, biplane, and tandem, are considered for the wing. The monoplane is highly efficient, easy to fabricate, and produces lower drag at high airspeeds than the other configurations. The biplane is considered due to its higher lift, but the added weight and interference are detrimental to any advantages. The tandem wing increases overall lift, but they show low stall characteristics as the forward wing’s tip vortices are likely to affect the rear wing. It can be avoided by keeping the rear wing at a lower position, which would interfere with the DRM. They are also heavier when compared to monoplane. So, the monoplane wing structure was chosen.

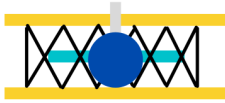
			
Figure of Merit	Monoplane	Biplane	Tandem
Flight Speed	3	2	2
Payload Capacity	2	3	3
Ease of Fabrication	3	2	1
Induced Drag	3	1	2
Total	11	8	8

Table 3.1: Configuration Selection for Type of Wing

(b) Wing Planform

The basic configurations considered are rectangular, elliptical and tapered wings. Rectangular wings are easy to design and fabricate while offering benign stall characteristics. Elliptical wings are efficient, as observed in their span-wise lift distribution, posing less drag, but they have poor lateral stability, poor stall recovery, and are difficult to design. Tapered wings offer lower induced drag while providing higher performance. The team dismissed tapered wing due to difficulty in manufacturing and its poor tip-stall characteristics. Hence, considering the flight speed, ease of fabrication, and high lift capacity, the rectangular wing was considered.

			
Figure of Merit	Rectangular	Elliptical	Tapered
Stall recovery	3	1	2
Control and Stability	3	1	2
Induced Drag	1	3	2
Ease of Fabrication	3	1	2
Total	10	6	8

Table 3.2: Configuration Selection for Wing Planform

(c) Position of the Wing

We considered three choices for the main wing position, namely high, mid and low. High wing configuration has better roll characteristics. Additionally, it the wing, which may occur in low-wing. Mid-wing configuration offers lower drag, but the wing root passing through the fuselage interferes with the shipping containers. Low-wings have low ground clearance and lesser roll stability. Considering all these factors, the high wing configuration was an apt choice.

			
Figure of Merit	High wing	Mid Wing	Low Wing
Payload Capacity	3	1	2
Control and Stability	3	1	2
Ground Clearance	3	2	1
STOL	2	1	3
Total	11	5	8

Table 3.3: Wing Position Selection

3.4.2 Empennage

Conventional Tail, T-Tail, and V-Tail were compared for the empennage. Conventional tails are easy to design and fabricate. They offer good stability and control at the required flight speed. The horizontal tail is free from wing wake and vortices in T-tail, making it highly efficient, but they are susceptible to a deep stall. V-tail contributes to least drag, but the control system’s design is intricate since two control surfaces are used to pitch and yaw simultaneously. Both conventional tail and T-tail configurations were designed and studied in successive iterations. The team concluded with the conventional configuration, as it provided better stability compared to the T-tail.

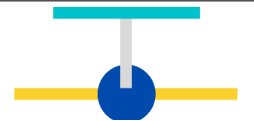
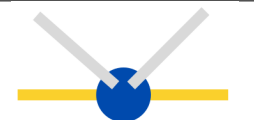
			
Figure of Merit	Conventional Tail	T-Tail	V-Tail
Interference with sensor	2	3	2
Control and Stability	3	2	2
Ease of Fabrication	3	2	2
Drag	3	2	3
Total	11	9	9

Table 3.4: Configuration Selection for Empennage Configuration

3.4.3 Landing Gear Configuration

Tricycle, tail dragger, and quadricycle landing gears were considered. The tricycle gear’s main wheels are located behind the Centre of Gravity (CG), allowing excellent stability. The landing gear doesn’t interfere with the deployment and recovery process. In case of taildragger, the wing has a higher angle of attack during take-off, and thus the take-off distance is shorter, but it is subjected to ground looping. For the quadricycle configuration, the added amount of weight and drag would be detrimental. Tricycle configuration is selected as it is most suitable among the considered configurations.

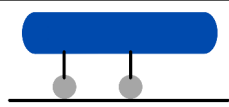
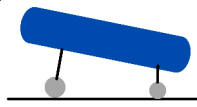
			
Figure of Merit	Tri-cycle	Tail Dragger	Quadricycle
Drag	2	3	1
Payload Capacity	2	2	3
Ground Control	3	2	1
Weight	3	2	1
Total	10	9	6

Table 3.5: Configuration Selection for Landing Gear Configuration

3.4.4 Container Placement

The containers are placed to occupy maximize fuselage volume. Two positions are considered where the shipping containers are placed along the airplanes’s roll axis - longitudinal storage configuration, or placed along the airplane’s pitch axis - lateral storage configuration. Based on the requirements of M2 and M3, longitudinal storage configuration utilizes the maximum volume of the fuselage while maintaining the system’s stability. Though, the lateral storage configuration reduces the volume, it also decreases the aircraft’s stability, thus the former is preferred.

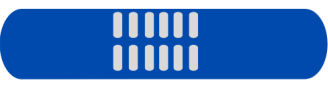
		
Figure of Merit	Longitudinal Storage	Lateral Storage
Drag	3	2
Assembly	3	2
Overall Area	3	2
Total	9	6

Table 3.6: Configuration Selection for Container Placement Configuration

3.4.5 Sensor

Intense research was conducted on various sensor designs to select a design that remains stable when deployed. Different configurations namely, 4 rectangular fins, 2 tapered fins, 4 tapered fins, and 4 elliptical fins, were designed and analyzed on ANSYS 2020. The drag of each configuration was inferred to be 0.076/bf, 0.057/bf, 0.066/bf, and 0.063/bf, respectively. Tapered with 4 fins was chosen based on drag, ease of implementation, effective area and stability.

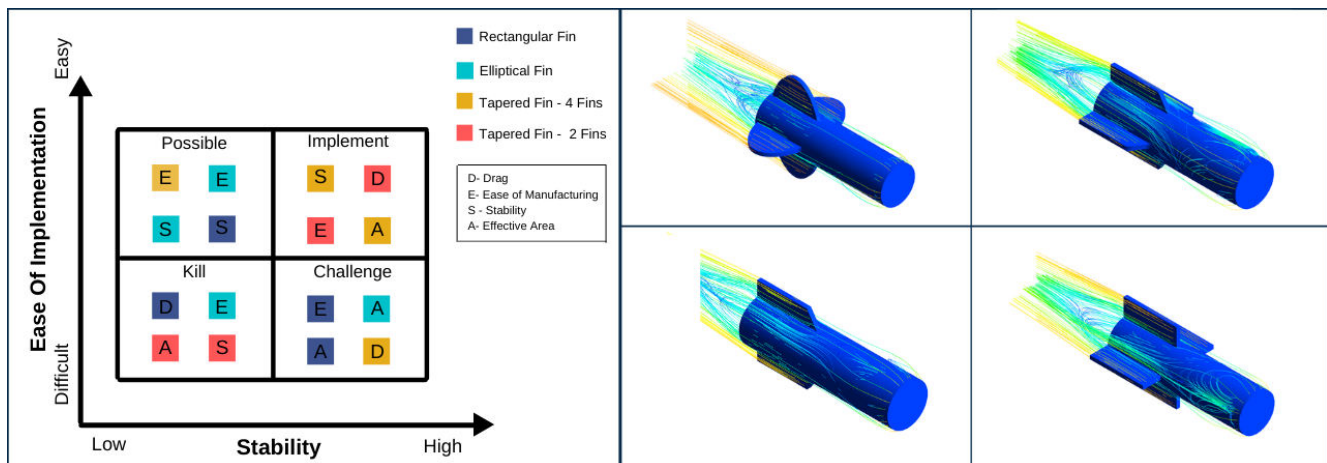


Figure 3.3: Configuration Selection for Sensor Design

3.4.6 Sensor Deployment and Recovery Mechanism

The GM requires quick loading and for which various possible mechanisms for M3 were examined. The team came up with three designs that satisfied the mission requirements.

Spring Shaft Mechanism: Deployment takes place when a servo releases the pin from the main shaft, and the sensor falls out due to its weight. For recovery, a tensioned spiral spring attaches to the main shaft on command from the receiver. The torque from the spiral spring used, turns the shaft back and recovers the sensor. The mechanism works similarly to a measuring tape that rolls in when required. It is lightweight, simple to use, and involves no motor.

Telescopic Boom Mechanism: This mechanism uses telescopic carbon fiber rods with the sensor attached at the end. The deployment is initiated using a motor that operates these telescopic rods using a string. The motor can deploy or retract the sensor on command. The sensor is stable during flight and allows for controlled deployment and recovery.

Servo Winch Mechanism: The servo winch mechanism acts as a motor with a gearbox; however, there is no feedback mechanism. The potentiometer is altered in such a way that the servo arm rotates 360° instead of 180°, so when the servo is actuated, the servo arm starts to rotate clockwise or anti-clockwise. A cylindrical shaft with a string wound over it is used instead of the servo arm. This string is used to deploy, tow, and retract the sensor. This uses a servo to provide the required torque to retrieve the sensor as opposed to a telescopic boom mechanism.

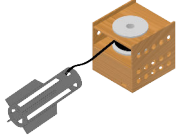
			
Figure of Merit	Spring Shaft Mechanism	Telescopic Boom Mechanism	Servo Winch Mechanism
Time	2	2	3
Cross-sectional Area	2	2	3
Ease of Fabrication	3	2	3
Weight	3	1	3
Total	10	7	12

Table 3.7: Configuration Selection for Sensor Deployment and Recovery Mechanism

From the research, we inferred that this mechanism is compact, lightweight, easy to build, and simple to operate, and thus was our most convenient choice.

3.4.7 Motor configuration

Four configurations were considered, namely pusher, push-pull, twin, and tractor. Tractor is aerodynamically stable, easier to fabricate, stabilize CG, and takeoff without the risk of a prop strike. Its major disadvantage is that it requires a longer fuselage and can cause an increased drag as it disturbs the airflow around the fuse.

				
Figure of Merit	Tractor	Pusher	Push-Pull	Twin wing mounted
Thrust	3	2	4	4
Weight	4	4	2	2
Ease of Fabrication	4	3	1	2
Endurance	4	4	2	2
Total	15	13	9	10

Table 3.8: Configuration Selection for Motor Configurations

The pusher mechanism requires a shorter fuselage, is less sensitive to crosswind, and has reduced prop-wash over wing and tail, but has low CG balance, more weight, and propeller strike risk during takeoff roll. Additionally, the pusher propeller can interfere with the towed sensor. The push-pull mechanism and wing-mounted configuration

gives more thrust and have better reliability due to dual motors. However, they have complex structures and has low endurance due to high power consumption. Moreover, differential thrust is also to be factored in while flying a dual-motor aircraft.

4 Preliminary Design

4.1 Design Methodology

The team followed an aircraft design process that was based on its past experiences. The work began with sensitivity analysis, ESA and thorough deliberation of the technical constraints and rules. Several configurations and structures were considered and evaluated, with the most useful being shortlisted.

These requirements were used to perform a constraint analysis and estimate the maximum takeoff weight and wing area to size the aircraft. Various propulsion systems were analyzed and tested, and the best was selected based on the mission requirements. Mission models were developed to simulate mission performance and these models allowed for refinement of preliminary analyses. The preliminary design was analyzed to determine if mission performance requirements were met and to ensure stability. The components and subsystems were then designed in detail, manufactured and flight-tested to evaluate performance.

Although the design process is presented above as linear, it is highly iterative, as seen in Fig 4.1. Results from analyses and testing were applied to improve previous studies and re-evaluate design choices. Intermediate results such as performance predictions, aerodynamic characteristics, and manufacturing issues were used to improve the design, leading to a higher scoring aircraft.

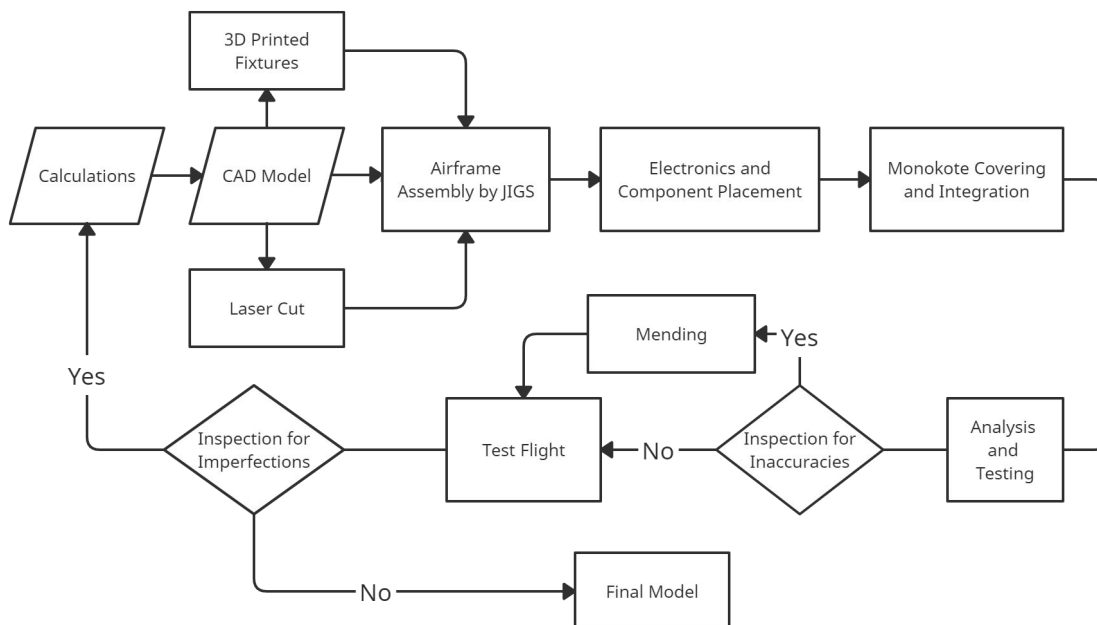


Figure 4.1: Design Methodology

4.2 Risk Analysis of Uncertainties

On commencement of the design process, risk factors that could influence the aircraft were collected and compiled. Based on the data obtained, three factors were seen to have the highest magnitude – Loss of Control, Structural Failure, Mechanism failure. Several steps were taken to overcome the chances of failure, which included multiple tests at every stage of manufacturing and having back-up components.

Risk Code	Risk	Likelihood	Severity	Risk index Factor
R01	Loss of Control	3	5	15
R02	Failure of Load Bearing Components	3	5	15
R03	Deployment and Recovery Failure	3	5	15
R04	Loss of Transmission	2	5	10
R05	Battery Discharging	2	5	10
R06	Propeller Damage	3	3	9
R07	Undesired CG Position	3	3	9
R08	Servo Failure	4	2	8
R09	Wind Boundary Layer Effects	2	4	8
R10	Propulsion System Malfunction	2	4	8
R11	Sensor Light Failure	2	4	8
R12	Failure of a Joint/Attachment/Fixture	3	2	6
R13	Wing Clapping	1	5	5
R14	Manufacturing Errors	2	2	4
R15	Detachment of Cover, Tape or Sticker	1	3	3

Table 4.1: Risk analysis

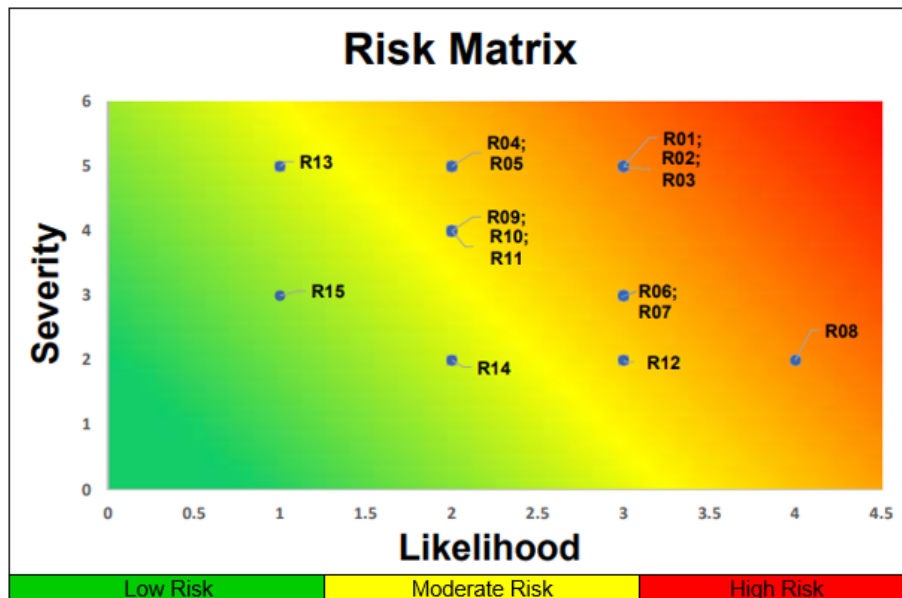
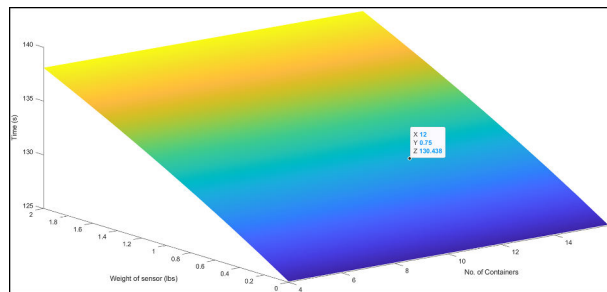


Figure 4.2: Risk Analysis of Uncertainties

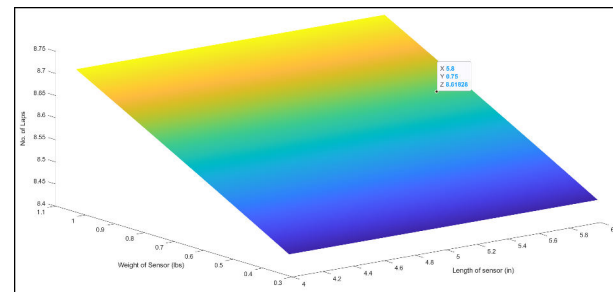
Mitigate	R01; R02; R03; R05; R10
Minimize	R04; R06; R07; R12; R13; R15
Accept	R08; R09; R11; R14

Risk minimization and mitigation strategies include employment of proper testing of aircraft before flight, precise manufacturing tools, and techniques with adequate safety margins, structural testing, static test for propulsion unit, ensuring proper bindings of all the electronics, checking the range of the aircraft during test flights, adoption of high mAh batteries, detailed preflight checks and finally flight tests to reveal other latent and hidden risks that may or may not require mitigation depending on the consequences.

4.3 Exhaustive Search Analysis (ESA)



(a) Exhaustive Search Analysis for M2



(b) Exhaustive Search Analysis for M3

Figure 4.3: Predicted Mission Performance

ESA is a Python code integrated with MATLAB that provides the desired aircraft combinations for maximizing the score. ESA utilizes the rules and limitations set by the DBF 2021 committee to generate all potential aircraft combinations for the flight missions. It employs the aircraft battery specifications and payload weight range to assess the sensor dimensions and the number of containers. The program evaluates 4.7 million possible combinations, on which the constraints on weight, aerodynamics, and avionics are applied.

The electronics selection is based on the conditions necessary to complete the four missions. The sizing of the aircraft was also computed using ESA. On iterating, the number of shipping container simulators and the sensor’s dimensions in compliance with the rules, the aircraft wing, tail, control surfaces, and suitable electronics range were obtained. Constraints on aspect ratio, thrust available, and time taken per lap were used to classify the possible combinations.

The most suitable aircraft configuration is selected based on the design constraints such as sensor length and wingspan to achieve the maximum score. These results are additionally tested and analyzed for further optimization. Finally, the combination which produced the highest score for the missions was selected to be designed. From the selected configuration from ESA, the weight and length of the sensor and the number of containers are used to determine the aircraft’s performance by determining the time required to complete M2 and M3.

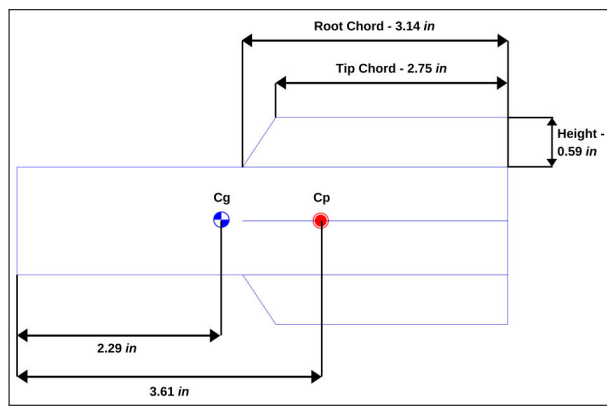
4.4 Fin Optimization

With Mission 3 requirements, we began our research on different configurations of DRM. Fins were added to the sensor casing to make it stable while being towed. However, its sizing and other parameters posed a challenge.

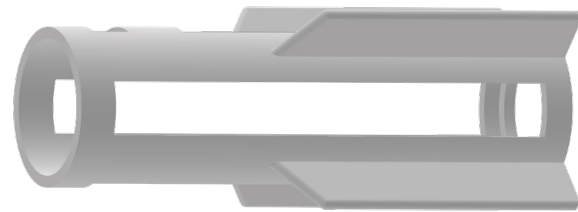
We considered a few thumb rules and constraints to find the best fit for sizing and number of fins. CG, Centre of Pressure (CP), available space within the fuse, and cruise velocity were considered before sizing the fins.

Initially, the distance between CP and CG was 1.32, equal to one body diameter. Various tests were done to optimize the fin sizing. OpenRocket [3] was used to find CP and was verified using the swing test. The sensor's aerodynamic response was tested in the wind tunnel and was found to be stable at a cruise speed of 65.61ft/s. The fins varied from 2 to 4, and different shapes for the fins were analyzed. Multiple iterations were tested, and the most suitable configuration was chosen.

We chose trapezoidal fins as it has a better effective area for a given height. Four trapezoidal fins were chosen as they were easy to fabricate and provided reasonable restoring force, while also protecting the sensor from impact damage.



(a) Fin Dimensions



(b) Sensor Casing

Figure 4.4: Fin Optimization

Fin	Fins Set	Thickness	Mass	Stability
Trapezoidal	4	0.11 in	0.32 oz	1.03 cal

Table 4.2: Fin Dimensions

4.5 Propulsion

Propulsion system selection began with the hunt for a motor and propeller combination that could provide the sufficient thrust required to fly the aircraft. Calculations were done with various motors, propellers, ESCs, and batteries to obtain the theoretical thrust value. A 6 cell LiPo battery was chosen due to the high energy density, low weight, and high cell capacity. Static thrust testing was performed to obtain the actual thrust values. The calculated and real values differed significantly.

As mentioned in the rule book, the LiPo propulsion batteries must have a fuse in line with the positive battery terminal with a maximum continuous current rate not to exceed the LiPo battery pack's maximum continuous discharge current rating. Hence, we finalized with a 9000mAh 25C rated battery. We chose LiPo batteries over NiMH because of their higher power and energy density.

We considered the below-mentioned motors for comparison. Scorpion SII 4035 330kV motor was appropriate for our plane requirements and gave us the required thrust to weight ratio.

Weight of 20/lbs was estimated from ESA. Accordingly, a motor and prop combination was chosen for a minimum T/W of 0.6. MotoCalc[4] and eCalc were used to compare different motors with different propeller configurations.

Few motors were shortlisted with a particular propeller configuration, and Scorpion SII 4035 330kV was chosen. Detailed iterations were done in the Scorpion Calc v355[5], the official calculator of Scorpion motors, and 22" x 12" propeller was finalized.

SI No.	Motor	T/W Ratio	Mixed Flight Time (min)	Weight (lbs)	Thrust (lbs)
1	SCORPION SII 4035	0.75	7.4	0.95	13.37
2	T-MOTOR MN 705-S	0.66	11.8	0.99	13.12
3	MAYTECH MTO6424-350MK	0.60	9	0.42	12.03
4	HYPERION Zs4045-12	0.68	11.7	1.36	13
5	FUTABA MA 5065	0.65	9.7	0.97	11.5

Table 4.3: Motors Considered

A T/W of 0.8 was kept in mind for the propeller selection, hence the selected motor was tested with 21" x 12", 22" x 12" and 23" x 12" Fiala propeller following the Diameter to Pitch ratio of minimum 1.5. The obtained values from the static thrust were considered and 22" x 12" was finalized.

Propeller	Thrust(lbf)	Current(A)
21" x 12"	12.78	56.3
22" x 12"	13.25	61.8
23" x 12"	14.08	68.4

Table 4.4: Static Thrust results

4.6 Airfoil Selection

Various airfoils like E420, FX-74modsm, MH 114 and S1223 were compared based on major parameters such as stall angle, coefficient of lift, coefficient of drag and fabrication ease. The main criteria for the airfoil selection is to get a high C_l value, maximum C_l/C_d value, minimum C_d and easy fabrication. Therefore, based on the above parameters a chart was obtained to relate the characteristics of each airfoil and a comparison was done. This comparison concluded with the selection of FX-74modsm because of its high C_l value and high C_l/C_d ratio as displayed in the ???. Further, FX-74modsm is most reliable during gusts since there is no sharp drop in lift coefficient after the stall angle.

Airfoil	Eppler 420	Fx74modsm	Martin Hepperle 114	Selig 1223
Max C_l	2.00	2.18	1.74	2.29
Min C_d	0.020	0.018	0.013	0.017
Max C_l/C_d	63.26	74.33	89.70	73.64
Fabrication	Moderate	Moderate	Easy	Difficult

Table 4.5: Airfoils Considered

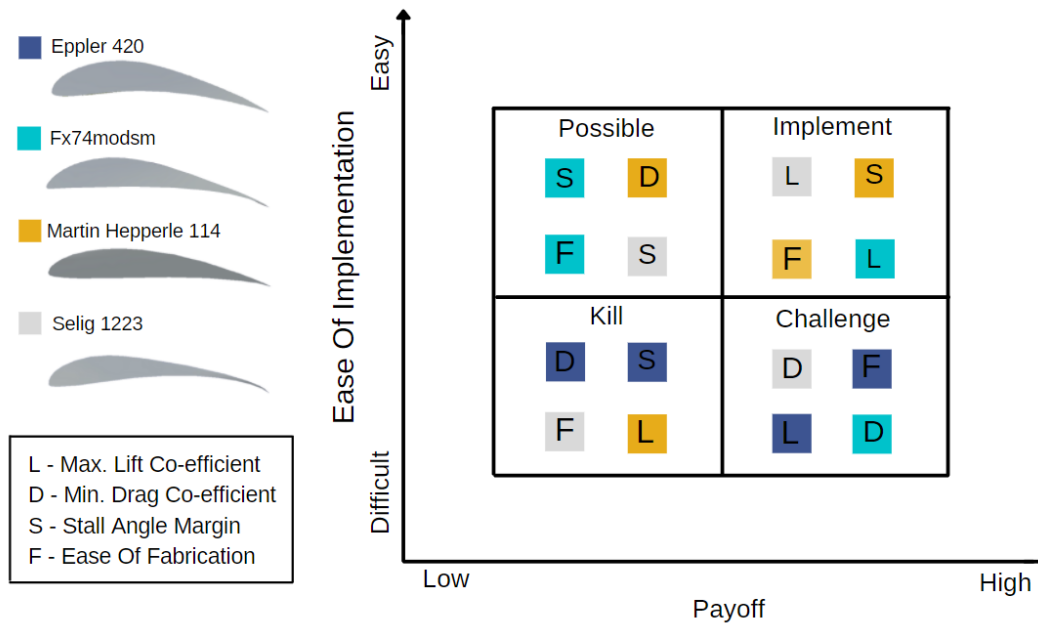


Figure 4.5: Airfoil Pick Chart

4.7 Sizing

4.7.1 Sensor Sizing

The size of the sensor was determined using ESA. To obtain the highest score for all four missions, the sensor is required to have a diameter of 1.29in with a length of 5.83in. The diameter allows for the secure attachment of lights necessary for M3. For M2, the highest advantage was obtained by carrying the sensor shipping container accompanied by twelve shipping container simulators.

4.7.2 Wing Sizing

ESA provides the desired aircraft combinations for maximizing the score. A maximum span of 60in is used, as provided by the competition requirement. Wing lift and drag were calculated for different wing areas in ANSYS 2020. On obtaining the iterations and the outputs from ESA, the wing area of 762.48in² was obtained with an aspect ratio of 4.72. Based on the obtained area, the chord was calculated to be 12.7in with a wing incidence angle of 2°.

4.7.3 Tail Sizing

The empennage was designed to withstand disturbances and control the aircraft. The first step in designing the empennage was to assume the Horizontal Tail Volume Coefficient (V_H) and Vertical Tail Volume Coefficient (V_V), and through the iteration process and test flight data, the V_H and V_V are determined to be 0.6 and 0.05, respectively. Further, the horizontal tail arm is calculated to be as 28in considering the number of containers in the fuselage and the length of the fuselage which is followed by Area of Horizontal Stabilizer (S_H) and Area of Vertical Stabilizer (S_V) calculations.[6]

$$l_{opt} = \sqrt{\frac{4C_S V_H}{\pi D_f}} \tag{7}$$

The span and Mean Aerodynamic Chord (MAC) are designed by an iterative process to meet the requirements of plane stability.

$$\overline{V}_H = \frac{l S_h}{\overline{C} S} \quad (8)$$

$$\overline{V}_v = \frac{l_v S_v}{b S} \quad (9)$$

	Horizontal	Vertical
Span (in)	25.56	12.35
MAC (in)	8.12	8.23
Root Chord (in)	8.12	10.58
Tip Chord (in)	8.12	5.29
Taper Ratio	1	0.5
Area (in ²)	207.63	101.66

Table 4.6: Tail Sizing

4.7.4 Control Surface Sizing

The control surface sizing was done after ESA. The aileron is designed based on the roll moments and the dimensions of the wing. It has a chord ratio of 0.25 and a span ratio of 0.36. Elevator has a chord ratio of 0.38, and the rudder has a chord ratio of 0.35. Similarly, the rudder and elevator are designed considering the downwash of the wing and relevant moment coefficients. The rudder is sized and positioned to avoid the wake of the horizontal stabilizer.

Control Surface	Span (in)	MAC (in)	Area (in ²)
Aileron	10.72	3.17	78.90
Elevator	25.56	3.09	78.98
Rudder	12.35	2.88	35.58

Table 4.7: Control Surface Sizing

The servo sizing was done after the control surface dimensions were calculated. The required torque for any particular deflection was determined using the formula:

$$Torque = 8.5 * 10^{-6} * [C^2 * V^2 * L * Sin(S_1) \frac{Tan(S_1)}{Tan(S_2)}] \quad (10)$$

Where C = Control Surface Chord in in, L = Control Surface Length in in, V = Speed in ft/s, S_1 = Max Control Surface Deflection in °, S_2 = Max Servo Deflection in °

A graph of Torque vs Deflection is plotted and used to find a suitable servo. Tower Pro MG90s servo is the preferred servo for all the control surfaces.

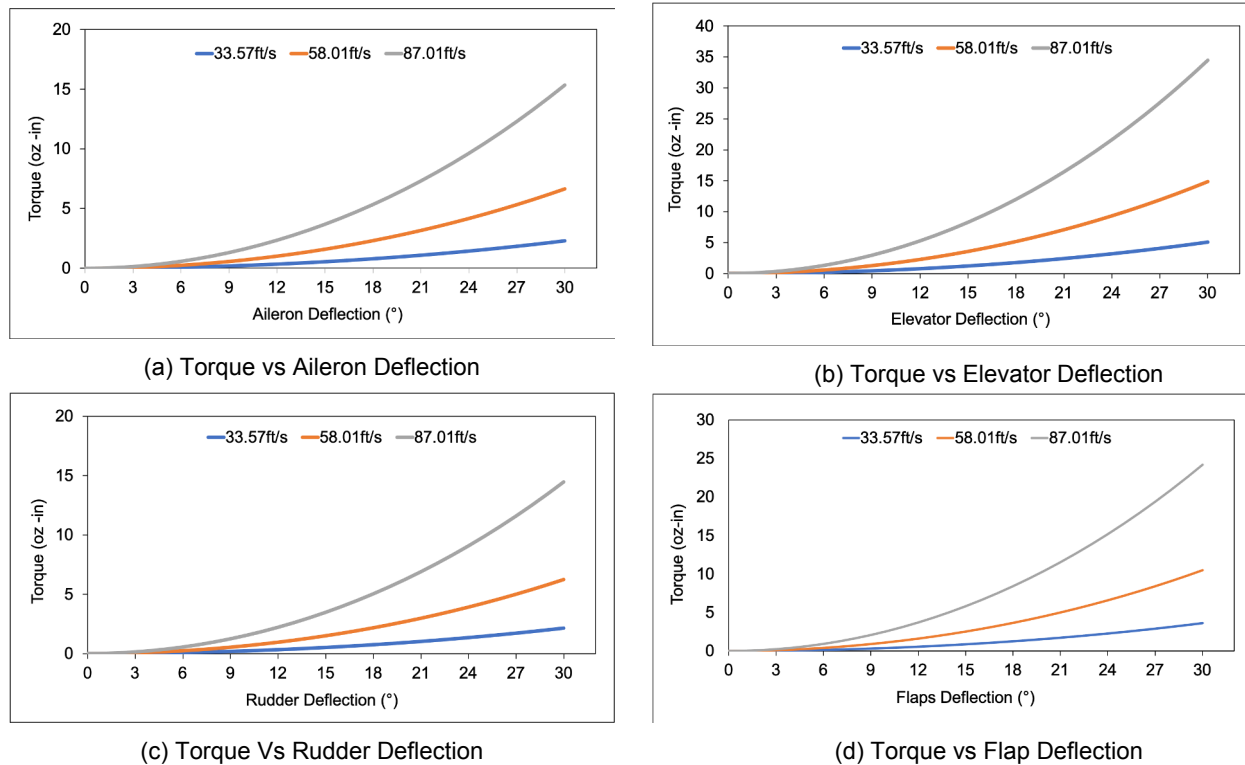


Figure 4.6: Torque vs Control Surface Deflection

4.7.5 Fuselage Sizing

The fuselage supports the payload and connects all the components of the aircraft. It is designed to accommodate the possible required payload and DRM to maximize the team’s score. The fuselage is lightweight while being able to carry the payload for M2 and deploy and recover the sensor in M3. Semi-monocoque structure is used in the design of the fuselage.

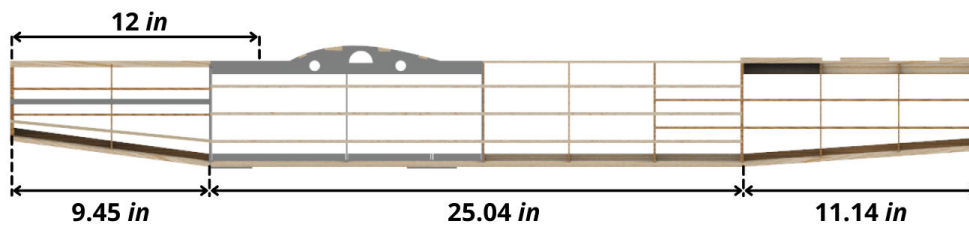


Figure 4.7: Fuselage Dimensions

4.7.6 Landing Gear Sizing

The landing gear holds the weight of the complete structure. It is designed to withstand shock and impacts to the fuselage with the ground and to have a safe and successful landing to obtain a score in all three missions. Mild steel rods of 0.20in were used to design the landing gear. The nose gear is placed at an angle of 30° and the main gear at 42.7° concerning the vertical axis to protect the gear from bending and shock loads. The angles were

selected based on analysis and previous experiences. Further, the thrust line is at an angle of 3° to the landing gear's horizontal axis.

4.8 Stability and Control

For static stability of the aircraft, the neutral point is calculated to be $6.01in$ from the leading edge of the wing. The range of CG positions of the aircraft is determined from the Stability Margin (SM). The tail volumes, aircraft design, and mass placement were iterated to ensure that the plane was stable. The CG position of the final iteration calculated from the wing's leading edge is as depicted in Table 4.8.[7]

Mission	CG(in)	SM
M1	4.88	8.88%
M2	4.50	11.89%
M3 (Before Deployment)	3.94	16.26%
M3 (After Deployment)	5.12	7.04%

Table 4.8: Centre of Gravity and Stability Margin for the Three Flying Missions

4.8.1 Static Stability

The stability derivatives were used to understand the aircraft characteristics for the chosen configurations and preliminary design details. The derivatives were calculated for the missions and used to understand the requirements of the three flying missions. The analysis was carried out at cruise velocity in trimmed condition with the rolling moment, pitching moment, and yawing moment equal to zero. The values were verified with Athena Vortex Lattice (AVL)[8], and it is observed that the derivatives obtained are within the acceptable range of the flight-determined derivatives.

$C_{L\alpha}$	4.46	$C_{L\beta}$	0.00	C_{Lp}	0.00	C_{Lq}	9.57	C_{Lr}	0.00
$C_{m\alpha}$	-1.79	$C_{m\beta}$	0.00	C_{mp}	0.00	C_{mq}	-8.59	C_{mr}	0.00
$C_{n\alpha}$	0.00	$C_{n\beta}$	0.09	C_{np}	-0.04	C_{nq}	0.00	C_{nr}	0.08

Table 4.9: Static Stability Derivatives

4.8.2 Dynamic Stability

Once the stability derivatives were determined, the dynamic derivatives were derived for the three flying missions for the aircraft's mass distribution and flight conditions. The derivatives for M1 and M2 are observed to be almost equal, while the derivatives calculated for M3 after deployment is as shown.

An aircraft is considered dynamically stable when the roots are plotted on the negative X-axis, with the Y-axis proportional to the oscillation frequency. It is observed that the aircraft is stable for all the modes except Spiral Mode during the flying missions.

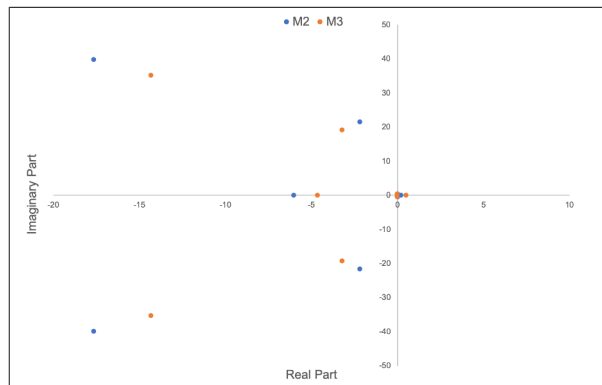


Figure 4.8: Root Locus Plot for the 3 Missions

The eigenvalues obtained from the root locus plot along their natural frequency (Hz) and damping ratio is as depicted in table 4.10.

Mission		Short Period	Phugoid	Roll	Dutch Roll	Spiral Mode
M2	Eigen Value	$-17.6 \pm 39.84i$	$-0.01 \pm 0.44i$	$-6.03 \pm 0.00i$	$-2.19 \pm 21.55i$	$0.2 \pm 0.00i$
	Undamped Frequency	2.59	0.03	-	3.24	-
	Damping Ratio	0.62	0.07	-	0.13	-
M3	Eigen Value	$-14.33 \pm 35.24i$	$-0.02 \pm 0.38i$	$-4.65 \pm 0.00i$	$-3.23 \pm 19.17i$	$0.49 \pm 0.00i$
	Undamped Frequency	0.31	0.09	-	0.38	-
	Damping Ratio	0.9	0.03	-	0.35	-

Table 4.10: Dynamic Stability for the 3 Missions

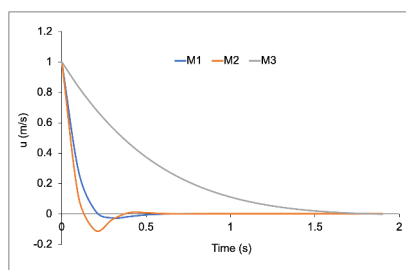


Figure 4.9: Time Response for Short Period

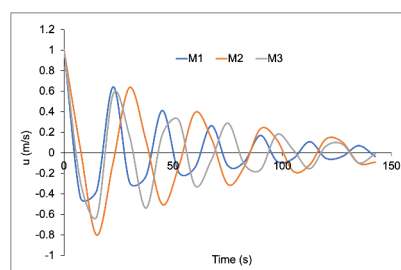


Figure 4.10: Time Response for Phugoid

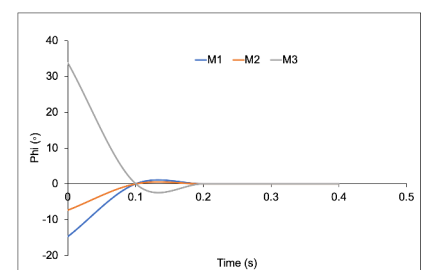


Figure 4.11: Time Response for Damping

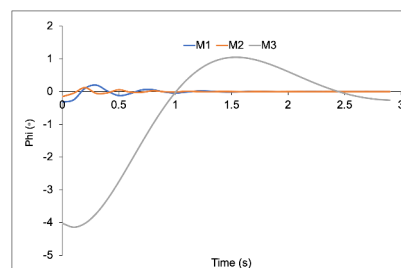


Figure 4.12: Time Response for Dutch Roll

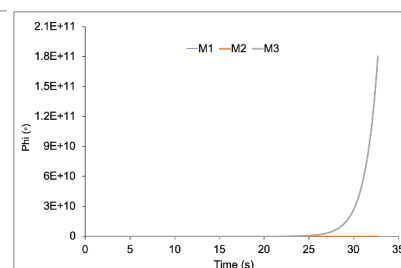


Figure 4.13: Time Response for Spiral Mode

4.9 Aerodynamics [1]

4.9.1 Lift Distribution

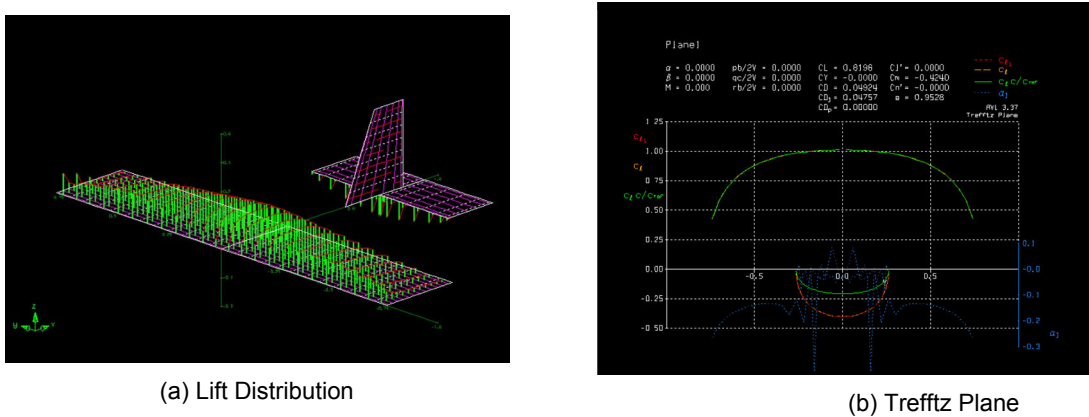


Figure 4.14: Aircraft Lift Distribution

AVL was used as our primary tool of choice to analyze the lift distribution of the wing and tail surfaces. Trefftz plane analysis of induced drag and trimmed condition was plotted as shown in Fig 4.14 and studied.

The Trefftz plane analysis revealed valuable information about the wing surfaces' aerodynamic stability. This mainly included the amount of air displaced by the wing whose results were used to determine the induced drag produced. This study was used to find the span-wise efficiency of the wing, which greatly affects its design and performance. The results obtained were extensively interpreted to improve various factors, namely, the cross-sectional area of the wing and fuselage, angle of attack, flight path and tail calculations.

4.9.2 Downwash

The wing and tail section of the aircraft were modeled in precise softwares such as Catia V6 and simulated in ANSYS 2020 to visualise the downwash. The results obtained were studied to understand the effect of downwash on lift and tail calculation with importance given to mainly study the downwash effect on the tail so that it could be effectively iterated to increase the stability and control and improve efficiency by keeping it outside the wing's downwash.

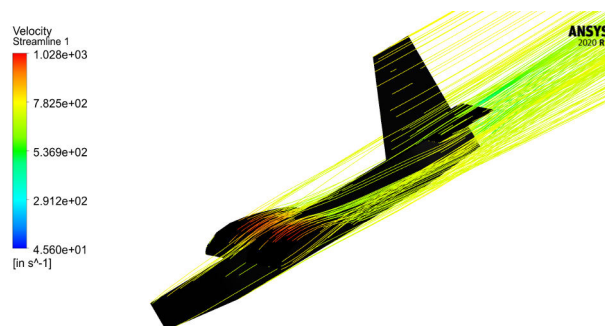


Figure 4.15: Downwash

4.9.3 Drag Analysis

The team carried out drag analysis on all the components of the aircraft namely fuselage, wings, tail, landing gear and the sensor. All the components were designed using a precise modelling software, Catia V6, which were later imported to ANSYS 2020, to perform CFX analysis and thus, record the drag contribution of various components. The results obtained from the CFX analysis were compared with the theoretical values, to enhance the performance of the aircraft.

From the analysis, it was evident that the wing contributed most to total drag of the aircraft in both M2 and M3. It was also evident from Fig 4.15 that the proportion of individual contribution of components to total drag remained the same for both M2 and M3. Analysis of M3 showed that the sensor contributed 4% of total drag.

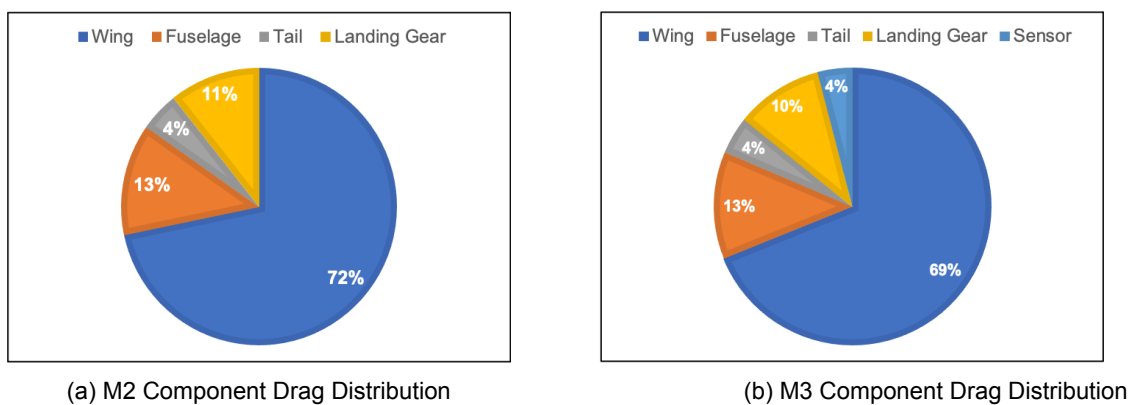


Figure 4.16: Component Drag Pie Chart

4.10 Performance [2]

4.10.1 Rate of Climb

Theoretically, we know that the maximum rate of climb occurs at the velocity when the power required is minimum and that state is achieved at a point where $(Coefficient\ of\ Lift(C_L))^{3/2}/(C_D)$ is maximum. Since the C_L of the aircraft for M1 is highest among the three missions, it translates to least power required in M1 when juxtaposed against other two missions. The rate of climb achieved for the individual missions is found to be 11.80 ft/s, 4.95 ft/s and 9.16 ft/s and is optimized to attain minimum lap time for a given payload in all the missions, as displayed in Fig 4.17.

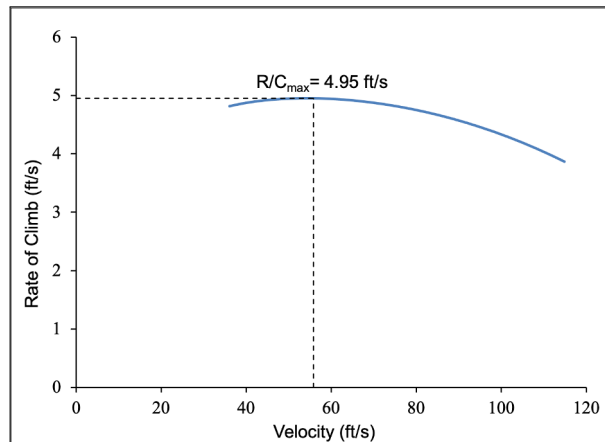


Figure 4.17: Rate of Climb

4.10.2 Drag Polar

The L/D_{max} point from the plotted curve is a salient point called the design point of the aircraft. The corresponding value of C_L at this point is termed the design lift coefficient for the airplane. The C_L value at L/D_{max} offers minimum total drag. For each of the missions, the L/D_{max} was found to be 8.74, 9.08 and 5.13 respectively as illustrated in Fig 4.18. Further, the design lift coefficient for M2 is found out to be 0.55.

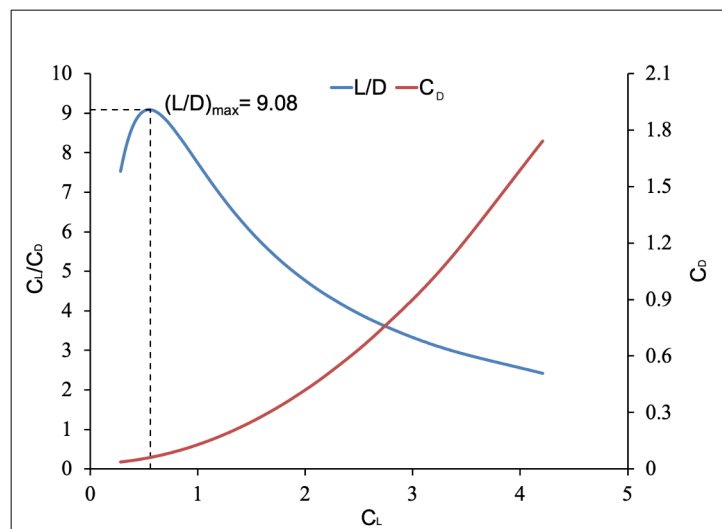


Figure 4.18: Drag Polar

4.10.3 Drag Vs Velocity

At the point of intersection of induced and parasitic drag curves, we obtain the minimum total drag point, which is equal to the minimum thrust required. The thrust decreases with an increase in L/D ratio, and therefore for each mission, to increase endurance, the minimum thrust required at L/D_{max} was found to be 1.01 lbf, 2.00 lbf and 1.88 lbf respectively, as presented in Fig. 4.20

In M1 and M2, the plane flies at cruise speed. However, in M3, the mission requirement being maximum laps, the plane is seen to fly at 65.61 ft/s which is higher than cruise speed, which provides the added advantage of flying

in the velocity stable region, wherein the gust loads have comparatively lesser influence on aircraft stability.

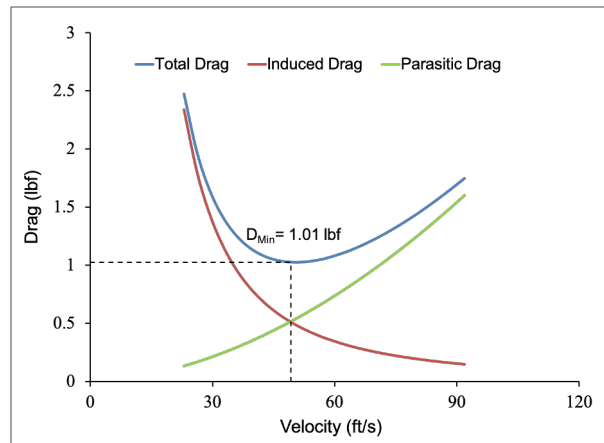
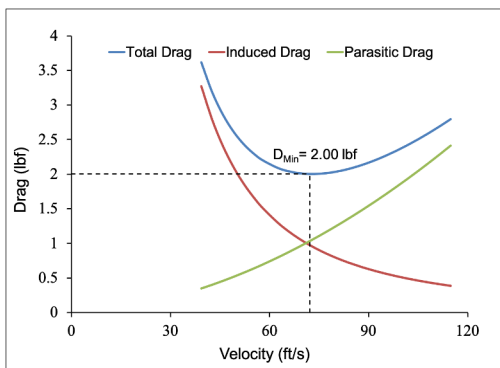
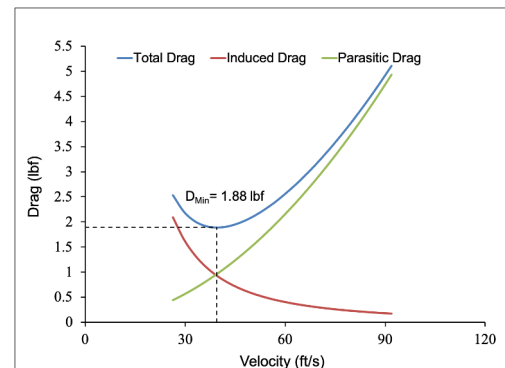


Figure 4.19: Drag vs Velocity - M1



(a) Drag vs Velocity - M2



(b) Drag vs Velocity - M3

Figure 4.20: Drag vs Velocity

4.10.4 Downwash Angle

The downwash angle is calculated using the formula,

$$\xi = \xi_0 + \frac{d\xi}{d\alpha} \times \alpha \tag{11}$$

The plot discloses the downwash of air produced due to wing tip vortices at some specific AOA and is plotted for determining the downwash effect on our aircraft. Hence, it is noticed that at zero AOA, there is a positive downwash which affects the wing AOA by 5.40° with a slope of 0.213, which defines the rise over the run.

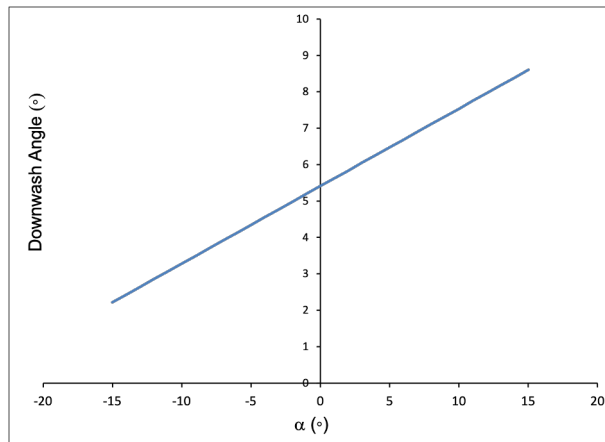


Figure 4.21: Downwash Angle

4.10.5 Landing and Takeoff Performance

During take-off and landing roll, the flaps were deployed in order to reduce the stall velocity to 30.52 ft/s which directly shortens the required take-off and landing distance. The aircraft covers a total take-off distance of 84.98 ft, climbing at an angle of 15.55° in 9 s by clearing an obstacle of height 7 ft at an acceleration of 7.9 ft/s² encountering a load factor of 1.19.

During landing our aircraft clears an obstacle of height 10 ft and takes 15.20 s to decelerate at 2.61 ft/s² with a descent angle of 3° and covers a distance of 300.80 ft before coming to rest. [6]

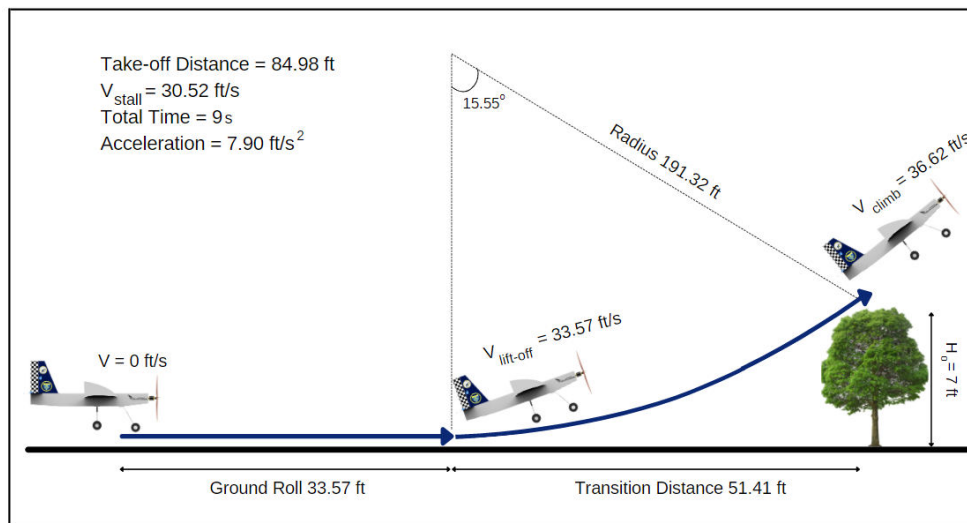


Figure 4.22: Takeoff Performance

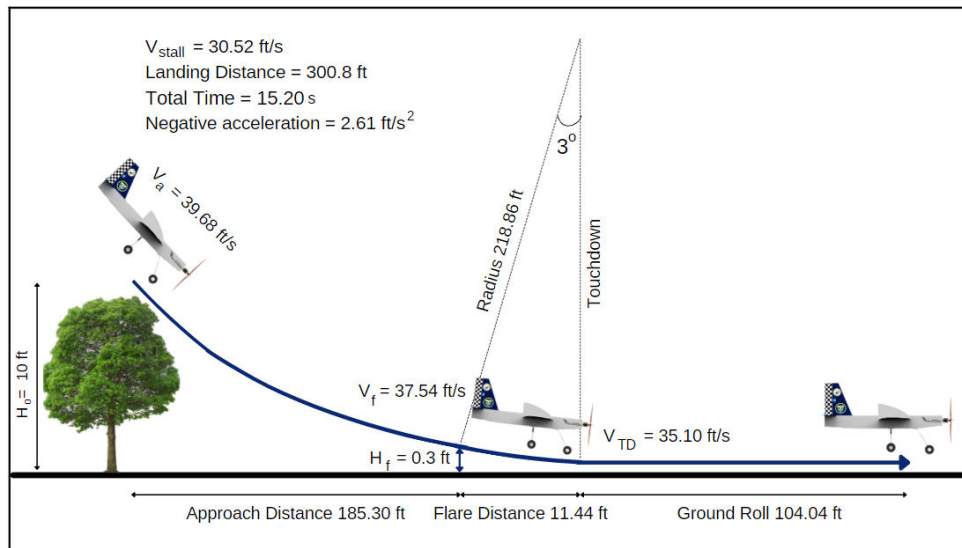


Figure 4.23: Landing Performance

5 Detailed Design

5.1 Dimensional Parameters

The characteristic dimensional parameters used for the aircraft's design are listed in Table 5.1.

	WING	TAIL	
Airfoil	Fx-74 modsm	Airfoil	Flat plate
Span(in)	60	Horizontal span(in)	25.56
Chord(in)	12.7	Horizontal MAC(in)	8.12
Area(in ²)	762.48	Horizontal Area(in ²)	207.63
AR	4.72	Vertical span(in)	12.35
Incidence angle	2°	Vertical MAC(in)	8.23
Taper ratio	1	Taper ratio(vertical)	0.5
Planform	Rectangular	Area(in ²)	101.66
Endplate area(in ²)	46.51	Tail arm(in)	28
CONTROL SURFACES		SENSOR	
Elevator Chord(in)	3.09	Length(in)	5.83
Elevator Span(in)	25.56	Diameter(in)	1.29
Rudder Chord(in)	2.88	Weight(lbs)	0.75
Rudder Span(in)	12.34	Total container Nos.	11+1
Aileron Span(in)	10.8	Deployment length(in)	58.3in
Aileron chord(in)	3.17	Length/Diameter	4.49
FUSELAGE		MOTOR	
Total length(in)	45.63	Model	Scorpion SII 4035 330KV
Nose length(in)	9.45	Gearbox	1:1

Tail length(<i>in</i>)	11.14	Effective KV	332 RPM/volt
Height(<i>in</i>)	5	Power Rating(<i>W</i>)	2400
Width(<i>in</i>)	4.37	No Load Current(<i>A</i>) @ 10V	1.41
Height from ground(<i>in</i>)	9.12	Internal Resistance(Ω)	0.031
		Weight(<i>lbs</i>)	0.96
HIGH LIFT DEVICES		PROPELLER	
Flap Span(<i>in</i>)	16.82	Manufacturer	Fiala Electric
Flap Chord(<i>in</i>)	3.17	Mission 1, 2, 3	22" x 12" + 0°
LANDING GEAR			
Overall Height(<i>in</i>)	9.75	Nose Gear Angle (<i>in</i>)	30°
Wheel base(<i>in</i>)	14.83	Track Length (<i>in</i>)	16.41

Table 5.1: Aircraft Dimensions

5.2 Structural Characteristics

The aircraft has a gross weight of 18.24*lbs* with a Factor of Safety (FoS) - 1.4. The aircraft is designed to minimize the structural weight while achieving the mission requirements. The rib placement of the wing is done to counteract the bending and torsion loads acting on it. The fuselage is a semi-monocoque structure holding shipping container simulators and DRM, which can withstand all flight loads, including motor thrust and torque. Tricycle landing gear was selected and it is designed to withstand enormous loads.

5.3 Subsystem Design

The aircraft constitutes of the Propulsion system, Fuselage, Wing, Empennage, Firewall, Landing Gear, and DRM. These subsystems are assembled to work together without causing any interference to the aircraft's performance or the other subsystems. The systems are elaborately examined and elucidated in the following sections.

5.3.1 Wing

The wing is designed to withstand aerodynamic, bending, and torsional loads. The wing structure is made of aeroply and balsa ribs. The ribs are designed to withstand the loads while being as lightweight as possible by incorporating lightning holes. 0.08*in* aeroply ribs is utilized in regions susceptible to higher loads. Sandwich ribs are used at the end of spars to ensure structural integrity. Servo slots are provided in the aeroply ribs for mounting servos for flaps and aileron deflection.

The wing consists of two I-section beams located at 25% and 70% of the chord length, two Carbon Fiber (CF) spars interconnecting the wings, and five additional



Figure 5.1: Isometric view of wing

flanges to withstand the loads acting on it and support the monokote. The static structural analysis shows higher deformation towards the wing’s trailing edge; hence, a second I beam is included at 70% chord length. The leading edge consists of a 0.16 x 0.11in CF rod covered with 0.04in balsa. Similarly, the trailing edge is reinforced with 0.02in CF batten due to the airfoil curvature and is covered with 0.04in balsa.

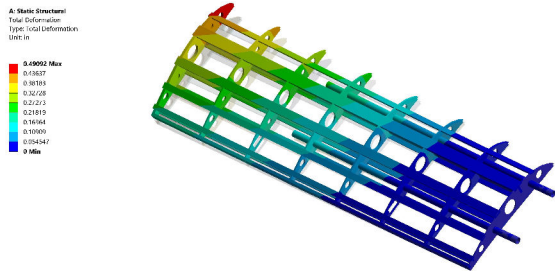


Figure 5.2: Wing Deformations

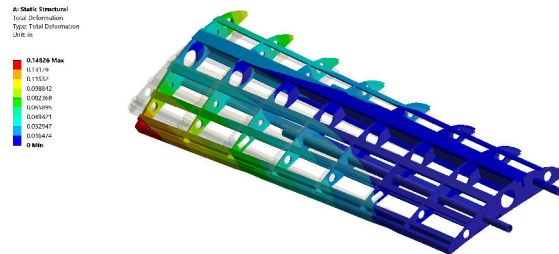


Figure 5.3: Wing Torsion

Static structural analysis is performed to determine the deflection of the wing for a bending load. A load of 18.24lbf is applied on the I sections, and maximum deformation of 0.49in is observed at the wingtip. A load of 5.29lbs-in is applied to the end of the wing and a maximum deflection of 0.98in is observed. It is inferred that the wing is capable of performing all the missions exceptionally. Modal analysis is conducted on the wing structure to observe its vibrational properties at a frequency of 23.58Hz and an average deflection of 23.14in is recorded.

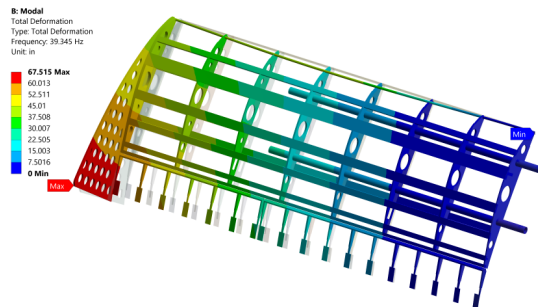


Figure 5.4: Modal Analysis

5.3.2 Endplates

Endplates are incorporated to reduce lift-induced drag. The increase in wetted area and interference drag due to the addition of endplates reduces the wingtip vortices created due to the generation of lift. Endplate of 0.12in balsa is utilised for this purpose. Its addition also increases the inertia and reduces the wing flutter by reducing the natural frequency.

Without Endplates	With Endplates		
L/D	h/b	L/D	Increase in L/D
10.57	0.1	11.021	0.0426
	0.105	11.06	0.046

Table 5.2: Endplates Comparison

An analysis is performed for endplates of different h/b ratios, where h/b ratio signifies the height of the endplate to the span of the wing. After optimization, the endplate with h/b ratio of 0.105 is calculated.

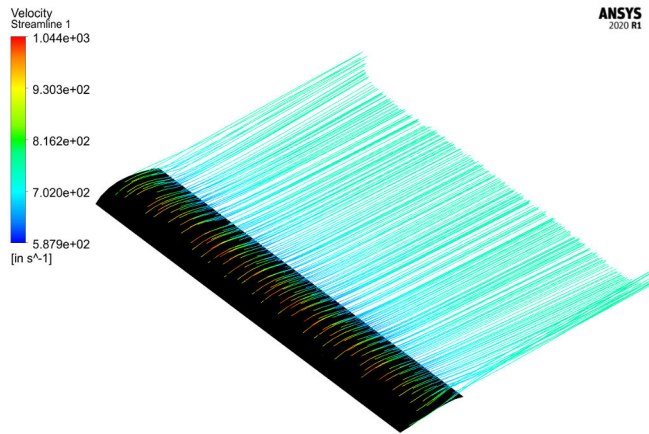


Figure 5.5: Wing without Endplates

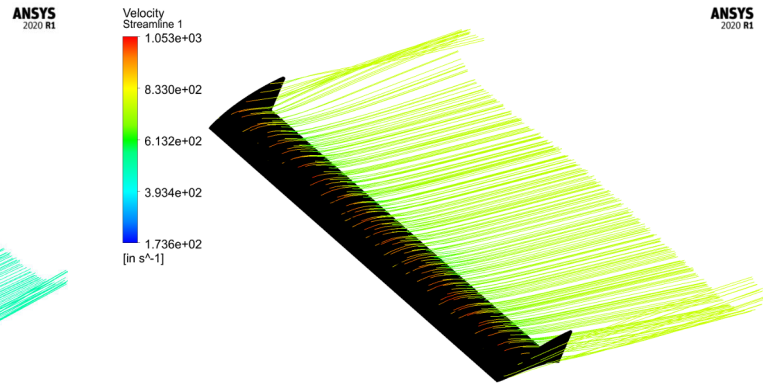


Figure 5.6: Wing with Endplates

The Aspect Ratio (AR) change is given by the formula:

$$\Delta AR \approx 1.9(h/b)AR \text{ for } h/b \text{ upto } 0.4 \tag{12}$$

The ΔAR for the chosen endplate is 0.94.

5.3.3 Trailing Edge Flaps

The team determined that to reduce the plane’s speed during landing, trailing edge flaps had to be employed with the design objective to minimize stall speed, reduce aircraft speed during landing and increase C_L of the wing when deployed. To maximize the C_L , flaps increase the camber of the wing temporarily during takeoff.

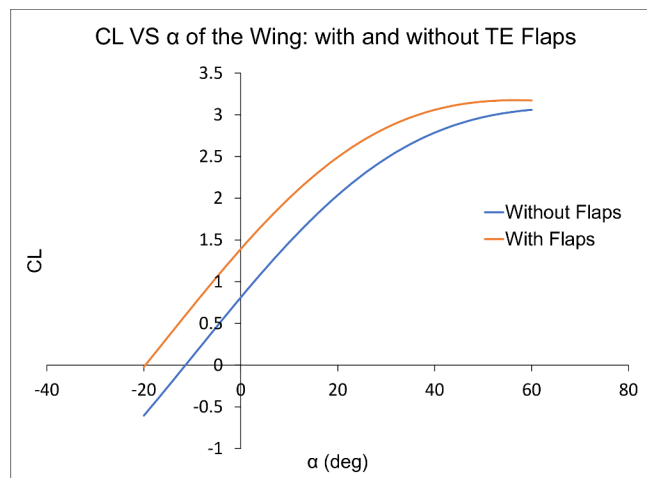


Figure 5.7: C_L vs α of the wing: with and without TE Flaps

The C_f/C ratio is calculated as 0.25 based on the Lifting Line Theory. Further, the span is iterated, and a span of $0.56b$ was estimated with a maximum deflection of 30° . Figure 5.7 demonstrates the change in lift coefficient of the wing when the flap is deflected.

The stall speed before deployment is 36.25ft/s . The stall speed reduction range obtained from the pilot feedback after the flight test was in the range of $5\text{-}8\text{ft/s}$. The stall speed after deployment of flaps is 30.52ft/s .

5.3.4 Empennage

Flat plate is employed for empennage, made of 0.16 in balsa. It is connected to the rear fuselage through its stringers and slots made in the horizontal stabilizer. The vertical stabilizer is mounted on the horizontal stabilizer in a similar method.

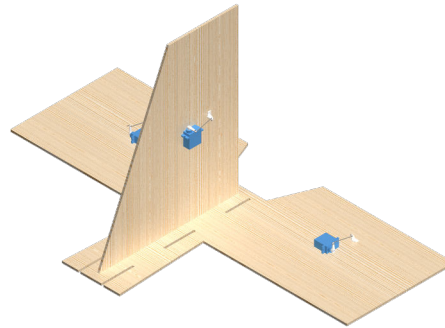


Figure 5.8: Empennage

5.3.5 Fuselage

The fuselage is a semi-monocoque structure that will accommodate all the shipping container simulators, the sensor with the DRM. This also includes the avionics such as the battery, ESC, and the receiver. The fuselage's central part houses the 12 shipping containers and is made to obtain a minimum cross-sectional area. To achieve this, the container boxes are placed longitudinally in 3 rows of 4 containers.



Figure 5.9: Fuselage

The avionics housed in the nose section is connected to the central fuselage through-bolts passing through aluminum formers. The aft fuselage cone houses the DRM of the sensor and a nozzle-like exit for the sensor deployment. The nozzle is kept open in the rear as the CFX analysis showed little change in drag for a closed and an open nozzle.

A semi-monocoque structure was finalized after an iteration of the truss structure was tedious to manufacture and could not provide adequate strength. The central fuselage has an aluminum framework with two aluminum

T-sections at the bottom to support the landing gear impact and two aluminum stringers in the top to house the wing spars, all connected by aluminum formers. The remaining structure is made of aeroply formers and balsa and aeroply stringers. The nose consists of 1 aluminum former and 2 aluminum stringers. The firewall is made of 0.2in aeroply to sustain high thrust.

The fuselage has a total length of 45.63in with the nose cone being 9.45in and the aft cone being 11.14in. The main fuselage has a cross-section of 5in x 4.37in. The nose cone tapers to 3.15in x 3.78in and the empennage tapers to 3.22in x 4.25in to facilitate deployment. The fuselage structure is analysed statically for a load of 17.78lbf considering load factor of 2 for the empty aircraft weight of 36.48lbs. The load is applied on the main landing gear plates of the fuselage. The analysis shows a maximum deformation of 0.657in at the flanges of the T-section.

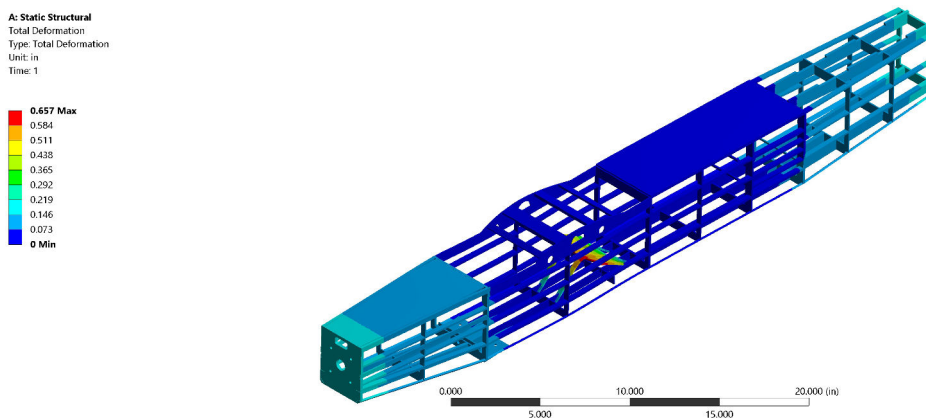


Figure 5.10: Fuselage

5.3.6 Firewall

The firewall is an aeroply structure made of 0.08in and 0.12in sandwich to provide adequate strength in order to withstand the load acting over it. It is connected through various stringers, namely 2 sandwich stringers of 0.08in aeroply and 0.12in balsa, 4 aeroply 0.12in stringers, 4 balsa 0.16in stringers, and 2 aluminum stringers. The firewall is 3.15in x 3.78in to facilitate mounting of the motor.

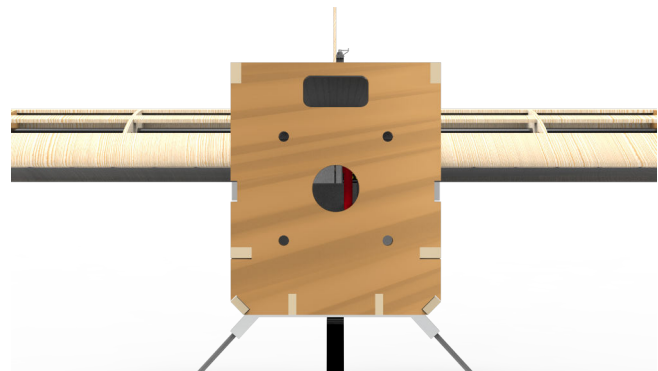


Figure 5.11: Firewall

5.3.7 Sensor

The sensor is a cylindrical body with diameter of 1.29in and length of 5.83in. The sensor's dimensions were opted after analyzing the scoring equation, and sizing was done according to ESA. The ratio of length to diameter comes up to 4.50. It consists of the following electronics, which are required for the mission performance as mentioned in the rulebook - battery, optocoupler, resistor, capacitor, buck booster, and servo controller. The sensor is enclosed within a 3D-printed case, which protects it from drop shock events. Trapezoidal fins are used on the sensor casing to provide aerodynamic stability to the sensor, which is essential for M3 performance and plays a

significant role in the sensor's stability while being towed. Upon analyzing the sensor, the lift and drag values of the sensor during flight is obtained to be $0.19/bf$ and $0.16/bf$.

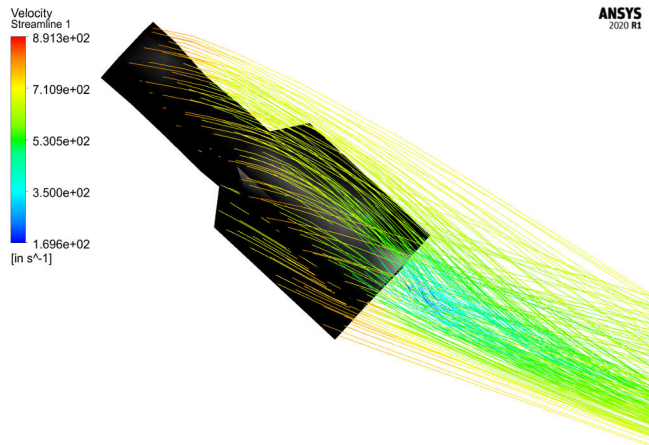


Figure 5.12: Velocity Streamline Analysis of Sensor

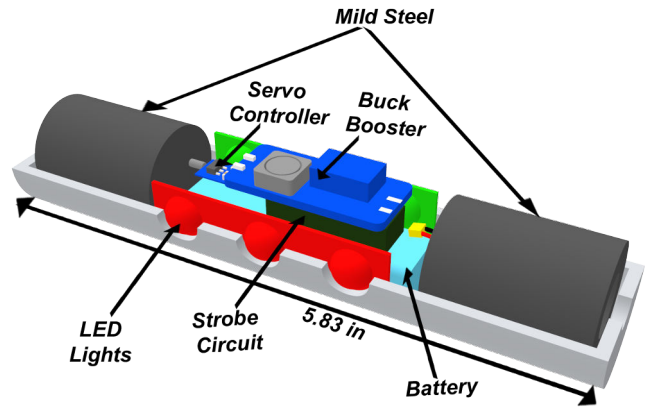


Figure 5.13: Sensor cross section

5.3.8 Container

The sensor shipping container was made out of 0.197in depron. The depron was laser cut in a jigsaw type pattern and then assembled into a box by using hot glue. The team chose this method as depron has a reasonable rigidity and can also take small compressive loads, which would be required in the sensor drop test. After testing the shipping container for the drop test, it was found that the depron container protected the sensor from any damage when dropped from a height of upto 14in.

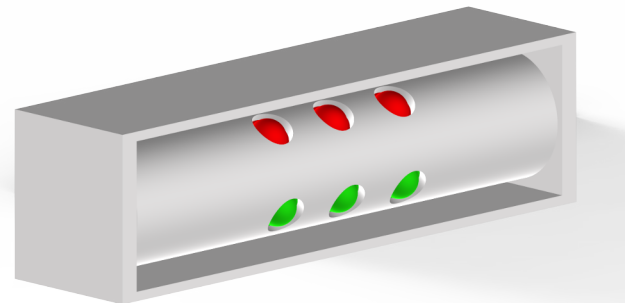


Figure 5.14: Sensor Container

5.3.9 Container Simulator

The shipping container simulators were fabricated from Polylactic Acid (PLA) using a 3D printer. The team chose the method as it allowed for the shipping container simulators to be extremely close to the shipping container dimensions and weight. The simulators have a hollowed centre which houses 5 steel washers each weighing 0.022lbs to give the exact required weight.

5.3.10 Sensor Lights

A 12V red LED strip and green LED strip containing 3 LEDs in each strip were used in the sensor. A servo was modified in such a way that it is capable of controlling any 2 terminal electric components operating at 5V. Since the LED was rated for 12V, a buck booster was used to step up the DC voltage to 12V, providing sufficient supply to glow the LED at its brightest range.

The servo's positive terminal was taken out and was given to an external 2S1P LiPo battery obeying the rule of having a separate battery for the sensor lights. The ground of the battery was given to the servo's ground terminal. The servo's ground and the signal terminal were given to the receiver to activate it from the transmitter. A strobe circuit was created with the help of transistors, resistors, and capacitors providing the strobe pattern. With increase and decrease in the PWM signal, the frequency of the strobe can be controlled. In contrast, the servo should handle a current draw of 1.5A, so a servo of more than 1.5A stall current draw was modified to overcome the drawback.

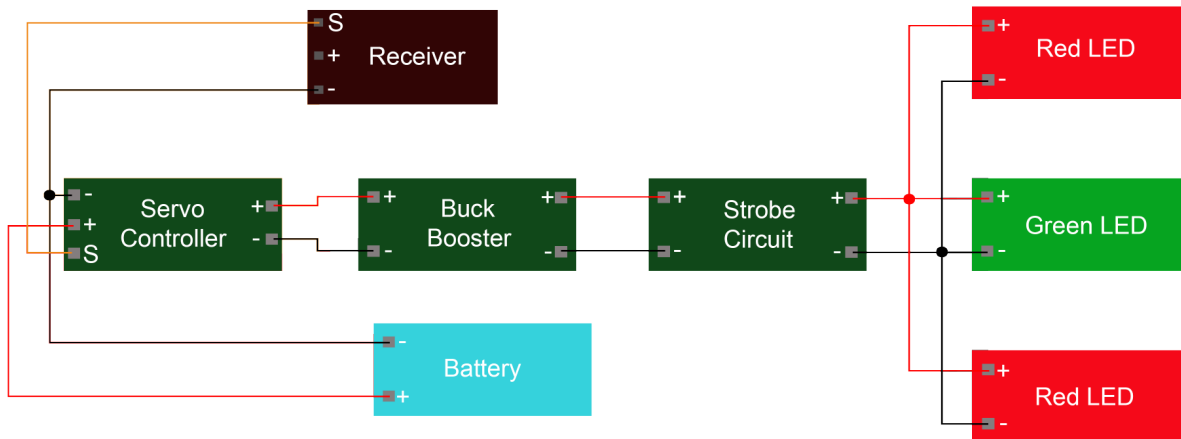


Figure 5.15: Circuit Diagram

5.3.11 Deployment and Recovery Mechanism

DRM consists of a manipulated servo, cylindrical shaft, copper cable, and sensor casing. It is enclosed in a cuboid container with dimensions of 3.74 x 3.74 x 3.93in. The aeroply used is 0.12in thick.

The servo used is a high torque (138.88oz*in) that can rotate approximately 180° (90° in each direction). However, as the mission required retracting the sensor, the servo was manipulated to rotate 360° by altering the potentiometer. The shaft was used as the servo arm for the smooth deployment and retraction of copper cable.

The shaft is placed on the servo longitudinally inside the container and rotates clockwise or anti-clockwise when the servo is actuated to deploy or retract the sensor during the mission. Insulated copper cable was to deploy and retract the sensor while in the air. The copper cable is wound over the cylindrical shaft and fixed tightly. One end of it is connected to the receiver and the other to the sensor lights. Many tests were conducted to check the copper cable's strength, wind tunnel tests, and the sensor was deployed and towed behind a vehicle at 40mph. The string did not bend or extend much. Minor changes were found.

Moreover, copper being an electric conductor, no other wiring was required separately to operate sensor lights. The copper wire has a diameter of 0.01in with 80in length. According to the scoring equations we considered, the

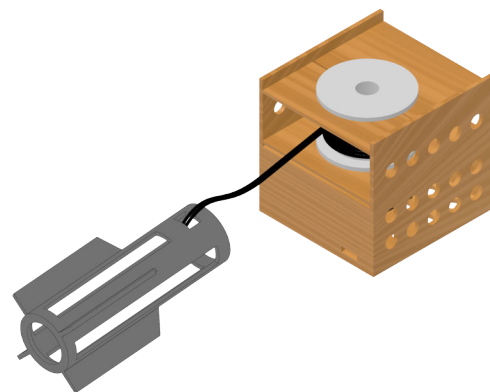


Figure 5.16: DRM

sensor's full deployment from aircraft is at 58.3in.

To achieve the time of deployment and recovery concerning the scoring equation, we experimented with the shaft dimensions, which were easy to fit in the container and reduce the time for deployment and recovery. We took the shaft diameter as 1.77in and length as 1.41in and it takes 12-13seconds for deployment and 14-16seconds for recovery.

The DRM container is placed in the aircraft's aft section - a nozzle in the tail was left for the sensor to pass through for deployment and recovery. The sensor dropped out due to its weight and recovered inside the aircraft when the servo is actuated.

5.3.12 Propulsion

The selection of avionics was derived from Section 3 and the limitations specified in the rule book. The Scorpion SII 4035 330KV motor with 22" x 12" Fiala propeller and Tattu 6S1P 9000mAh 25C battery, giving us a thrust of 13.25lbs with a max current consumption of 61.8A which did not exceed the maximum continuous current rating of the motor. An endurance of 8mins helped us achieve the projected time and number of laps in respective missions.

A Hobbywing Platinum 100A v3 ESC was chosen to ensure that it doesn't get affected due to burst discharge rating and considering the FoS. A Hobbywing 5A UBEC is connected inline with the ESC for safety and also to power the receiver. FrSky X8R receiver is an 8 channel receiver that is capable of controlling all the control surfaces, DRM and lights. A slow-acting blade fuse of 65A was chosen, which obeys the specified rule and also acts as a switch that can be accessed from outside the aircraft without having to operate the battery all the time.

5.3.13 Landing Gear

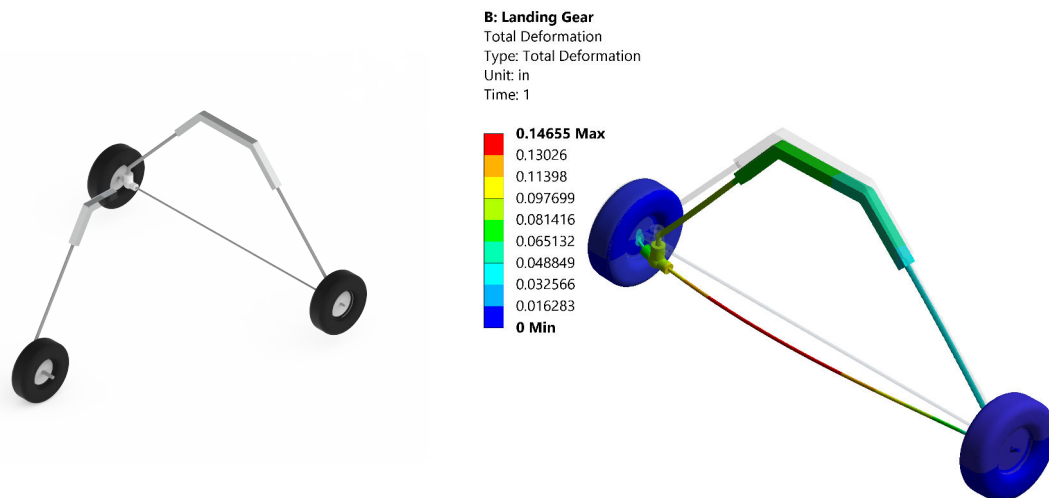


Figure 5.17: Landing Gear

The landing gear is designed to withstand impact loads and balance the aircraft's total weight on the ground. The nose gear and the main gear structure were made using 0.20in mild steel rods. Additionally, four aluminum plates were employed, two plates of 0.12in thickness on top and bottom of the mild steel rod and two plates of 0.12in width to lock the mild steel rod on sides. A 0.12in mild steel rod was used to connect the main wheels and reduce the

impact loads. Aluminum plates were employed to minimize the bending loads on the mild steel rod and add more strength to the gears. The whole structure was fixed to the fuselage using bolts.

Static structural analysis is performed to determine the deflection of the landing gear for a bending load. A load of 179.85 lb_f is applied on the aluminum plates and a maximum deformation of 0.147 in is observed.

5.4 Weight and Balance

Balancing the moments of the aircraft components was done using the weight and balance table. The CG obtained from the predictions are cross-verified on CATIA developed by Dassault Systèmes and by performing wing tip tests on the manufactured model. All lengths are taken from the leading edge of the aircraft.[9]

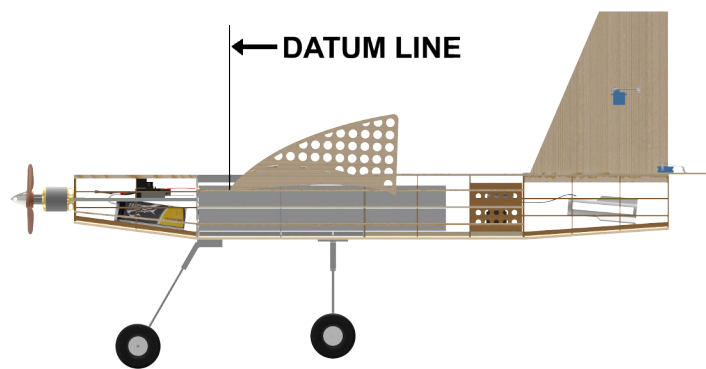


Figure 5.18: Side View of Datum Line Position

Components	Weight(lb)	Length(in)	Moment(lb-in)
Propeller	0.29	-16.34	-4.68
Motor	0.96	-14.17	-13.59
ESC	0.22	-6.89	-1.52
Receiver	0.04	-6.89	-0.30
Red Arming Plug	0.08	-6.89	-0.53
Fuselage	1.34	7.36	9.89
Wing	0.92	5.21	4.82
Nose Landing Gear	0.38	-2.56	-0.97
Main Landing Gear	0.69	7.82	5.42
Horizontal Tail	0.18	32.73	6.04
Vertical Tail	0.09	29.42	2.65
Aileron and Flap Servos	0.08	7.86	0.62
Elevator Servos	0.04	33.30	1.32
Rudder Servos	0.02	29.78	0.66
Wires	0.22	-2.56	-0.56
DRM	0.66	20.39	13.49
Mission 1			
Battery	2.76	7.68	21.16

Total	8.98		43.84
Mission 2			
Battery	2.76	-6.89	-18.99
Shipping Containers	9.26	8.46	78.38
Total	18.24		82.07
Mission 3			
Battery	2.76	-1.18	-3.25
Sensor	0.75	25.28	18.95
Total	9.73		38.37

Table 5.3: Weight and Balance Table for the 3 Missions

5.5 Performance

5.5.1 Flight Envelope

The operating limits of the aircraft needs to be well defined for superior performance, control and endurance. The flight envelope shows the parameters within which the aircraft can be operated or maneuvered safely, without aerodynamic or structural compromises. The load factor limits were increased for M1 and M3 due to less gross weight than in M2. The different velocities obtained for M1, M2 and M3 from the V-n diagram are displayed in the Table 5.4. The dive velocity, V_D , was found out to be 87.01 ft/s and is set to be 1.5 times the cruise velocity to avoid flutter and buffeting.

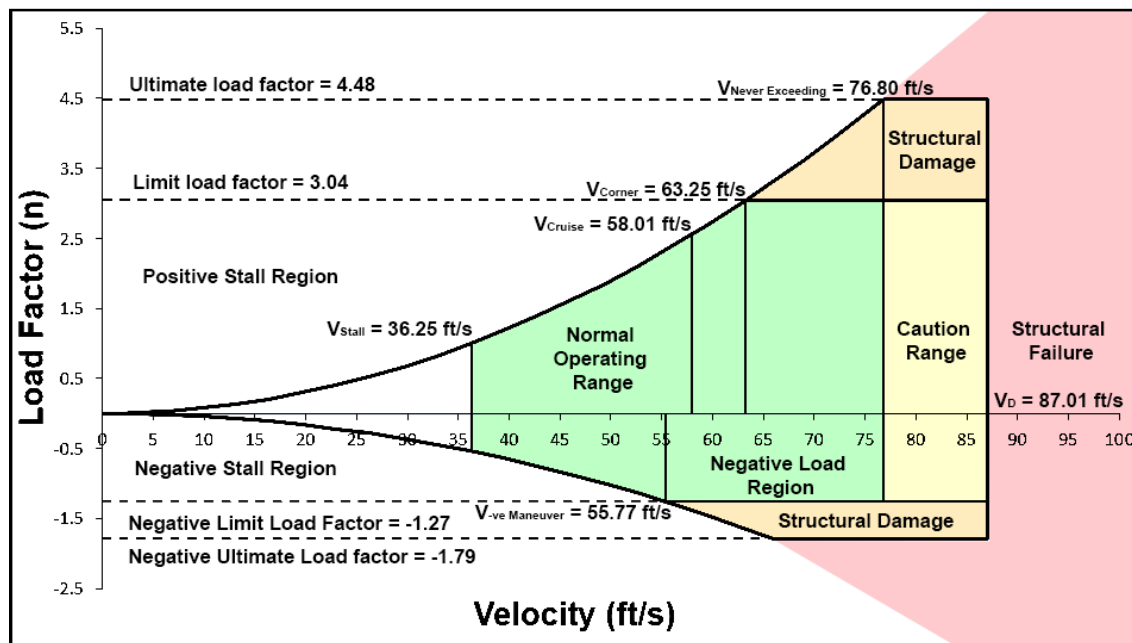


Figure 5.19: V-n Diagram for M2

Parameters	Mission 1	Mission 2	Mission 3
Positive $V_{Stall}(ft/s)$	25.4	36.25	26.58
$V_{Cruise}(ft/s)$	40.68	58.01	42.52
$V_{Corner}(ft/s)$	44.00	63.25	45.97
Negative $V_{Stall}(ft/s)$	34.68	49.24	36.08
$V_{NeverExceeding}(ft/s)$	56.20	76.80	58.01

Table 5.4: Velocity Parameter Table

5.5.2 Predicted Mission Performance

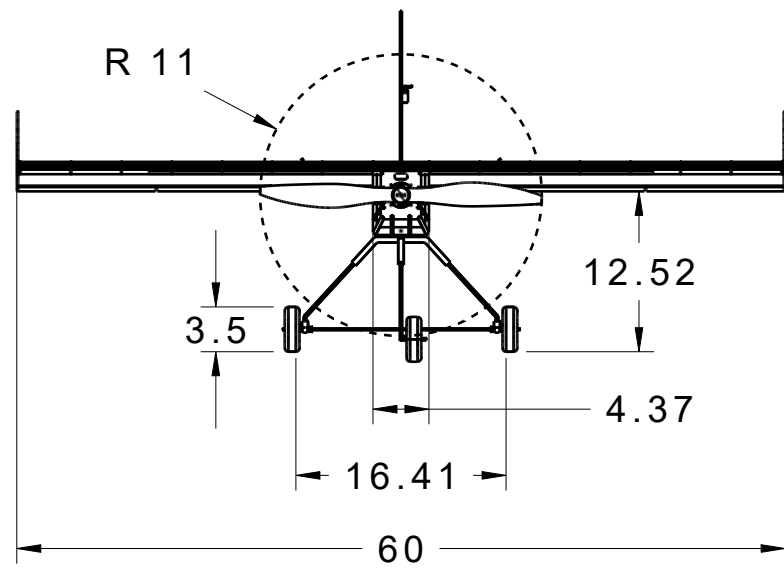
Parameters	Mission 1	Mission 2	Mission 3
C_{L-Max}	2.20	2.20	2.20
$C_{L-Cruise}$	0.87	0.85	0.84
C_{D0}	0.04	0.04	0.04
L/D_{Max}	8.74	9.08	5.13
L/D_{Cruise}	7.95	8.27	5.07
Rate of Climb(ft/s)	11.8	4.95	9.16
Power Required(W)	60.23	172.08	88.19
Thrust Required(lbf)	1.01	2	1.88
$W/S(lb/ft^2)$	1.69	3.45	1.84
Gross Weight(lbs)	8.92	18.24	9.70

Table 5.5: Predicted Performance parameters for Flight Missions

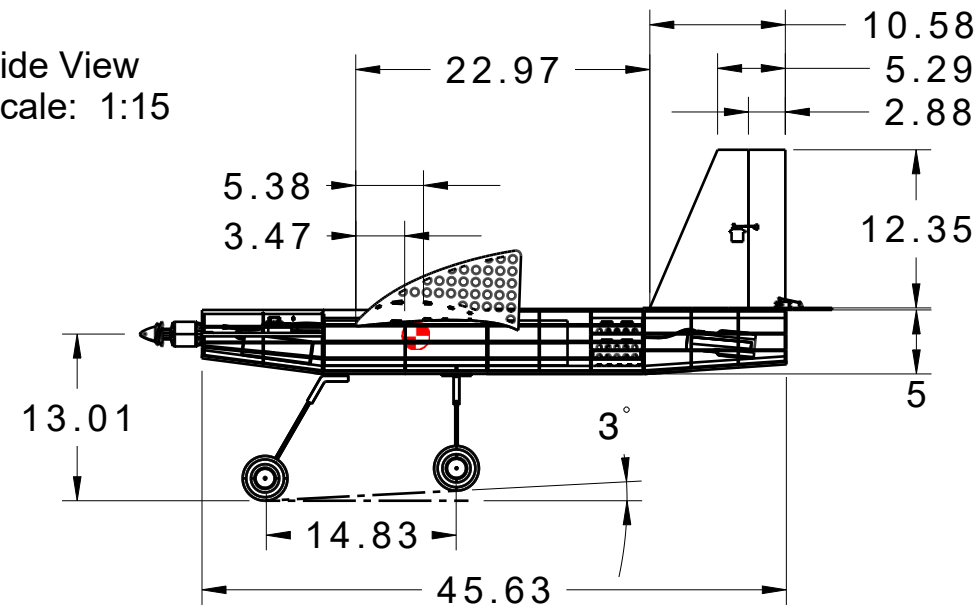
5.6 Drawing Package

The following four pages illustrate the detailed CAD of the PRIMIS 2. The first sheet contains the three-view diagram with relevant dimensions. The second sheet contains the structural arrangement of all major components. The third sheet shows the system layout of the electronics and allied subsystems. The fourth sheet contains payload accommodation and DRM.

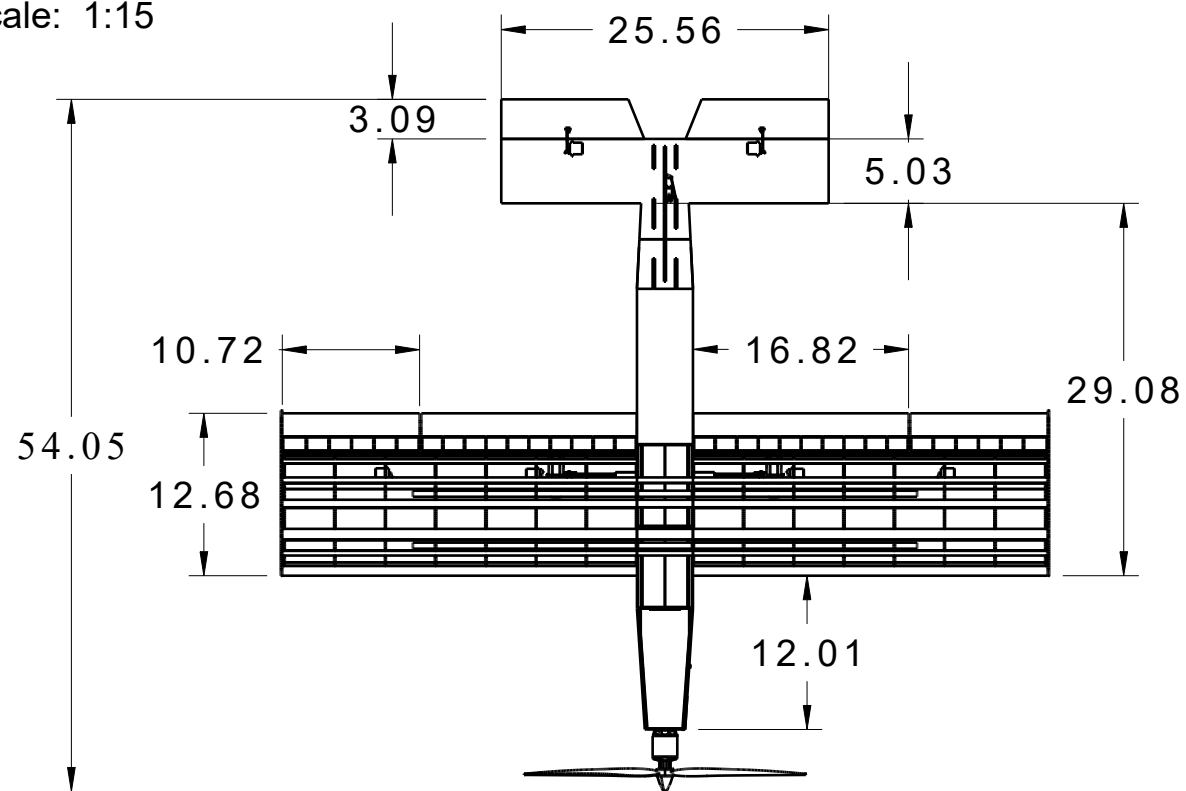
Front View
Scale: 1:15



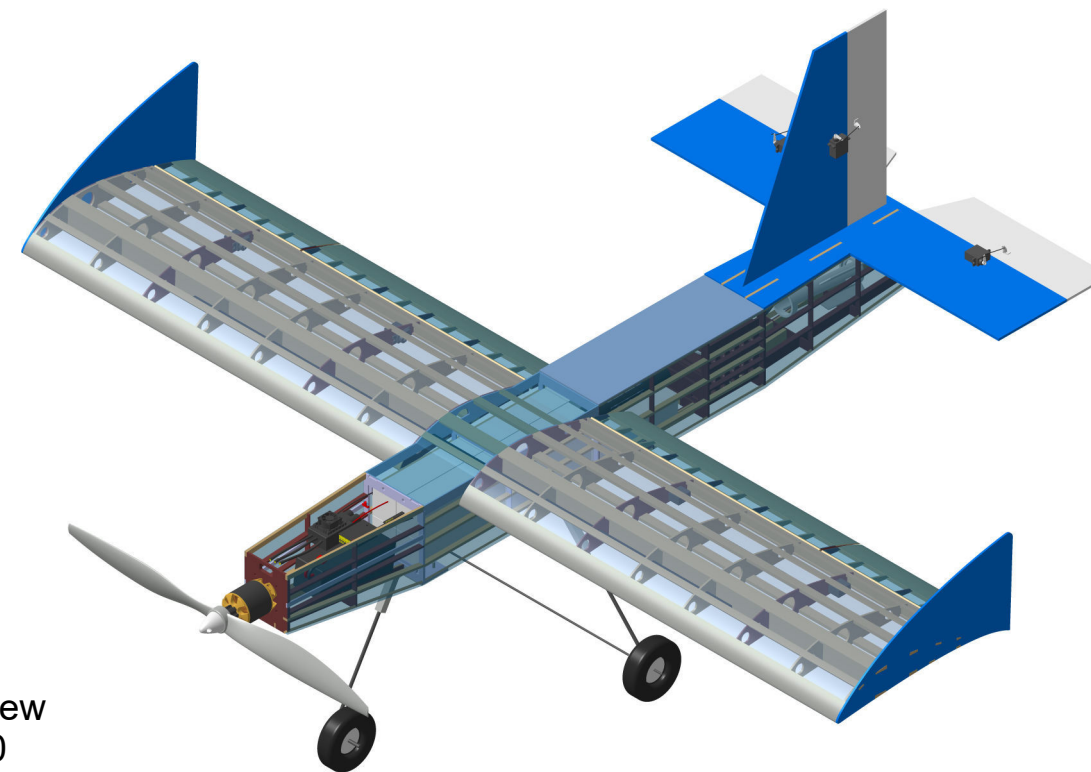
Side View
Scale: 1:15



Top View
Scale: 1:15



Isometric view
Scale: 1:10



*All dimensions in inches



DAYANANDA SAGAR COLLEGE OF
ENGINEERING

DRAWING TITLE

Aircraft Three View with Dimensions

DRAWN BY
Dhruv Dhaduk

DATE
14-02-2021

CHECKED BY
Dr. Hareesha NG

DATE
16-02-2021

SIZE
B

DRAWING NUMBER
DBF_2021_DSCE_DRW_01

DESIGNED BY
Dhruv Dhaduk

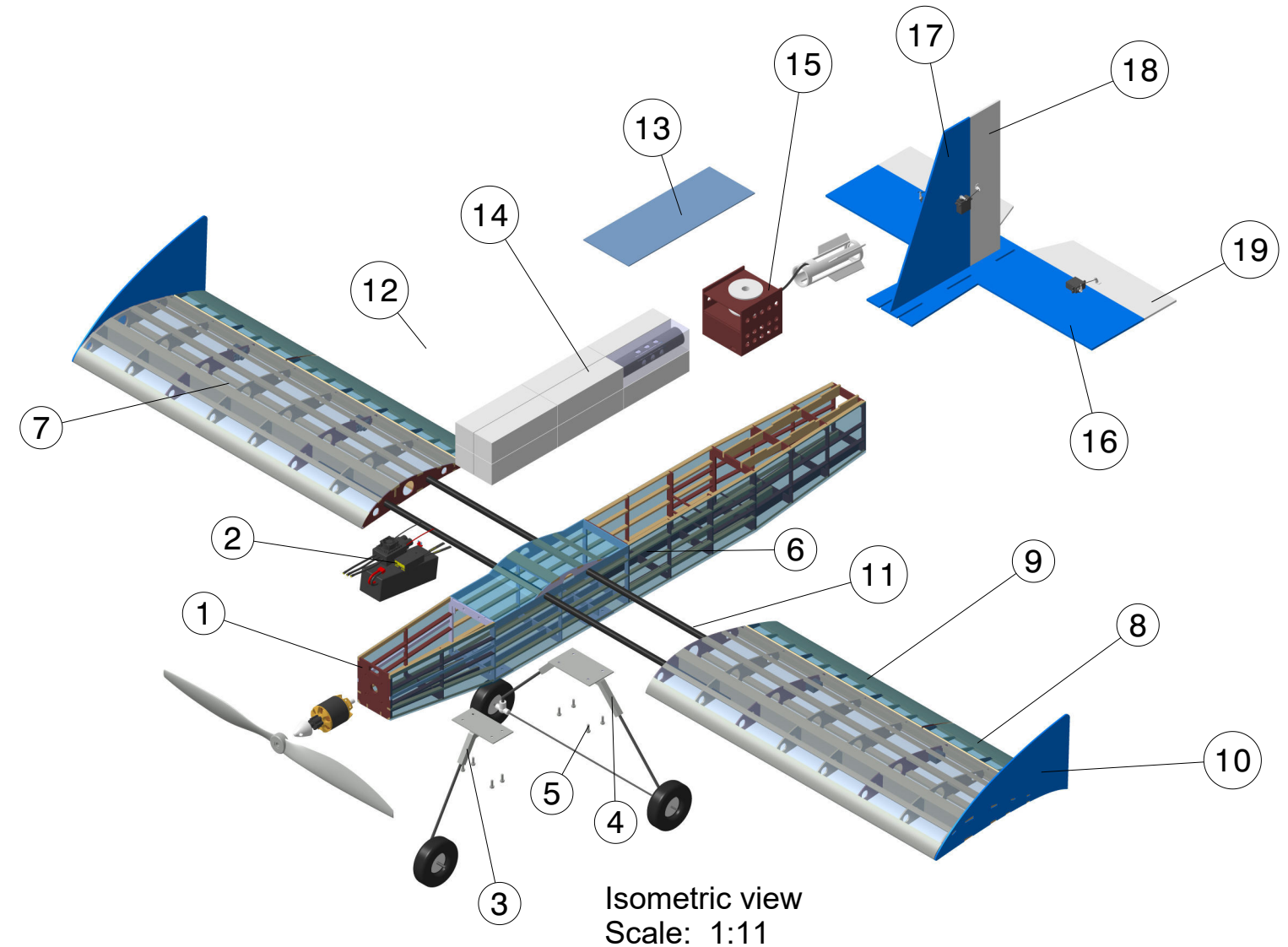
SCALE 1:15

WEIGHT(lb) 18.24

18.24

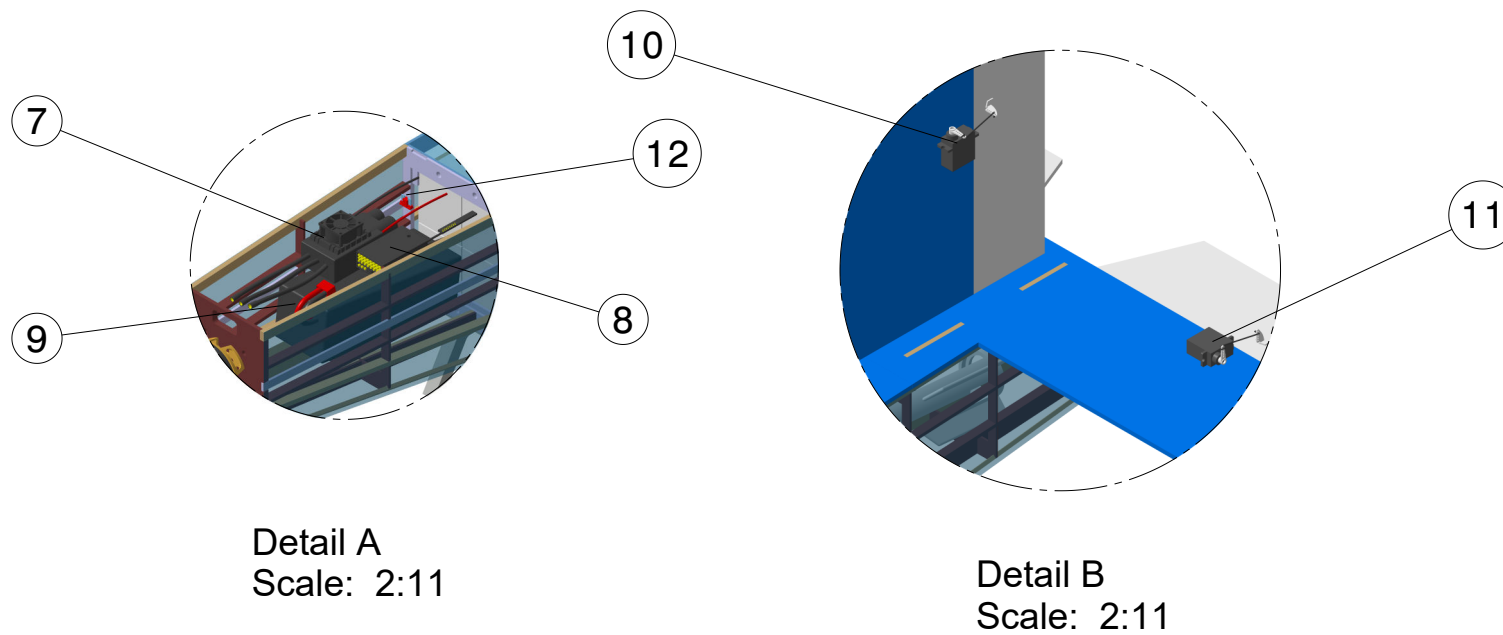
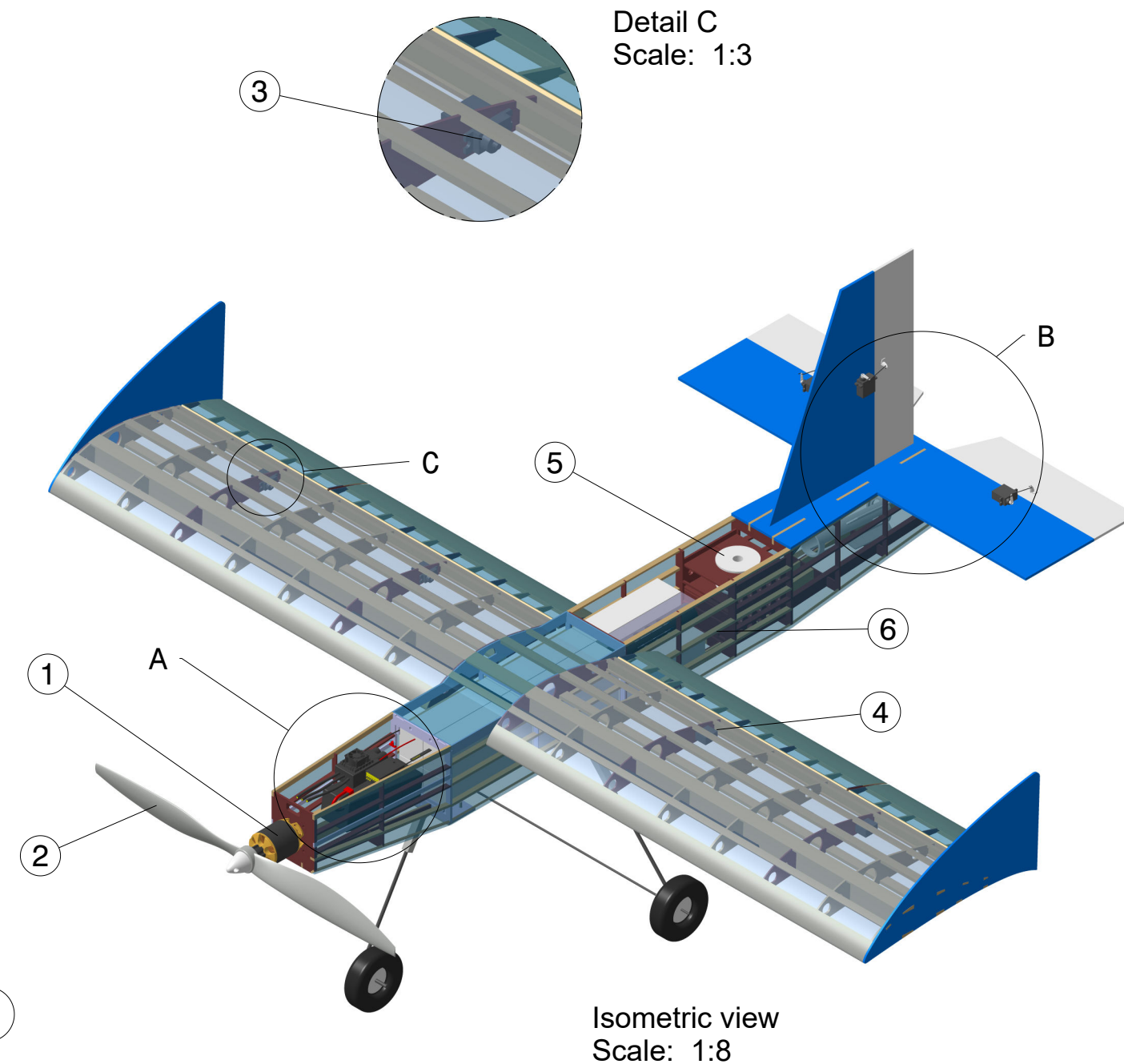
SHEET 1/4

ITEM NO.	COMPONENT	DESCRIPTION	QTY.
1	Firewall	Aeroply	1
2	Avionics	Battery, Receiver, ESC	1
3	Nose Gear	Aluminium, Mild Steel	1
4	Main Gear	Aluminium, Mild Steel, PLA	1
5	Bolts	SS	8
6	Fuselage	Balsa, Aeroply, Aluminium	1
7	Wing	Balsa, Aeroply, CF	1
8	Aileron	Balsa, Aeroply, CF	2
9	Flap	Balsa, Aeroply, CF	2
10	End Plate	Balsa	2
11	Spar	CF	2
12	Front Hatch	Balsa	1
13	Rear Hatch	Balsa	1
14	Payload	Shipping Container, Simulators	12
15	DRM	Aeroply, PLA	1
16	Horizontal Stabiliser	Balsa	1
17	Vertical Stabiliser	Balsa	1
18	Rudder	Balsa	1
19	Elevator	Balsa	2

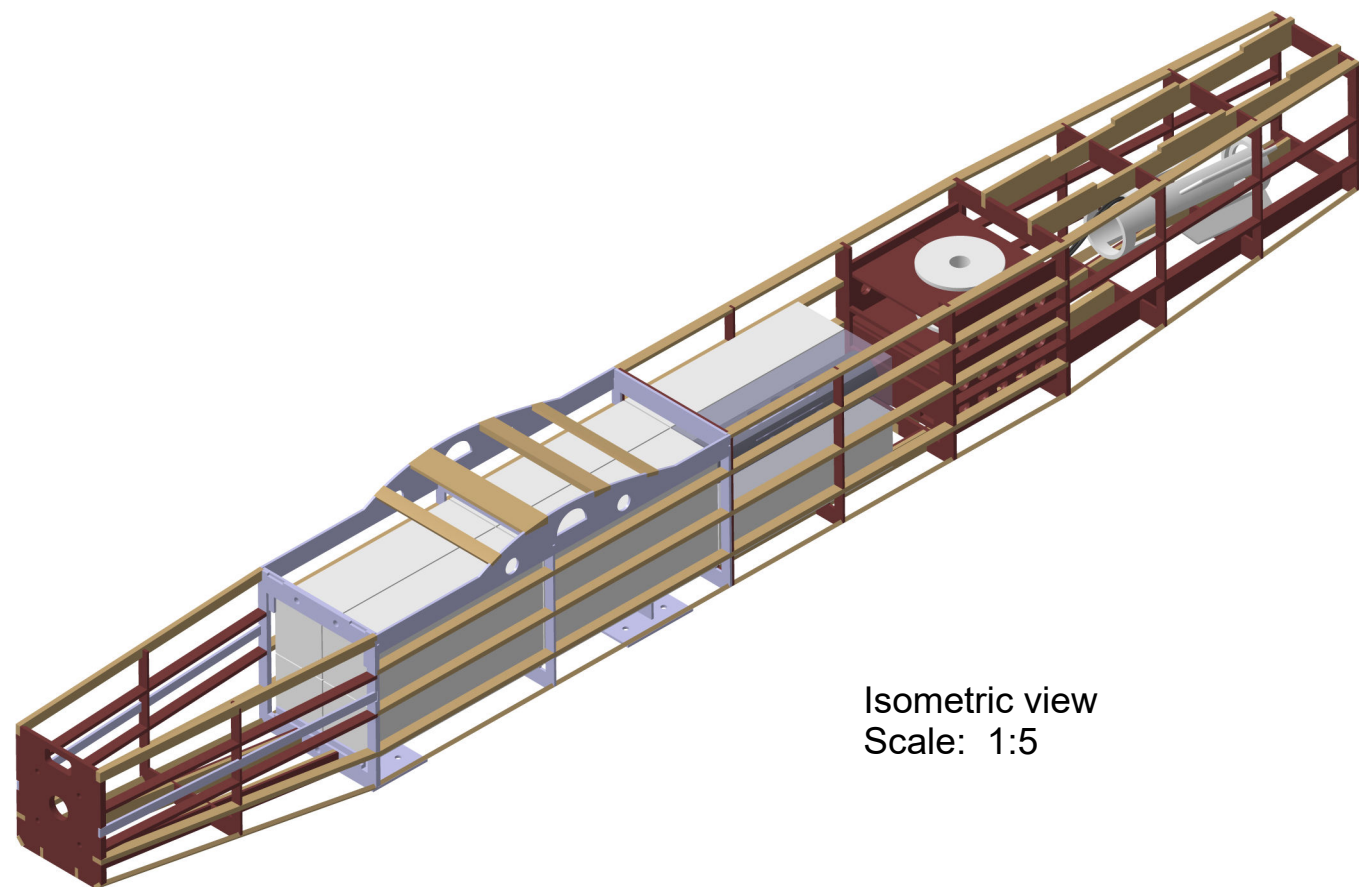


		DAYANANDA SAGAR COLLEGE OF ENGINEERING			
		DRAWING TITLE			
DRAWN BY		DATE		Structural Arrangement	
Dhruv Dhaduk		14-02-2021			
CHECKED BY		DATE		SIZE	DRAWING NUMBER
Dr. Hareesha NG		16-02-2021		B	DBF_2021_DSCE_DRW_02
DESIGNED BY		SCALE		WEIGHT(lb)	SHEET
Dhruv Dhaduk		1:11		18.24	2/4

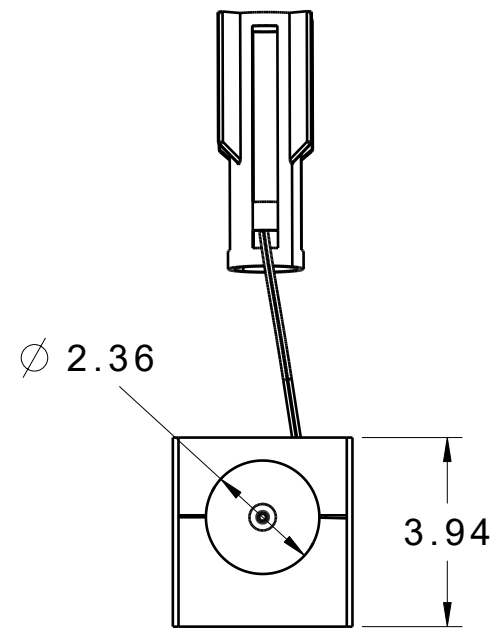
ITEM NO.	COMPONENT	DESCRIPTION	QTY.
1	Motor	Scorpion SII-4035-330 KV	1
2	Propeller	Fiala 22X12E	1
3	Aileron Servo	Tower Pro MG90s	2
4	Flap Servo	Tower Pro MG90s	2
5	DRM	Tower Pro MG996R	1
6	Fuselage	Basla, Aeroply, Al	1
7	ESC	Hobbyking Platinum 100A v3	1
8	Receiver	FrSky X8R	1
9	Battery	Tattu 9000mAh 22.2V 25C 6S1P LiPo	1
10	Rudder Servo	Tower Pro MG90s	1
11	Elevator Servo	Tower Pro MG90s	2
12	Fuse	65A Blade Fuse	1



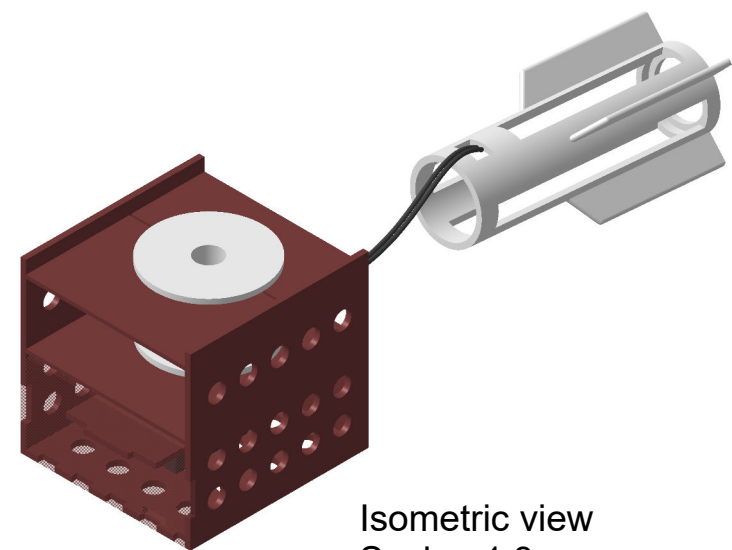
		DAYANANDA SAGAR COLLEGE OF ENGINEERING			
		DRAWING TITLE			
DRAWN BY	DATE	Systems Layout			
Dhruv Dhaduk	14-02-2021				
CHECKED BY	DATE	SIZE	DRAWING NUMBER		
Dr. Hareesha NG	16-02-2021	B	DBF_2021_DSCE_DRW_03		
DESIGNED BY		SCALE	WEIGHT(lb)	SHEET	
Dhruv Dhaduk		1:8	18.24	3/4	



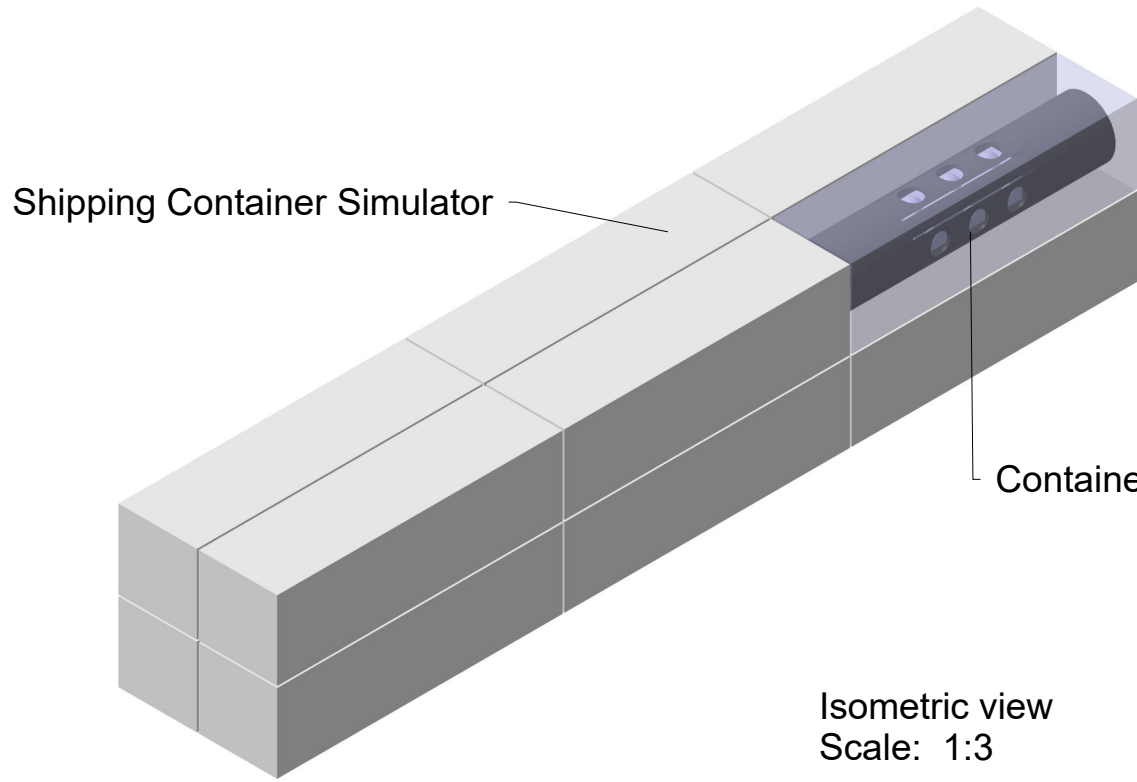
Isometric view
Scale: 1:5



Top view
Scale: 1:4



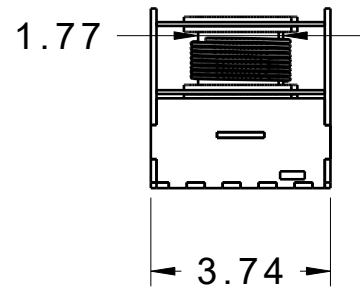
Isometric view
Scale: 1:3



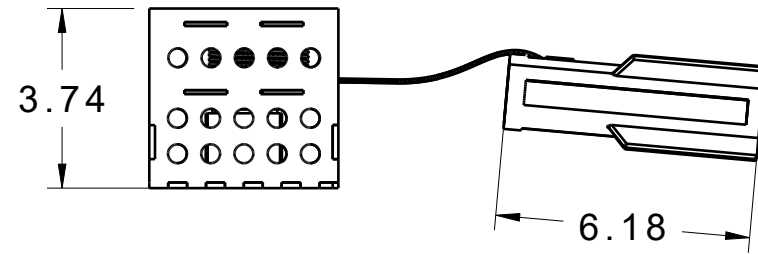
Shipping Container Simulator

Container with Sensor

Isometric view
Scale: 1:3



Front view
Scale: 1:4



Side view
Scale: 1:4



DAYANANDA SAGAR COLLEGE OF ENGINEERING

DRAWING TITLE

DRAWN BY
Dhruv Dhaduk

DATE
14-02-2021

Payload Accomodation and DRM

CHECKED BY
Dr. Hareesha NG

DATE
16-02-2021

SIZE DRAWING NUMBER

B DBF_2021_DSCE_DRW_04

DESIGNED BY
Dhruv Dhaduk

*All dimensions in inches

SHEET 4/4

6 Manufacturing Plan

6.1 Investigated Processes and Materials

Critical parameters such as strength to weight ratio, ease of fabrication, repairability, experience, and cost were considered and scored on a scale of 1 to 5, with five being the most favorable, in Pugh matrix method of computation. The comparison is tabulated below:

Criteria	Priority	Observation
Strength to Weight	5	Strength to weight was considered as the most important factor.
Repairability	5	As the team can only use one aircraft for the competition, the design would have to enable the team to repair the aircraft easily in the event of crash during the competition.
Cost	4	The team operated on a limited budget, due to the pandemic, and thus it was necessary for manufacturing to be economic.
Ease of fabrication	3	Ease of fabrication is necessary for the team to be able to quickly manufacture prototypes for testing.
Experience	3	Choosing a method with which the team already has experience allows for the aircraft to be of high quality with efficient design.

Table 6.1: Comparison of Manufacturing Parameters

6.1.1 Balsa and Aeroply Build

Balsa has very good strength to weight ratio and hence can be effectively used with reinforcement with aeroply in areas with high stress concentration. Parts are designed in a CAD software and are laser cut for greater precision and accuracy. Carbon fibre composites and 3D printed fixtures can be included in the design for reinforcement and attachment respectively. TIG welding can also be employed to use effectively integrate aluminum. Heat shrunk monokote is then wrapped around the complete structure together to provide torsional stiffness.

6.1.2 Foam Core Composites

Foam blocks can be cut out of styrofoam using a hot-wire to get the desired shape such as that of the wing. These structures do not have good strength and need to be reinforced heavily to bear the flight loads. These can be coated with a layer of carbon fibre, fibreglass or kevlar to provide strength, which comes at the cost of weight.

6.1.3 Carbon Fibre Composites

Carbon fibre is combined with other polymers like epoxy, vinyl ester, etc. to bind the structure and create a CF composite. Layering of the sheet is done using a mold in shape of the final product. Vacuum bagging is used in case of high strength composites. Making carbon fibre composites is an expensive and time intensive process.

6.1.4 3D Printing

3D printing can generate complex designs that would be extremely difficult to manufacture with any other technique. A 3D printer fabricates a part from a CAD design, which is input via STL format. This can be used to

make certain parts that can act as fixtures and do not need relatively high strength-to-weight ratio.

6.1.5 Comparison of Manufacturing Processes

The above mentioned processes were juxtaposed against each other by assigning a weight using a Pugh matrix. The scores were given from 1 to 5, with five being the highest. The comparison is tabulated below,

Criteria	Figure of Merit	Balsa and Aeroply Build	Composite Moulding	3D Printed PLA	Foam
Strength to Weight	5	5	4	3	5
Repairability	5	3	1	2	2
Cost	4	3	1	3	3
Ease of Fabrication	3	4	2	3	3
Experience	3	4	2	4	3
Total		78	63	62	62

Table 6.2: Pugh Matrix for Material Selection

Based on the above data, it was determined that Balsa and aeroply build was the most effective process for the aircraft. Other methods such as 3D printing can also be implemented to get an efficient aircraft design.

6.2 Manufacturing Process

6.2.1 Wing

The wing consists of 9 laser-cut ribs made of Balsa and aeroply. The structure is glued together using Cyanoacrylate glue. The wing is assembled using jigs that help to hold the structure together and reduce error during fabrication. Lightning holes are included to reduce the weight without compromising on the strength. Carbon Fiber spars are also incorporated along the wingspan to add strength. Heat shrink Monokote is then applied on the surface using a hobby iron and a heat gun.

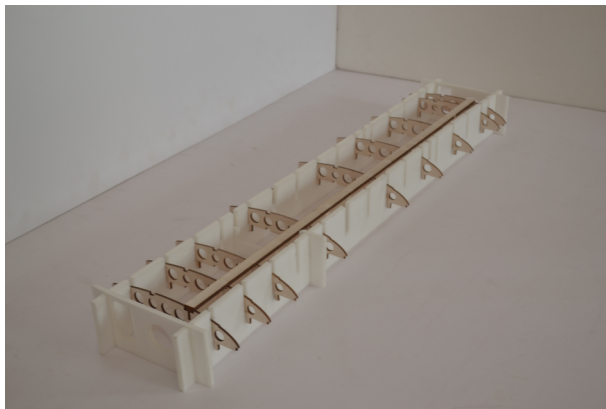


Figure 6.1: Wing construction

6.2.2 Wing and Fuselage

Wing was fabricated mainly out of balsa and aeroply. Precision of components like ribs, webs and flanges was ensured by employing laser-cutting. Additionally, errors were minimised during assembly using depron jigs which were laser cut. The structure was assembled using Cyanoacrylate glue. Any rough edges in the airframe that might affect the aerodynamics are sanded. After the incorporation of servos, the entire airframe is covered with a heat shrink Monokote.

Fuselage is a semi-monocoque structure which has a laser-cut central aluminum chassis to support high loads. The chassis is put together by TIG welding the aluminum former and stringers to form the core structure. Areas which encounter low stresses are manufactured in a similar manner to that of the wing using aeroply formers and stringers made of balsa and aeroply. The fuselage is then enclosed with a heat shrink Monokote.

6.2.3 Tail

The empennage section is made of 0.16in balsa flat plates for stabilizers and control surfaces. Lightening holes are incorporated in the flat plate to reduce weight. The tail is then Monokoted to maintain the aerodynamics. The control surfaces are attached using CA hinges. As mentioned before, the empennage is connected to the fuselage via slots in stringer of the fuselage.

6.2.4 Landing Gear

The landing gear is made of 0.2in mild steel struts and 0.12in aluminum plate fixtures. This fixture is welded to another aluminum plate that connects to the fuselage via nuts and bolts. The aluminum plate fixture surrounds the steel strut thus providing a surface for welding and to bear loads on impact. The main gear also has a 0.12 in in mild steel axle connecting the wheels. This axle is connected to the main strut through Tee joints.

6.2.5 Shipping container

The shipping container is made of 0.2in depron and houses the sensor to protect it as per the ground mission requirements. The sides of the container are laser cut and have slots for proper alignment while assembling it. The sides are attached together using hot glue gun.

6.2.6 Sensor

The sensor is manufactured using 3D printed PLA. LED lights are incorporated into the design with the circuit components. CG and the required weight are achieved by adding mild-steel cylinders inside the sensor. The mild steel cylinders are manufactured to the desired dimensions by lathe machining for accuracy.

6.2.7 Deployment and Recovery Mechanism

DRM employs a servo winch mechanism. A cuboid container was designed and manufactured using laser cut aeroply to hold the components. It consists of a manipulated servo, a cylindrical shaft and a copper cable. The servo is placed at the bottom of the container and is held in place using aeroply pieces. The shaft is placed on the servo longitudinally inside the container. The shaft is a hollow cylinder made 3D printed PLA around which a copper cable is wound. One end of the cable joins the sensor lights and the other joins the Rx. Additionally, the DRM has a 3D printed PLA casing to house the sensor. The casing has fins for aerodynamic stability.

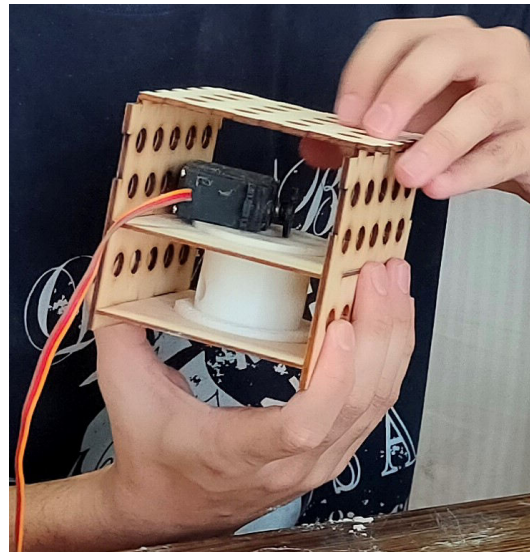


Figure 6.2: DRM construction

6.3 Manufacturing Milestones

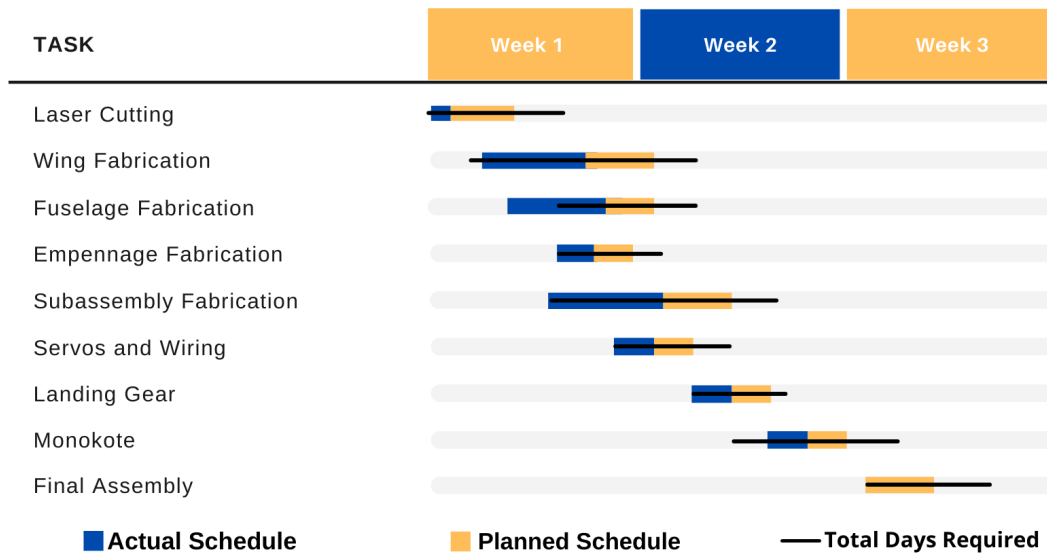


Figure 6.3: Manufacturing Milestone

A manufacturing milestone chart was prepared to facilitate coordination between the sub-teams and finish the test prototypes and the final model in time. The following Gantt chart shows the planned timing and the actual timing that the team takes to manufacture one aircraft while optimization into the next model is in progress.

7 Testing Plan

7.1 Test Objectives

7.1.1 Structural

Initially, structural testing was performed to verify the design integrity of the aircraft before the flight test. Bending and torsion tests were conducted on the wing to determine the structural integrity and load-carrying capacity of the I-section. Impact test was carried out on the landing gear to simulate landing and understand its behaviour to sudden and shock loads. Wingtip test was performed for the assembly, to confirm the CG of the aircraft. Drop test was conducted on the fuselage to substantiate its structural integrity under impact loads.

7.1.2 Propulsion

The propulsion system was tested to compare the experimental values of voltage, endurance and thrust with the theoretical values. Static thrust testing provided the maximum thrust for various combinations of propellers and battery packs. To determine the variation of thrust with the increase in airspeed, dynamic thrust test and endurance tests were conducted to obtain the limitations of the battery at a constant throttle setting.

7.1.3 Cargo

Sensor lights were tested to verify their brightness in broad daylight. The sensor drop test was conducted on all sides to ensure it is structurally sound to protect the sensor. The DRM was also tested to verify its smooth action during flight.

7.1.4 Test Flight

Test flights proved to be the most fruitful and convenient method of improving the aircraft. The aircraft was tested for all the flight missions. Pilot's inputs were taken in regards to the stability, control authority and general flying characteristics. These inputs were implemented in successive flight tests.

7.2 Test Milestone

A test milestone chart was plotted with the primary motive to ensure that the planned goals and essential deadlines were followed. Various tests were conducted to ensure the strength and behaviour of the materials in flight. The following gantt chart shows the planned and the actual timing utilized by the team to meet the testing deadlines.

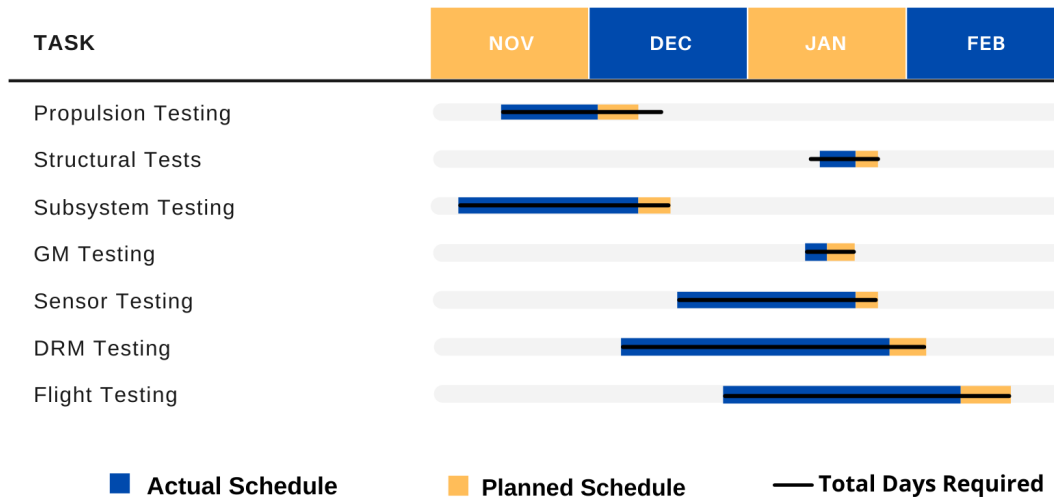


Figure 7.1: Test Milestones

7.3 Test Results

7.3.1 Propulsion Tests

Static Thrust Test: Static thrust tests were conducted to determine the maximum thrust, battery endurance and power consumed for different motor-propeller combinations.

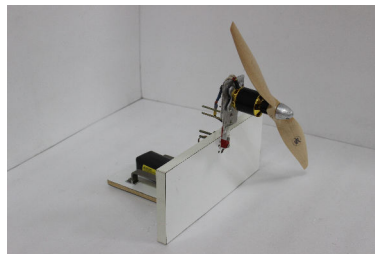


Figure 7.2: Static Thrust Setup

The apparatus consists of an Analog to Digital Converter, Arduino Uno and a load cell. The load cell has one end fixed to a test rig and the other end is fitted to the firewall on which the motor is attached. The load cell provides continuous analog readings of thrust which are fed into the Arduino after the Analog to Digital Converter converts the signals into digital format. The thrust values are continuously printed on the serial monitor in the Arduino interface. A wattmeter is also connected to the circuit to note down power consumption and current drawn at different throttle percentages.

Propellers were narrowed down to 3 sizes keeping in mind calculated thrust required and necessary propeller clearance. Static thrust test was conducted on all the 3 propellers to evaluate the thrust produced and current drawn. The data obtained is tabulated below.

Throttle (%)	Thrust (lbs)	Current (A)	Power W
25	2.86	20.8	524.16
50	6.61	30.1	652.57
75	10.36	44.7	863.45
100	13.22	61.6	1108.62

Table 7.1: Static Thrust results

Dynamic Thrust Test: The effect of flight velocity on the thrust generated was evaluated in a dynamic thrust test conducted in a subsonic wind tunnel with a maximum operating speed of 164.04ft/s, contraction ratio of 9:1 and a maximum suction fan speed of 1500rpm. The wind tunnel was operated at flight cruise velocities of the aircraft which were obtained from simulated and theoretical data. The thrust readings from the load cell test rig were noted for each velocity and thrust readings obtained at different velocities were compared against the readings obtained from the static thrust setup. The 22" x 12" propeller was chosen as it provided the desired thrust without exceeding the fuse current limit.

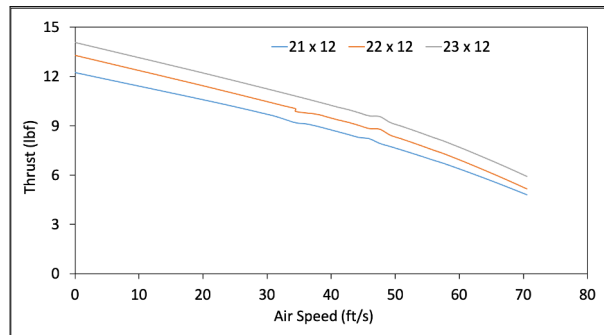


Figure 7.3: Thrust Vs Airspeed

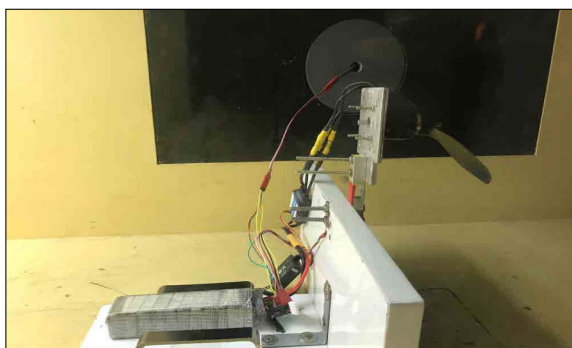
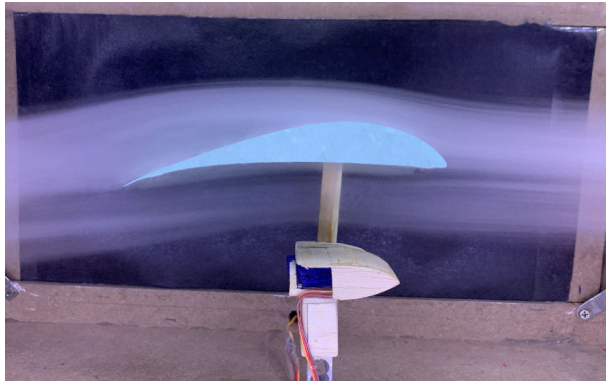


Figure 7.4: Dynamic Thrust Test

7.3.2 Aerodynamic Tests

Flow visualization was performed in a wind tunnel for the chosen airfoil Fx74modsm. The flow pattern around the airfoil at 49.2ft/s velocity was observed. The lift and drag values were measured using load cells. Foam replicas of airfoils were used within the test section. Hotwire cutting method was used to cut the foam airfoil section. The sensor was hung to the ceiling of the wind tunnel, and the flow pattern was visualized at 60ft/s.



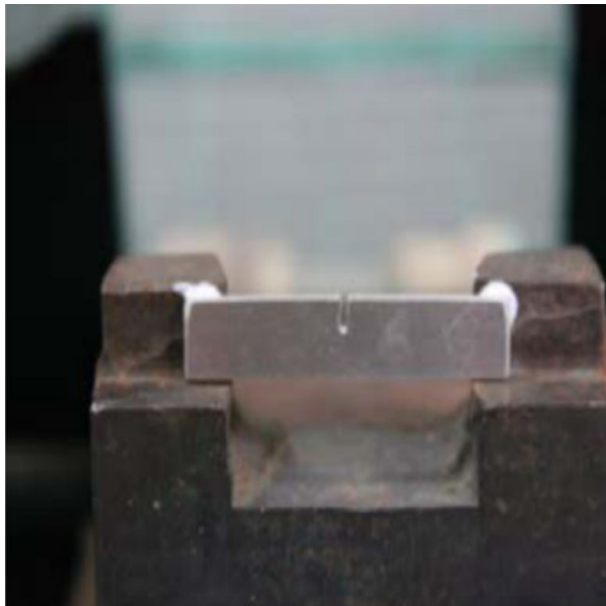
(a) Fx74modsm



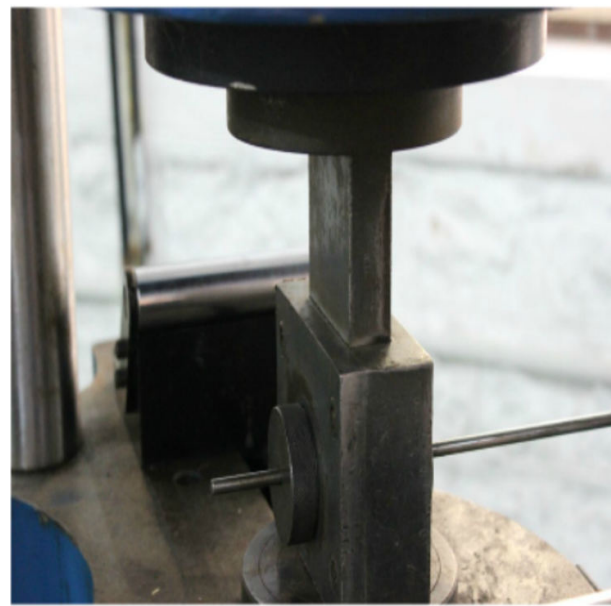
(b) Sensor wind tunnel testing

7.3.3 Material Tests

Charpy Test for Aluminum: An aluminum specimen with a U notch was supported at both ends as a simply supported beam. Then with a falling pendulum, the specimen was struck on the opposite face behind the notch. The impact strength was obtained from the energy absorbed by the specimen, which was determined by the subsequent rise of the pendulum.



(a) Charpy Test for aluminum



(b) Bending Test for mild steel

Figure 7.6: Material Tests

Bending Test for Mild Steel: A mild steel specimen was placed on the UTM (Universal Testing Machine) in a simply supported position. Then loads were applied, and the corresponding deflections were measured using a dial gauge. A graph of load Vs deflection was plotted, and the W/δ was obtained, to measure the bending stress on the specimen.

Material	Density (<i>Slug/ft³</i>)	Length; Thickness (<i>in</i>)	Impact Energy (<i>J</i>)	Bending Strength (<i>lbf</i>)
aluminum	5.2388	0.393; 0.118	5	-
Mild Steel	15.231	18;0.157	-	449.618

7.3.4 Structural Tests

Wing Tip Test: Wingtip test was performed to verify the CG location of the aircraft. This test was conducted by lifting the fully loaded plane by the last rib of the wings. The results confirm the static stability of the aircraft and the wing flex deformation of 0.7in was observed.



Figure 7.7: Wing Tip Test

Wing Bending Test: To test the structural integrity of the wing structure, the wing root was mounted to the table in a cantilever position, and then loads were gradually applied to observe the maximum deflection of 0.6in.

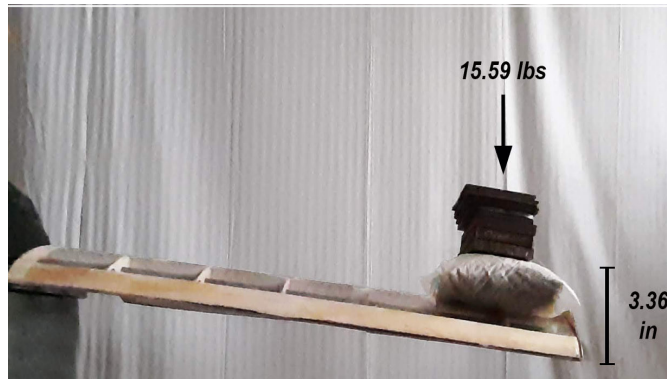


Figure 7.8: Wing Bending Test

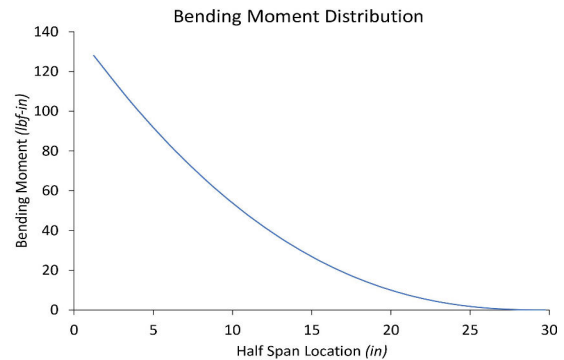


Figure 7.9: Bending Moment Deflection

Wing Torsion Test: While testing, a torsional load was applied at the wingtip and the resulting angular twist along several points along the span was observed. A force of 5.29lbs-in was applied on the wingtip and a deformation of 0.15in and angular twist 24° was observed.

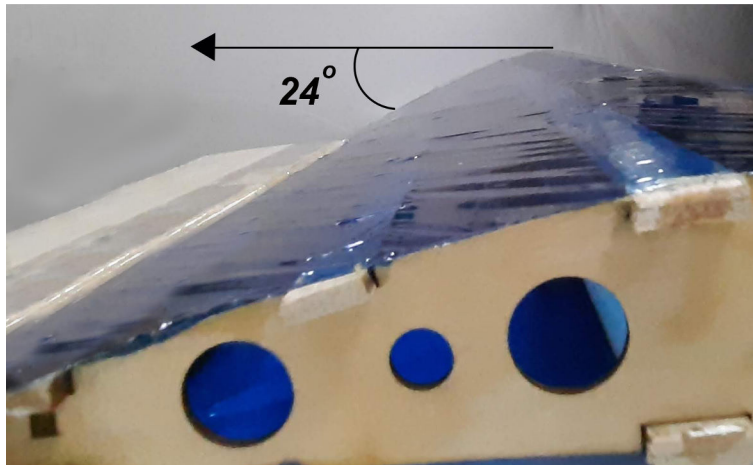


Figure 7.10: Wing Torsion Test

Sensor Deployment and Recovery Test: To verify the stability, the sensor was towed using a vehicle, at a speed of 65.16ft/s. From the test results, the angle of inclination and net torque were obtained. These results were the basis to conclude the position of the sensor and the effective length of the tow cable when deployed. During the flight test, the sensor was deployed from the DRM for a length of 58.3in which is 10X the length of the sensor adhering to the competition requirements. The test results provided experimental validation to the sensor DRM in M3. [10]

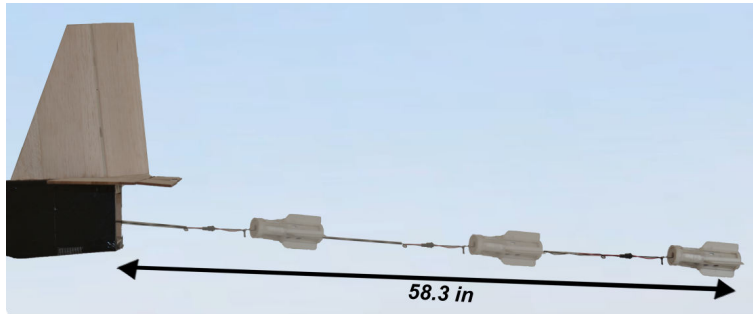


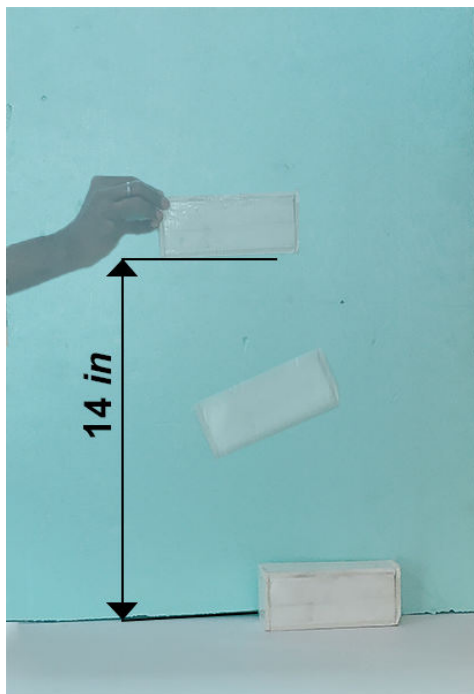
Figure 7.11: Sensor deployment and recovery test

Sensor Lights Test: To check the brightness of the sensor lights, the team chose to conduct the sensor light test in bright sunlight. Different light configurations namely RGB strip, SMD LEDs were tested. The team chose to go with SMD LEDs as it gave better brightness compared to the RGB strips.

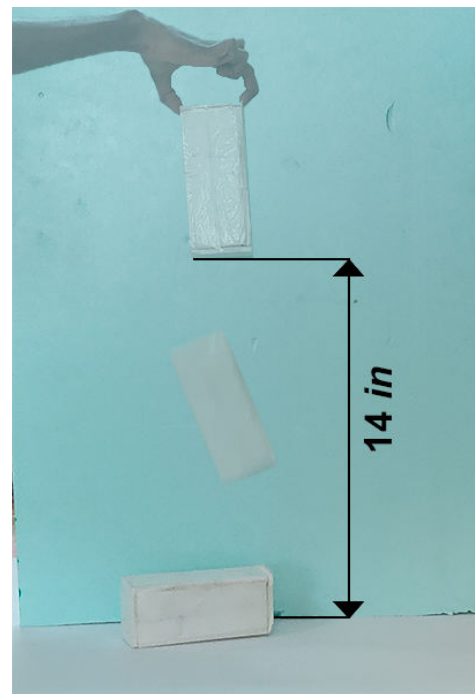


Figure 7.12: Sensor lights test

Sensor Container Drop Test: To demonstrate the ability of the shipping container to protect the sensor, a drop test was conducted. A depron container was used to enclose the sensor due to its better strength to weight ratio to protect the sensor from damages of the drop test. The container was dropped from a distance of 14in to conduct the test and it was observed that the sensor sustained minimal or no damages.



(a) Drop test (Horizontal)



(b) Drop test (Vertical)

Figure 7.13: Sensor Drop test

Landing Gear Drop Test: The drop test was conducted by dropping a fully loaded aircraft from a height of 15in. This helped to simulate a moderately harsh landing shock load of 22.56/bf. Due to impact, the landing gear was lowered by 0.5in and most of the impact was absorbed by the main landing gear.

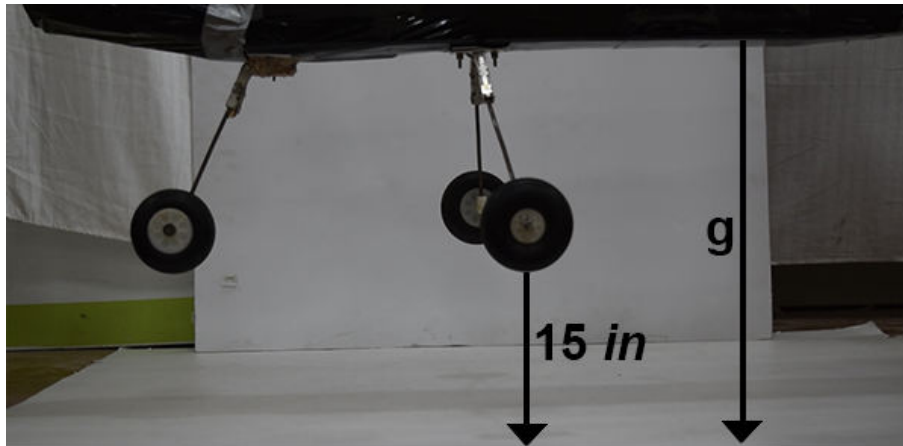


Figure 7.14: Landing gear drop test

Ground Mission: The team approached the ground mission with comprehensive practice sessions to minimize the time taken for GM. The sessions were practiced with different members of the team to strategize the time taken. The drop test for the ground mission is already verified in earlier sections. The aircraft’s DRM is a modular design capable of displaying excellent loading and unloading qualities. The entire mission was averaged to a time of 50s, keeping 10ft mission constraint.

7.4 Flight Checklists

COMPONENT	STEPS	REQUIREMENTS	GO	NO-GO
Aircraft	1	Check if the plane is statically stable		
	2	Check if the lateral CG and longitudinal CG are within the range		
Fuselage	1	Fuselage is free from cracks		
	2	All the sub-components are fastened properly		
	3	Longitudinal stability of the fuselage		
	4	No torsions		
Wings	1	Check for proper functioning of the control surfaces		
	2	Neutral stability of ailerons and flaps		
	3	Wings are secured to the fuselage		
Tail	1	Check for proper functioning of the control surfaces		
	2	Neutral stability of elevators and rudder		
	3	Tail is secured to the fuselage		
Landing Gear	1	Landing gear is secured to fuselage		
	2	Stability of the landing gear		
	3	Wheels are proper and are free to spin		
	4	Fasteners are secured		
	5	No torsion or bending movements		
DRM	1	All the shipping containers are placed properly		
	2	DRM fully encloses the sensor		
	3	DRM is secured internally to the fuselage		
	4	General integrity of payload system		
Sensor	1	Check if the lights are visible in a bright sunlight		

	2	Check if the sensor is free from damages after drop test		
--	---	--	--	--

Table 7.2: General Requirements Checklist

Component	STEPS	REQUIREMENTS	GO	NOGO
TX	1	Check if the component is calibrated		
	2	Check if the signals are within the range		
RX	1	Check if the component is calibrated		
	2	Check for proper connections		
	3	Check if the signals are within the range		
Motor	1	Motor is mounted properly and secured		
Propeller	1	Propeller is secured to the shaft of the motor		
	2	Proper functionality of the propeller		
Battery	1	All the batteries are fully charged		
	2	Visual inspection of the electronic wiring		
Fuse	1	Check if the fuse is broken or working		
Servo	1	Check if all the control surfaces are connected to the servo		
	2	Check if the servo's arm can be reached from outside		

Table 7.3: On-board checklist for Avionics

7.5 Flight Tests

Flight tests played the most crucial part in influencing our design changes. Various test flights were conducted to test the different sub-components in flight. Flight tests allowed the team to prove the airworthiness of the aircraft and collect performance data for the different flight missions with different configurations to arrive at the optimum design.

PixHawk Px4 Ardupilot was used with an external digital airspeed sensor to calculate the aircraft speed according to the airspeed, which helped us practically verify the time taken for one lap in all three flying missions. The Ardupilot also has an inbuilt altimeter that reads the altitude of the aircraft. The obtained altitude values were further evaluated to find the error between the calculated and the practically obtained Rate of Climb (RoC).

The aircraft was flown without payload to check for airworthiness, trim, and stability. The time of the lap was recorded for each flight. The obtained results indicate that the performance calculations predicted are realistic.

We initially flew the aircraft in the M2 configuration with four shipping containers. Different parameters such as time, maximum speed, and takeoff distance were recorded using the flight controller. The aircraft was also flown in the M3 configuration with the sensor deployed. This allowed the team to assess the endurance of the aircraft and compare it to the theoretical performance.

Parameters such as tail configuration, fuselage, and landing gear dimensions were iterated over the aircraft's prototypes. The team decided on the optimum configuration after considering the flight data and the pilot's input.

PARAMETER	TEST FLIGHT 1	TEST FLIGHT 2		TEST FLIGHT 3	
Mission	1	2	2	2	3
Empty Weight	8.5lbs	8.81 lbs	8.8 lbs	8.98lbs	8.98 lbs
Time of Flight	2min, 21s	3min, 34s	3min	3min, 50s	5min, 16s
Laps completed	3	3	3	3	5
Empennage	T-tail	T-tail	T-tail	Conventional	Conventional
No. of containers	-	4	4	8	-
Payload (lbs)	-	3.08	3.08	6.35	0.77

Table 7.4: Test Flight



Figure 7.15: Configuration 1



Figure 7.16: Configuration 2



Figure 7.17: Configuration 3

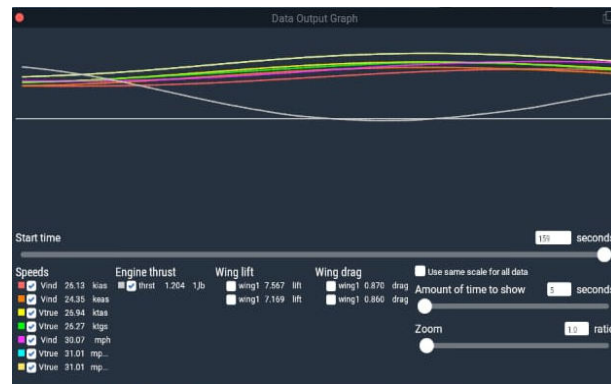
8 Performance Results

8.1 Predicted and Actual Capabilities

Flight simulator X-Plane 11 was used to replicate the flight path, obtain the flight data and verify with our calculations. We flew our plane and simulated it in the atmospheric conditions of Arizona and gust loads. The team’s pilot utilized X-plane simulations to understand the plane’s characteristics and capabilities before approaching flight tests.



(a) Aircraft flying in X-Plane simulator



(b) Live Graph from X-Plane

Figure 8.1: X-Plane Simulation

The calculated theoretical values were compared with the values obtained from the simulation and checked for

accuracy. Pixhawk px4 Ardupilot was used to obtain real-time flight data. The values are tabulated below. The values obtained through theoretical calculations and simulation were within ten percent of the actual values.

	No. of Laps			Time Taken (s)			Max Velocity (ft/s)		
	Theoretical	Simulated	Actual	Theoretical	Simulated	Actual	Theoretical	Simulated	Actual
M1	3	3	3	150	157	164	85.76	84.33	78.74
M2	3	3	3	130	206	214	76.51	78.67	63.69
M3	10	10	9	430	498	512	83.25	74.05	72.32

Table 8.1: Theoretical vs Simulated vs Actual Comparison

8.2 Improvements and Advancements

8.2.1 Wing

From our first test flight, it was observed that wings without flaps had more stall velocity; thus, the take-off and landing distance increased. Hence, for the 2nd test flight, wings with flaps were employed, which reduced stall velocity. As a result, the take-off and landing distance decreased.

8.2.2 Fuselage

The first prototype developed used a truss structure for its fuselage. From post-flight inspection, it was found that the airframe was structurally weak and had failed in the areas of high-stress concentration. The truss was unable to handle stress at specific points, such as the fuselage former joints. The team decided to use semi-monocoque to overcome the truss structure's shortcomings, which proved to be structurally strong in the coming test flights.

8.2.3 Tail Selection

Initially, the conventional configuration was selected on account of its more comfortable design and construction. It was also efficient to torsional loads and convenient to rotate at a lower airspeed. Since DRM was the primary focus, the team chose to experiment with different tail configurations. T-tail and V-tail were the alternatives as mentioned in section 3.4.2. The V-tail configuration helps in easy deployment and recovery of the sensor, but they are likely to interfere with the DRM. The other option was T-tail; hence the team chose to experiment with it in the 2nd Test flight. However, the T-tail configuration was not without merits as the horizontal stabilizer position improved pitch authority and sensor recovery and deployment was easier. The aircraft's CG was not within the range of the assumed stability margin in M3 with a T-tail configuration. Hence, considering better stability response of the conventional tail over T-tail, the Conventional tail was finalized.

8.2.4 DRM

Initially, the team was interested in the spring shaft mechanism as it was easy to fabricate. It uses a spiral spring to deploy/recover the sensor and cannot be controlled once deployed. It also had low reliability and thus seemed obsolete for the mission. However, it is not stable compared to the telescopic boom, which is much heavier. The servo winch mechanism is used over the other configurations as it is easy to fabricate and deploys the sensor in less time.

8.2.5 Sensor

The sensor was inherently unstable without fins. The team experimented with various fin configurations to obtain the optimum design. It was found through spin tests that the sensor was unstable with two fins. Although the three fin configuration was stable, the four fin configuration proved to be the most proficient. Further, the team tested rectangular, trapezoidal, and elliptical four fin setups, and the trapezoidal fin was selected based on the low drag and the more excellent stability offered.

References

- [1] Anderson Jr, J. D., *Fundamentals of Aerodynamics*, Tata McGraw-Hill Education, 2010.
- [2] Anderson, J. D., *Aircraft Performance & Design*, McGraw-Hill Science Engineering, 1999.
- [3] "OpenRocket v15.03," Online, 2021. URL <http://openrocket.info/>.
- [4] "MotoCalc 8," Online, Trial Version, 2018. URL <http://www.motocalc.com/>.
- [5] "Scorpion Calc v3.86," Online, 2021. URL <https://www.scorpionsystem.com/support/downloads/>.
- [6] Sadraey, M. H., *Aircraft Design: A Systems Engineering Approach*, John Wiley & Sons, 2012.
- [7] Nelson, R. C., et al., *Flight Stability and Automatic Control*, Vol. 2, WCB/McGraw Hill New York, 1998.
- [8] Mark Drela, H. Y., "AVL," Online, 2017. URL <http://web.mit.edu/drela/Public/web/avl>.
- [9] Pegram, J. P., and Anemaat, W. A., "Preliminary estimation of airplane moments of inertia using CAD solid modeling," Tech. rep., SAE Technical Paper, 2000. URL [://doi.org/10.4271/2000-01-1700](https://doi.org/10.4271/2000-01-1700).
- [10] Ma, D., Wang, S., Yang, M., and Dong, Y., "Dynamic simulation of aerial towed decoy system based on tension recurrence algorithm," *Chinese Journal of Aeronautics*, Vol. 29, No. 6, 2016, pp. 1484–1495. URL <https://doi.org/10.1016/j.cja.2016.09.003>.

List of Acronyms

AIAA American Institute of Aeronautics and Astronautics	GM Ground Mission
AR Aspect Ratio	MAC Mean Aerodynamic Chord
AVL Athena Vortex Lattice	M1 Mission 1
CG Centre of Gravity	M2 Mission 2
CF Carbon Fiber	M3 Mission 3
C_L Coefficient of Lift	RoC Rate of Climb
CP Centre of Pressure	S_H Area of Horizontal Stabilizer
DRM Deployment and Recovery Mechanism	S_V Area of Vertical Stabilizer
DBF Design, Build, Fly	SM Stability Margin
ESA Exhaustive Search Analysis	TOGW Takeoff Gross Weight
FoS Factor of Safety	V_H Horizontal Tail Volume Coefficient
	V_V Vertical Tail Volume Coefficient
	FoM Figure of Merit

THE UNIVERSITY OF CENTRAL FLORIDA
PRESENTS



THE DARK KNIGHTS

“THE KNIGHTMOBILE”



UCF

Table of Contents

List of Figures	3
List of Tables	4
1. Executive Summary	6
1.1. Design Overview	6
1.2. System Performance Parameters	6
2. Management Summary	7
2.1. Organization Description	7
2.2. Project Milestone Chart	8
3. Conceptual Design	9
3.1. Mission Requirements	9
3.2. Scoring Sensitivity Analysis	10
3.3. Subsystem Design Requirements	14
3.4. Aircraft Configuration Selection	15
4. Preliminary Design	20
4.1. Design and Analysis Methodology	20
4.2. Design and Sizing Trades	21
4.3. Aerodynamic and Stability Parameters	27
4.4. Mission Performance Prediction	31
5. Detail Design	32
5.1. Dimensional Parameters	32
5.2. Structural Characteristics	32
5.3. Systems Integration and Architecture	33
5.4. Weight and Balance	37
5.5. Flight and Mission Performance	39
5.6. Drawing Package	40
6. Manufacturing Plan	45
6.1. Manufacturing Methods Investigated	45
6.2. Selected Methods	45
6.3. Component Manufacturing Processes and Results	46
6.4. Milestones and Schedule	48
7. Test Planning	49
7.1. Subsystems Testing	49
7.2. Flight and Mission Testing	51
7.3. Test Cards	54
8. Performance Results	55
8.1. Key Subsystem Performance	55
8.2. Complete Aircraft Solution	57
8.3. Concluding Remarks	59
9. Bibliography	60

List of Figures

1.1. The Knightmobile Mk.3	6
2.1. Chart of design personnel and assignment areas	7
2.2. Milestone chart showing planned and actual timing of major elements	9
3.1. Architecture flowchart of scoring sensitivity analytic model	12
3.2. Score comparison of M3 versus M2	13
3.3. Score sensitivity of mission design parameters	13
3.4. Sensor shipping container CAD model	20
3.5. Conceptual sketch of the first prototype	20
4.1. 2D airfoil coefficients	21
4.2. C_L/C_D vs. α	23
4.3. δ vs. taper ratio	23
4.4. Sensor weight vs. number of laps	24
4.5. Sensor weight vs. battery energy	24
4.6. Thrust required vs. flight speed	25
4.7. Power required vs. flight speed	25
4.8. Power variation of propellers	27
4.9. Thrust variation of propellers	27
4.10. C_L vs. C_D M2 cruise comparison	28
4.11. AVL model of the aircraft (left) and C_l vs. span plot of the aircraft at M2 cruise condition (right)	29
4.12. Root Locus plots	30
5.1. Fuselage structure stress analysis	33
5.2. Knightmobile Mk.3 fuselage structure	33
5.3. Left wing CAD model	34
5.4. Empennage exploded view	34
5.5. Sensor CAD model (left) and sensor component view (right)	35
5.6. Deployment and recovery system multi-view	36
5.7. Full payload storage system	37
5.8. Aircraft coordinate system (origin is set to the motor mounting location)	38
5.9. Predicted thrust curves for each mission	40
6.1. Manufactured wing (left) and tail (right)	46
6.2. Constructed fuselage	47
6.3. Manufactured landing gear	47
6.4. Manufactured subcomponents	48
6.5. Manufacturing milestones chart (planned timing vs. actual)	49
7.1. Testing schedule overview	49
7.2. Initial sensor testing out of a car window	50
7.3. Functional mechanism prototype setup (left) and initial testing out of a car window (right)	50
7.4. Wing tip testing results	51
7.5. Mk.1 conceptual flight test final landing approach	52
7.6. Photographic progression through the aircraft iterations	52
7.7. Knightmobile Mk.3 vertical flight with no payload	53
8.1. Simulated extreme case wingtip load test	56
8.2. M1 flight path (using GPS data) compared with the provided course sketch	57

List of Tables

1.1. System performance and capabilities	6
2.1. Sub-team organization table	8
3.1. Mission requirements and scoring	10
3.2. Figures of merit	15
3.3. Main fuselage shape	16
3.4. Wing mounting	16
3.5. Wing shapes	17
3.6. Motor mounting	17
3.7. Tail configurations	18
3.8. Landing gear configurations	18
3.9. Deployment and recovery mechanism configurations	19
3.10. Sensor configurations	19
4.1. Drag breakdown (M3 cruise conditions)	25
4.2. Motor selection short list	26
4.3. Battery selection short list	26
4.4. Propeller selection short list	27
4.5. Aerodynamic parameters per iteration	28
4.6. Stability parameters at M2 cruise	29
4.7. M1 stability modes parameters (takeoff conditions/cruise conditions)	30
4.8. M2 stability modes parameters (takeoff conditions/cruise conditions)	30
4.9. M3 stability modes parameters (takeoff conditions/cruise conditions)	31
4.10. Aircraft mission performance prediction	31
5.1. Final aircraft design dimensions	32
5.2. Selected aircraft propulsion package	37
5.3. Weight and balance table	38
5.4. Final design mission performance and flight performance parameters	39
7.1. Test Card 1 (pre-flight checklist)	54
7.2. Test Card 2 (in-flight and post-flight checklist)	55
8.1. Wingtip loading test results	56
8.2. Subcomponent function verification test card	56
8.3. Detailed flight test results	58
8.4. Extreme payload case vs M2	59

Acronyms and Abbreviations

ABS Acrylonitrile Butadiene Styrene

AIAA American Institute of Aeronautics and Astronautics

APC Advanced Precision Composites

AVL Athena Vortex Lattice

AWG American wire gauge

CG Center of Gravity

CNC Computer Numerical Control

DBF Design/Build/Fly

GM Ground Mission

GPS Global Positioning System

LiPo Lithium Polymer

M1 Mission 1

M2 Mission 2

M3 Mission 3

Mk. Mark

NiCad Nickel–cadmium

NiMH Nickel–metal hydride

PETG Polyethylene Terephthalate Glycol

PLA Polylactic Acid

TC Test Card

UCF University of Central Florida

1. Executive Summary

This design report presents the University of Central Florida team's design process for accomplishing the objectives set forth for the 2020-2021 AIAA Design, Build, Fly competition. The team's objective was to design, analyze, fabricate, and demonstrate an unmanned, remote-controlled aircraft capable of achieving all mission requirements while maximizing the final competition score. The aircraft will be required to complete three flight missions and a ground mission; these missions include tests of the aircraft's ability to carry cargo and to deploy, operate, and recover a towed sensor. A "divide and conquer" strategy was employed by decomposing the competition mission requirements into subsystems managed by small sub-teams. These sub-teams implemented rapid prototyping and frequent testing to mitigate risks and ensure steady, continuous, iterative improvements.

1.1 Design Overview

A sensitivity study of the mission scoring system determined that the overall mission score is most sensitive to design parameters that maximize score for the third mission. Therefore, the team designed for an optimized sensor weight and length to maximize this score. Furthermore, in order to increase velocity and decrease structural mass in favor of payload mass, a light airframe constructed primarily from balsa and plywood was chosen.

A number of conceptual solutions were generated and analyzed to determine the optimal design to meet competition specifications and mission requirements. After careful consideration, the team decided on a high wing, taildragger aircraft with a single motor. This design prioritized stability, ease of manufacturing, and optimized cargo capacity. It was determined that a rigid telescoping rod with two degrees of freedom would be used for the towed sensor system. This design was chosen for its high stability characteristics and ability to be reduced to a compact size for storage within the aircraft.

Preliminary sizing of an initial prototype was conducted to provide a baseline aircraft upon which to iteratively improve. The results of the conceptual study, including the selected aircraft configuration, were used along with significant factors of safety to design and construct the team's initial aircraft, the Knightmobile Mk.1. Initial experimental testing of Mk.1 was then considered and used to make design improvements in fabricating a second aircraft, Knightmobile Mk.2. Detailed analysis and in-depth flight tests of Mk.2 drove refinements of key subsystems, leading to the mission-capable Knightmobile Mk.3.

1.2 System Performance Parameters

Key performance parameters of the complete system solution are outlined in Table 1.1.

Table 1.1: System performance and capabilities

Mission 1	Mission 2	Mission 3
Cruise Velocity: 55.6 mph	Cruise Velocity: 50.36 mph	Cruise Velocity: 46.46 mph
Takeoff Distance: 5 ft	Takeoff Distance: 35 ft	Takeoff Distance: 20 ft
Lap Time: 28.33 sec	Lap Time: 31.33 sec	Lap Time: 34.06 sec
Empty Aircraft Weight: 5.5 lbs	Payload Weight: 6.33 lbs	Payload Weight: 2.9 lbs

The Knightmobile Mk.3 aircraft was designed to transport three 1.62 pound shipping containers and the sensor deployment and recovery mechanism during Mission 2. The aircraft was also designed to deploy, tow, and recover a 4.25 inch long sensor weighing 1.4 pounds at a deployment length of 43 inches during Mission 3.

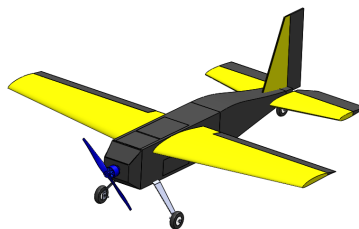


Figure 1.1: The Knightmobile Mk.3

2. Management Summary

2.1 Organization Description

The UCF team consists of 12 undergraduate students united under a faculty advisor, including eight seniors and four underclassmen. During initial team formation, senior students organized into sub-teams, with each student leading an effort which best reflects their expertise. The students also participate in other sub-teams to aid those efforts, ensuring that each member's expertise is properly utilized in making contributions, while also allowing flexibility for members to grow in areas of interest. Underclassmen students joined sub-teams of their choice to learn new skills and take on project initiatives as assigned by sub-team leads, with an eye toward continued involvement in future DBF competitions at UCF. The team employs a hierarchical leadership system as shown in Figure 2.1 which promotes team communication, collaboration, and accountability.

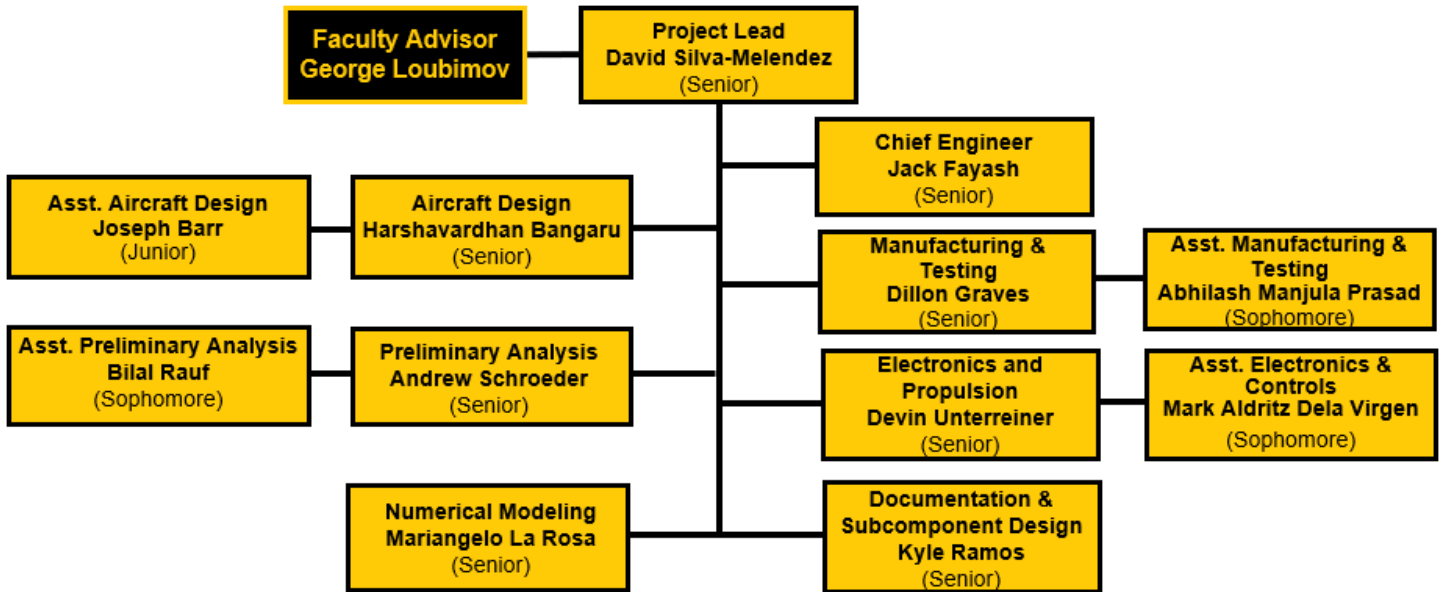


Figure 2.1: Chart of design personnel and assignment areas

The faculty advisor provides guidance and support to the team on a weekly basis. The project lead is responsible for managing the team, including organizing project efforts and team logistics. The chief engineer acts as a consultant for the team, aiding in all facets of the project and helping the team make key decisions. The rest of the team is organized into seven sub-teams, each responsible for addressing an essential component of the project as described in Table 2.1.

Table 2.1: Sub-team organization table

Sub-teams	Team Roles	Skill Set Requirements
Aircraft and Structural Design	<ul style="list-style-type: none"> • Design structural components, sensor and sensor shipping container. • Select and continuously improve a main aircraft design. 	<ul style="list-style-type: none"> • Quickly and efficiently use CAD software. • Recognition of design manufacturability.
Prototype Manufacturing and Testing	<ul style="list-style-type: none"> • Rapidly manufacture and provide feedback on new designs. • Flight test each prototype and keep records of aircraft performance. 	<ul style="list-style-type: none"> • Machining and part production. • Expedient assembly techniques.
Subcomponent Design	<ul style="list-style-type: none"> • Design and analysis of subcomponent systems. • Flight and ground testing of sensor and deployment/recovery mechanism. 	<ul style="list-style-type: none"> • Knowledge of fundamental aerodynamics. • Recognition of design manufacturability.
Electronics, Controls and Propulsions	<ul style="list-style-type: none"> • Research and select electronics and propulsion packages. • Lead design of sensor electronics incorporation. 	<ul style="list-style-type: none"> • Understanding of electronics compatibility. • Electronic component design.
Preliminary Analysis	<ul style="list-style-type: none"> • Optimization of mission objectives based on score sensitivity. • Aircraft sizing, stability and performance based on aerodynamic calculations. 	<ul style="list-style-type: none"> • Programming and logical problem-solving. • Modeling of multi-variable systems.
Numerical Modeling	<ul style="list-style-type: none"> • Use simulation programs to assess preliminary design decisions. • Physical verification of simulated results. 	<ul style="list-style-type: none"> • Use of CFD and FEA software. • Practical application of simulation results.
Documentation and Technical Reporting	<ul style="list-style-type: none"> • Write and format project proposal and design report. • Compile, track, and present data collected across all sub-team efforts. 	<ul style="list-style-type: none"> • Technical writing and reporting. • Data analysis and synthesis.
Project Management	<ul style="list-style-type: none"> • Supply structural design and manufacturing sub-teams with design constraints. • Facilitate external and cross-team communication. 	<ul style="list-style-type: none"> • Group management and conflict resolution. • Communication proficiency.

Each sub-team meets weekly to distribute tasks and discuss ideas; a weekly "all-hands" meeting involving all team members and the faculty advisor is also held to discuss accomplishments made, current tasks and goals, and any roadblocks faced. With guidance from the faculty advisor and other team members, roadblocks are then promptly addressed and eliminated.

2.2 Project Milestone Chart

Figure 2.2 displays a Gantt Chart of the team's chosen schedule and contains the major design milestones for the team. The project lead and chief engineer keep this chart updated to ensure that all goals progress according to schedule.

UCF DBF 2020-2021	Sept.	Oct.	Nov.	Dec.	Jan.	Feb.	Mar.	Apr.	
Aircraft Design								Major Initiatives:	
Research								Sub-Initiatives:	
Missions Study								Completed:	
Conceptual Design								Due dates:	
Conceptual Design Due	Oct. 31		★					★	
Sensor Design									
Preliminary Design									
Detailed Design									
Detail Design Due	Feb. 13					★			
Manufacturing									
Components Development									
Prototyping									
Final Aircraft Production									
Testing & Integration									
Aerodynamics									
Electronics & Controls									
Structural									
Propulsion									
Flight Testing									
Deliverables									
Design Proposal									
Proposal Due	Oct. 31		★						
Design Report									
Report Due	Feb. 19					★			
DBF Competition	Apr. 15-18						★		★

Figure 2.2: Milestone chart showing planned and actual timing of major elements

3. Conceptual Design

3.1 Mission Requirements

The mission requirements outlined in the AIAA DBF 2020-2021 rulebook [1] simulate a multi-purpose, high-speed cargo aircraft capable of carrying a number of shipping containers and towing an aerodynamically stable sensor. The competition is made up of 3 flight missions, each with a different payload configuration, and a ground mission. All three flight missions require the aircraft to take off within 100 ft before flying some number of laps of the competition course and landing fully intact on the runway. The competition course consists of a 180° turn in the clockwise direction at either end of a 1000 ft straightaway, as well as a 360° turn in the counterclockwise direction. Table 3.1 details the general requirements of each mission.

Table 3.1: Mission requirements and scoring

Mission	Mission Requirements	Scoring Formula
Mission 1 (M1)	- The aircraft must complete 3 laps of the course within a 5-minute flight window.	$M1 = 1.0$ for a successful mission
Mission 2 (M2)	- The aircraft must complete 3 laps of the course as quickly as possible within a 5-minute flight window. - The aircraft must also carry the sensor in a shipping container, the deploying and recovery mechanism in a stowed configuration, and some number of additional shipping container simulators.	$M2 = 1.0 + \frac{(N_{\text{containers}} / \text{time})_{\text{UCF}}}{(N_{\text{containers}} / \text{time})_{\text{Max}}}$
Mission 3 (M3)	- The aircraft must deploy a sensor after takeoff, fly as many laps as possible within a 10-minute flight window, recover the sensor, and then land successfully. - The sensor must remain aerodynamically stable while deployed, and must not affect the aircraft's stability.	$M3 = 2.0 + \frac{(N_{\text{laps}} * L_{\text{sensor}} * W_{\text{sensor}})_{\text{UCF}}}{(N_{\text{laps}} * L_{\text{sensor}} * W_{\text{sensor}})_{\text{Max}}}$
Ground Mission (GM)	- The assembly crew member will load the Mission 2 payload, remove the payload, and install the deploying and recovery mechanism and sensor as quickly as possible. - The pilot will then demonstrate sensor deployment and recovery.	$GM = \frac{T_{\text{Min}}}{T_{\text{UCF}}}$

The total competition score is calculated as shown in Equation 1.

$$\text{Score} = \text{Written Report Score} * (\text{GM} + \text{M1} + \text{M2} + \text{M3}) \quad (1)$$

3.2 Scoring Sensitivity Analysis

An analysis of the sensitivity of mission score to design parameters was performed to determine the most beneficial approach for maximizing total score. The mission scoring formulas outlined in Table 3.1 were used to guide the analysis. Given that M1 is a test flight scored for completion alone, it was assumed for the sake of score calculation that the mission was successfully completed and 1 point was added to the team's score. M2 and M3 were considered as the focus of the analysis.

3.2.1 Mission Constraints and Assumptions

To develop an in-depth scoring sensitivity analysis, initial engineering constraints and assumptions were derived from the rules and restrictions of the competition. These constraints are outlined below:

Aircraft Constraints

- The aircraft must survive a 2.5g wing tip load test and have a wingspan of no more than 5 ft.
- The aircraft must perform a rolling takeoff within 100 ft for all missions.
- The aircraft must be propeller driven and electric powered and may use any number of motors and/or propellers.
- The aircraft's power system has the following limitations:
 - The total stored energy of all battery packs cannot exceed 200 watt-hours.
 - Each individual battery pack cannot have stored energy greater than 100 watt-hours.

Subcomponent Constraints

- The mechanism, upon remote activation, must deploy the sensor a minimum of 10 times the total length of the sensor from the exit location of the aircraft.



- The sensor must have a minimum diameter of 1 inch with a minimum length-to-diameter ratio of 4.
- All shipping container simulators must be the same size and at least the same weight as the sensor shipping container with sensor inside.

In order to simplify the scoring sensitivity analysis for the purpose of rapid, iterative improvement, initial values were estimated for certain parameters. A preliminary propulsion package (an E-flite Power 60 motor and a 6s Lithium Polymer (LiPo) battery) was chosen based on material availability to provide a starting point for the analysis. Similarly, an airfoil was chosen based on faculty advisor recommendation. Additional self-imposed constraints and assumptions are stated below:

- Propeller efficiency was assumed to be 50% at take-off and 80% at cruise.
- A rectangular wing planform was initially used for simplicity and ease of manufacturing.
- Assumed environmental properties (i.e. air density and runway friction coefficient).
- A minimum chord length was given due to structural strength considerations.
- An average wing density and initial fuselage weight were estimated based on material properties.
- An initial mass of the deployment and recovery mechanism was estimated.

3.2.2 Description of Analysis

An analytic model was developed in MATLAB to determine which payload for each mission leads to the best overall score, and what kind of aircraft is required in order to transport that payload. The constraints and assumptions outlined in Section 3.2.1 were used to establish a set of boundary conditions for the model. The model assumed that the takeoff condition for M2 was the most aerodynamically limiting (highest required lift) case for the aircraft, given that it requires the heaviest payload. A wide range of payload configurations was considered, each defined by varied sensor length, sensor mass, and number of shipping containers carried during M2. For each payload configuration, the required wing planform area to satisfy the takeoff distance requirement during M2 was calculated using the chosen propulsion package and airfoil. Equations 2 and 3 were used to predict the stall velocity of the aircraft and estimate the acceleration of the aircraft during the takeoff roll.

$$V_{\text{STALL}} = \sqrt{\frac{2nW}{\rho S C_{L_{\text{MAX}}}}} \quad (2)$$

$$S_G = \frac{V_G^2}{2\bar{a}} \quad (3)$$

A parasitic drag coefficient for the total aircraft was then estimated based on the resultant wing and tail configuration. Using the calculated aircraft structure and drag coefficient along with the chosen propulsion package, the M2 and M3 takeoff distances and cruise velocities were then estimated and used to predict mission scores. Finally, the payload configurations were ranked by score and normalized with respect to the top-scoring configuration. The ranked configurations were then plotted and observed for trends. Figure 3.1 outlines the basic analytic model architecture.

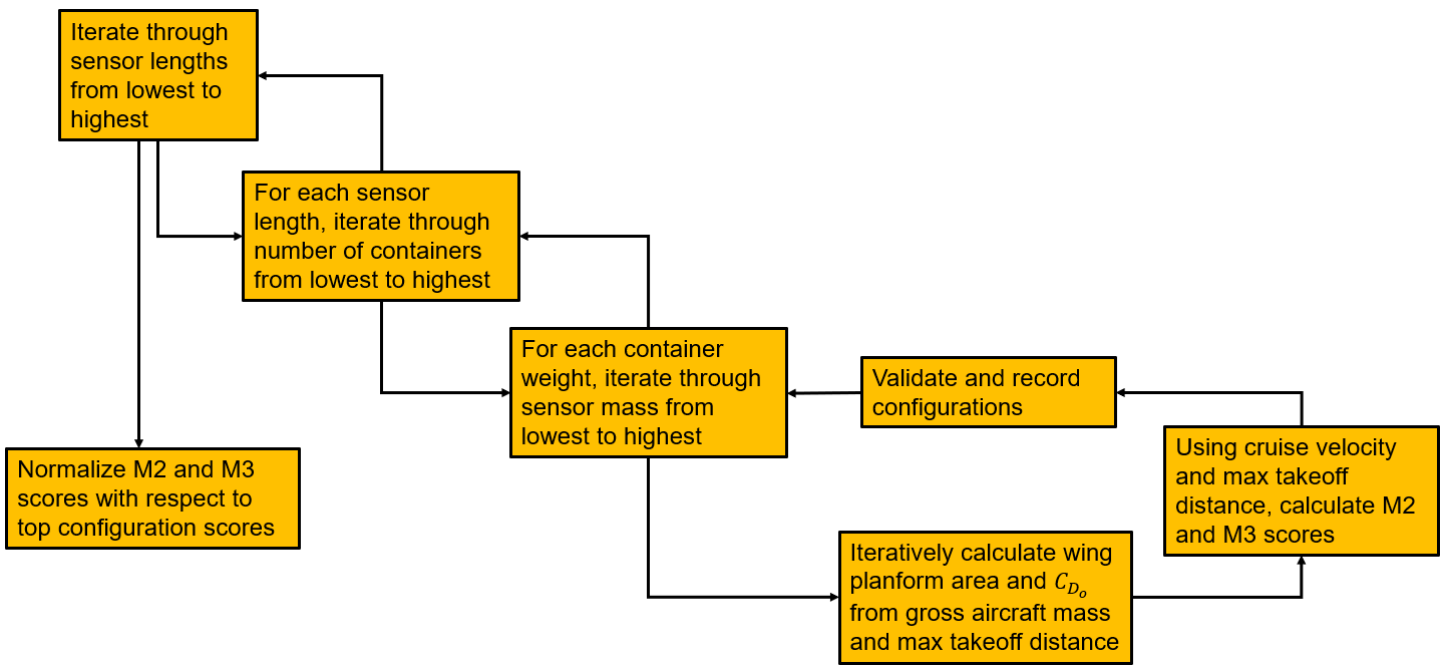


Figure 3.1: Architecture flowchart of scoring sensitivity analytic model

3.2.3 General Trends Toward an Optimal Solution

Several trends were observed in the plotted data from the scoring sensitivity analysis. It was found that M2 score increased with aircraft velocity and number of shipping containers, while M3 score increased with sensor length, sensor mass, and aircraft velocity. The most important trend, however, was that M2 and M3 showed a strong inverse relationship for their scores.

The M2 score has an implicit inverse relationship with the size and weight of the sensor. An aircraft with a fixed propulsion power has a maximum payload weight that it can carry; for a fixed payload weight, increasing the weight of each sensor decreases the number of shipping container simulators that the aircraft can carry, decreasing M2 score. This relationship indicates that optimization of M2 score favors a large number of small, light-weight sensors.

The M3 score has an explicit positive relationship with the length and weight of the sensor as seen in the M3 scoring formula described in Table 3.1. However, increasing sensor length increases total aircraft drag due to the larger sensor body. Additionally, it must be guaranteed that the aircraft has enough battery power to fly for ten minutes. Depending on the mechanism used, the increased towing distance due to changes in sensor length could also increase aircraft drag, although this was not considered in conceptual analysis. Similarly, increasing the length of the sensor also requires the sensor to be deployed at a further distance from the aircraft. The combination of a heavy sensor and a long deployment distance may necessitate a larger and heavier deployment mechanism, and also may lead to stability issues for the aircraft due to the enlarged moment created by the deployed sensor. The conceptual analysis performed largely left complex relationships for later analysis and experimental consideration, as is discussed in Section 3.2.4.

The scores for M2 and M3 display a strong inverse relationship as can be seen in Figure 3.2. Increasing the length or weight of the sensor increases M3 score but reduces the number of shipping container simulators that can be carried by the same aircraft in M2. The total payload weight for M2 will always be greater than that for M3, meaning that the wing size required for M2 will be greater than that required for M3. Additionally, this payload weight discrepancy increases with the number of shipping container simulators carried in M2. A larger wing and cargo hold both create more drag, meaning that an aircraft designed to carry the largest number of shipping containers possible in M2 will have far more drag than is optimal for M3.

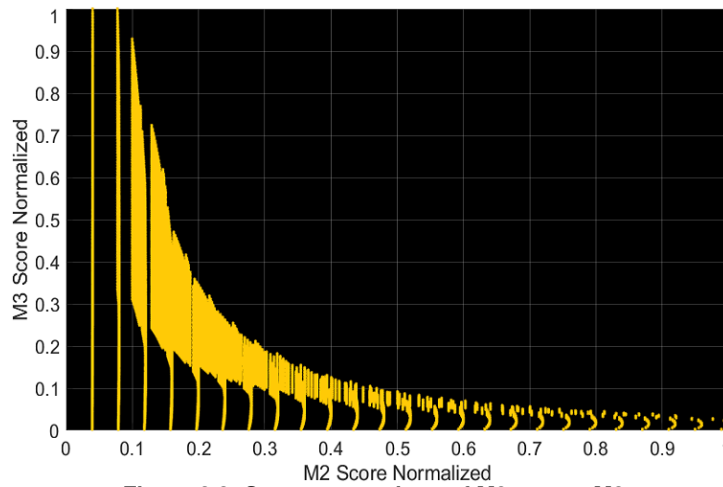


Figure 3.2: Score comparison of M3 versus M2

The total score was found by summing the M2 and M3 scores, and the relationships between total score and several key design parameters are displayed in Figure 3.3. The peak in total score vs. number of shipping containers on the left side corresponds to a configuration optimizing M3 score, while the peak on the right side corresponds to a configuration optimizing M2 score. The M3 peak is higher than the M2 peak, indicating that optimizing for M3 yields a higher total score than optimizing for M2. Furthermore, it is practically easier to load the aircraft with a small number of heavy shipping containers compared to a large number of light shipping containers. Therefore, it was decided that optimization of M3 would be the ideal focus for aircraft design going forward.

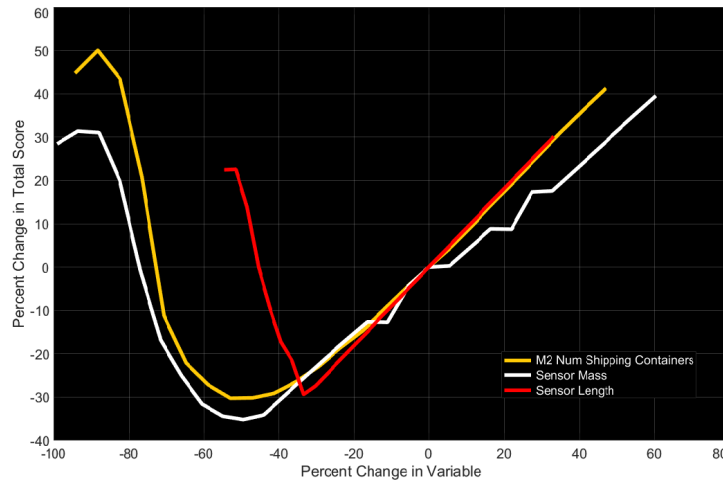


Figure 3.3: Score sensitivity of mission design parameters

For additional consideration, M2 is coupled with the GM with an inverse relationship for their scores. The more shipping container simulators carried in M2, the higher the M2 score, but the more difficult and time consuming it is to load the aircraft during the ground mission, decreasing the ground mission score.

3.2.4 Shortcomings of the Analysis

The scoring sensitivity analysis model had several unavoidable shortcomings due to a lack of real-world experimental data and a number of decisions made to simplify the analysis. To compensate for this lack of data, the model incorporated numerous safety factors. These safety factors primarily aimed to underestimate rather than overestimate mission performance. Furthermore, the optimal cases calculated by the model are likely impractical due to unforeseen or incalculable difficulties in their implementation.

The architecture of the aircraft structure was undecided at this stage, making calculation of the structural strength a very

abstract and difficult problem, potentially limiting the fidelity of boundary conditions. Since a propeller choice had not yet been determined, simplified assumptions of propeller efficiencies were also used in the model. In practice, the propeller efficiency would vary with velocity, but the model assumed constant efficiencies. Additionally, with no functional prototype to test, it is impossible to predict GM performance. With regards to M3 score prediction, without experimental data or further in-depth analysis, it is difficult to predict how sensor deployment distance affects drag and stability. The deployment and recovery mechanism design was undecided at this stage, so a constant mechanism weight was used in the model, potentially skewing score results slightly.

In general, it was difficult to predict the properties of designs that had not yet been determined. Despite these inaccuracies in the actual magnitudes of the calculated values, the general trends observed were deemed valid for analysis, as the observed relationship directions among variables were unlikely to be significantly affected by these inaccuracies. For example, the constant propeller efficiency assumption was applied to both M2 and M3, and is therefore unlikely to invalidate comparisons between the two missions.

3.3 Subsystem Design Requirements

After analyzing the results from the scoring sensitivity study, subsystem requirements were determined. The primary subsystems affected by these requirements were the sensor, fuselage, lifting surfaces (wing and tail), and propulsion systems. Setting guidelines and parameters for these separate systems allows the team to be more efficient in design and overall usage of time.

3.3.1 Subcomponents

The shipping container, sensor, and deployment and recovery mechanism have different priorities per the sensitivity analysis. It was determined that the sensor's weight would be maximized and its length kept as long as possible within real-world constraints and without requiring a deployment length that compromises the overall stability of the sensor and aircraft. Furthermore, the sensor must have adequate space in the interior for the placement of the electronics package.

It was also determined that the shipping container would be kept as light as possible so as not to add extraneous weight in M2. Allowing for most of the payload weight during M2 to be from the sensor allows for an optimized score that is close to the score predicted by the sensitivity analysis. Fulfilling this goal would involve analyzing different materials and their properties to determine which would provide the lowest weight while providing sufficient protection for the sensor. The mechanism would have similar priorities in M3; minimizing its weight without compromising its ability to efficiently deploy and recover the sensor is imperative to maximizing M3 score.

3.3.2 Fuselage

It was determined that the fuselage would have an internal structure containing ample cargo hold volume for placement of the deployment and recovery mechanism and the number of shipping container simulators determined to be carried to first maximize the M3, then M2, score. This subsystem will also undergo iterative testing and experimentation to minimize parameters such as aerodynamic drag.

3.3.3 Lifting Surfaces

As shown in Figure 3.1, one of the processes required to predict the optimal M2 and M3 scores was the calculation of wing planform area from a given aircraft mass and maximum takeoff distance. Similarly to this analysis, the planform area should be sized to have sufficient lift for takeoff during M2 (the heaviest load case). However, an excessively large wing creates unnecessary drag, decreasing cruise velocity. Therefore, it was determined that the lifting surfaces would be tested to determine optimal sizing for M2 and M3.

3.3.4 Propulsion System

Overall, the goal of the propulsion system must be to maximize flight speed and endurance. There must be sufficient battery energy to fly for the full duration of M3, creating a lower boundary for propulsion design. Optimization of both M2 and M3

score necessitates a powerful propulsion system to maximize cruise velocity and meet the 100 ft takeoff requirement. However, available payload capacity can be increased by minimizing weight of the propulsion system. As such, it was determined that a propulsion system that delivers a high power to weight ratio was necessary for score optimization.

3.4 Aircraft Configuration Selection

3.4.1 Selection Criteria

Analysis of mission and subsystem requirements, as well as mission scoring, led to a list of conceptual focuses as outlined in Table 3.2. A Figures of merit system was used in evaluating each concept and in final selection of an optimal configuration.

Table 3.2: Figures of merit

Criteria	Score Factor
Structural Weight	5
Velocity	5
Aerial Stability	4
Design Simplicity	3
Structural Strength	3
Maneuverability	2
Cargo Capacity	1

Structural weight was considered an important design consideration for improving aircraft stability, strength, and cargo capacity. More cargo capacity leads to more shipping container simulators carried, improving M2 score; reduced structural weight also allows the aircraft to trim at lower angles of attack, increasing number of laps completed with the sensor deployed in M3.

Aircraft cruise velocity was also given a high priority, as it directly impacts the team’s mission score in both M2 (through time to completion of 3 laps while encumbered) and M3 (through number of laps completed with the sensor deployed).

Aerial stability was deemed significant both to improve aircraft maneuverability and M3 score, which can only be completed if the deployed sensor and aircraft remain aerodynamically stable throughout the flight.

Design simplicity was given moderate consideration, both to remind the team to consider the feasibility of potential solutions and to improve the Ground Mission (GM) score, which is dependent on assembly time of internal aircraft mechanisms and thus requires those mechanisms to be simple to assemble under pressure.

Structural strength was also given moderate consideration to ensure that the aircraft withstands aerodynamic forces in flight.

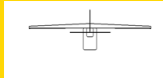
Aircraft maneuverability was deemed a secondary goal, since the aircraft must complete several turns during flight but will not need to perform expert aerobatic maneuvers.

Cargo capacity was considered a low priority. M2 requires cargo to be carried and thus space for at least 2 sensors will be necessary, but score sensitivity analysis as detailed in Section 6 led the team to prioritize M3 score by increasing each sensor’s weight and decreasing the number of sensors carried in total.

For each subsystem and configuration concept, Figures of merit were assigned based on a scale from 1 to 3 for each relevant criterion. Configurations within a subsystem were compared to one another based on these criteria, with a 1 on the scale given to a configuration which does not satisfy the goal or which satisfies it poorly relative to the other designs, and with a 3 on the scale given to a configuration which satisfies the goal exceedingly well. These Figures of merit were then multiplied by the score factors shown in Figure 3.2 and the total was then used to quantitatively evaluate the concepts and select optimal configurations.

3.4.2 Fuselage

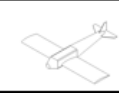
Table 3.3: Main fuselage shape

			
Criteria	Score Factor	Rectangular	Circular
Design simplicity	3	2	1
Cargo Volume	1	3	1
Structural strength	3	2	3
Velocity	5	2	2
Total Score		25	23

The goal of the main fuselage structure was to be structurally strong to take the loads of flight, cargo, and landing, while also keeping a large amount of space for electronic and sensor storage. The shape of the main fuselage should also maintain an aerodynamic shape to positively affect velocity. The circular bulkhead design is strong and a bit more aerodynamic and thus might provide a higher velocity. However, it was considered that the amount of viable cargo space required within the fuselage would necessitate a larger cross-sectional area or a longer body. Thus, any increase in velocity was considered minimal due to increased drag. The rectangular fuselage is easy to construct and provides a good amount of storage without sacrificing significant structural strength; therefore, the rectangular design proved to be the best option.

3.4.3 Wing

Table 3.4: Wing mounting

				
Criteria	Score Factor	High Wing	Mid Wing	Low Wing
Stability	4	3	2	1
Design simplicity	3	3	1	2
Structural strength	3	3	2	1
Maneuverability	2	1	2	3
Total Score		32	21	19

In terms of wing mounting locations, design simplicity and structural strength were emphasized because the wing had to be removable for transportation purposes and also had to hold cargo, which meant it needed the ability to withstand higher stresses. Along with these, stability and maneuverability were also chosen as important criteria for mission flying purposes. Based on this criteria, the high wing was chosen. This configuration allows for better handling of higher stresses, increased stability, and easily replaceable attachment points. Its only downside is that it is not as maneuverable as the low wing.

Table 3.5: Wing shapes

				
Criteria	Score Factor	Elliptical	Tapered	Rectangular
Structural Strength	3	1	2	3
Design simplicity	3	1	2	3
Velocity	5	3	3	1
Total Score		24	27	23

For the criteria to decide the optimal wing shape, design simplicity, structural strength, and velocity were chosen. Because this aircraft is designed to hold heavy cargo, the wings will undergo higher stresses and will need to have a higher lift factor. With that in mind, the tapered wing was selected as the optimal choice. Although the elliptical wing was the most efficient, its lack of structural strength (comparatively) and the intricacy of the design far outweighed its one advantage.

3.4.4 Motor Mounting

Table 3.6: Motor mounting

			
Criteria	Score Factor	Single, Nose Mounted	Dual, Wing Mounted
Weight	5	3	1
Velocity	5	2	3
Structural Strength	3	3	1
Design Simplicity	3	3	1
Total Score		43	26

The team decided to highlight weight, velocity, strength, and design simplicity as the most important criteria when considering motor mounting. These criteria were chosen to maximize mission scores and reduce possibility of over-engineering. The single, nose-mounted motor design was the lighter, simpler and structurally stronger design when compared to dual, wing-mounted motor design. Although the dual-motor package had a better propulsion package, the single, nose-mounted motor design was the overall better choice.

3.4.5 Empennage

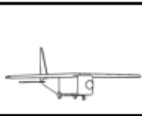
Table 3.7: Tail configurations

				
Criteria	Score Factor	Conventional	T- tail	Cruciform tail
Design simplicity	3	2	1	3
Stability	4	3	1	2
Structural strength	3	3	2	1
Total Score		23	13	21

Stability, structural strength and design simplicity were the primary criteria for choosing an empennage configuration. Stability of the given tail configuration was seen as most important because the wing configurations were also primarily decided based upon the stability. Design simplicity and structural strength were also chosen as important criteria because a modular tail setup was considered for the first prototype for testing purposes. With all these criteria in mind, the cruciform and t-tail underperformed while the conventional tail came out on top as the optimal choice.

3.4.6 Landing Gear

Table 3.8: Landing gear configurations

			
Criteria	Score Factor	Taildragger	Tricycle
Stability	4	3	2
Design simplicity	3	3	2
Structural strength	3	2	1
Total Score		27	17

The landing gear configurations were judged based on structural strength, design simplicity, and stability. The structural strength focused more on landing gear placement rather than the structure of the landing gear itself. For example, with the taildragger design, the front wheels are placed slightly forward of the CG, while the tricycle design has the wheels distributed around the CG. Stability when landing and taking off was also a huge part of the decision-making process. Because the taildragger had a more spread out configuration, it proved far more stable than the tricycle configuration. With all of these considerations in mind, the taildragger configuration was chosen for the design.

3.4.7 Deployment and Recovery Mechanism

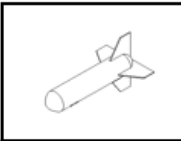
Table 3.9: Deployment and recovery mechanism configurations

				
Criteria	Score Factor	Stiff Wire, Single Spool Motor	Telescoping Rods	Two motors and two connection points
Design simplicity	3	1	2	1
Weight	5	3	1	2
Cargo Capacity	1	3	2	2
Stability	4	1	3	2
Total Score		25	25	23

The deployment and recovery mechanism configurations were judged based on design simplicity, weight, cargo capacity, and stability. The goal of the mechanism is to efficiently deploy and recover the towed sensor while maintaining stability. The mechanism should be relatively compact in the cargo area while having a minimal contribution to the overall weight. The telescoping rods give the sensor more stability, but take up space in the cargo bay and are relatively heavy. The two motors with two connection points might provide some stability, but are heavy and require mechanical and electrical complexity. The single spool motor paired with a stiff wire is the lightest option and provides the most cargo space, but is dependent on the sensor itself for stability and therefore seems to lack feasibility, which decreases its design simplicity score. Given a tie between the telescoping rods and the single spool motor, the telescoping rods were chosen due to the guaranteed stability they provide.

3.4.8 Sensor

Table 3.10: Sensor configurations

			
Criteria	Score Factor	Cylinder with Ellipsoid Caps and Fins	Cylinder with Ellipsoid Caps and no Fins
Cargo Capacity	1	1	3
Stability	4	3	2
Design Simplicity	3	2	3
Total Score		18	20

The sensor configurations were judged based on cargo capacity, stability, and design simplicity. The sensor concepts were considered on the basis that the sensor must be aerodynamically stable and have sufficient volume to store the sensor electronics. The first concept was a simple missile-shaped configuration, consisting of a cylinder body with caps based on a truncated ellipsoid to decrease drag and additional fins for stability. This model takes up significant cargo volume, which could severely limit the number of shipping container simulators carried during M2, and could lead to clearance issues within the fuselage during deployment in M3. This led to consideration of a design that does not include fins to decrease cargo volume taken and increase design simplicity. Based on the criteria as presented, along with general bias based on the chosen mechanism, the cylinder without fins was selected.

3.4.9 Sensor Shipping Container

The shipping container was designed as a concept with a sliding door and pin to insert and remove the sensor. The shipping container shape chosen was an internally-padded rectangular prism, as shown in Figure 3.4.

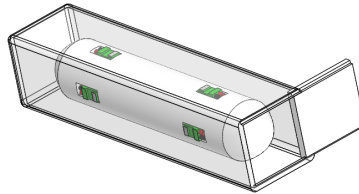


Figure 3.4: Sensor shipping container CAD model

3.4.10 Final Concept

Given the results of the evaluations as shown, a single-motor aircraft with high-mounted, tapered wings, a rectangular bulkhead-based fuselage, boom-based rear fuselage, conventional empennage, and taildragger landing gear was chosen for the final design. An initial prototype was developed to test certain systems; however, for that prototype certain concessions were made to promote rapid design and manufacturing. These included not using a tail wheel for takeoff, and the use of a rectangular wing with a modular design that allowed testing of multiple wing shapes and chord lengths. The mission subcomponents will consist of a telescoping rod system with Kevlar wire that deploys and recovers the sensor, which will be a cylinder with ellipsoid-based caps. A preliminary conceptual sketch of the prototype and its initial sizing is seen in Figure 3.5.

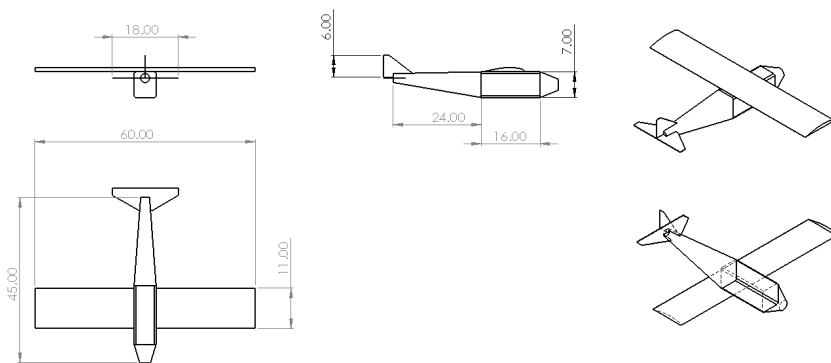


Figure 3.5: Conceptual sketch of the first prototype

4. Preliminary Design

4.1 Design and Analysis Methodology

An aircraft configuration was chosen during conceptual design based on the scoring sensitivity analysis. The focus then transitioned to the creation of an initial functional prototype, known as Knightmobile Mk.1, to serve as a baseline for an iterative design approach. This design methodology was chosen for the purpose of following trends toward an optimal solution. Various trade studies were conducted in the development of the Knightmobile Mk.1. The trade studies include airfoil selection, wing sizing, sensor sizing, and propulsion selection. An airfoil was selected and the wing was sized based on the takeoff distance requirement and minimizing drag at cruise conditions; however, careful consideration was given toward not compromising structural integrity. The sensor was sized to prioritize M3 score over M2 score. Finally, the propulsion package was selected based on power required at cruise velocity and completing the entire flight duration of M3. These sizings were used to create the Mk.1 aircraft, which was then subjected to experimental flight testing; the results of these tests were used to construct an improved aircraft, Knightmobile Mk.2. A final aircraft, Knightmobile Mk.3, was designed as a complete overhaul of the preliminary Mk.1 and Mk.2 designs with the knowledge gained from both experimental testing and analytical modeling. The static and dynamic stability characteristics and mission performance of the Mk.3 design were then predicted.

4.2 Design and Sizing Trades

4.2.1 Airfoil Selection

Selecting an optimal airfoil is an important first step in determining flight characteristics and maximizing mission scores. Given the design criteria of maximizing aircraft cruise velocity and meeting the 100 ft takeoff distance requirement, it was determined that an ideal airfoil would have a high C_l/C_d ratio at cruise with sufficient lift for takeoff when fully encumbered during M2. Based on the typical Reynolds number calculated in the scoring sensitivity analysis model discussed in Section 3.2.2, airfoils were analyzed using XFOIL [2] at a Reynolds number estimate of 500,000. Because changes in theoretical design parameters were negligible with respect to Reynolds number, this was the only Reynolds number considered. Four airfoils were compared before selection: PSU 94-097, NACA 4415, NACA 2411, and Clark-Y. These airfoils were all chosen based on recommendations by the team's faculty advisor and analysis of previous winning competition reports. The polars for the chosen airfoils are shown in Figure 4.1.

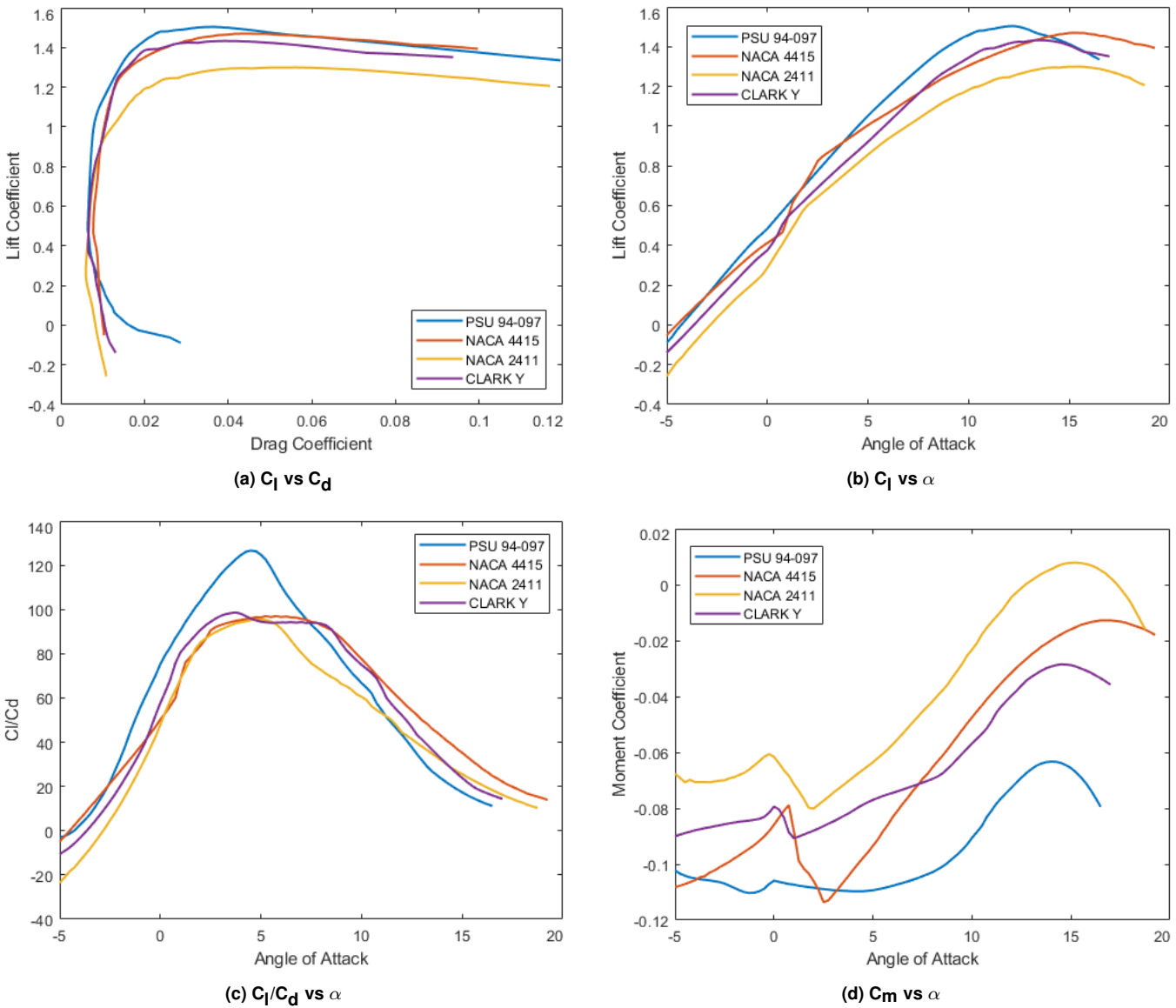


Figure 4.1: 2D airfoil coefficients

For the purpose of meeting the aforementioned criteria, Figure 4.1 clearly shows that the PSU 94-097 airfoil is the most

advantageous choice. This airfoil has the highest C_l/C_d ratio between about -2 and 7 degrees, which contains the typical range of cruise angles of attack. Furthermore, this airfoil's drag bucket extends the furthest in the positive lift coefficient direction, which allows for an incremental increase in C_l compared to the other airfoils without leading to a significant increase in drag. The airfoil also generally has the best lift coefficient at any given angle of attack, as shown in Figure 4.1(b). Lastly, the PSU 94-097 has the highest maximum lift coefficient, which will give the best takeoff performance as the aircraft will have a decreased takeoff distance at any given cargo weight. Therefore, the PSU 94-097 was deemed the best airfoil choice for achieving the stated design criteria.

4.2.2 Wing Sizing

With an optimal airfoil chosen, a trade study was performed to determine the wing sizing for Knightmobile Mk.1. For design simplicity and ease of manufacturing, it was decided that the initial wing would be rectangular rather than tapered. In sizing the wing, the main considerations were the planform area, wingspan, and chord length. Wing design criteria included sufficient lift generation and limited induced drag, with the added constraint of not compromising structural strength.

Based on analysis of aircraft parameters in previous competition reports, it was initially predicted that the aircraft would have a gross mass of roughly 10 pounds. Applying a factor of safety of 1.5, a maximum M2 gross mass for Mk.1 was estimated to be 15 pounds. Based on this gross mass and the 100 ft maximum takeoff distance requirement, a wing planform area of 616 in² was implemented, using a procedure similar to that discussed in Section 3.2.2.

The next consideration was the wingspan, which was chosen based on a goal of maximizing the aspect ratio. Aspect ratio has an inverse relationship with lift induced drag as shown by Equation 4; furthermore, increasing the aspect ratio increases the C_L/C_D ratio as shown in Figure 4.2.

$$C_{D_i} = \frac{C_L^2}{(\pi * e * AR)} \quad (4)$$

Maximizing the wingspan to chord length ratio of a rectangular wing also maximizes the aspect ratio, as demonstrated by Equation 5.

$$AR = \frac{b^2}{S} = \frac{b^2}{b * c} = \frac{b}{c} \quad (5)$$

Thus, it was decided to use the maximum allowable wingspan of 5 feet or 60 inches. However, due to concerns of overshooting the maximum wingspan outlined in the competition rules [1] during manufacturing, this was initially reduced to 56 inches.

Finally, a chord length of 11 inches and an aspect ratio of 5.22 were calculated by utilizing Equation 5. This chord length was considered to be greater than the estimated minimum chord length required for sufficient structural strength. Additionally, an aspect ratio of 5.22 falls within the recommended range of 5-8 for RC aircraft [3].

Although a tapered wing was not used on the first prototype in order to simplify design and manufacturing, research [4] was conducted on the effects of taper ratio on aerodynamic parameters (for use in later iterations of the aircraft). It was found that applying a taper ratio of less than 1 increases the Oswald Efficiency Factor (e) and thus decreases induced drag, as shown in Equation 4. The Oswald Efficiency Factor is equal to $\frac{1}{1+\delta}$, where δ is a function of the taper ratio and aspect ratio. The relationships between these variables were found in [4] and are plotted in Figure 4.3. It is clear that decreasing the value of δ increases the value of e , which corresponds to a decrease in induced drag. Based on the figure, therefore, the optimal taper ratio appears to be somewhere between 0.3 and 0.4 for any given aspect ratio. However, it was also noted that strong taper can lead to tip stall effects [5], so a factor of safety of 1.5 was considered when initially sizing a tapered wing.

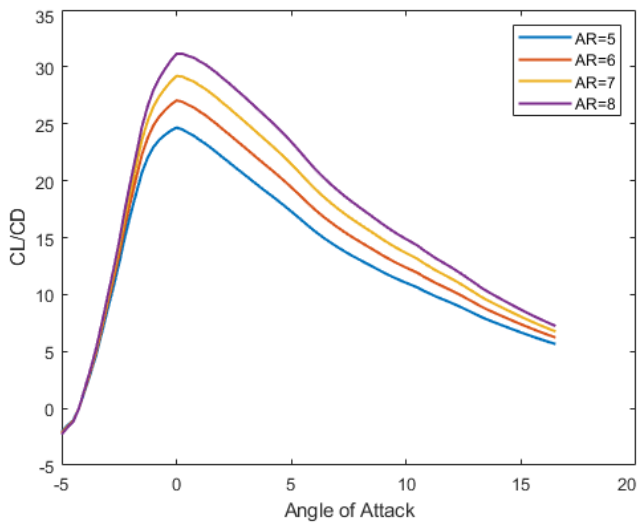


Figure 4.2: C_L/C_D vs. α

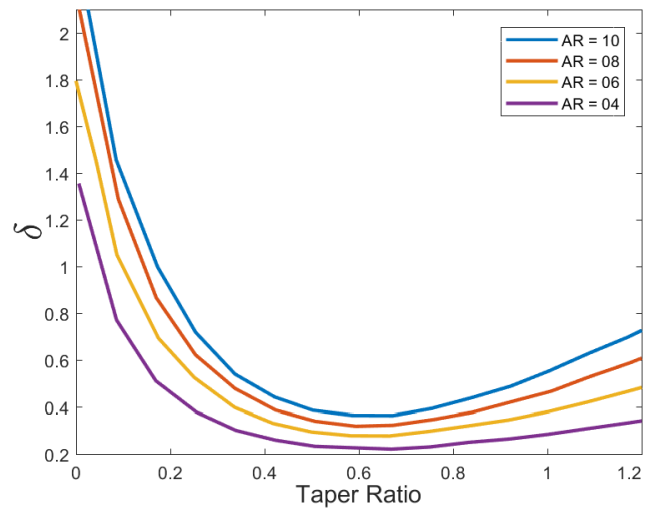


Figure 4.3: δ vs. taper ratio

4.2.3 Sensor Sizing

A trade study was performed to determine an ideal sensor size to maximize score. This study was conducted as an extension of the scoring sensitivity analysis outlined in Section 3.2. It was determined that overall competition score is maximized when focusing on increasing M3 score. Given a determined optimal sensor size configuration for M3, a resulting M2 score analysis was then performed in order to maximize total score. A finalized Mk.1 aircraft was used as a baseline for the sensor sizing study, and the initial propulsion package from Section 3.2.1 was used for analysis, along with the previously determined wing sizing results.

The sensor deployment and recovery mechanism plays an important role in determining practical constraints to mission performance. A telescoping rod design was previously chosen for the mechanism. It was assumed that structural strength degrades with length; similarly, an increase in mechanism length requires a longer fuselage for storage, which was considered impractical at a certain limit. Therefore, it was determined that the deployed length of the telescoping rods would be kept to a minimum. This required that the sensor length was kept minimal since the sensor deployment length must be 10 times the sensor length. A baseline lighting package was considered, and it was determined that the minimum required sensor diameter was 1.05 inches, leading to a minimum sensor length of 4.2 inches. This was increased to 4.25 inches for tolerance, requiring a sensor deployment length of 42.5 inches.

Given an assumed sensor length, the remaining parameters for consideration were sensor weight and number of laps completed in ten minutes. The following boundary conditions were determined based on the Mk.1 aircraft and initial propulsion package:

- The maximum power draw of the motor is 1200 W.
- The aircraft shall carry at least two 22.2v 2200 mAh LiPo batteries.
- A 15x8 APC propeller shall be used for assumptions based on pilot recommendation.
- The estimated Mk.1 empty weight, including batteries, is roughly 7.34 pounds.

Initial flight test data was compared alongside aerodynamic propeller solutions produced by Advanced Precision Composites (APC) [6]. The APC solutions were useful in determining velocity from power output. Power required for the motor was determined based on payload weight using Equation 6.

$$P_{\text{prop}} = TV = DV = \frac{1}{2} \rho V^3 S C_D = \left(\frac{2W^3}{\rho S} \right)^{1/2} \frac{C_D}{C_L^{3/2}} \quad (6)$$

The next significant factor was payload weight. From Equation 6, an upper boundary of 7.32 pounds of total payload weight was determined for the chosen motor based on its maximum allowable power draw. Total aircraft weight was then varied via sensor and battery weight alongside variations in cruise velocity (as a function of aircraft weight) over the ten minute flight time. The results of this study were analyzed to determine the best combination of sensor weight and battery weight.

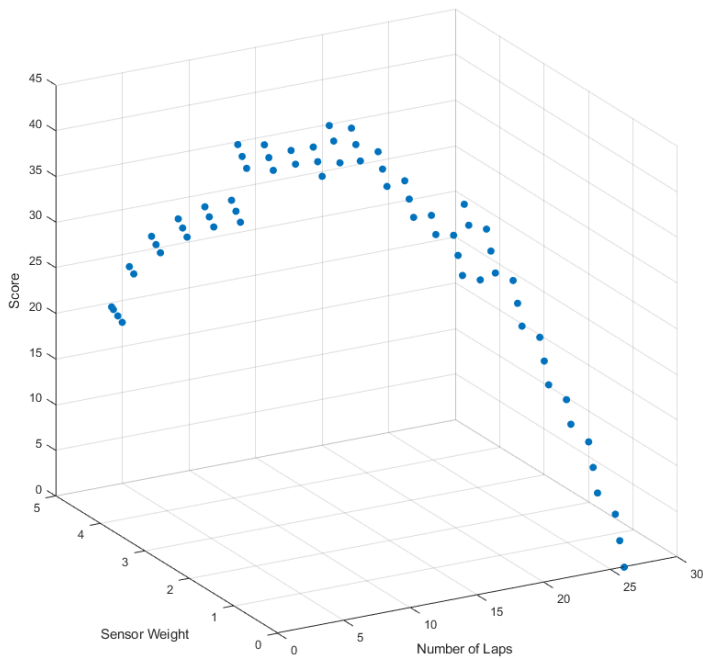


Figure 4.4: Sensor weight vs. number of laps

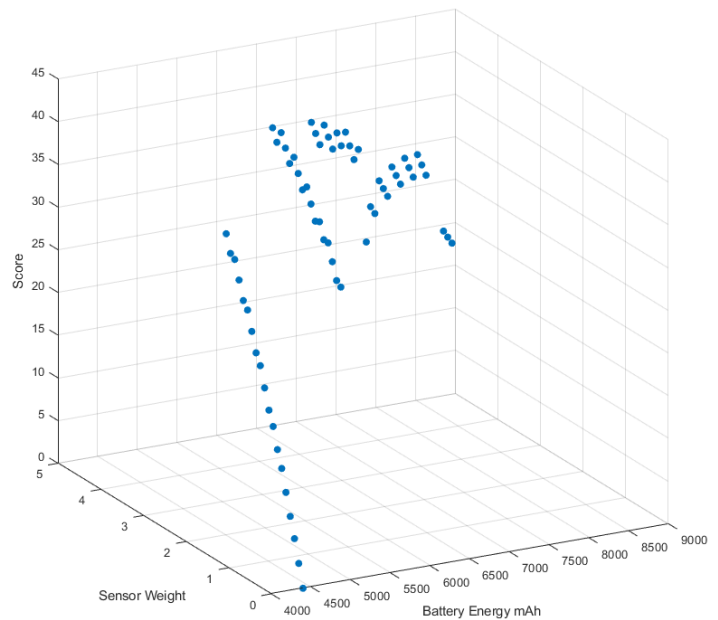


Figure 4.5: Sensor weight vs. battery energy

Figure 4.4 displays the variation of sensor weight with the number of laps flown. It can be seen that M3 score is optimized by a compromise between speed and sensor weight. The best combinations of sensor weight and battery energy to use to increase score are seen in Figure 4.5, which displays the variation of sensor weight with battery energy. These results show that using any more than 5650 mAh of battery energy does not increase M3 score. The best performing M3 configurations, excluding sensor weights requiring more than 5650mAh battery energy, were considered for M2 analysis. The two highest-scoring sensor weights for M3 according to this analysis were 1.8 pounds with 4400 mAh of battery energy and 2.84 pounds with 5650 mAh of battery energy. While these configurations contribute to the best M3 score, they do not necessarily contribute to the highest total competition score, so further analysis was conducted to find an optimal configuration for maximizing total score.

The score for M2 is a function of the number of sensors carried and flight time for 3 laps. The results of the M3 analysis were analyzed to determine the sensor weight that would best contribute to the combined M2 and M3 score. Given the estimated maximum payload weight of 7.32 pounds, a data matrix of the best performing M3 configurations was created, varying sensor weights and number of sensors. Cruise velocity was also calculated as a function of payload weight, leading to a decrease in velocity for any increase in payload.

From further analysis, the best performing sensor weight was 1.4 pounds. As noted in Section 3.2.3, this analysis was based on developing and observing general trends toward an optimal solution. This sensor weight, while advantageous for the current aircraft design, may still be improved upon in future design iterations. The calculated 1.4 pound sensor corresponded to carrying 3 shipping containers and flying all three laps in 110 seconds. This combination also corresponded to the top total score; given these results, the goal sensor weight was finalized at 1.4 pounds. The predicted cruise velocity for M2 was therefore 41 mph while carrying 3 sensors. The predicted cruise velocity for M3 was 54.6 mph while containing 4400 mAh battery energy and flying 21 laps.

4.2.4 Propulsion Selection

The propulsion selection process began with estimating aircraft drag. Table 4.1 presents a theoretical drag breakdown which was conducted with the following assumptions: a cruise speed of around 54.6 mph, Mk.1 wing and tail geometries, air density for the elevation of Tucson, AZ, and a preliminary towed sensor system. M3 was selected as the most demanding drag condition for the propulsion selection process. An XFLR5 [7] Vortex Lattice Method (VLM) analysis was utilized for study of the Mk.1 wing and tail with the purpose of computing predicted drag polars. ANSYS Fluent [8] was used for obtaining drag coefficients for the fuselage and towed sensor system.

Table 4.1: Drag breakdown (M3 cruise conditions)

Drag Components (Reference Wing Area)	CD Total (profile drag + induced)
Mk.1 Wing and Tail	0.016
Mk.1 Fuselage	0.01834
Towed Sensor System	0.1388

From the predicted drag coefficient results, drag force was calculated using Equation 7.

$$F_D = \frac{1}{2} \rho v^2 C_D S \quad (7)$$

The drag force was computed for each 10 mph flight speed increment as calculated in XFLR5 and plotted in Figures 4.6 and 4.7.

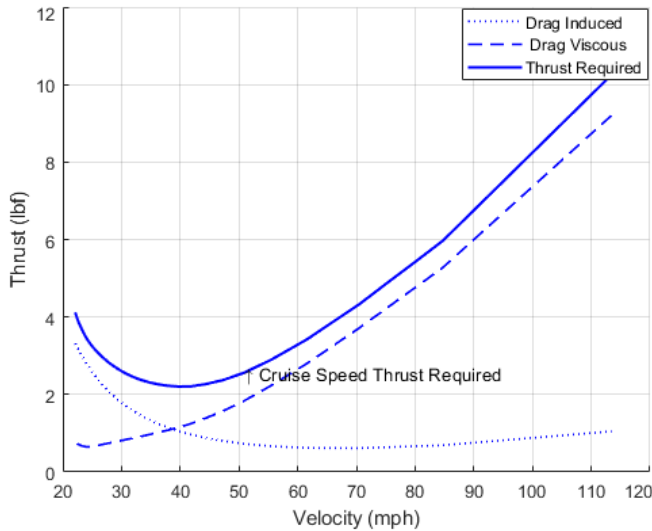


Figure 4.6: Thrust required vs. flight speed

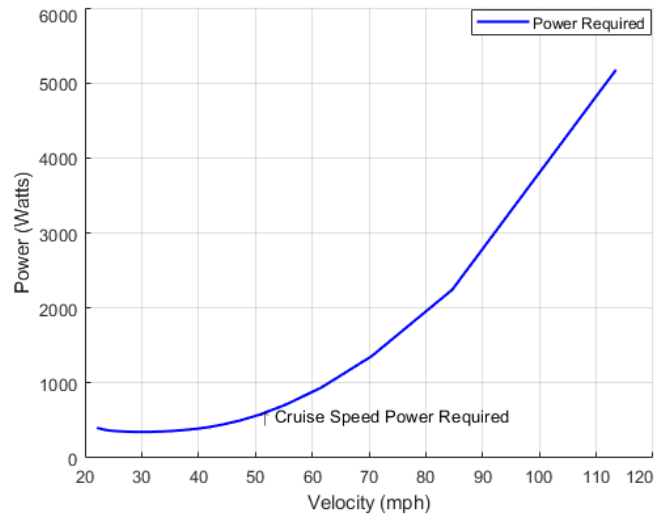


Figure 4.7: Power required vs. flight speed

The calculated drag force was used to drive propulsion selection via power required using Equation 8.

$$P_{\text{Required}} = F_D * v \quad (8)$$

The motor and battery selection process began with the theoretical thrust and power required set by the chosen cruise velocity of 54.6 mph, indicated by an arrow in Figures 4.6 and 4.7. The thrust and power required values were roughly 3 lbf and 600 W, respectively. Tables 4.2 and 4.3 demonstrate a short list of motors and batteries.

Table 4.2: Motor selection short list

Motor Name	Kv Rating	Max Current (Amps)	Max Power (Watts)	Mass (grams)
DYS D3548-04	1100	70	911	156
E-flite Power 32	770	60	800	233
Scorpion SII-4025	520	100	2000	389
E-flite Power 60	470	80	1200	380
Cheetah A4130-8	380	60	1500	420
E-flite Power 160	245	80	2700	675

Table 4.3: Battery selection short list

Battery Name	Cells	Voltage (Volts)	Capacity (mAh)	Discharge C	Watt-Hours	Mass (grams)
Gens Ace	3	11.1	2200	25	24.4	170
Ovonic	3	11.1	8000	50	88.8	430
Floueron	3	11.1	8000	40	88.8	540
HRB	4	14.8	5000	50	74	500
GForce	5	18.5	4000	30	74	450
Gens Ace	6	22.2	2200	45	48.8	370

After an iterative process of selecting motors and batteries given a flight time constraint of at least 10 minutes for M3, the Scorpion SII-4025 and the Gens Ace 6s were chosen as the desired motor and battery. Previously, the E-flite Power 60 and a 6s battery were chosen in the conceptual design process and utilized in Mk.1 due to material availability. The Scorpion SII-4025 motor proved to be more efficient compared to the Power 60 with higher threshold limits in current and power, and a higher Kv rating with negligible weight differences. The previously chosen 6s battery proved to still be the best option for the design. The 2000 W maximum power of the selected motor is more than sufficient to meet the required cruise power of the design with a current draw of 27 A, calculated using Equation 9, at 600 W with a 6s battery. With a known flight time of 10 minutes and calculated current draw, the theoretical required battery capacity for M3 was calculated to be around 4000 mAh to 4500 mAh using Equation 10 and 99.9 watt-hours using Equation 11. This can be accomplished with two 2200 mAh batteries connected in parallel, resulting in an energy capacity within the 200 watt-hour limit.

$$\text{Watt-Hours} = \frac{\text{Current(mAh)} * \text{Voltage(V)}}{1000} \quad (9)$$

$$\text{Current Draw} = \frac{\text{Wattage Rating}}{\text{Voltage}} \quad (10)$$

$$\text{Battery Capacity} = \text{Flight Time} * \text{Current Draw} \quad (11)$$

Using the above drag results and selected motor and battery combination as boundary conditions, a numerical iterative model was developed based on aerodynamic propeller solutions to converge on an optimal propeller. The results of this analysis are shown in Figures 4.8 and 4.9.

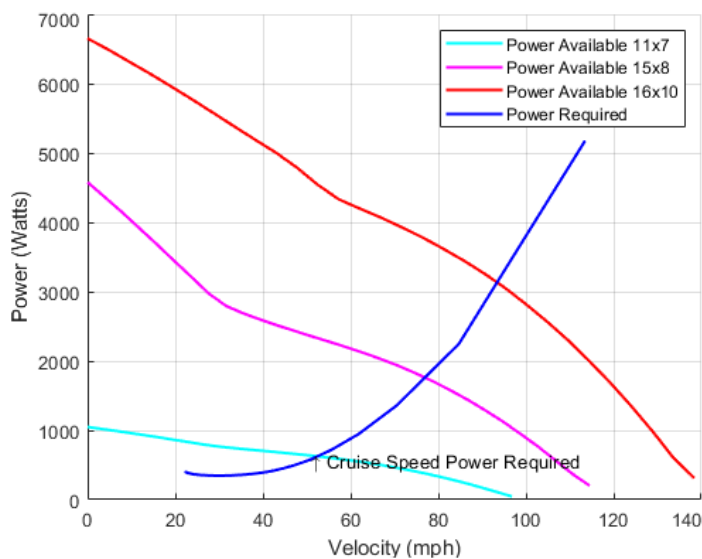


Figure 4.8: Power variation of propellers

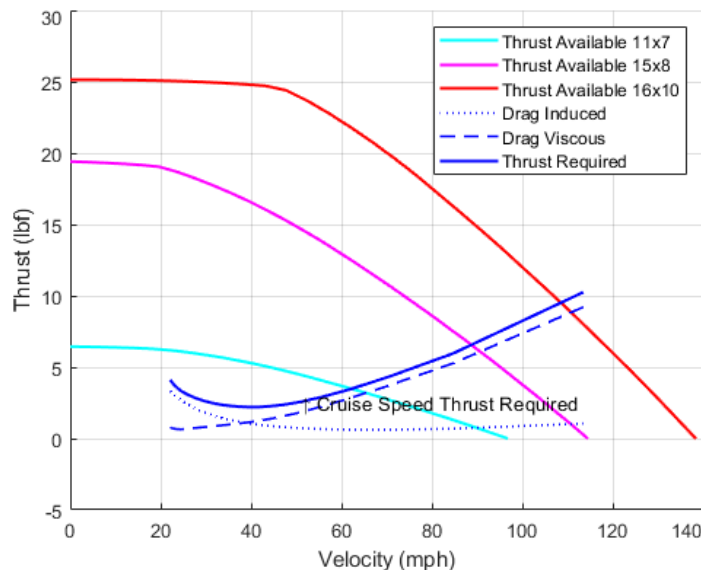


Figure 4.9: Thrust variation of propellers

The theoretical RPM calculated with the selected package was 11,544 as shown by Equation 12.

$$\text{RPM} = \text{Voltage} * \text{Motor Kv Rating} \quad (12)$$

Table 4.4 shows a short list of propellers for selection.

Table 4.4: Propeller selection short list

Diameter (in)	Pitch (in)	Cruise Propeller Efficiency (11000 RPM)
11	7	0.732
12	5.5	0.7528
14	8.5	0.6332
15	8	0.6714
16	10	0.5438

The largest considered propeller affords a higher maximum power output, but is less efficient at the chosen cruise velocity. The smallest considered propeller is more efficient than the largest propeller at the chosen cruise velocity, but cannot meet the thrust and power required. The APC 15x8 electric propeller was therefore chosen as the most efficient choice for meeting M3 cruise conditions.

4.3 Aerodynamic and Stability Parameters

With the initial prototype Knightmobile Mk.1 sized, analysis of predicted aircraft performance began alongside construction and experimental testing of multiple aircraft iterations. This analysis was performed to improve upon the preliminary aircraft sizing and drive it toward a final, optimal design, taking into account the results of the initial model described in Section 3.2.2 as well as experimental data to make predictions of eventual performance. Mk.1 was the first prototype in the design process, and after experimental testing was conducted, longitudinal static stability issues were discovered. To address this, Mk.2 was created to introduce larger empenage sizing, thereby increasing the tail volume ratio according to Equation 13, where l_t represents length from tail lift center to the aircraft CG, S_t represents horizontal tail area, c represents wing chord and S represents wing area.

$$V_H = \frac{l_t S_t}{c S} \quad (13)$$

Mk.3 was intended to be the final design; therefore, the transition from Mk.2 to Mk.3 involved a larger number of changes. Mk.3 introduced a tapered wing, a structurally efficient fuselage, and similar empennage sizing to Mk.2.

4.3.1 Lifting Surface Analysis

An analysis was also conducted using XFLR5 in order to analyze the lifting surfaces of each iteration. Table 4.5 shows key geometric differences between the lifting surfaces of each aircraft. Key parameters observed were the horizontal tail volume ratio and wing area differences between iterations. Mk.2 and Mk.3 were given larger empennage sizing relative to Mk.1. A larger wing area was chosen for Mk.3 to decrease wing loading, lower stall velocity, and increase cargo capability. The wing was also tapered for the purpose of improving efficiency as described in Section 4.2.2 while the tail volume remained at an intermediate value between those of the previous iterations.

Table 4.5: Aerodynamic parameters per iteration

Iteration #	Wing Span (in)	MAC (in)	Wing Area (in ²)	Aspect Ratio	Elevator Lever Arm (in)	Fin Area (in ²)	Horizontal Tail Volume Ratio
Mk.1	56	11.024	617.32	5.08	31.56	44.71	0.61
Mk.2	56	11.024	617.32	5.08	31.67	100.09	0.98
Mk.3	59	11.44	679.15	5.221	27.13	103.35	0.85

Figure 4.10 demonstrates key differences in the lift to drag ratio under an M2 cruise condition analysis among Mk.1, Mk.2, and Mk.3.

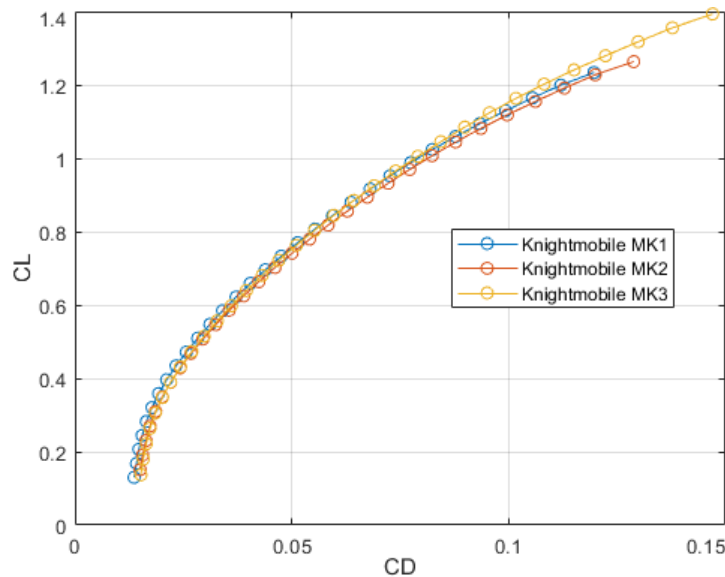


Figure 4.10: C_L vs. C_D M2 cruise comparison

The drag computed by the XFLR5 does not account for fuselage-wing interaction or drag from the payload; however, from the trends observed it can reasonably be inferred that Mk.3 generates more lift at higher drag coefficients. Given this data and the previous trade studies, the wing and tail sizing was converged toward the final, detailed design developed to successfully complete all missions with an optimized score.

The wing, horizontal stabilizer and vertical stabilizer were modeled and analyzed using Athena Vortex Lattice (AVL) [9]. The Vortex Lattice Method (VLM) models lifting surfaces as thin sheets, neglecting viscosity, and calculates lift and induced drag by simulating flow around the aircraft. Static and dynamic stability can also be analyzed using this method, and AVL can use a slender body model for the inclusion of a fuselage. For the purposes of this project, the determined wing sizing was entered into AVL, along with the resulting stabilizer sizing and control surfaces. The fuselage shape was estimated and modeled using the area of cross-sections along its length. Figure 4.11 shows a model of the aircraft in AVL, along with a C_l vs.

span plot of the lifting surfaces (simulated for M2 cruise). An elevator deflection of -2.7 (degrees) was found for this condition, along with a spanwise efficiency of 0.87.

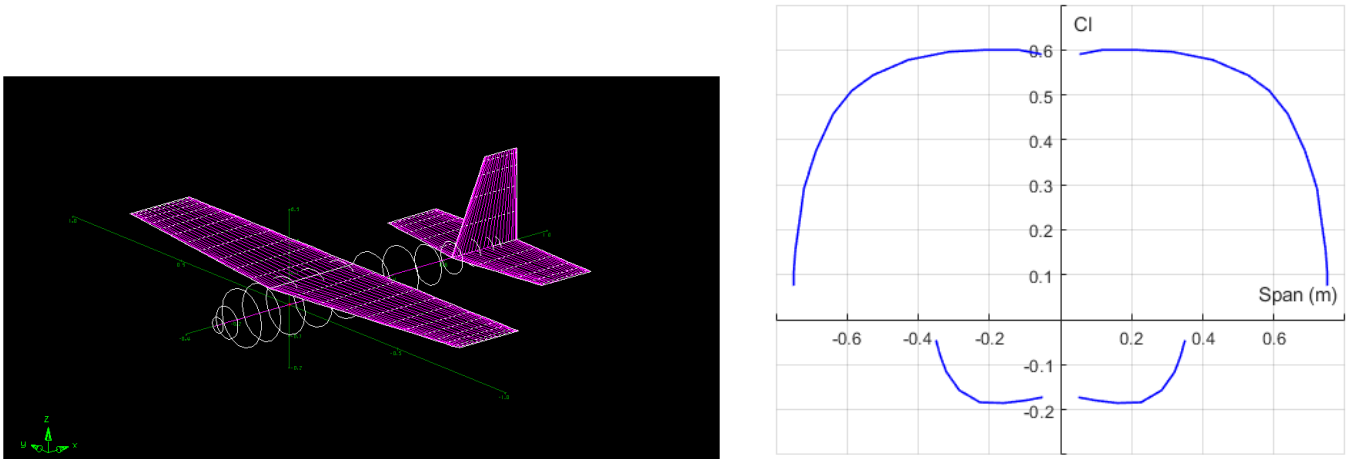


Figure 4.11: AVL model of the aircraft (left) and C_l vs. span plot of the aircraft at M2 cruise condition (right)

4.3.2 Static Stability Analysis

Static stability was also analyzed using AVL. Flight testing of the initial prototype revealed instabilities that required analysis and correction; test data and pilot feedback showed yaw instability and decreased elevator control authority during flight. This was attributed in part to downwash effects due to the placement of the tail in the same horizontal plane as the wing, as well as to insufficient sizing of the stabilizer surfaces for control authority and trim. For the second and third iterations of the aircraft, these issues were addressed by increasing the horizontal tail volume ratio, increasing the relative sizes of both the elevator and rudder, and offsetting the tail from the horizontal plane of the wing. The stability derivatives and trim conditions shown in Table 4.6 were evaluated for the third aircraft iteration with the highest projected cargo weight and lowest velocity configuration, which was determined to be the most strenuous trim condition. From the static stability parameters shown, it was determined that the Mk.3 aircraft is longitudinally and laterally statically stable according to the conventions indicated in Yechout's Introduction to Aircraft Flight Mechanics [10].

Table 4.6: Stability parameters at M2 cruise

	Parameter	Trim Results
M2 Cruise Conditional Parameters	α	2.658°
	β	0.0°
	C_L	0.481
	δ_e	-3.488°
Stability Derivatives	$C_{m,\alpha}$	-2.139 (rad ⁻¹)
	$C_{l,\beta}$	-0.082 (rad ⁻¹)
	$C_{n,\beta}$	0.101 (rad ⁻¹)
Primary Control Derivatives	C_{m,δ_e}	-0.041 (rad ⁻¹)
	C_{l,δ_a}	0.007 (rad ⁻¹)
	C_{n,δ_r}	0.002 (rad ⁻¹)
Damping Derivatives	$C_{l,p}$	-0.416 (rad ⁻¹)
	$C_{m,q}$	-17.605 (rad ⁻¹)
	$C_{n,r}$	-0.156 (rad ⁻¹)

4.3.3 Dynamic Stability Analysis

AVL was used to analyze the aircraft's dynamic stability modes for each flight mission. Figure 4.12 shows a root locus plot with the stability modes plotted for each mission, including takeoff and cruise conditions.

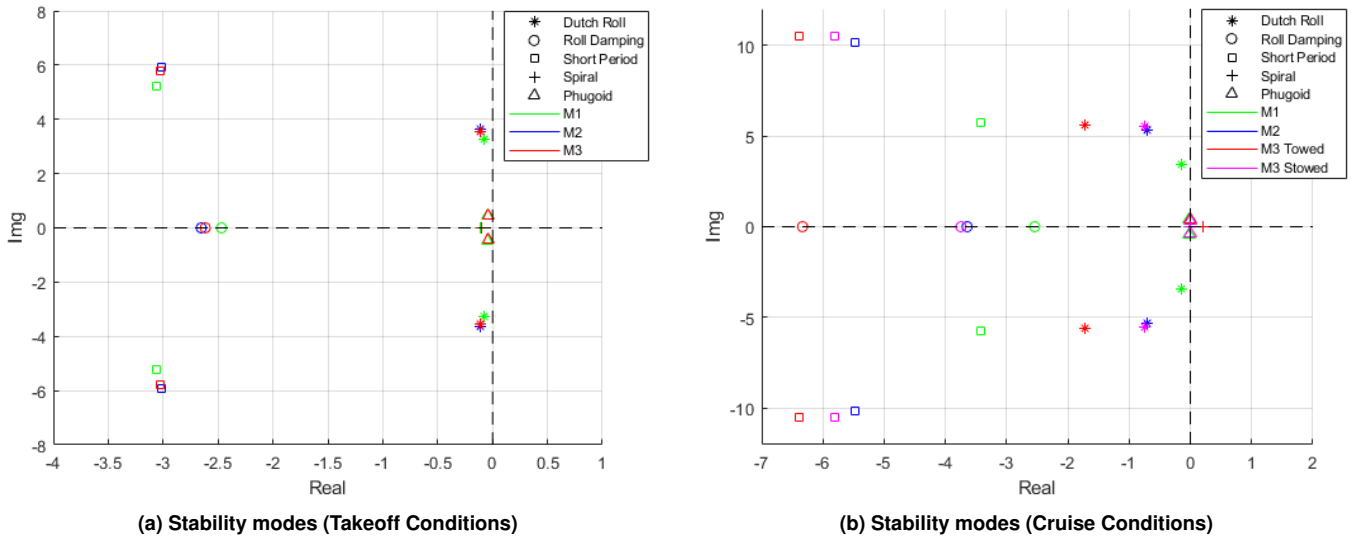


Figure 4.12: Root Locus plots

The deployment and recovery mechanism to be used for M3 is planned to be mounted at the CG of the aircraft. As such, stability analysis has determined the projected change in stability due to the mechanism being deployed to be negligible, and therefore the cruise conditions analyzed were assumed to be before deployment. For actual flight conditions, however, it was predicted that the decrease in stability mode damping characteristics due to sensor deployment will not be negligible. The stability modes were analyzed with respect to the MIL-F-8785C flying qualities criteria for a Class 2 (Medium weight, low-to-medium maneuverability) aircraft [11]. Mode stability was also considered, and is determined by a mode's position to the left of the imaginary axis on the root locus plot (having a negative real part of the corresponding eigenvalue(s)). Every mode was stable upon analysis for both cruise and takeoff, except for spiral mode under cruise conditions. The mode characteristics are shown in Figures 4.7, 4.8, and 4.9, represented as takeoff value / cruise value / MIL-F-8785C criteria. Values that meet the MIL-F-8785C standards are highlighted green, and values that fail to meet the standards are shown in red.

Table 4.7: M1 stability modes parameters (takeoff conditions/cruise conditions)

Stability Mode	ζ	ω_n (rad/s)	$\zeta\omega_n$ (rad/s)	τ (s)
Roll	-	-	2.470 / 2.543	0.405 / 0.393 / < 1.4
Spiral	-	-	0.107 / 0.022 / > 0	9.346 / 46.034
Dutch Roll	0.023 / 0.045 / > 0.08	3.276 / 3.408 / > 0.4	0.074 / 0.152 / > 0.15	13.514 / 6.579
Short Period	0.505 / 0.513 / > 0.35	6.070 / 6.677	3.064 / 3.422	0.326 / 0.292
Phugoid	0.092 / 0.051 / > 0.04	0.476 / 0.416	0.044 / 0.021	22.727 / 47.619

Table 4.8: M2 stability modes parameters (takeoff conditions/cruise conditions)

Stability Mode	ζ	ω_n (rad/s)	$\zeta\omega_n$ (rad/s)	τ (s)
Roll	-	-	2.653 / 3.646	0.377 / 0.274 / < 1.4
Spiral	-	-	0.101 / -0.00638 / > 0	9.901 / -156.740
Dutch Roll	0.031 / 0.129 / > 0.08	3.626 / 5.396 / > 0.4	0.114 / 0.697 / > 0.15	8.772 / 1.435
Short Period	0.453 / 0.474 / > 0.35	6.656 / 11.526	3.014 / 5.467	0.332 / 0.183
Phugoid	0.094 / 0.0056 / > 0.04	0.435 / 0.346	0.041 / 0.00194	24.390 / 515.464

Table 4.9: M3 stability modes parameters (takeoff conditions/cruise conditions)

Stability Mode	ζ	ω_n (rad/s)	$\zeta\omega_n$ (rad/s)	τ (s)
Roll	-	-	2.616 / 3.747	0.382 / 0.267 / < 1.4
Spiral	-	-	0.102 / -0.00782 / > 0	9.804 / -127.877
Dutch Roll	0.029 / 0.134 / > 0.08	3.556 / 5.568 / > 0.4	0.106 / 0.747 / > 0.15	9.433 / 1.339
Short Period	0.462 / 0.485 / > 0.35	6.539 / 11.970	3.021 / 5.804	0.331 / 0.172
Phugoid	0.093 / 0.0044 / > 0.04	0.443 / 0.351	0.041 / 0.00155	24.390 / 645.161

The spiral mode for M2 and M3 during cruise was unstable and therefore failed to meet the MIL-F-8785C criteria; however, it is mentioned that an unstable spiral mode with a time to double of greater than 20 seconds can still meet level 1 requirements [11]. The spiral mode times to double for M2 and M3 during cruise are 108 s and 88 s, respectively, so these values were considered satisfactory for the scope of this competition.

The dutch roll characteristics of all missions during takeoff also failed to meet MIL-F-8785C criteria, leading to consideration of improving directional stability or relaxing lateral stability; however, flight testing and pilot appraisal of the aircraft's performance during takeoff conditions revealed such changes to be unnecessary. Similarly, the long period of the phugoid mode (which failed to meet the standards for M2 cruise), coupled with pilot evaluation of aircraft stability during cruise conditions, deemed the small phugoid damping ratio insignificant given sufficient manual control by the pilot.

4.4 Mission Performance Prediction

The mission performance of Knightmobile Mk.3 was predicted prior to manufacturing and compiled in Table 4.10.

Table 4.10: Aircraft mission performance prediction

	Mission 1	Mission 2	Mission 3
Cruise Velocity (mph)	40	41	54.6
Flight Duration (sec)	112	110	600
Payload Weight (lbs)	0	6.09	2.9
Gross Weight (lbs)	6.316	12.406	10.032
Takeoff Distance (ft)	4.6369	27.7258	15.488
Number of Shipping Containers	N / A	3	N/A
Sensor Length (in)	N / A	4.25	4.25
Sensor Mass (lbs)	N / A	1.4	1.4
Number of Laps	3	3	21
Absolute Mission Score	1	0.0272 containers / sec	124.95 lbs * inches * laps
Absolute Best Team Theoretical Score	1	0.2857 containers / sec	346.752 lbs * inches * laps
Normalized Mission Score	1	1.0952	2.36

The mission score predictions were an amalgamation of previous analyses and models. The cruise velocities, flight durations, numbers of laps, sensor weight, and M2 number of shipping containers were found in Section 4.2.3. The payload weights were found as a function of the sensor and predicted mechanism weights. The absolute and normalized mission scores were found using the scoring formulas outlined in Section 3.1. The takeoff distance values were found using a method similar to the one used in the scoring sensitivity analysis model from Section 3.2. Finally, that initial model was also used to provide the absolute best team theoretical scores.

One uncertainty involved in the predictions was the actual flight distance of the flight course, likely leading to an overestimate of the number of laps flown in M3 and an underestimate of the M2 flight duration. It is difficult to predict pilot error and the turn radius of the aircraft. The sensor mass used was also an ideal value that may be unattainable for a sensor of only 4.25 inches in length due to material property limitations. The predicted takeoff distances may be slightly underestimated due to possible inaccurate predictions of the rolling friction coefficient and takeoff drag coefficient. However, the takeoff distance estimates have a large margin for error and are considered within safe bounds. The absolute best team theoretical scores are likely unattainable in practice due to real world constraints since they are based on a true optimal solution with little margin for error. Therefore, the normalized mission scores were likely underestimated. Despite the aforementioned uncertainties, the estimates of absolute mission score and cruise velocity are considered only a slight overestimate, if not fully accurate. Even

if the predictions somewhat overestimate the true mission performance results, they serve as an optimal solution to guide the continuing design and iteration process.

5. Detail Design

With preliminary modeling and analysis complete, detailed testing and improvements began. Key design parameters and subsystems were finalized, taking into account small-scale improvements that could be made. Structural strength, weight optimization, and drag minimization were prioritized in order to produce the most competitive mission-ready aircraft with sub-components that would perform well during the competition.

5.1 Dimensional Parameters

Table 5.1 shows the dimensional parameters of the final design, Knightmobile Mk.3.

Table 5.1: Final aircraft design dimensions

Fuselage Parameters		Wing Parameters	
Length	45.79 in	Airfoil	PSU94-097
Width	6 in	Root Chord	13.6 in
Height	7 in	Tip Chord	9 in
Nose Structure Length	2.79 in	MAC	11.44 in
Cargo Structure Length	21 in	Wing Span	59 in
Tapered Section Length	22 in	Area	679.15 in ²
Height Taper Ratio	0.1428	Taper Ratio	0.6617
Width Taper Ratio	0.4243	L.E location	5.55
Horizontal Tail Parameters		Vertical Tail Parameters	
Airfoil	NACA0012	Airfoil	None
Root Chord	10 in	Root Chord	10.5 in
Tip Chord	7 in	Tip Chord	5 in
Span	27.5 in	Height	12.65 in
Taper Ratio	0.7	Taper Ratio	0.476
L.E location	38.57	L.E location	40.04

5.2 Structural Characteristics

The aircraft was designed to maximize overall cargo space in the fuselage while minimizing weight without compromising structural integrity. The aircraft consists primarily of plywood and balsa composites to simplify the manufacturing process and reduce construction time for each iteration. The wings and stabilizers were given a modular design to allow for efficient replacement when necessary. Finite element analysis was conducted on the fuselage of the aircraft in order to predict potential failure points during flight performances and landing. The analysis, which fixed the connection points between the wings and the fuselage, simulated a 6 lb load caused by lift force from the wings, a 1 lb force on the empennage caused by lift from the horizontal stabilizer, and a 6.2 lbf*in counterclockwise torque on the motor mount caused by the propeller. Figure 5.1 shows that the most likely points of failure are the balsa formers aft of the wings. These formers were constructed from balsa; as such, these potential failure points could be mitigated in the future by changing the material to plywood, which has a higher elastic modulus. On the other hand, the main cargo hold was insignificantly affected by the stress. This could be revisited in a future iteration to redistribute unnecessary structure to higher-stress locations on the aircraft. This would increase the structural strength of the overall aircraft without additional weight.

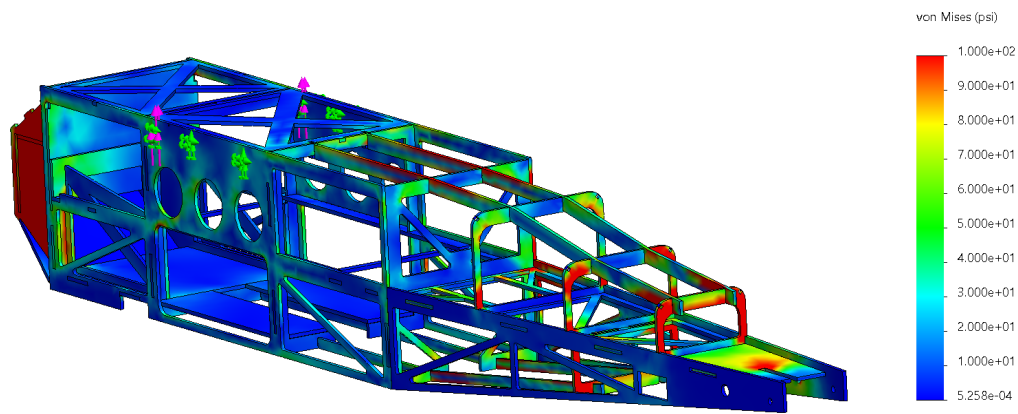


Figure 5.1: Fuselage structure stress analysis

5.3 Systems Integration and Architecture

The key systems and subsystems of the Knightmobile Mk.3 are described herein, including their integration into the overall design. These systems and subsystems include the fuselage, wing, tail, sensor, mechanism, shipping container, and propulsion system.

5.3.1 Fuselage

The bulk of the aircraft's fuselage was constructed from plywood, while a few non-load bearing panels and strips were made with balsa. These materials were chosen for their relatively high strength to weight ratio, ease of manufacturing, and cost effectiveness. The material thickness of plywood and balsa was 1/8 in.

The main structural layout of the fuselage consists of two side panels encompassing the cargo section of the aircraft, two side panels and one horizontal panel that connects the cargo section to the tapered section of the aircraft. These parts were constructed out of plywood and had various cutouts strategically placed to maximize strength and minimize weight. Figure 5.2 shows the locations of the panels (highlighted in yellow). Four panels aft of the wing act as formers to fit the overall shape of the aircraft itself. They were constructed from balsa to reduce weight, as they were not designed to withstand as much stress as other fuselage sections. In the main cargo section of the aircraft, the formers were also designed to fit mission-specific needs, including proper placement of electronics, payloads and mechanism (in stowed configuration) in M2, and mechanism with deployable sensor in M3.

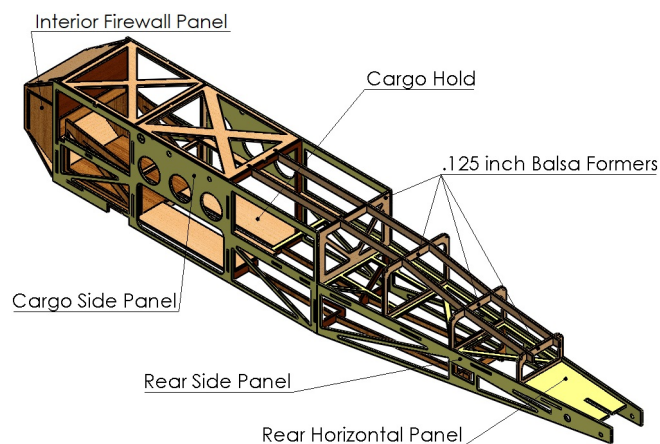


Figure 5.2: Knightmobile Mk.3 fuselage structure

5.3.2 Wing

Detailed wing design focused on maximizing lift without adding excess structural weight. The design has been modified several times to account for structural weaknesses revealed during testing. One such weakness was the wing's lack of rigidity under high load cases, leading to lateral instability during flight. The current iteration has a carbon fiber forward spar that passes through 1/3 of the wingspan and is used both for preventing in-flight flexing of this kind and for mounting the wing to the fuselage. An aft spar, also carbon fiber, passes through the entire wingspan; the spar's primary purpose is additional structure, but it also acts as a second mounting point for the wing. In order to increase takeoff lift and thus reduce takeoff distance, the wing's full-length ailerons double as flaps during ground roll. A CAD model of the final wing design is seen in Figure 5.3.

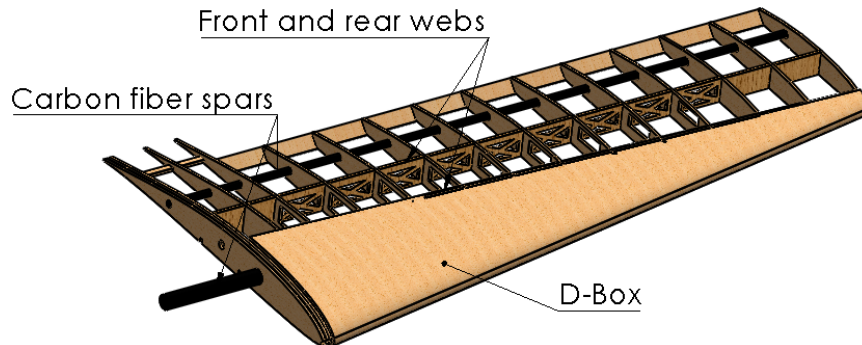


Figure 5.3: Left wing CAD model

5.3.3 Tail

One of the main goals of design was to limit structural weight aft of the wing to maintain optimal aerodynamic characteristics. A symmetrical airfoil shape was chosen for the horizontal stabilizer, decreasing the need for excess structure in the fuselage to integrate the horizontal stabilizer section, thereby decreasing weight in the fuselage without sacrificing structural integrity. The horizontal stabilizer consisted of eight balsa ribs connected through two main carbon fiber rods. These rods helped hold the shape of the tail and also connected the fuselage and vertical stabilizers to the horizontal stabilizers. Meanwhile, a thin flat plate of was used for the vertical stabilizer, allowing for a simple sliding implementation into the fuselage. Figure 5.4 displays an exploded view of the tail structure.

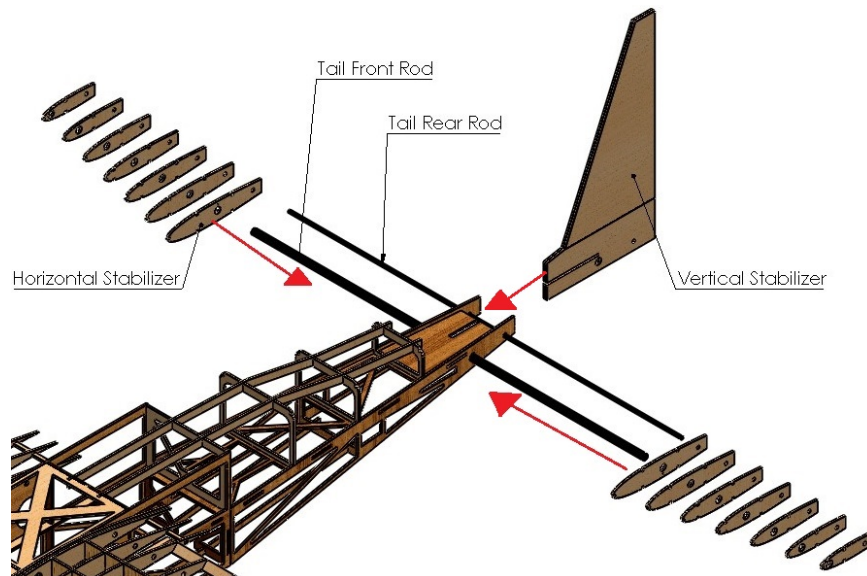


Figure 5.4: Empennage exploded view

5.3.4 Sensor

The sensor body, seen in Figure 5.5(a), was fabricated from Acrylonitrile Butadiene Styrene (ABS) plastic at 100% infill in order to maximize body weight while keeping ease of manufacturing high and sensor diameter and length minimal. The size of the electronics to be placed inside the sensor forced the pipe to remain fairly hollow, but a lip was designed at the bottom of the sensor as a platform for the battery and microcontroller. The sensor was constructed with recesses included for the sensor lights, which were glued to the body in 4 locations, with two on either side. Aerodynamic truncated ellipsoid caps were glued on the forward and aft sides of the sensor to reduce drag and add mass. It was decided that both caps would be constructed from lead that was melted down and molded into the cap shapes. An extrusion was also included at the top of the sensor as an attachment point between the sensor and the telescoping rods. The sensor light configuration consists of 4 LED lights (two forward, green lights and two aft, red lights) across the bottom face of the sensor fuselage body. The lights were programmed in a rectangular clockwise rotation pattern where each light turns on and off individually through inputs from the transmitter. A 350mAh single cell LiPo battery was chosen to power the lights and, connected to a programmable light controller board, was stowed inside the sensor as seen in Figure 5.5(b). The controller board has a single wire (ground and signal only) that runs along the interior of the telescoping rod and is connected directly to the aircraft's main receiver. This allows for the lights to be controlled by "physical connection to the aircraft" and hence controlled by the pilot through the transmitter.

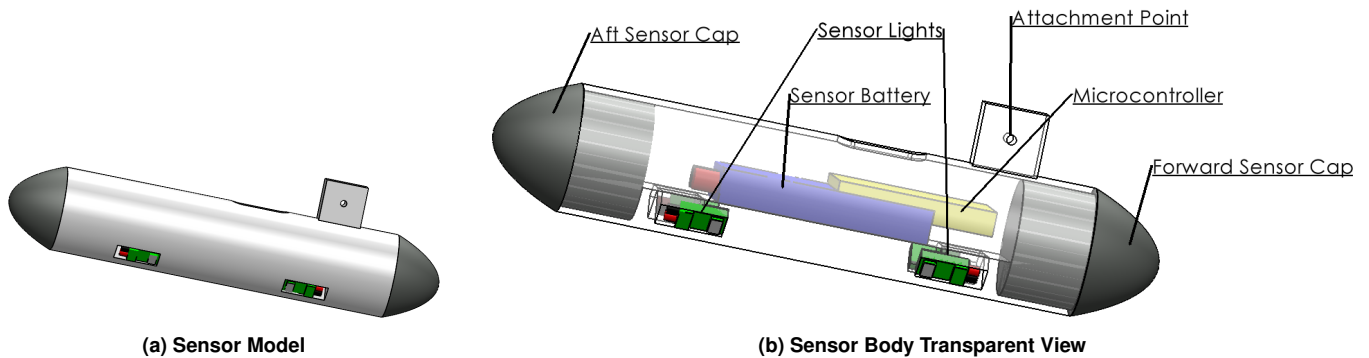


Figure 5.5: Sensor CAD model (left) and sensor component view (right)

5.3.5 Deployment and Recovery Mechanism

The deployment and recovery mechanism was constructed from aluminum square stock tubes. A telescoping rod design had been selected for enhanced stability with low risk of failure, so the mechanism was designed to consist of three long rods of varying outer wall lengths as seen in Figure 5.6, with attachments made from ABS to stop the tubes from overextending. An attachment was also developed for temporary connection between the sensor and the telescoping rods, in which a bolt would be inserted to fasten the two together. Holes were cut in the base rod in order to attach it to a servo, which would swing the rod assembly and sensor downward 90 degrees through a permanent slit in the bottom of the fuselage for deployment. Cuts were also made along the length of each rod to decrease the weight of the telescoping rod assembly, and covered with thin tape to prevent a large increase in drag. The mechanism was designed to contain a continuous rotation servo that controls the rate of lowering or raising the telescoping rod system via a Kevlar wire that was braided with the sensor electronics wires and wrapped around a spool. The deployment process therefore followed this pattern:

- A small hatch door under the sensor opens
- The base servo begins rotating the rod assembly through the fuselage
- The continuous servo unspools the wires at a controlled rate until full deployment

Recovery would then occur in the reverse pattern, with the rods collapsed before rotation of the assembly back inside the fuselage. As seen in Figure 5.6(a), the mechanism is 44.3 inches long, and was designed to tow the sensor 43 inches away

from the aircraft when accounting for clearance within the fuselage. This satisfies the minimum towing distance of 10 times the sensor length, which was 42.5 inches for the constructed sensor.

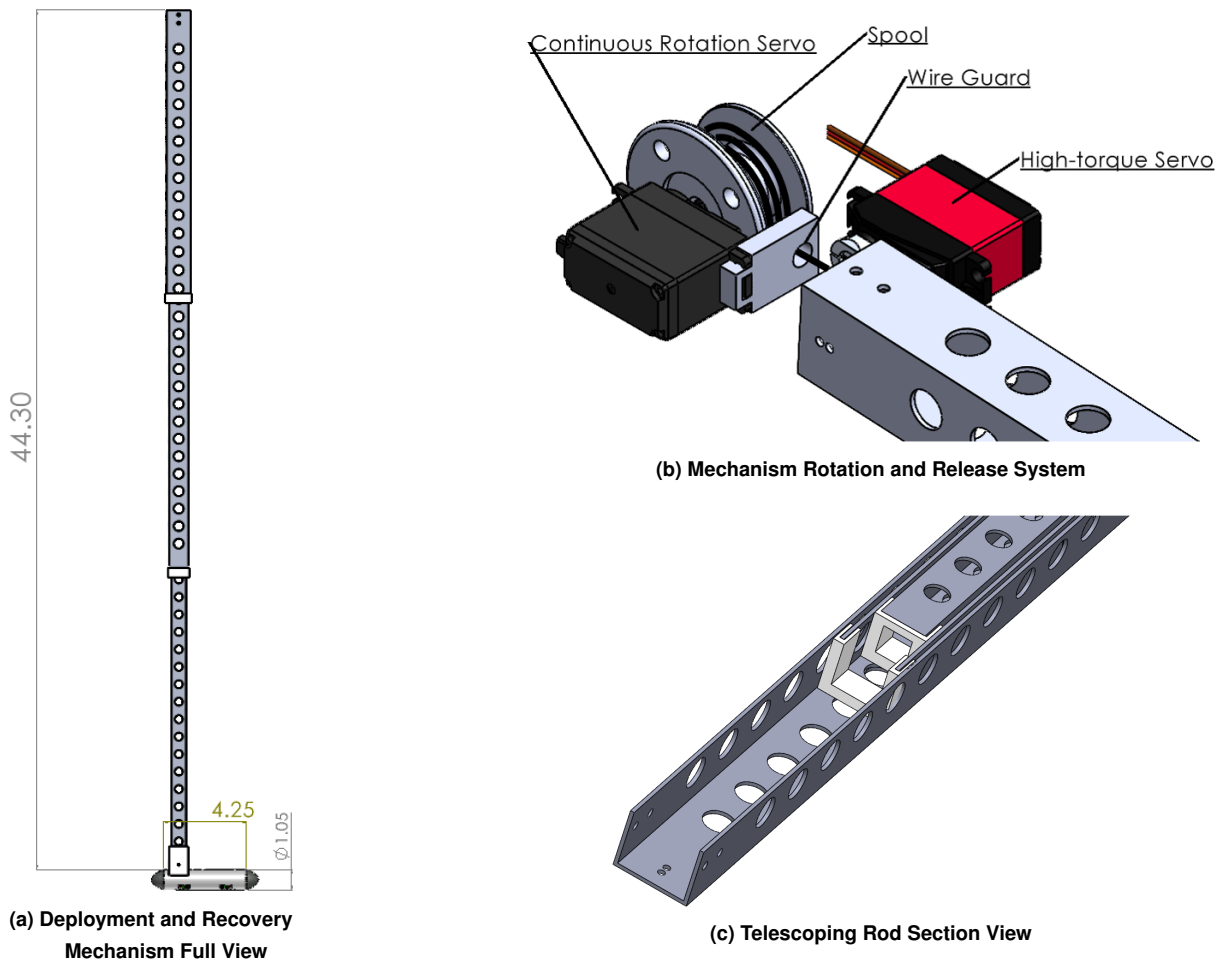


Figure 5.6: Deployment and recovery system multi-view

5.3.6 Sensor Shipping Container

Since the team’s mission scoring analysis revealed that a relatively heavy sensor results in an optimum score, the container was designed to be light so as to add as little payload weight as possible while remaining structurally strong enough to withstand shock forces during the drop test. With this in mind, ABS plastic was chosen due to its relatively high strength to density ratio. Another auxiliary advantage was its ability to withstand higher temperatures than other 3D printed materials, such as Polylactic Acid (PLA). From there, a thin rectangular prism shape as seen in Figure 5.7 was chosen for the container in accordance with the guideline that the container will be drop tested “on all six sides” [1]. The design also includes a sliding door that closes flush with the outer surface of the container for insertion and removal of the sensor. The interior of the container was fitted with thin foam sheets to protect the sensor from damage by the interior of the structure during drop testing. For M2, the sensor weight was simulated by gluing lead weights into the container until the target weight was reached. The container itself was designed to be secured onto the aircraft’s upper-level cargo area via hook-and-loop straps to quickly and efficiently secure or remove the containers from the aircraft when required.

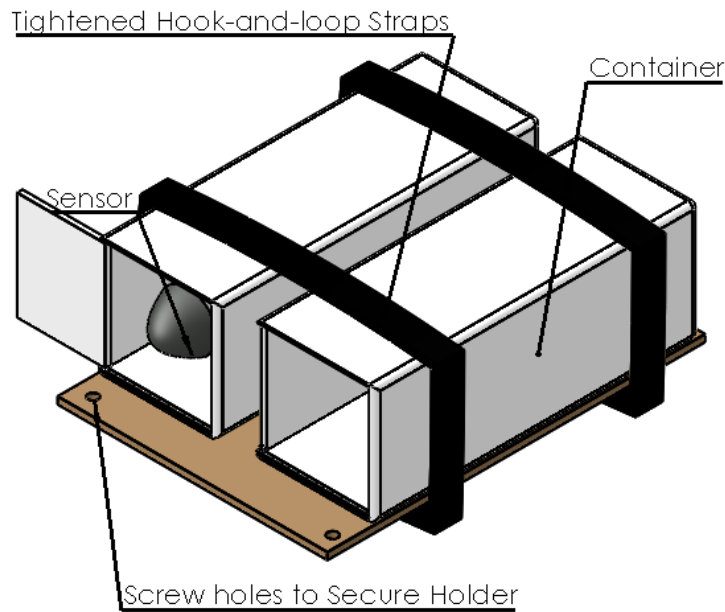


Figure 5.7: Full payload storage system

5.3.7 Propulsion Package and Electronics

The Mk.3 aircraft's propulsion selection is shown in Table 5.2. This package ensures that all mission requirements are fulfilled. The avionics used on the aircraft are a 2.4 GHz Airtronics transmitter with an Airtronics 8 channel receiver. Hitec HS-5985MG metal gear servos were used for the control surfaces. With respect to energy, LiPo batteries were chosen due to their high energy density. LiPo battery cells have a nominal voltage of 3.7 volts and a 6S battery was initially chosen, giving the aircraft a nominal voltage of 22.2V. Using two 2200 mAh batteries therefore gives a power rating of 97.68 Wh. However, per the competition rulebook [1], battery configurations can change between missions. It is likely that the aircraft will only use one 2200 mAh battery for both M1 and M2 in order to reduce unnecessary weight and increase flight velocity, while M3 will use two 2200 mAh batteries in order to sustain flight for ten minutes. Detailed flight testing as described in Section 7 will be used to empirically verify the feasibility of this decision, however.

Table 5.2: Selected aircraft propulsion package

Propulsion Components	Relevant Info
Battery (Gens Ace)	6S, 2200 mAh, Discharge 45C
Motor (Scorpion SII-4025)	520 Kv, 2000 W Max Power, 100 A max current
ESC with 5A BEC (FMS)	70 A, Built-in 5A SBEC.
Propeller (APC)	15 x 8 inch 2-Blade Thin Electric propeller

5.4 Weight and Balance

Figure 5.8 shows the coordinate system used for aircraft definition. The motor mount was used as the origin given its central location in the YZ-plane, as well as its position as the furthest structural point longitudinally. For reference, the leading edge of the wing is located at $X = 5.54$ in.

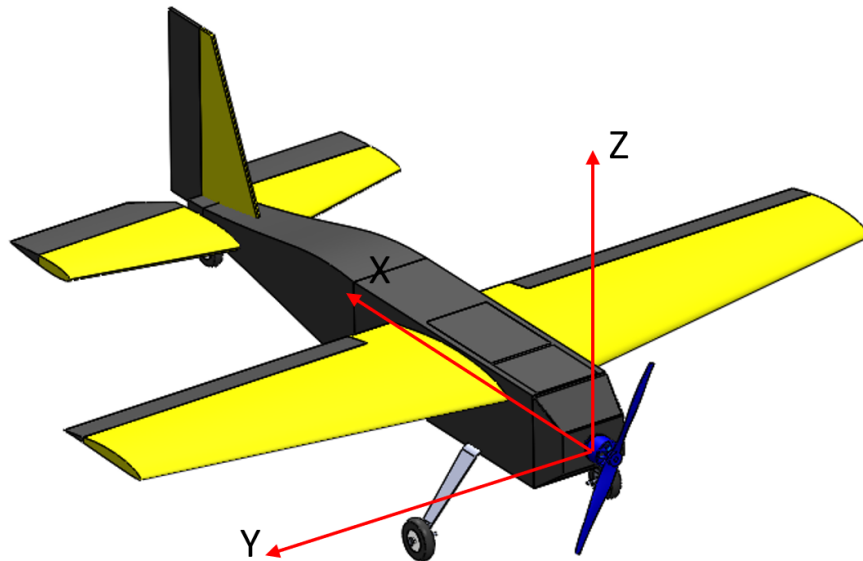


Figure 5.8: Aircraft coordinate system (origin is set to the motor mounting location)

Table 5.3 presents the approximate weight and CG of the aircraft and its subsystems for all missions. For each configuration, every subsystem's weight and location was factored into a total mission CG.

Table 5.3: Weight and balance table

System	Mass (lbs)	CGx (in)	CGy (in)	CGz (in)
General				
Motor	0.86	-1.156	-0.01	-0.0226
Fuselage	1.8	19.515	0.01	0.1784
Landing Gear	0.82	7.39	0	-8.7286
Wing	1.02	12.113	-0.019	2.9004
Horizontal Tail	0.1	42.943	0.007	-0.7586
Vertical Tail	0.2	43.796	0	4.0164
Total Empty Weight	5.428	12.086	0.039	0.8424
Mission 1				
15 X 8 Propeller	0.097	-2.386	0.02	-0.0226
Battery	0.816	5.56	-0.041	-2.0946
Total Mission 1 Weight	6.341	11.025	0.028	0.2914
Mission 2				
15 X 8 Propeller	0.097	-2.386	0.02	-0.0226
Battery	0.816	5.56	-0.041	-2.0946
Payload System	4.858	15.496	0.03	0.9894
Mechanism	1.5	17.719	-0.016	-2.0306
Total Mission 2 Weight	12.699	13.526	0.026	0.4054
Mission 3				
15 X 8 Propeller	0.097	-2.386	0.02	-0.0226
Battery	1.632	5.56	-0.041	-2.0946
Mechanism (Stowed / Deployed)	1.5	17.719 / 9.793	-0.016	- 2.0306 / -22.6037
Sensor (Stowed / Deployed)	1.4	27.172 / 12.397	0.01	0.9693 / -46.6687
Total Mission 3 Weight	10.057	13.911 / 10.571	0.03	-0.0586 / -8.5427

5.5 Flight and Mission Performance

Table 5.4 documents the final design mission performance and flight performance parameters, calculated using data from several flight tests.

Table 5.4: Final design mission performance and flight performance parameters

	Mission 1	Mission 2	Mission 3 (estimated)
Oswald Efficiency Factor (e)	0.9	0.9	0.9
Aspect Ratio	5.1255	5.1255	5.1255
C_{D0} , cruise	0.0462	0.0462	0.185
$C_{L,max}$ (no flaps)	1.38	1.38	1.38
$C_{L,max}$ (with flaps)	1.47	1.47	1.47
Empty Weight (lbs)	5.5	5.5	5.5
Battery Weight (lbs)	0.816	0.816	1.632
Payload Weight (lbs)	0	5.862	2.734
Gross Weight (lbs)	6.4	12.648	9.946
Wing Loading (lbs/ft ²)	1.3570	2.6818	2.1088
Stall Velocity (mph)	20.82	27.57	24.293
Takeoff Distance (ft)	5	35	20
Cruise Velocity (mph)	55.96	50.36	46.46
C_L (cruise conditions)	0.169	0.4139	0.3771
C_D (cruise conditions)	0.048	0.058	0.195
C_L/C_D (cruise conditions)	3.5083	7.1336	1.934
Energy Drain (Wh)	16.23	19.59	78.144
Number of Shipping Containers	N/A	3	N/A
Sensor Weight (lbs)	N/A	1.234	1.234
Sensor Length (in)	N/A	4.25	4.25
Number of Laps	3	3	17.6
Flight Duration (sec)	85	94	600
Absolute Mission Score	1	.03184 containers / sec	92.3032 lbs * inches * laps
Absolute to Predicted Mission Score Ratio	1	1.17	0.7387

These tests simulated the approximate lap length and aircraft maneuvers required to traverse the course, as well as gross weight carried by the aircraft in M1 and M2. The takeoff distances, cruise velocities, and flight durations for M1 and M2 were recorded by a GPS tracker placed inside the aircraft during the flight test. The battery energy used during the flight tests was found by recording charging data before and after each flight test. Since a detailed M3 flight test has not yet occurred, the M3 cruise velocity was found by setting power available (based on battery parameters) equal to power required (based on an approximated C_D value). That velocity was then used to estimate the number of laps flown during M3.

Figure 5.9 shows the predicted thrust curves for the selected propulsion package and final design aerodynamic data from XFLR5.

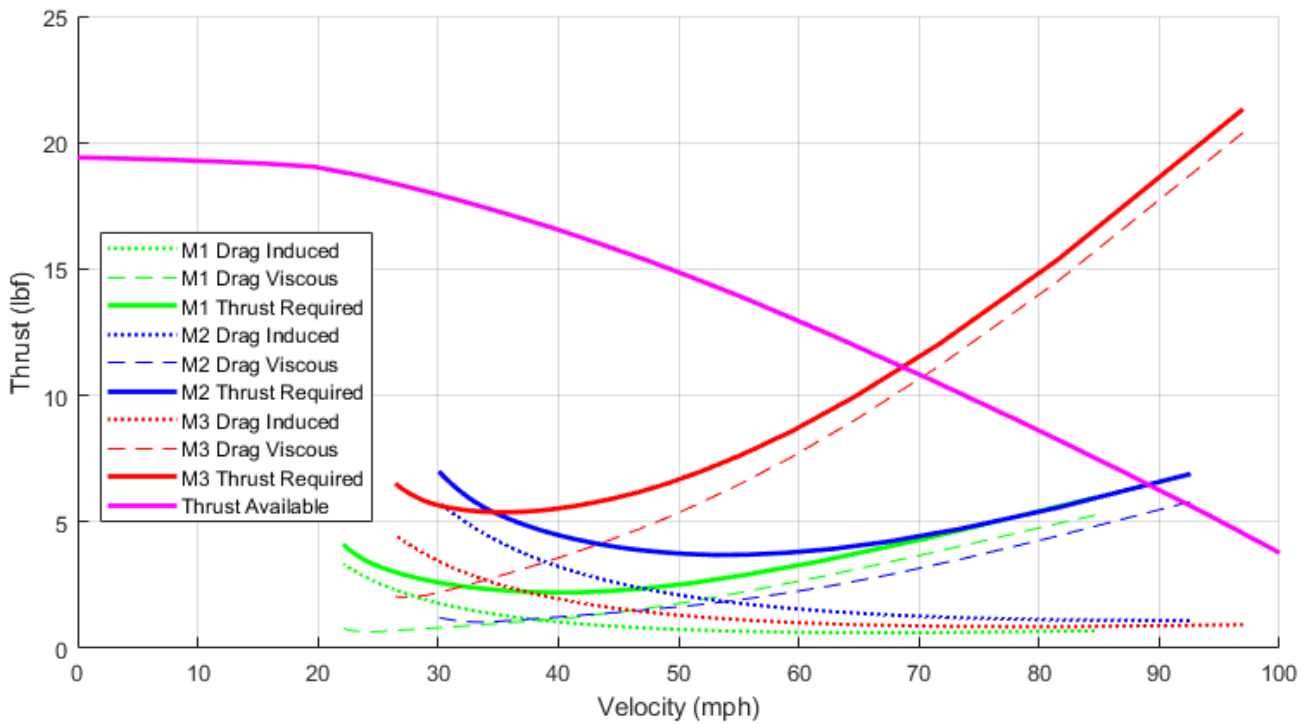


Figure 5.9: Predicted thrust curves for each mission

The drag data was calculated by setting lift equal to weight at each velocity under steady, level flight conditions. The lift induced drag changes between missions due to differing payload weights; in M3, there is an additional parasitic drag component included in the estimate due to the towed sensor. The maximum velocity is determined by the intersection of the thrust available and thrust required curves, while the minimum velocity occurs at stall. M1 and M2 have very similar maximum velocity intersection points due to diminishing effects of induced drag at high velocities. Stall velocity is directly related to payload weight; therefore, M1 has the lowest stall velocity as the lightest payload case, and M2 has the highest stall velocity as the heaviest payload case.

5.6 Drawing Package

Following is the drawing package, containing full, detailed models of the Knightmobile Mk.3's systems and subsystems. Included are the general configurations of the aircraft, the structural arrangement, systems layout and location, and payload accommodation. All drawings were produced using SolidWorks [12].

4

3

2

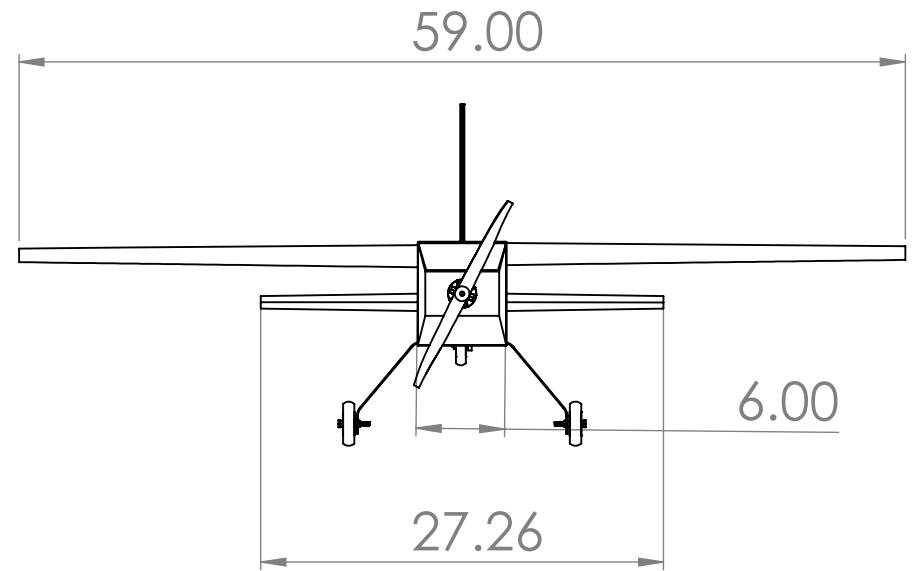
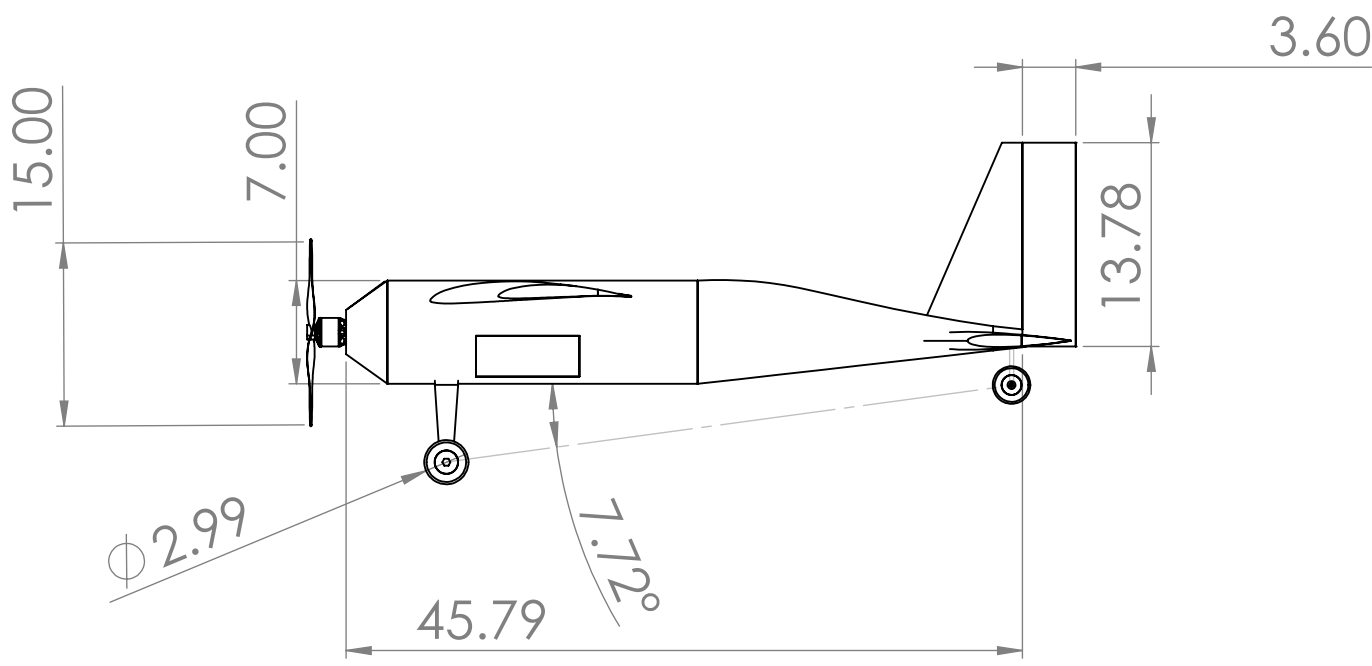
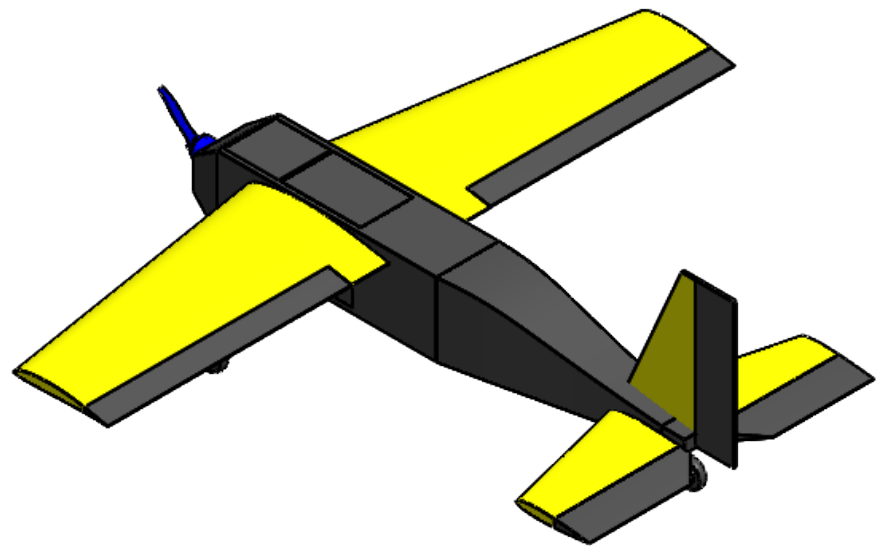
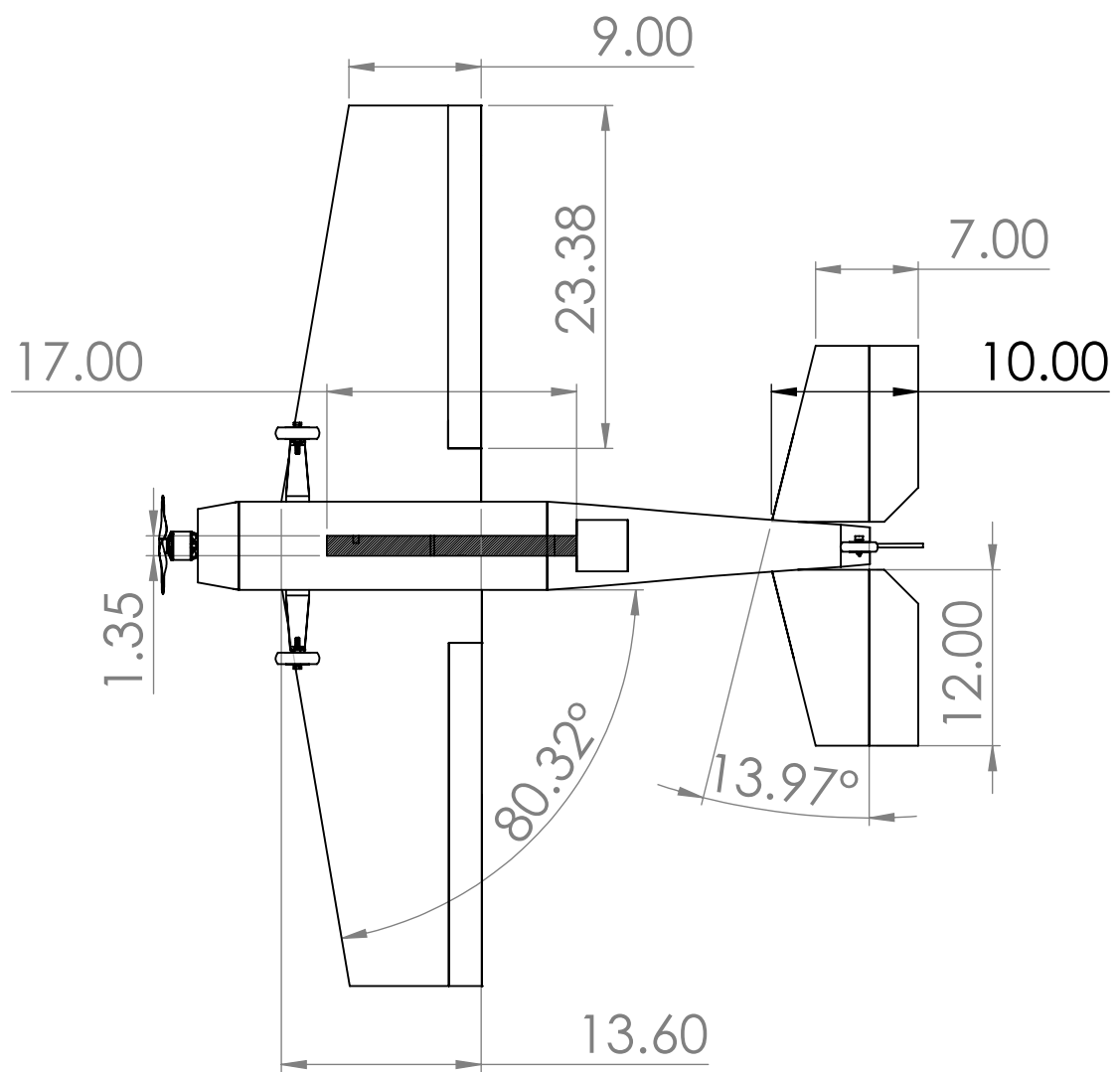
1

B

B

A

A



	NAME	3 View Drawing		
DRAWN	HB	TITLE: Knightmobile Mk.3		
CHECKED	GL			
ENG APPR.	JF			
MFG APPR.	DG			
Q.A.	KR			
COMMENTS:		SIZE	DWG. NO.	REV
Dimensions in inches (unless otherwise specified)		B	1	
		SCALE: 1:13		SHEET 1 OF 4

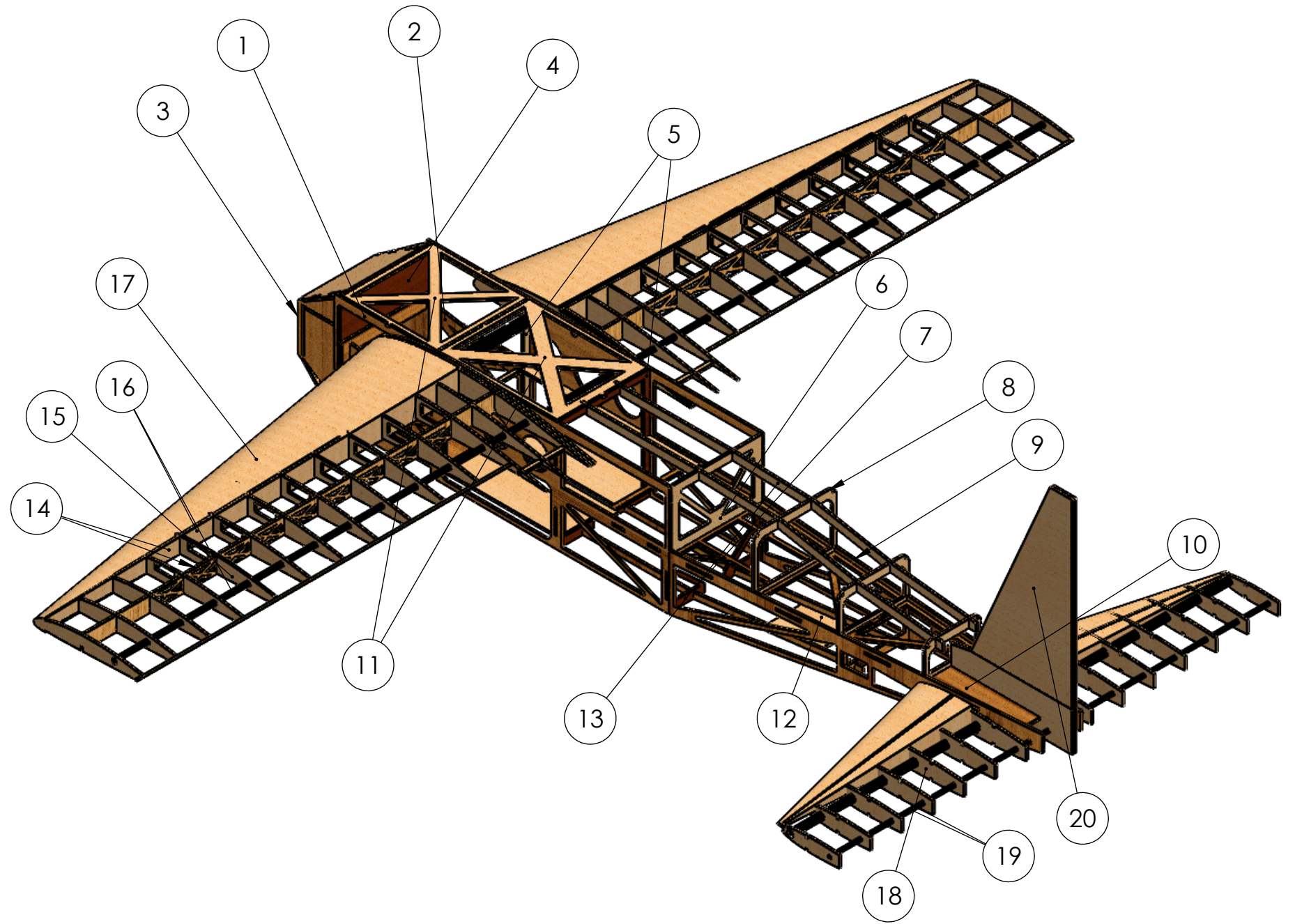
4

3

2

1

Item No.	Part Name	Description	QTY.
1	Main Side Panel	1/8" plywood	2
2	Interior Fire Wall	1/8" plywood	2
3	Motor Mount	1/8" plywood	1
4	Front Panel 1	1/8" plywood	1
5	Front Panels 2 & 3	1/8" balsa and plywood	2
6	Back Panel 1- Top	1/8" balsa	1
7	Back Panel 1 - Bottom	1/8" plywood	1
8	Rear Formers	1/8" balsa	5
9	Back Side Panel	1/8" plywood	2
10	Back Horizontal Panel	1/8" plywood	1
11	Top Access Hatch	non load bearing 1/8" balsa	2
12	Sensor Access Hatch	non load bearing 1/8" balsa	1
13	Rear Fuselage Strips	1/8" plywood	4
14	Wing - Front and Rear Webs	1/8" plywood balsa	2
15	Wing - Structural Ribs	1/8" balsa and plywood ribs	15
16	Wing - Front and Rear Spars	carbon fiber rods	1
17	Wing - D-Box	1/32" balsa sheeting	1
18	Horizontal Stabilizer	1/8" balsa ribs with 1/32" balsa D-Box	2
19	Empennage - Front and Rear Spars	Carbon fiber rods	1
20	Vertical Stabilizer	1/4" cross grained balsa	1



	NAME	Structural Arrangement	
DRAWN	HB	TITLE: Knightmobile Mk.3	
CHECKED	GL		
ENG APPR.	JF		
MFG APPR.	DG		
Q.A.	KR		
COMMENTS: Dimensions in inches (unless otherwise specified)		SIZE B	DWG. NO. 2
		SCALE: 1:6	REV
		SHEET 2 OF 4	

4

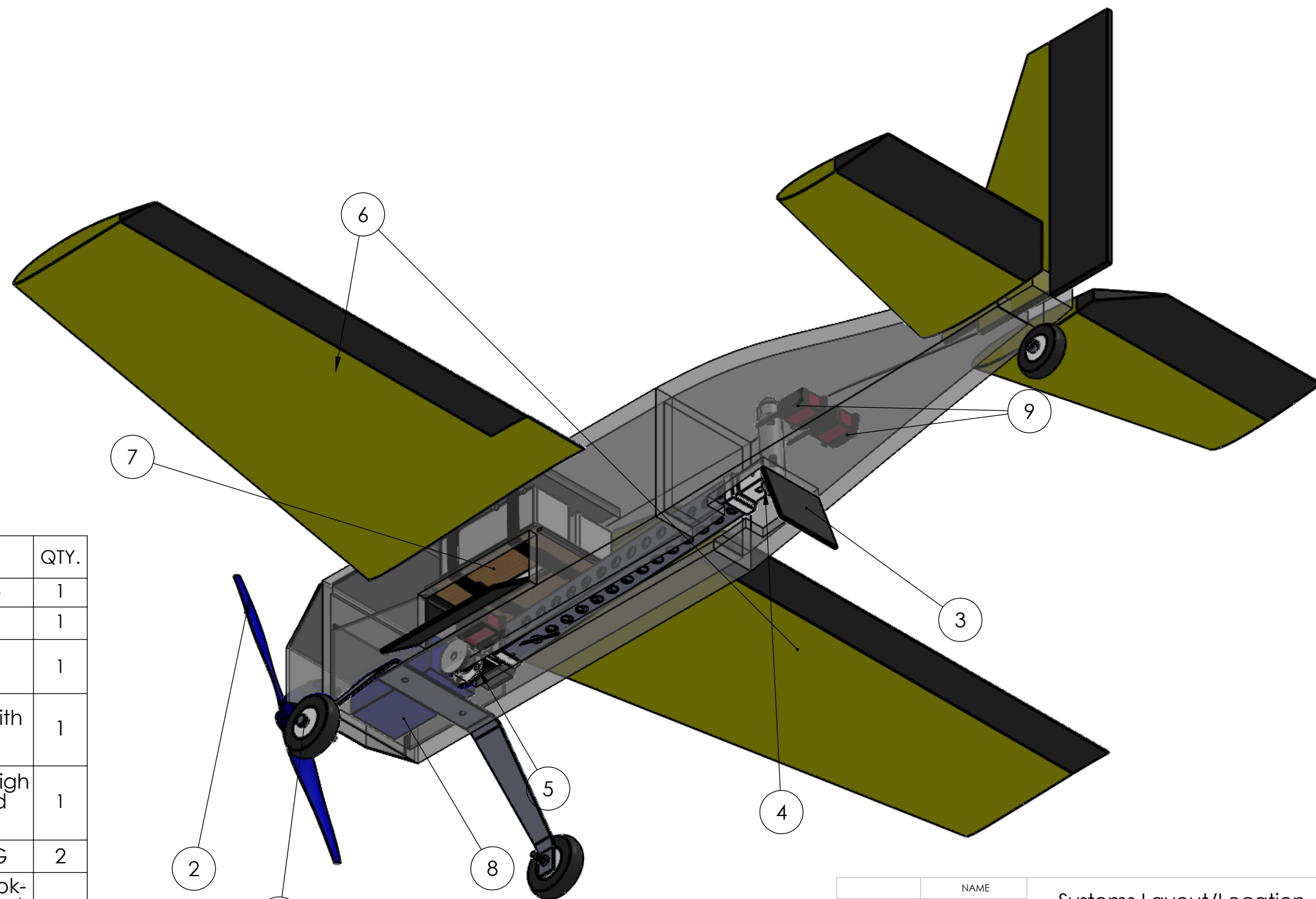
3

2

1

B

B



ITEM NO.	PART NAME	DESCRIPTION	QTY.
1	Motor	Scorpion SII-4025	1
2	Propeller	15 X 8 plastic	1
3	Sensor release door	1/8" balsa sheet	1
4	Sensor	3D printed body with lead caps	1
5	Mechanism	continuous servo, high torque servo, and telescoping rods	1
6	Aileron Servos	Hi-tec HS-5985MG	2
7	Payload System	ABS containers, hook-and-loop straps, and 1/8" balsa sheet	1
8	Battery	Gens Ace 6S 2200mAh	1
9	Elevator and Rudder Servos	Hi-tec HS-5985MG	2

A

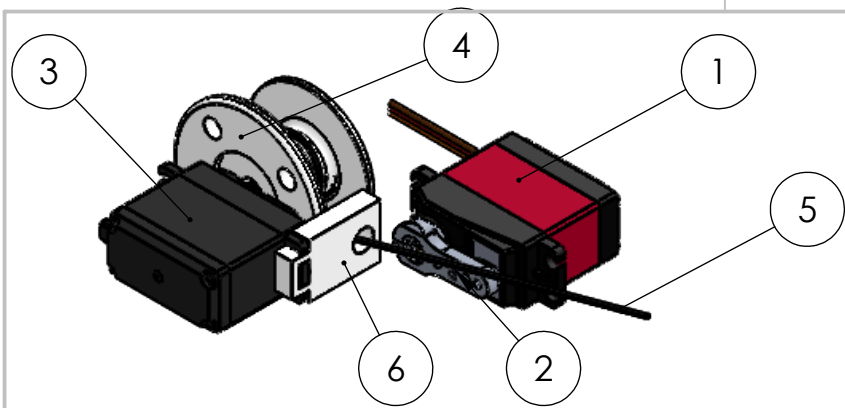
A

		NAME		
DRAWN		HB	Systems Layout/Location	
CHECKED		GL	TITLE:	
ENG APPR.		JF	Knightmobile	
MFG APPR.		DG	Mk.3	
Q.A.		KR		
COMMENTS:			SIZE	DWG. NO.
Dimensions in inches (unless otherwise specified)			B	3
			SCALE: 1:5	SHEET 3 of 4

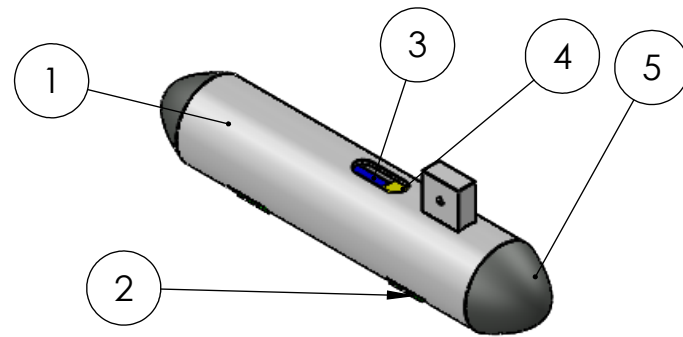
3

2

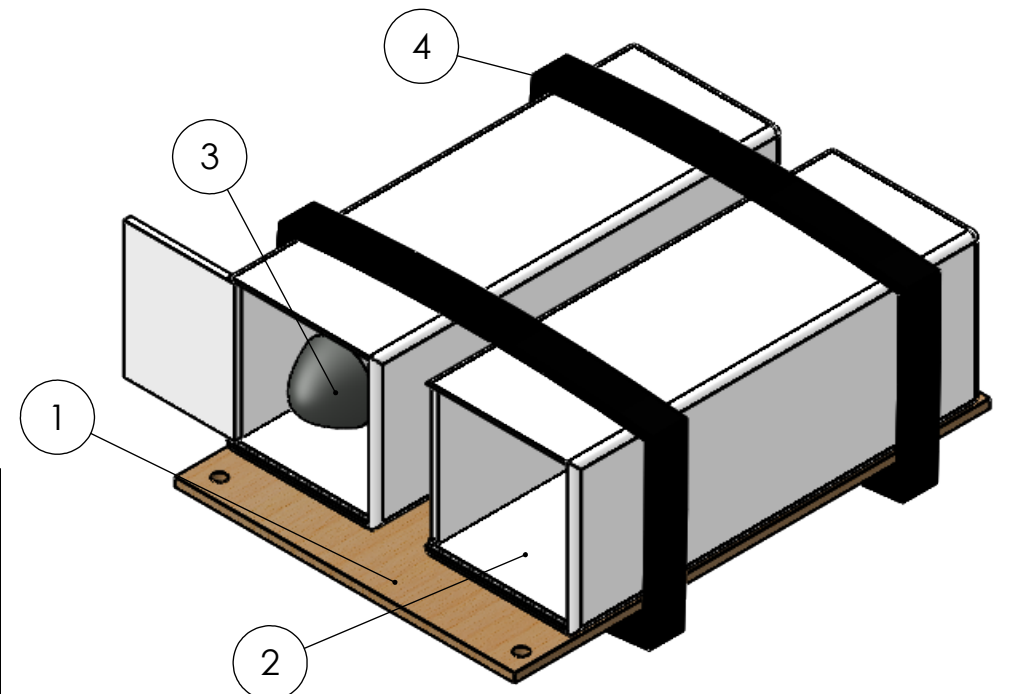
1



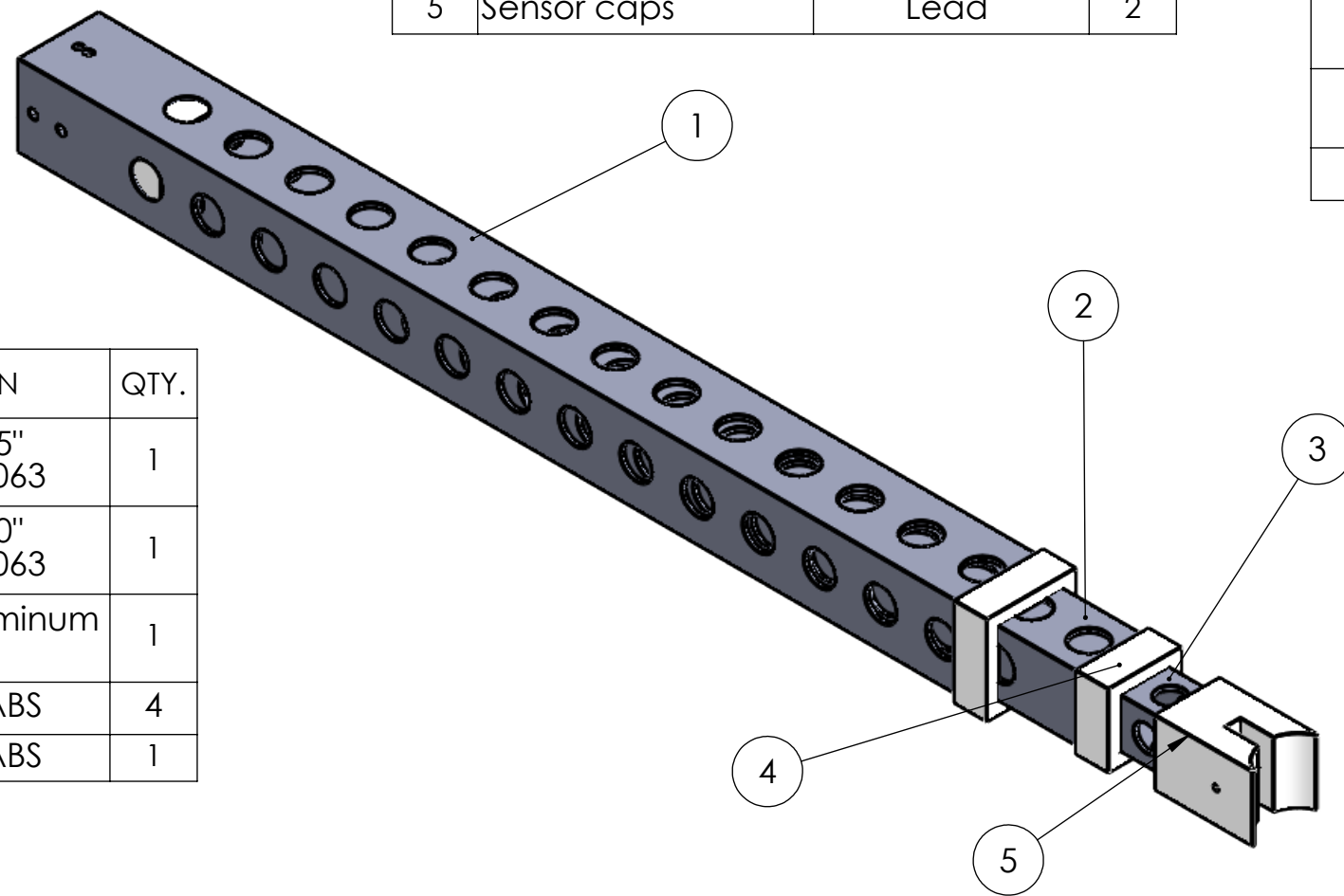
ITEM NO.	PART NAME	DESCRIPTION	QTY.
1	Mechanism servo	HiTec HS-5985MG	1
2	Mechanism servo arm	Aluminum 25T	1
3	Continuous servo	HiTec HS - 311	1
4	Wire spool	3D printed ABS	1
5	Wire	Kevlar	1
6	Wire guard	3D printed ABS	1



ITEM NO.	PART NAME	DESCRIPTION	QTY.
1	Sensor body	3D printed ABS cylinder	1
2	Sensor lights	Red and green LED lights	4
3	Sensor battery	350 mAh 1S LiPo	1
4	Controller	Programmable light control board	1
5	Sensor caps	Lead	2



ITEM NO.	PART NAME	DESCRIPTION	QTY.
1	Container holder	1/8" balsa sheet	1
2	Container	ABS container with sliding door	2
3	Sensor	ABS body with lead caps	1
4	Fasteners	hook-and-loop straps	2



ITEM NO.	PART NAME	DESCRIPTION	QTY.
1	Telescoping rod 1	Square 1.25" Aluminum 6063	1
2	Telescoping rod 2	Square 1.00" Aluminum 6063	1
3	Telescoping rod 3	Square .75" Aluminum 6063	1
4	Rod caps	3D printed ABS	4
5	Pin connector	3D printed ABS	1

		NAME	Payload Accommodation	
DRAWN	HB	TITLE:	Knightmobile Subcomponents	
CHECKED	GL	SIZE	DWG. NO.	REV
ENG APPR.	JF	B	4	
MFG APPR.	DG	COMMENTS:		
Q.A.	KR	Dimensions in inches (unless otherwise specified)		
		SCALE: 1:2	SHEET 4 OF 4	

6. Manufacturing Plan

This plan includes all manufacturing methods investigated during design and manufacturing planning. Also included are a detailed layout of the fabrication process of each component of the aircraft, major manufacturing milestones, and a schedule for delivery of those milestones.

6.1 Manufacturing Methods Investigated

Balsa Wood Build Up

Balsa is readily available in many different sizes from 1/32 inch thin sheets to large 4 inch by 12 inch blocks. Since balsa sheets have incredibly high tensile strength [13], they are easily malleable and thus beneficial for adding strength to the wings and tail. Larger blocks of balsa work well for Computer Numerical Control (CNC) machining strong, solid parts that are lightweight. Balsa can also be stacked with the grains running perpendicular to each other to provide extra support against shearing.

Plywood Build Up

Plywood is exceptionally strong for its weight and density due to its cross-grain properties [14]. Plywood is useful in radio-controlled aircraft structures where high strength is needed such as landing gear fixtures, wing mounts and firewalls for the motor. When using plywood, the extra weight needs to be considered for CG placement.

3D Printing

3D printing is an extremely versatile additive manufacturing process, allowing virtually any design to be printed layer by layer. Some of the most commonly used plastics in 3D printing are PLA, Polyethylene Terephthalate Glycol (PETG), and ABS. ABS is being considered for manufacturing the sensor body, as it is low cost, very strong, and readily available for use in privately owned 3D printers [15]. PLA is similarly common and used for lightweight purposes in low temperature environments. PETG is strong and has a higher glass transition temperature than other 3D printing plastics, allowing a more supportive application, but is less accessible and can not be used in many privately owned 3D printers.

Acrylic Sheeting

Acrylic is a lightweight material with high heat resistance [16]. Acrylic sheets are often manufactured to specific shapes by using either electric or CO2 laser cutters and engravers. Sheeting comes in many different thicknesses and dimensions for various uses.

Composite Layups

Several composite materials are often found inside of model aircraft. These materials include carbon fiber of various weaves, fiberglass weaves, Kevlar string, G10 pre-impregnated fiberglass and pre-impregnated carbon fibers. Carbon fiber weaves and fiberglass weaves are helpful for covering an existing material (such as a balsa airfoil). Kevlar string provides flexibility and strength while also being affordable.

Lead Molding

Lead requires caution when handling but is strong, dense and highly malleable [17]. Typically, lead would not be considered for small-scale aircraft applications outside of ballast due to its density; however, it was investigated for the purpose of increasing sensor weight.

6.2 Selected Methods

Wood Build Up

Ultimately, balsa and plywood were chosen as the primary material for construction of all prototypes of the aircraft due to ease of manufacturing, availability, and strength-to-weight characteristics. Balsa is known for its high density, low weight, and tensile strengths. Plywood is used for sections that require greater strength; for the purposes of the aircraft, it was chosen for use in places that will experience distributed loads, including landing gear mounts, motor firewall, and tail section mounts.

Other types of wood, such as spruce and pine, were not considered since they have grains that are not as tight as balsa and plywood, which would make CNC machining and laser cutting more difficult and reduce the strength of the resultant structure.

3D Plastics

ABS plastic was chosen for subcomponent manufacturing due to its high density and temperature resistance relative to PLA. PETG was not chosen due to limited 3D printer access, which forced usage of 3D printers that are incompatible with PETG. 3D printing allows for a customizable body shape, which was deemed necessary for the sensor to include complex shapes and attachments, such as aerodynamic fins, slots for lights, battery mounting, and towing. Infill can also easily be changed for weight adjustments, assuming the resulting difference in material strength has a negligible effect on its utility. It was also deemed necessary to make attachments for the telescoping rods used in the deployment and recovery mechanism, so as to allow for adaptability in design given any unforeseen complications in manufacturing the rods. The low cost, versatile and accessible nature of design for a privately-owned 3D printer made it more practical for low-stress environments than a metal or acrylic body.

Acrylics

It was determined that various thicknesses of acrylic sheeting would be used during the manufacturing of the aircraft due to availability and ease of manufacturing. Since the sheeting is easily sized and shaped via laser cutter, washers and plating for mounts and other plastics for the aircraft could be quickly created privately, as opposed to ordering parts. Using acrylic sheeting for these components was also advantageous due to its high strength-to-weight ratio compared to materials with similar uses.

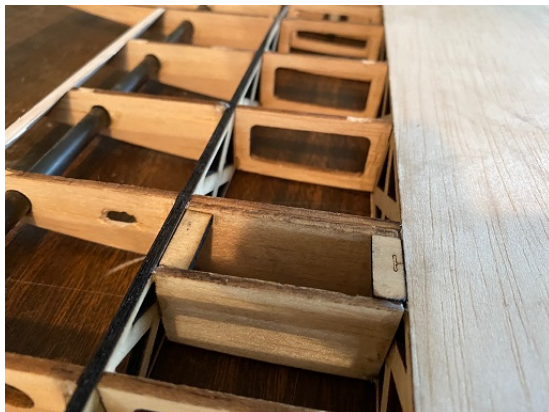
Lead

A dense, malleable material was required for balancing the CG of the aircraft during initial test flights and for adding weight to the sensor. Lead was chosen for its low melting point and high density. To add weight to the sensor design, it was also determined that the sensor caps would be cast out of lead.

6.3 Component Manufacturing Processes and Results

6.3.1 Wing and Tail

The ribs of the wing were laser cut from a sheet of balsa wood, and a carbon fiber spar was passed through the ribs at 3/4 chord length. Two sets of cross-hatched shear webs were notched and glued in between each rib to distribute shear loads. A D-Box was created by bending a balsa sheet around the front of the ribs and over the first set of spacers. The ailerons were created by truncating the rib airfoil shapes and gluing a balsa sheet to them. Small, angled ribs that finished the airfoil shape were glued to this sheet, and a balsa spar was used to connect them and form the final control surface. Diagonal balsa sticks were then added for support and spacing of the ribs. Holes were drilled for servo attachment, and the wings and ailerons were fitted with UltraKote to create a smooth surface to reduce drag.



(a)



(b)

Figure 6.1: Manufactured wing (left) and tail (right)

Manufacturing for the tail followed a similar process. A central spar was passed through airfoil- shaped ribs to form the horizontal stabilizer. A D-box was also created and fitted around the front of the tail ribs and over a shear web that was notched into the ribs. The vertical stabilizer was created using multiple layered sheets of balsa cut out into the shape required, the central spar was also run through the bottom of the vertical stabilizer, and ribs were added to support against shear.

6.3.2 Fuselage Structure

The fuselage was designed to be manufactured quickly and easily, with a continuous structure used to increase strength while decreasing manufacturing complexity. The pieces were designed to fit into one another using notches to prevent the need for external mounts. The nose structure consists of a front nose box and two firewall pieces that glue to the sides. The side panels of the fuselage are then slid into the firewall. The rear, tapered horizontal panel is then notched into the front of the fuselage. The formers for the structure aft of the wing were then set in place. The hatches were integrated, one for electronics access and one for installing the subcomponents. Full-length plywood strips were included for shaping, and the full fuselage was wrapped in MonoKote and fitted using a heat gun.

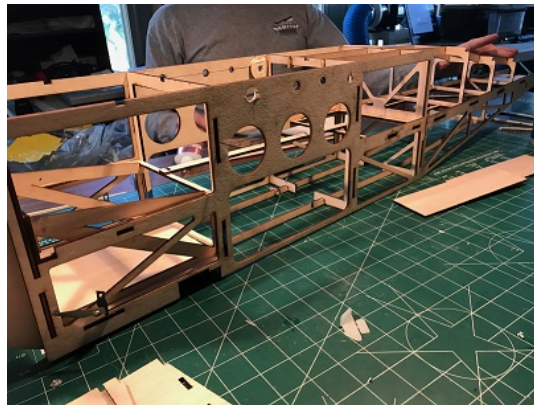


Figure 6.2: Constructed fuselage

6.3.3 Landing Gear Mounting

The landing gear was placed under the two firewalls to help transfer the force of landing through the aircraft structure during landing. It was placed forward of the CG to increase propeller clearance during takeoff and prevent the nose from tipping forward into the runway upon landing. Plywood was chosen for the landing gear mounting point due to its strength, since this was considered a high-stress area. For the tail wheel, springs were used to attach the wheel to the rudder in order to add ground steering functionality to the aircraft.



(a) Landing gear mounting point



(b) Tail wheel (springs added for steering)

Figure 6.3: Manufactured landing gear

6.3.4 Sensor and Mechanism

The sensor body was 3D printed from ABS at 100% infill to add weight to the design. The DELight Starter Kit [18] was used for the lights and controller system. A 1S Heli-Max LiPo battery was chosen to power the lights. The lights were glued to their respective mounts and the receiver and battery were placed on top of a lip within the sensor. The telescoping rod was cut from aluminum square tubes using a CNC Milling laser, and then holes were drilled along the sides to decrease mechanism weight as shown in Figure 6.4(a). A thin layer of tape was used to reduce drag from the weight cuts during flight. ABS attachments were fitted to each of the square tubes, with a 3D printed connector piece used for the final rod to attach it to the sensor for M3. Smaller holes were cut into the rod at the base of the assembly to attach it to a high torque servo motor. A spool was attached to a continuous rotation servo, and Kevlar wire was braided with the wires for the electronics system and spooled. A small wire guard made from ABS was used to guide the wire as it was fed down the rod and into the sensor. The caps for the sensor were 3D printed for testing purposes as initially planned, but it was determined that a higher density material was necessary to increase sensor mass and achieve the predicted optimal mission score. Lead cast caps were chosen for this purpose for the final sensor design, and will be completed for the final detailed flight test as described in Section 7. The caps will be sand cast using a 3D printed cap as a core, and lead weights will then be melted and poured into the molds and rapidly cooled into the cap shape.



(a) Telescoping rods drilling process



(b) Initial sensor lights and electronics test

Figure 6.4: Manufactured subcomponents

6.4 Milestones and Schedule

A manufacturing milestone chart was created to track the progress of the Mk. 3 build among all sub-teams, and is seen in Figure 6.5. The major objective of manufacturing the Mk.3 design was to improve upon the structural strength and complexity of the previous iterations, as well as to decrease the manufacturing turnaround in order to add time to testing (and, time allowing, construct another, final aircraft iteration for minor improvements). The wing and fuselage were both manufactured rapidly due to optimized design features, as well as the experience gained from previous builds. The telescoping rod mechanism and payload systems were manufactured slightly behind schedule due to issues with purchasing the desired material in the size and shape required for manufacturing. However, the schedule was designed with the possibility for this complication in mind, and it did not delay the initial detailed test flights.

UCF DBF 2020-2021	Week 1 (1/11)	Week 2 (1/18)	Week 3 (2/1)	Week 4 (2/8)
Knightmobile Mk.3				
Laser Cut Components				
Wing and Tail				
Main Wing Assembly				
Horizontal Stabilizer				
Vertical Stabilizer				
Control Surfaces				
Fuselage				
Assembly				
Sensor and Mechanism				
Sensor Body				
Telescoping Rod System				
Payload System				
Lights				
Landing Gear				
Assembly				
Final Integration				
Electronics Integration				
Test Flight				2/16 ★

Figure 6.5: Manufacturing milestones chart (planned timing vs. actual)

7. Test Planning

This testing plan outlines fulfillment of necessary requirements for the aircraft systems, tests performed for experimental evaluation of the aircraft solution, and test cards used for verification of requirements during testing. A rapid prototyping and testing methodology is used in order to mitigate risks and continuously improve the aircraft and simulated mission score. Figure 7.1 captures the master testing schedule used through the duration of the project.

DBF Testing Schedule 2020-21	Nov.	Dec.	Jan.	Feb.	Mar.	Apr.
Conceptual Testing						
Aircraft Flight Test						
Sensor and Mechanism Test						
Preliminary Testing						
Aircraft Flight Test						
Sensor and Mechanism Test						
Detail Testing						
Mission Flight Tests						
Exploratory Flight Tests						
Competition Practice Flight Tests						

Figure 7.1: Testing schedule overview

7.1 Subsystems Testing

7.1.1 Sensor and Mechanism Aerodynamic Testing

During M3, it is required that the sensor remain aerodynamically stable. Therefore, it was imperative to test a mechanism that would allow for the sensor to be deployed reliably while also aiding in fixing the sensor's orientation. During conceptual design, telescoping rods were chosen for this purpose; however, for verification of initial design decisions in real-world application, proof-of-concept tests were performed for all potential design choices. Three different designs were tested for the mechanism:

a stiff wire connected at two points on the sensor, a stiff wire connected at one point on the sensor with sensor fins added, and a telescoping rod with the sensor fixed to one end. Conceptual testing was conducted by towing each design out of the window of a car at various speeds.

The stability of each towing configuration was analyzed and compared to determine its viability in the aircraft. The stiff wire configuration with two connected points was aerodynamically stable in both yaw and roll, but its pitch fluctuated significantly. The stiff wire with a single connection point and additional sensor fins had very little stability and consistently rolled in flight. The telescoping rod was the only design that provided stability in all three directions.



Figure 7.2: Initial sensor testing out of a car window

The stiff wire configuration with two connected points was aerodynamically stable in the yaw and roll directions, but its pitch fluctuated significantly. The stiff wire with a single connection point and additional sensor fins had very little stability and consistently rolled in flight. The telescoping rod was deployed using a weight at the end to simulate towing the sensor. The telescoping rod was the only design that provided stability in all three directions. Additionally, at the presumed M3 cruise velocity the telescoping rod held the sensor in place and suffered no bending or pitching moments.

7.1.2 Preliminary Mechanism Testing

With a telescoping rod system proven as a viable method of providing aerodynamic stability in real-world application, testing was performed on a more detailed mechanism to deploy and recover the rod with ease. A deployment and recovery prototype mechanism was created as seen in Figure 7.3 using a high power servo to move the telescoping rods from stored configuration to deployed, along with a low power motor programmed to extend and retract the telescoping rods via a nylon string attached to the sensor.



Figure 7.3: Functional mechanism prototype setup (left) and initial testing out of a car window (right)

After a successful proof of concept, a second prototype was created. This mechanism used a continuous servo to replace the low power motor in order to reduce weight and system complexity. A test was performed out of a car window at speeds of up to 50 mph. In this test, the rod was rotated 90 degrees out of the fuselage and fully extended to simulate deployment, then collapsed and rotated 90 degrees to simulate recovery back into the fuselage. Stable deployment, towing, and recovery of the sensor were demonstrated.

7.1.3 Wing Load Testing

A wing load test was performed on the initial prototype to determine its loading capabilities. Each wing tip was fixed to simulate the structural verification test to be performed in the competition, and the middle of the wing was loaded with weight until failure occurred. Figure 7.4 shows the test setup, along with its results.

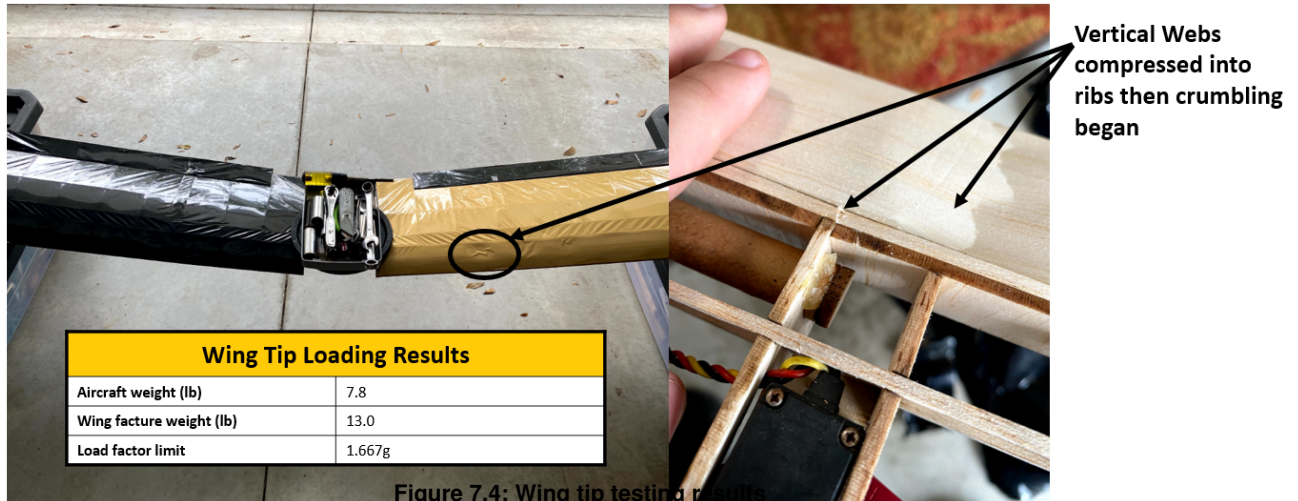


Figure 7.4: Wing tip testing results

This test simulated a heavy cargo load case, featuring a strong force concentrated at the wing roots to act as an encumbered fuselage. The resultant fracture occurred at a lower total weight than was desired, revealing inherent weaknesses in the initial prototype's wing structure. To counter this, the shear webbing needed to be improved to better distribute shear and bending loads. For later wing iterations, a second, aft carbon fiber rod was added that extended through the entire span of each wing, and the initial, forward carbon fiber rod was extended slightly. A second, rear shear web was added, and the thickness of both webs was increased. The D-Box was also extended over the front shear web for added support. With the wing strength thoroughly bolstered, expected cargo capacity increased given improved maximum structural loading potential, and significant stability improvements were later demonstrated in flight.

7.2 Flight and Mission Testing

7.2.1 Conceptual Flight Testing

An initial conceptual flight test was performed following completion of the Mk.1 aircraft. The objectives of this test were to verify flight performance, test the propulsion system, and provide the pilot with a base aircraft to evaluate and make recommendations for improvement. During the flight, special attention was given to aircraft stability and sensitivity to control input, and it was determined that inherent yaw instability was present, along with insufficient pitch and yaw control authority. However, the propulsion system performed as expected, and pilot control allowed the aircraft to cruise and land without sustaining damage.



Figure 7.5: Mk.1 conceptual flight test final landing approach

Given these results, the Mk.2 design included larger tail surface areas per stability requirements and larger relative stabilizer control surface sizes per pilot input. The horizontal stabilizer was also raised to offset it slightly from the wing, as it was determined that downwash effects likely contributed to fluctuations in dynamic stability. The propulsion system was deemed sufficient for flight and was carried over to the Mk.2 aircraft.

7.2.2 Preliminary Flight Testing

The preliminary flight test was performed on the Mk.2 aircraft in order to evaluate the efficacy of stability improvements between the first and second aircraft iterations. More detailed improvements were also sought, particularly with respect to wing sizing. Unlike conceptual testing of Mk.1, however, preliminary testing of Mk.2 also considered mission performance. A GPS monitoring system was used for data collection; position, velocity, and altitude data were collected at regular intervals during flight. Battery voltage and power draw were also tracked, and the results of this data was used to determine an experimental estimate of the aircraft's drag coefficient. This drove further detail design decisions, including streamlining the fuselage and increasing the Oswald efficiency factor from 0.7 to 0.9 by adding a taper to the aircraft wing. The horizontal tail shape was also revised from a flat plate to a symmetric airfoil in order to increase structural strength of the tail and slightly decrease drag based on requests from the pilot. Figure 7.6 captures the progression from Mk.1 to Mk.3.



(a) Knightmobile Mk.1



(b) Knightmobile Mk.2



(c) Knightmobile Mk.3

Figure 7.6: Photographic progression through the aircraft iterations

7.2.3 Detailed Flight and Mission Testing

Detailed flight and mission tests are conducted in order to simulate all three competition missions. Flight data is collected to drive minor adjustments to the aircraft and its subsystems for the purpose of improving eventual mission scores. Knightmobile Mk.3 was used for flight tests of M1 and M2, and will be used for a flight test of M3 in late February.

Flight testing of M1 was used as a baseline for comparison; the other two missions follow the same course under different conditions, so direct comparisons of relevant parameters (such as takeoff distance, average velocity, and power drain) can be made. In turn, detailed improvements will be made based on evaluation of these parameters, as they give empirical evidence for the accuracy and shortcomings of analytic models when accounting for real-world conditions.



Figure 7.7: Knightmobile Mk.3 vertical flight with no payload

M2 testing focused on testing of aircraft stability and cargo capacity. The aircraft was loaded with payload simulators to a heavier load case than is planned for M2, to obtain an upper bound for takeoff within the 100 ft limit imposed by the competition. The difference in average aircraft velocity between the M1 and M2 tests was compared to the difference predicted by original analytic model results for verification. Current analysis of these results is aimed toward improving the current mission solution.

M3 testing will focus on in situ testing of sensor deployment, operation and recovery, with an eye toward analysis of aircraft stability and structural integrity under an increased drag force and the resultant bending moments. Comparison of aircraft velocity during M3 testing to M1 will be used to quantify the effect of the telescoping rod mechanism and deployed sensor on aircraft drag. This will drive decisions regarding improvements of mechanism aerodynamics.

7.2.4 Exploratory Flight Tests

Exploratory flight tests are to be conducted for experimental trade studies, in addition to the theoretical trade studies detailed in Section 4. These experimental trade studies will aim to verify or improve upon previous analysis in order to iterate toward a maximized score. While the main aircraft will remain substantially the same, configurations may be updated in terms of power used, specific electronics, subcomponent sizing, and aircraft surface sizing in order to further increase mission scores.

The first exploratory flight test to be conducted shall be an aircraft performance test with multiple variations considered. The major focus will be on data collection in order to better predict mission score. This test will also utilize a current sensor to collect power consumption data during flight. The aircraft will vary through speeds as well as payload weight while monitoring power draw in order to map out power efficiencies and possible flight configurations. Once this flight test is performed, an experimental mission score analysis will be performed using experimental data rather than aerodynamic propeller solutions,

which will allow for a high fidelity evaluation of the complete aircraft solution.

Given new mission score predictions based on experimental data, a sensor flight test will be performed. Multiple sensor masses will be tested to verify or improve results from the experimental mission score analysis in terms of both calculated score and pilot satisfaction. Evaluation of these results will aim to determine the final sensor mass.

The third exploratory test to be performed will focus on the wings. The aircraft wings were manufactured to be interchangeable, so flight tests of M2 and M3 will be performed on the Mk.3 aircraft using two alternative sets of wings. Each wing set will have a smaller planform compared to the current configuration, in order to determine the possibility of iterating aircraft weight and drag toward a final, optimal configuration while maintaining the previously defined subcomponent solution.

7.3 Test Cards

Each test is divided into two phases known as Test Cards (TC's), which cover the pre-flight, in-flight and post-flight checklist. After each TC is fully completed, the Pass and Fail results will be analyzed by relevant sub-teams to discuss solutions for any failures, evaluate reasons for successes, and consider improvements to overall solution performance. TC 1 covers all ground testing prior to flight; this group of tests covers requirements pertaining to mission readiness, aircraft design constraints, airworthiness of the aircraft, and ground crew performance. TC 2 covers all testing to be performed during and post flight; this group of tests evaluates the structural and flight capabilities and the flight envelope of the aircraft. In-flight subcomponent functionalities will also be checked, as well as aircraft structural integrity. The test cards used for the M2 detailed flight test are shown in Figures 7.1 and 7.2. This format will continue to be used for all future flight tests.

Table 7.1: Test Card 1 (pre-flight checklist)

Step Number	Step Instructions	Pass / Fail	Test Notes
1	Ensure batteries and electronics are properly installed into aircraft and connected for flight.	P	Battery and electronics are properly installed and connected.
2	Verify that the location of the CG without payload is in the front third of the wing.	P	CG is in front third of wing.
3	Verify the location of the CG (loaded and unloaded) is marked on the bottom of the wing.	P	CG (loaded and unloaded) is marked.
4	Secure payload (if applicable) and verify the location of the CG is acceptably close to the marked location.	P	Payload is secure and CG is near the marked location.
5	Verify the propeller has enough clearance with the current configuration.	P	Propeller has proper clearance.
6	Verify that the aircraft landing gear are in working condition.	P	All wheels are in working condition, landing gear is mounted securely.
7	Verify wingspan is no more that 60in.	P	Wingspan is 59in.
8	Flip the external switch and verify that all electronics are turned on/off.	F	External switch has not yet been added.
9	Flip the kill switch and verify all electronics are turned off.	F	Kill switch has not yet been added.
10	Apply a 2.5g load case to the wings and verify structural integrity.	P	Aircraft survived a 2.5g load case.

Table 7.2: Test Card 2 (in-flight and post-flight checklist)

Step Number	Step Instructions	Pass / Fail	Test Notes
During Flight			
1	Flip external switch to turn on aircraft.	F	External switch has not yet been added.
2	Verify that the aircraft can take off in no more than 100 ft.	P	Takeoff occurred well below 100 ft.
3	Verify that the sensor is deployed and recovered without affecting aircraft stability (M3 Flight).	N/A	Mission 3 was not flown.
4	Verify that the sensor remains aerodynamically stable while deployed (M3 Flight).	N/A	Mission 3 was not flown.
5	Verify that the sensor lights turn on and are visible while the sensor is deployed (M3 Flight).	N/A	Mission 3 was not flown.
6	Verify the aircraft does not bounce on runway when landing.	P	Aircraft did not bounce on landing.
Post Flight			
7	Turn off external switch to turn off aircraft.	F	External switch has not yet been added.
8	Verify all aircraft components are intact.	P	All components are intact.
9	Verify total flight time is less than 5 min (M2 Flight).	P	Total flight time was less than 5 min.
10	Verify total flight time is greater than 10 min (M3 Flight).	N/A	Mission 3 was not flown.
11	Verify all battery cells have 3.7 V remaining.	P	Cells had 3.7 V remaining.

8. Performance Results

8.1 Key Subsystem Performance

Wing and fuselage structural tests were conducted via a wingtip loading test followed by an over-encumbered flight. The aircraft cargo hold was filled with the M2 payload configuration, then ballast was added until a total gross weight of 16 pounds (roughly 3.27 pounds greater than the actual M2 gross weight) was achieved. The Mk.3 aircraft survived a wingtip load test with a similar, simulated loading configuration as shown in Figure 8.1 and was then able to complete three laps of the flight course.



Figure 8.1: Simulated extreme case wingtip load test

Upon inspection, there was no structural damage to the wing or fuselage after the load test or after the flight test. The results of the wingtip loading test are shown in Table 8.1.

Table 8.1: Wingtip loading test results

	Mk.1 Wingtip Test	Mk.3 with M2 Payload Wingtip Test	Mk.3 Extreme Weight Wingtip Test
Empty Weight with Battery (lbs)	7.5	6.4	8.032
Payload Weight (lbs)	5.5	6.33	7.968
Gross Weight	13	12.73	16
Results	Fail	Pass	Pass

The desired M2 payload of 6.33 pounds was used as a baseline for comparison for wingtip loading tests. The aircraft must survive a 2.5g load test during the competition under this desired M2 max payload condition. While the Mk.1 wing failed to meet this requirement, the Mk.3 wing passed this case with minimal flexing. It was previously predicted that, when subjected to the extreme weight case, the aircraft would be able to survive due to structural improvements made to the wing, including additional shear webs and elongated carbon fiber spars as discussed in Section 7.1.3. Upon testing, it was found that the aircraft was able not only to survive the wingtip test, but also to complete the full M2 flight course with this payload.

8.1.1 Subcomponent Tests

Table 8.2 shows a subcomponent-specific test card used for verification of mission subcomponent functions.

Table 8.2: Subcomponent function verification test card

Subcomponent Test	Pass / Fail	Test Notes
The sensor shall have a minimum diameter of 1 inch with a length 4x its diameter	P	Sensor diameter is 1.05 inches Sensor length is 4.25 inches
The sensor shall be deployed a minimum distance of 10x its length from the exit location of the aircraft	P	Sensor deployment length is 43 inches
The sensor shall have at least 3 working visible lights	P	Sensor has 4 LED lights
The sensor lights shall flash in a series configuration (pattern determined by team)	P	Lights flash in a rectangular pattern
The sensor shall be operated and controlled by use of an external tow cable.	P	Lights are operated by a cable connected to the aircraft
The sensor lights shall turn on/off remotely.	P	Lights are controlled via a remote transmitter
The towing mechanism shall fit in the cargo bay in specified storage configuration during M2.	P	Mechanism is stored securely during flight

Shipping Containers

It was predicted that the shipping container would provide adequate shock absorption for the sensor during the drop test and would remain securely in place inside the fuselage during all flight tests. When implemented in the Mk.3 flight tests, the shipping container performed as expected by not shifting from its set position when checked before and after flight. Additionally, the container provided sufficient protection to the sensor when dropped from 10 inches onto each of its six sides.

Sensor

The sensor lights were designed to flash one at a time in a rectangular pattern, bright enough to be viewed from the ground during flight tests. After conducting a sensor electronics test, it was found that the sensor lights performed as expected; the lights were sufficiently bright to be viewed from a distance and could be turned on and off remotely, as required by the competition rules. During initial testing out of a car window as described in Section 7.1.1, the sensor also demonstrated aerodynamic stability by maintaining a fixed orientation without spinning or rotating.

Deployment and Recovery Mechanism

The deployment and recovery mechanism was required to fit inside of the fuselage in a stowed configuration during M2. The mechanism was also predicted to fully deploy the sensor 10x its length from the fuselage. After manufacturing, the mechanism's complete extended deployment length was measured to be 43 inches, slightly longer than required and therefore satisfying mechanism requirements.

8.2 Complete Aircraft Solution

Figure 8.2 shows the flight path for the M1 detailed flight test flown by the Mk.3 aircraft, overlaid with the course sketch provided in the competition rules [1].

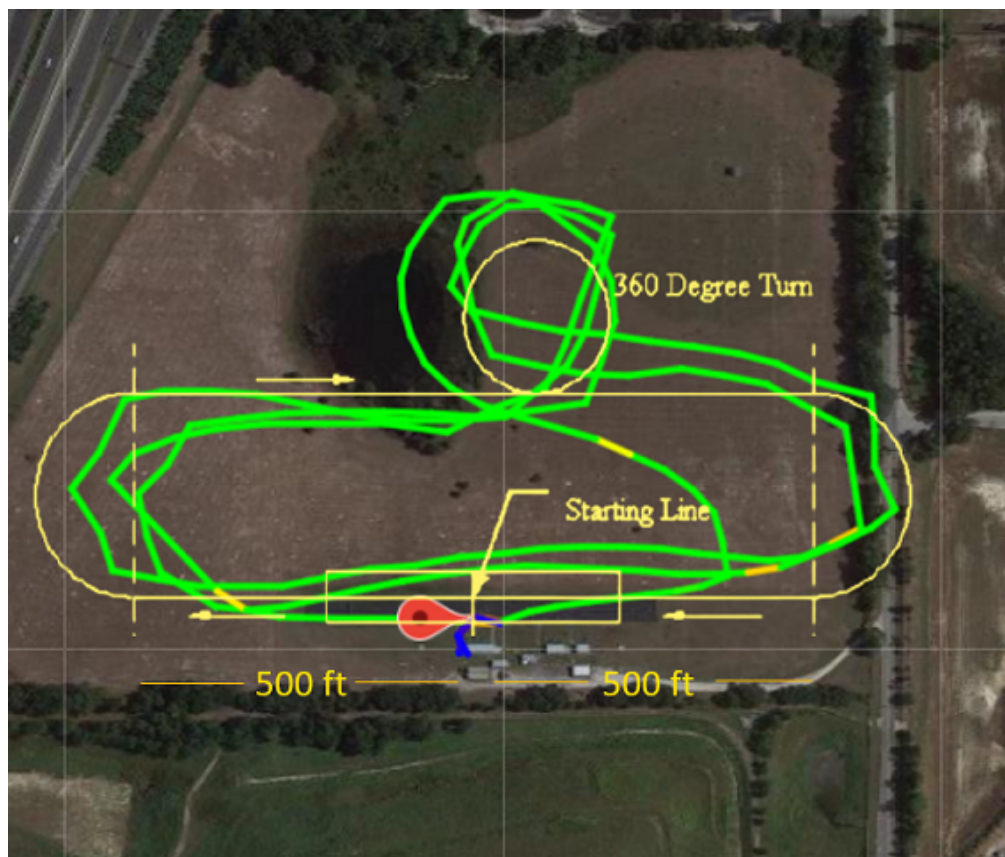


Figure 8.2: M1 flight path (using GPS data) compared with the provided course sketch

Mk.3 completed the course in 85 seconds with an average lap time of 28.33 seconds. For the purpose of data collection,

takeoff was not included in the initial lap time. Uncertainty due to rough visual estimation of the flight course by the pilot resulted in a decreased lap 3 flight distance, but the overall data was deemed a valid baseline for future detailed flight tests. Detailed flight testing for M2 was conducted in a similar manner, with Mk.3 completing the course in 94 seconds with an average lap time of 31.33 seconds (once again, takeoff was not included in the initial lap time).

Using test flight data from the Mk.3 detailed flight tests, a comparison was performed with the predicted mission parameters gathered from design studies. Per the testing plan, an M3 detailed flight test has not yet occurred, but estimated performance was calculated via an approximated system drag coefficient (using sensor and deployment mechanism drag values obtained during CFD analysis and calculated M1 aircraft drag). The results of this comparison are shown in Table 8.3.

Table 8.3: Detailed flight test results

	Parameter	Predicted	Flown	Δ%
Mission 1	Flight Speed (mph)	40	55.96	+39.9%
	Cruise Current (A)	70.739	30.962	-56.23%
	Takeoff Distance (ft)	5.1022	5	-2%
	Mission Completion (s)	112	85	-24.11%
Mission 2	Flight Speed (mph)	41	50.368	+22.84%
	Cruise Current (A)	71.975	33.995	-52.77%
	Takeoff Distance (ft)	30.5616	35	+14.52%
	Payload Weight (lbs)	6.09	5.862	-3.74%
	Mission Completion (s)	110	94	-14.54%
	Absolute Mission Score (containers / sec)	0.0272	0.03184	17%
Mission 3	Flight Speed (mph)	54.6	46.46 (estimated)	-14.91%
	Cruise Current (A)	13.199	21.16 (estimated)	+60.32%
	Takeoff Distance (ft)	17.058	20 (estimated)	+17.24%
	Payload Weight (lbs)	2.9	2.734 (estimated)	-6.07%
	Number of Laps	21	17.6 (estimated)	-16.19%
	Absolute Mission Score (lbs * in * laps)	124.95	92.30 (estimated)	-26.13%

Knightmobile Mk.3 was flown approximately 40% faster than expected for M1 and 20% faster than expected for M2, resulting in a score increase of 17% compared to the predicted results. It was noted that the potential M1 flight speed was intentionally underestimated during predictions due to the relaxed conditions of the flight; however, pilot experience allowed for aircraft control authority at a significantly higher velocity than expected during M2. The estimated M3 performance resulted in an updated score prediction that was 26.13% lower than initially predicted in Section 4.4. This was considered a consequence of an initial underestimate of the sensor deployment and recovery mechanism drag coefficient. A resulting decrease of 16% in the estimated number of laps flown during M3 accounts for the bulk of the discrepancy between the predicted and estimated M3 scores. An M3 simulation test flight is planned to be flown in late February per the testing schedule outlined in Section 7 to validate these estimates.

For the detailed M2 flight test, a gross aircraft weight of 12.64 pounds was flown, including a payload of three shipping containers as well as a 0.816 pound battery. The total mission time was 94 seconds, which was 16 seconds faster than predicted. During the three laps, roughly 900 mAh was drained from the 2200 mAh battery. The results of the flight test reveal a potential opportunity to further maximize score during M2 by analyzing ways to utilize the leftover battery energy. Increasing flight speed or the number of shipping containers carried will be considered, as well as a potential decrease in battery size to decrease weight and increase flight speed. For example, moving to a 1250 mAh battery would decrease battery, and therefore total aircraft, weight by approximately 0.35 pounds with no decrease in performance.

Given these results, a trade study was conducted by comparing the experimental data from the detailed M2 flight test to the exploratory structural extreme payload case discussed in Section 8.1. The gross weight of 16 pounds flown in the higher

payload case simulated carrying the weight of roughly four total shipping containers. This comparison is presented in Table 8.4.

Table 8.4: Extreme payload case vs M2

	Detailed M2 Flight Test	Extreme Payload Case Flight Test	Δ%
Payload Weight (lbs)	5.862	7.968	+ 35.93%
Number of Containers	3	4	+ 33.33%
Cruise Velocity (mph)	50.36	53.4	+ 6.04%
Flight Duration (sec)	94	89	- 5.32%
Absolute Mission Score (containers / sec)	0.0318	0.0449	+ 41.19%

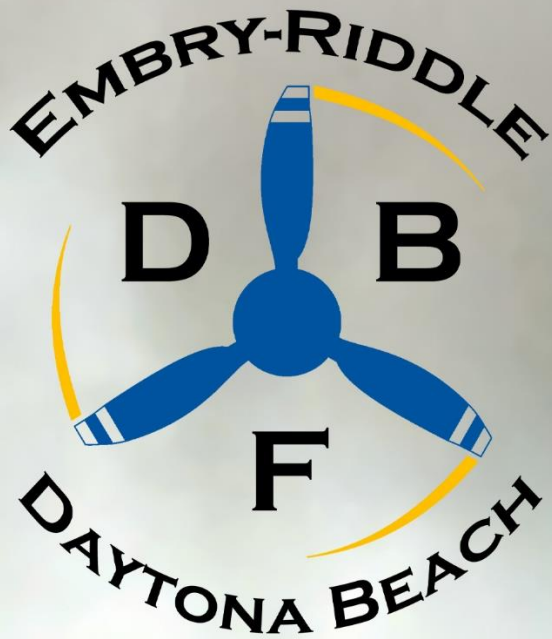
Using the same battery as in the M2 flight test, the pilot was able to fly three laps in 89 seconds, which was a flight time decrease of 5 seconds. This was attributed to a velocity increase due to the pilot taking advantage of more of the available battery energy by increasing throttle after observing the excess battery energy that went unused during the M2 flight test. This resulted in an increase of approximately 100 mAh used between the two tests, from 900 mAh to 1000 mAh. The 41.19% score increase between the detailed and extreme payload case flight tests reflects a significant improvement in M2 performance compared to the predictions. The aircraft has higher capabilities than expected, both due to structural improvements made during manufacturing that increased the payload weight capacity of the aircraft and to improved stability between the Mk.2 and Mk.3 aircraft, which afforded the pilot sufficient control authority even under extreme load at high velocity. However, it was noted that further investigation into the takeoff distance performance of the extreme payload configuration is required. During the flight test, the takeoff distance estimate appeared dangerously close to the 100 ft takeoff distance limit.

8.3 Concluding Remarks

It has been proven that the Mk.3 aircraft is capable of flying the first two missions for competition, with potential design parameter improvements to increase M2 score in consideration. Upon completion of the manufacturing plan for the lead sensor caps as discussed in Section 6.3.4, a detailed M3 flight test is scheduled to be conducted in late February. The results of this test will be used to perform high-fidelity analysis to consider and implement further improvements to the sensor deployment and recovery mechanism for optimization of M3 score. A final aircraft design, Knightmobile Mk.4, will be manufactured for the competition using the knowledge gained from testing and analysis of the previous design iterations. This aircraft will fly final, detailed mission simulations in order to verify competition readiness.

9. Bibliography

- [1] AIAA, "2020-2021 DBF Rules," Reston, VA, 2020.
- [2] M. Drela, "XFOIL," MIT, 2013. [Online]. Available: <http://web.mit.edu/drela/Public/web/xfoil>. [Accessed 1 February 2021].
- [3] Sadraey, Mohammad. Chapter 5 Wing Design. Daniel Webster College, 2015, Available: wpage.unina.it/fabrnico/DIDATTICA/PGV_2012/MAT_DID_CORSO/09_Progetto_Ala/Wing_Design_Sadraey.pdf.
- [4] Nita, M., and Scholz, D., "Estimating the Oswald Factor from Basic Aircraft Geometrical Parameters" Available: https://www.fzt.haw-hamburg.de/pers/Scholz/OPerA/OPerA_PRE_DLRK_12-09-10_MethodOnly.pdf.
- [5] "Wing Taper Considerations," MIT OpenCourseWare Available: <https://ocw.mit.edu/courses/aeronautics-and-astronautics/16-01-unified-engineering-i-ii-iii-iv-fall-2005-spring-2006/systems-labs-06/spl8a.pdf>.
- [6] "Performance Data," APC Propellers Available: <https://www.apcprop.com/technical-information/performance-data/>.
- [7] "XFLR5," [Online]. Available: <http://www.xflr5.com/xflr5.htm>.
- [8] ANSYS, "ANSYS Fluent - CFD Software | ANSYS" Available: <http://www.ansys.com/products/fluids/ansys-fluent>.
- [9] M. Drela and H. Youngren, "AVL," web.mit.edu, 2017. [Online]. Available: <http://web.mit.edu/drela/Public/web/avl/>.
- [10] Yechout, T. R., Introduction to aircraft flight mechanics: performance, static stability, dynamic stability, classical feedback control, and state-space foundations, Reston, VA: American Inst. of Aeronautics and Astronautics, 2014.
- [11] MIL-F-8785C, Flying Qualities of Piloted Planes, Military Specification, 1980.
- [12] "SolidWorks," Dassault Systemes, [Online]. Available: <https://www.solidworks.com/>
- [13] Borrega, Marc, and Lorna J. Gibson, "Mechanics of Balsa (Ochroma Pyramidale) Wood," Mechanics of Materials, 2015, pp. 75–90.
- [14] Forest Products Laboratory, "Properties of Normal Wood Compared with Plywood," Madison, Wisconsin, USDA Forest Service, 1952.
- [15] "Evaluating the Mechanical Properties of Commonly Used 3d Printed ABS and PLA Polymers with Multi Layered Polymers," International Journal of Engineering and Advanced Technology, vol. 8, 2019, pp. 2351–2356.
- [16] Dielectric Manufacturing, "Material Properties of Acrylic – An Insulating Thermoplastic," Dielectric Manufacturing Available: <https://dielectricmfg.com/knowledge-base/acrylic-thermoplastic/>.
- [17] Davis, J. R., "Properties of Lead," Metals handbook: desk edition, Materials Park, OH: ASM International, 1998.
- [18] Dimension Engineering, "DELIGHT Starter Kit," [Online]. Available: <https://www.dimensionengineering.com/products/delight-starter-kit>.



STAT

AIAA DESIGN, BUILD, FLY
2020 – 2021
DESIGN REPORT

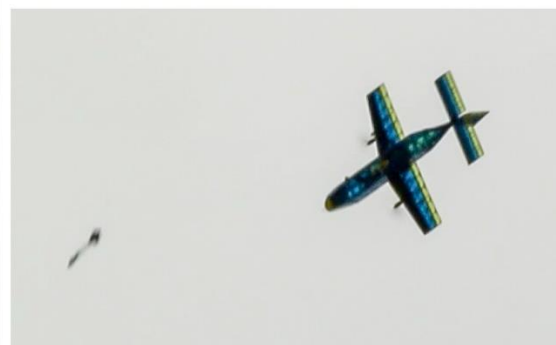




Table of Contents

Nomenclature	3
1 Executive Summary	4
1.1 Aircraft Design Summary	4
1.2 Performance Capabilities	4
2 Management Summary	5
2.1 Milestones	5
3 Conceptual Design	6
3.1 General Requirements and Restrictions	6
3.2 Scoring Analysis	9
3.3 Configurations Considered	11
3.4 Configuration Selection Process	13
4 Preliminary Design	14
4.1 Design Methodology	14
4.2 Design Trade Studies	15
4.3 Lift and Drag	18
4.4 Stability and Control Analysis	21
4.5 Estimated Mission Performance	24
5 Detail Design	26
5.1 Final Dimensional Parameters	26
5.2 Structural Design Methodology and Characteristics	27
5.3 Landing Gear	31
5.4 Weight and Balance	36
5.5 Mission Performance	37
5.6 Drawing Package	38
6 Manufacturing	43
6.1 Manufacturing Processes	43
6.2 Manufacturing Processes Selection	43
6.3 Manufacturing Milestones	45
7 Testing Plan	45
7.1 Test Objectives	45
7.2 Subsystems Testing	46
7.3 Test Schedule	48
7.4 Test Checklists	49
8 Performance Results	50
8.1 Components and Subsystems	50
8.2 Complete Aircraft Performance	54
Bibliography	56



Nomenclature

Symbols

α	Angle of Attack
V_∞	Freestream Velocity
C_L	Coefficient of Lift
C_D	Coefficient of Drag
C_M	Coefficient of Moment
$C_{M_{C_L}}$	Stability Derivative WRT C_L
C_{M_α}	Stability Derivative WRT α
$C_{l_{\delta_a}}$	Aileron Control Power
C_{l_p}	Roll Damping
C_{l_β}	Lateral Stability Derivative
C_{n_β}	Directional Stability Derivative
P_{δ_a}	Aileron Roll Rate
ω_n	Natural Frequency
ζ	Damping Ratio
λ	Eigenvalue
S	Wing Area
L/D	Lift to Drag Ratio
T/W	Thrust to Weight
W/S	Wing Loading

Units

A	Amp
deg	degree
ft	foot
h	hour
in	inch
lb	pound
mAh	milliamp hour
min	minute
oz	ounce
psi	pounds per square inch
rpm	rotations per minute
s	second
V	Volt
W	Watt

Abbreviations

AIAA	American Institute of Aeronautics and Astronautics
CAD	Computer Aided Design
CCW	Counter-Clockwise
CG	Center of Gravity
CNC	Computer Numerical Control
CW	Clockwise
DBF	Design, Build, Fly
DWG	Drawing
ERAU DB	Embry-Riddle Aeronautical University - Daytona Beach
ESC	Electronic Speed Control
FEA	Finite Element Analysis
FS	Fuselage Station
GM	Ground Mission
GPS	Global Positioning System
HT	Horizontal Tail
LED	Light-Emitting Diode
LiPo	Lithium Polymer
M#	Mission #
MAC	Mean Aerodynamic Chord
MSL	Mean Sea Level
NACA	National Advisory Committee for Aeronautics
NTS	Not to Scale
PWM	Pulse-Width Modulation
QTY	Quantity
REV	Revision
SDRM	Sensor Deployment and Release Mechanism
STAT	Sensor Towing Air Tractor
UAV	Unmanned Aerial Vehicle
VT	Vertical Tail
WRT	With Respect To



1 Executive Summary

This report discusses the design and analysis of Embry-Riddle Aeronautical University - Daytona Beach's aircraft for the 2020–2021 AIAA Design, Build, Fly Competition, STAT (Sensor Towing Air Tractor). The UAV was designed to perform all four AIAA missions, including a ground mission and three flight missions. The first flight mission proves the flight characteristics of the aircraft. The second is a flight simulating the delivery of multiple sensors to the deployment zone. The third flight deploys, operates, and retracts a towed sensor in flight.

The aircraft was designed, manufactured, and tested by a team of 25 students. The conceptual design was centered on analyzing the mission requirements along with a scoring analysis which drove selection of the overall aircraft configuration best suited to the missions. The preliminary design sized the chosen aircraft configuration and provided initial weights, power requirements, performance, and dynamic stability behavior. The detail design finalized the internal aircraft structure, the propulsion system, and initial subsystems for sensor operation and storage. The manufacturing team constructed the airframes using laser cut, 3D-printed, and composite materials. The aircraft was manufactured to be lightweight but robust enough to sustain a high maneuver load factor at maximum weight while performing aggressive turns with good agility. Through the flight test plan, every subsystem of the aircraft was tested to ensure adequate performance. Any issues with subsystems or mechanisms were determined during ground and flight tests and corrected on subsequent iterations of the aircraft.

1.1 Aircraft Design Summary

The selected aircraft configuration was a conventional, twin-motor, high-wing airplane with tricycle landing gear. This configuration provided enough volume in the fuselage to hold the design goal of eight sensor containers and still have excess capacity for the sensor deployment and release mechanism (SDRM). The twin motor configuration provided ample thrust to overcome the sensor drag and achieve satisfactory flight at maximum takeoff weight. This configuration also provided the capability to quickly complete the required laps, which was essential for maximizing the scores in Mission 2 and Mission 3. The propulsion system was designed to fit the maximum available power and capacity on the aircraft to achieve the requirements of Mission 3.

1.2 Performance Capabilities

A total of 14 flight tests over multiple days and wind conditions were conducted to evaluate and measure the performance capabilities of the aircraft. For Mission 2, the aircraft was designed to carry eight sensor containers and complete three laps in 1.94 minutes. As tested, the aircraft was able to adequately carry the sensor containers and complete three laps within 1.75 minutes. Additionally, ground test data indicated the ability to increase capacity to 18 sensor containers. For Mission 3, the predicted performance was to fly 17 laps while towing a sensor and take off in 38.5 ft. During flight tests, the aircraft was shown to have a 25.0-ft takeoff distance and completed 15 laps. Further refinements of the aircraft in the subsequent iterations will improve on the mission scores before the actual competition.

2 Management Summary

The 2020–2021 ERAU DB DBF team comprised 25 students, ranging from freshmen to seniors, with a faculty advisor and six team leads to organize the sub-teams. There were four different teams that worked under the Team Lead and the Chief Engineer, which included Manufacturing, Flight Test, Production Design, and Finance. The Team Lead ensured that the project remained on schedule, worked with the other leads to delegate tasks, and served as the main point of contact for the team. The Chief Engineer oversaw the design team and approved any changes that needed to be made to the aircraft. The Finance Lead was responsible for purchasing items and tracking the budget. The Manufacturing Lead led a team who constructed each iteration of the aircraft and subsystems. The Flight Test Lead organized the testing and collection of data for the aircraft. The Production Design Lead created all the CAD models of the aircraft and prepared files for 3D printing and laser cutting. The leadership team met using video conferences and in-person meetings. Figure 2-1 shows the leadership structure of the team with general members participating in the manufacturing, flight test, and production design teams. During the design, manufacturing, and flight test stages, all members were encouraged to contribute to the project by designing subsystems, constructing the aircraft, assisting with flight test operations, and writing the report.

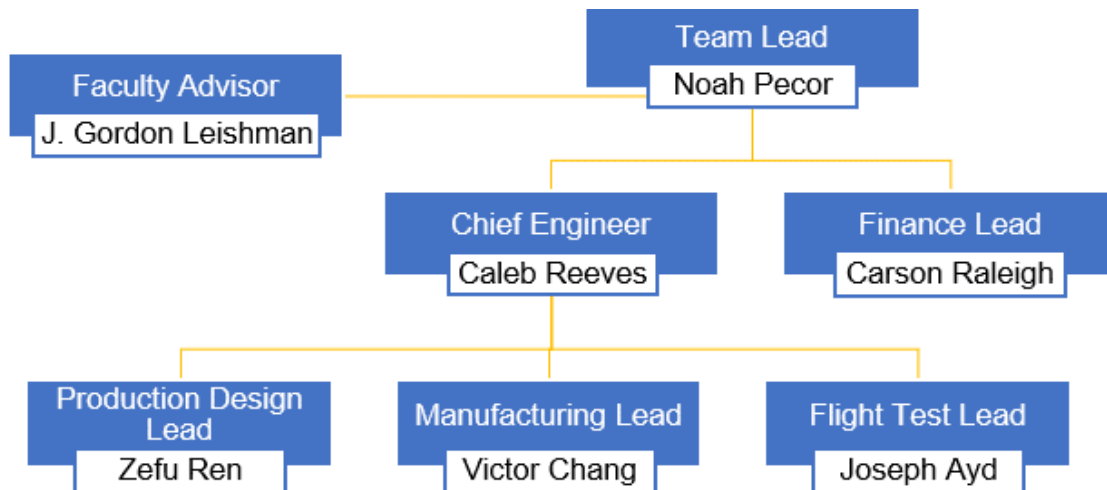


Figure 2-1: Management structure.

2.1 Milestones

A schedule was defined at the start of the Fall 2020 semester that outlined the major goals and a timeline of events and milestones. The timeline was designed so that three iterations of the aircraft could be manufactured and tested before the competition, with the third airframe being the competition version. The developed schedule allowed teams to work in parallel so that flight test data could be acquired while another iteration of the aircraft was being built. The team worked throughout the year, meeting four times a week to work on the aircraft, with flight tests occurring on weekends. The Team Lead and Chief Engineer updated the faculty advisor on progress during weekly meetings. Figure 2-2 shows the major timelines and milestones summarized in the form of a Gantt chart.

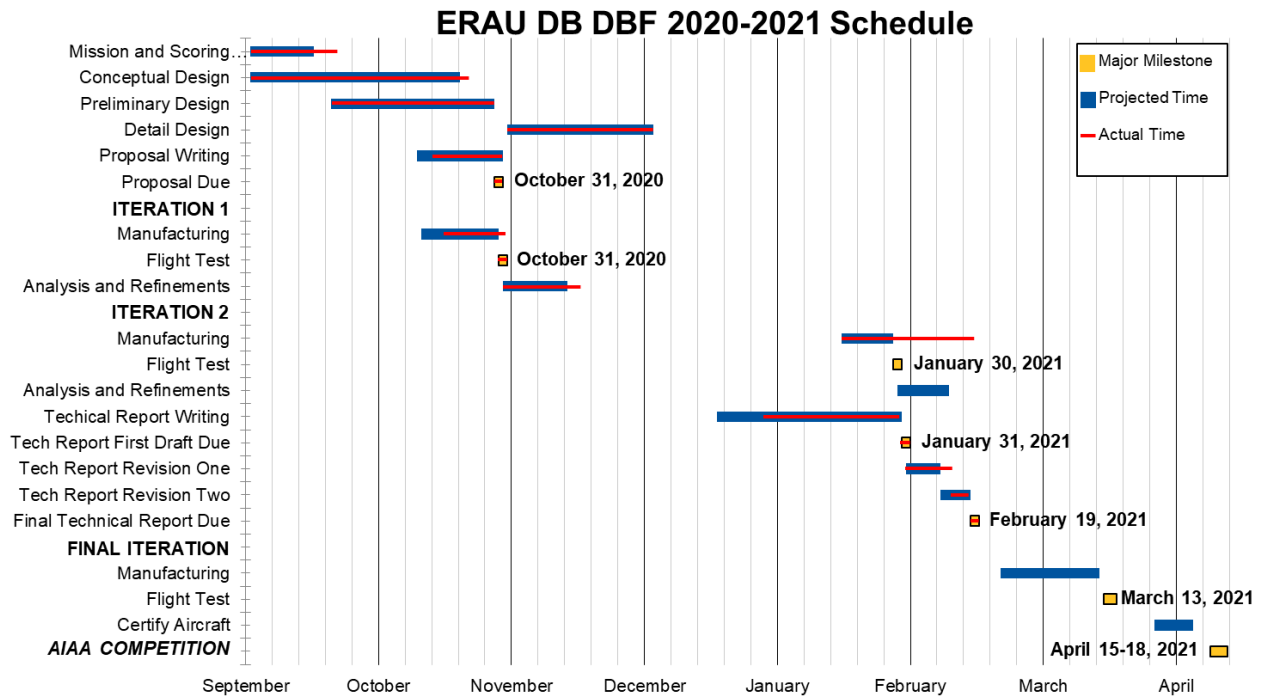


Figure 2-2: Major milestone Gantt Chart.

3 Conceptual Design

The goal of the conceptual design phase was to select an aircraft configuration that maximized the mission scores. This was accomplished through requirements, restrictions, and scoring sensitivity analysis to create subsystem goals and requirements that could be applied to configuration selection.

3.1 General Requirements and Restrictions

The following sections detail the specific requirements and limitations of the sensor towing UAV, which pertain to the delivery flight, the sensor flight, and the ground mission.

3.1.1 Aircraft

The wingspan was limited to 5 ft under the AIAA rules [1]. Additionally, the aircraft must fully contain the SDRM for Mission 2 and Mission 3, the sensor containers for Mission 2, and the sensor for Mission 3. The propulsion system was limited to an electrically driven propeller powered by a 200 Wh battery pack. Lastly, the aircraft must take off within a 100-ft ground roll.

3.1.2 Sensor Container

The sensor container must house the towed sensor for transport in Mission 2. According to the rules, the shipping container must fully enclose and protect the sensor from a 10-in drop test in the Ground Mission. Sensor container simulators used to increase the Mission 2 score must be the same weight and size as the actual shipping container.

3.1.3 Sensor

The sensor must have a minimum diameter of 1.00 in and a minimum length-to-diameter ratio of 4:1. The sensor must remain aerodynamically stable during all phases of flight. The functionality of the sensor must



include three separate internal lights visible from the ground, which must be powered by a battery internal to the sensor and controlled using a hardwire to the airplane. When not in use, the sensor must be carried internal to the aircraft.

3.1.4 Sensor Deployment and Recovery Mechanism

The SDRM must be carried inside the airplane for Mission 2 and Mission 3, although not necessarily in the same configuration. The distance of sensor deployment from the exit of the aircraft must be at least 10 times the sensor's length.

3.1.5 Ground Mission

The Ground Mission aimed to test the aircraft and ground crew's ability to perform Mission 2 and Mission 3 objectives. The first task was to validate the durability of the sensor and the shipping container, accomplished by dropping the container from a height of 10 in on all six sides. Following the drops, it must be demonstrated that the sensor has not experienced damage and remains functional. The Ground Mission must then be timed starting with the loading of the full Mission 2 payload. Then, the crew members remove the Mission 2 payload and prepare the aircraft for Mission 3 by installing the SDRM. Finally, an untimed demonstration of the deployment and recovery of the sensor concluded the Ground Mission. Equation 1 gives the score for the Ground Mission, where the fastest team's score is normalized resulting in a score of one; all other teams score less than one. Table 3-1 summarizes the Ground Mission requirements and subsequent team subsystem requirements.

$$\text{Ground Mission Score} = (\text{Fastest time})/(\text{Team time}) \quad (1)$$

Table 3-1: Ground Mission requirements.

Type	Requirement
Mission	Demonstrate shipping container and sensor durability via drop test
Mission	Ground mission box must be a 10 ft by 10 ft square
Mission	The aircraft must be in flight configuration in the mission box with the following to be stored: sensor in shipping container, container simulators, and deployment mechanisms
Mission	Prove flight controls are active, demonstrate Mission 2 payload, and Mission 3 sensor deployment
Subsystem	Container loading system that allows for quick removal/replacement
Subsystem	Door or hatch required for easy payload accessibility

3.1.6 Mission 1

Mission 1 served as a proof of flight consisting of three laps around the course shown in Figure 3-1. No payload was required for this mission. Therefore, it was scored on the successful completion of the flight within the time window, as shown in Equation 2. Table 3-2 summarizes the Mission 1 requirements.

$$\text{Mission 1 Score} = \begin{cases} 1, & \text{Completion} \\ 0, & \text{Failure} \end{cases} \quad (2)$$

Table 3-2: Mission 1 requirements.

Type	Requirement
Mission	Take off within a 100-ft field length
Mission	Complete three laps within a five-minute flight window
Mission	Successful landing

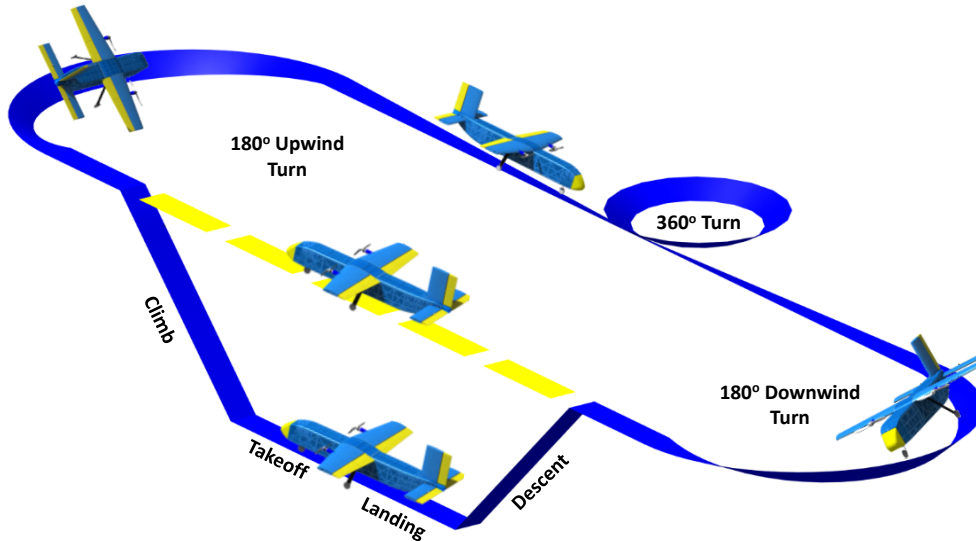


Figure 3-1: Flight lap pattern.

3.1.7 Mission 2

Mission 2 was a demonstration of the cargo carrying capability of the aircraft. Three laps around the same course as Mission 1 must be completed within five minutes. The sensor in the shipping container, shipping container simulators, and SDRM must be loaded before the flight. The number of shipping container simulators could not exceed the maximum amount determined at the technical inspection. The score for Mission 2 is a function of the number of containers carried and the time to complete three laps, shown in Equation 3. Table 3-3 summarizes the Mission 2 requirements.

$$\text{Mission 2 Score} = 1 + \left(\frac{\text{Number of containers}}{\text{Time to fly 3 laps}} \right)_{\text{Team}} \Bigg/ \left(\frac{\text{Number of containers}}{\text{Time to fly 3 laps}} \right)_{\text{Max}} \quad (3)$$

Table 3-3: Mission 2 requirements.

Type	Requirement
Mission	Take off within a 100-ft field length
Mission	Complete three laps within a five-minute flight window (landing is not included)
Mission	Successful landing
Subsystem	The fuselage must have ample space to enable weight shifting capability to maintain desired CG
Subsystem	The container restraint system must support payload inertial loads
Subsystem	Relocation of SDRM to accommodate sensor containers



3.1.8 Mission 3

Mission 3 was a sensor flight demonstration. The sensor and SDRM must be configured accordingly inside the aircraft before takeoff. The sensor must fully deploy before the first 360-degree turn, shown in Figure 3-1. The goal of this mission was to fly as many laps as possible in 10 minutes, after which the sensor must be fully recovered into the aircraft before landing. Other factors that contribute to the score are the sensor length and weight, as shown in Equation 4. Table 3-4 summarizes the Mission 3 requirements.

$$\text{Mission 3 Score} = 2 + \frac{(W_{\text{sensor}} \times l_{\text{sensor}} \times n_{\text{laps}})_{\text{Team}}}{(W_{\text{sensor}} \times l_{\text{sensor}} \times n_{\text{laps}})_{\text{Max}}} \quad (4)$$

Table 3-4: Mission 3 requirements.

Type	Requirement
Mission	Take off within a 100-ft field length
Mission	Fully deploy sensor before the first 360-degree turn
Mission	Successfully recover the sensor inside the aircraft before landing
Mission	Successful landing
Subsystem	Arrange fuselage cargo space and deployment mechanisms to prioritize sensor length
Subsystem	Ensure structural integrity of tow cable mechanisms to support sensor inertial loads
Subsystem	Prioritize reliability and simplicity in deployment and recovery mechanisms

3.2 Scoring Analysis

A scoring analysis helped the team identify which scoring parameters have the largest effect on the mission scores, allowing the team to alter requirements by prioritizing parameters to ensure a more competitive aircraft. The team considered two different scoring analysis approaches, which resulted in a similar conclusion.

The first method was based on an energy cost-benefit analysis. This approach weighed the energy cost of increasing a scoring parameter with its respective increase in score, where the primary performance constraint was the amount of potential energy available to the aircraft through the batteries. This method was beneficial because the amount of work the aircraft could do was limited by the maximum energy density. Table 3-5 shows that increasing the aircraft's cruise velocity to improve the mission score is more expensive than increasing the weight and length of the sensor and the number of containers.

The second analysis method involved the quantification of diminishing returns of the given scoring equations. The ground mission scoring was excluded from the study because it depended on the flight crew's skills and was not a direct design criterion. However, increasing payload weight and size inherently increases loading time, potentially reducing the ground mission score.

Table 3-5: Energy expense analysis of scoring parameters.

	Parameter		Variation	Cost	Benefit
Mission 2	Number of Containers	n_c	Linear increase in weight and volume	Linear increase in energy consumption	Linear score increase
	Time	t	Increase in flight velocity	Quadratic increase in energy consumption	Linear score increase
Mission 3	Number of Laps	n_{laps}	Increase in flight velocity	Quadratic increase in energy consumption	Linear score increase
	Sensor Length	l_{sensor}	Linear increase in volume and drag	Linear increase in energy consumption	Linear score increase
	Sensor Weight	W_{sensor}	Linear increase in weight	Linear increase in energy consumption	Linear score increase

Figure 3-2 shows the normalized score changes when the other teams at the competition have achieved a given maximum raw score.

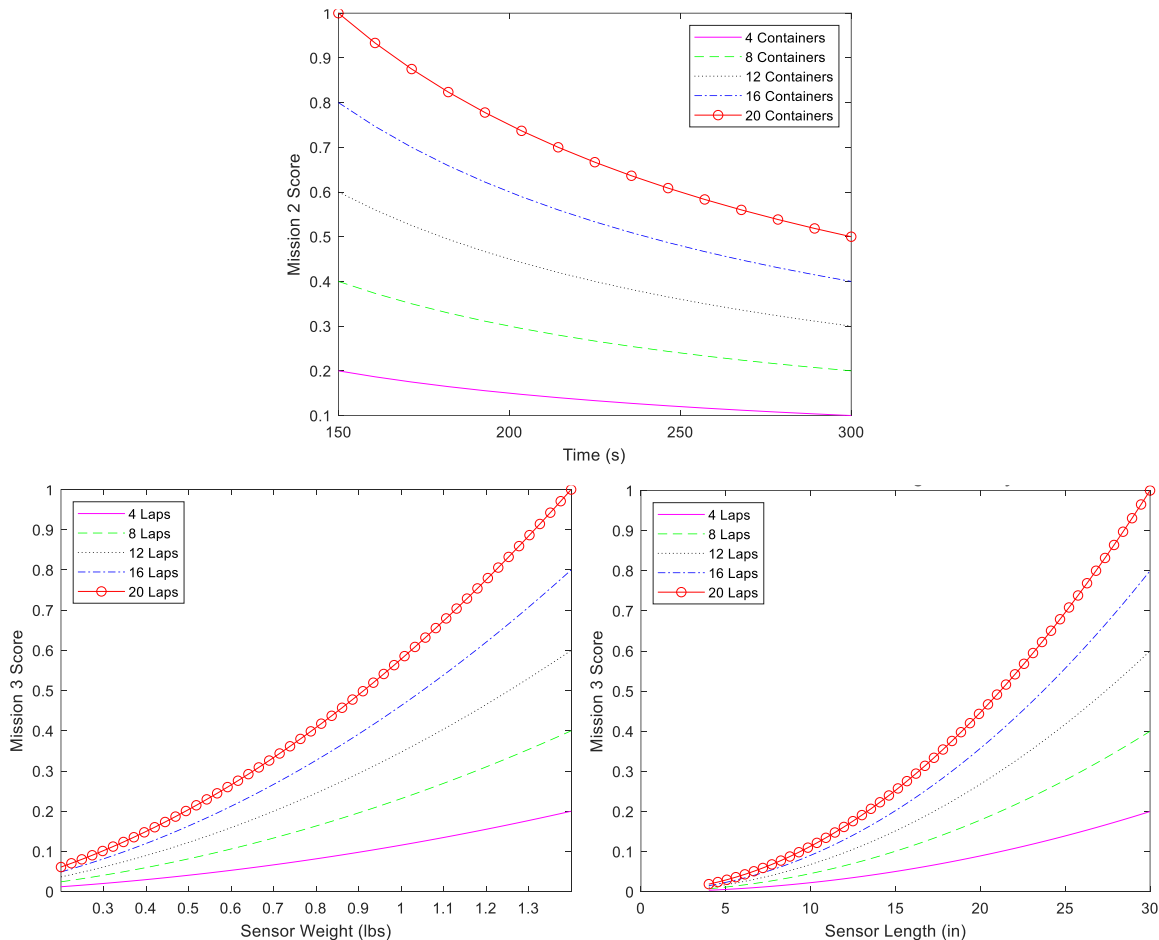


Figure 3-2: Mission 2 (top) and Mission 3 (bottom) scoring sensitivity.

For Mission 2, increasing the number of sensor containers being carried had a greater effect than increasing lap time across most of the scoring range. However, lap time became more significant as the number of

sensors approached the maximum. For Mission 3, increasing sensor length and sensor weight had a larger effect when the lap numbers approached the maximum. Both scoring analyses suggest that a design that prioritizes payload volume, length, and lifting capability over aircraft speed would be more successful.

3.3 Configurations Considered

An aircraft's design is always tailored for a specific mission or set task(s) but follows realistic constraints. To meet the mission objective, high power, high lifting capability, and generous payload section are favorable design traits for the aircraft but are limited by wingspan and power plant constraints. Out of the many configurations available, three were considered and compared to select the best aircraft to excel at mission criteria. They consisted of conventional, canard, and twin-boom configurations. These configurations are further discussed below.

The twin-engine layout was chosen for all configurations because of its many advantages. Twin motors create more space in the fuselage and allow for a simplified nose cowl and reduced fuselage structure, compared to a single-engine design. However, this advantage is slightly offset by additional wing structure. Twin motors and propellers can be spun in opposite directions to cancel out unfavorable lateral aerodynamic forces and moments such as P-factor, improving overall aircraft stability and handling qualities. One of the greatest advantages of twin electric aircraft with large propeller disk areas is the “blown wing” effect: at low airspeeds and high throttle settings, the propellers considerably increase the dynamic pressure at the wing, improving lift and control authority [2].

3.3.1 Conventional Twin

The first conceptual design considered was a twin-engine monoplane with a conventional tail and fuselage arrangement, shown in Figure 3-3. This configuration's primary advantage was a large payload volume to accommodate a long sensor for Mission 3 and several sensor containers for Mission 2. Additionally, a large payload bay allowed for increased flexibility in designing the SDRM. To compensate for the adverse effect of a long, wide fuselage on the aircraft's longitudinal stability, a particularly large horizontal tail was proposed to ensure a neutral point of about 50% of the MAC. This was satisfied by a later stability analysis.

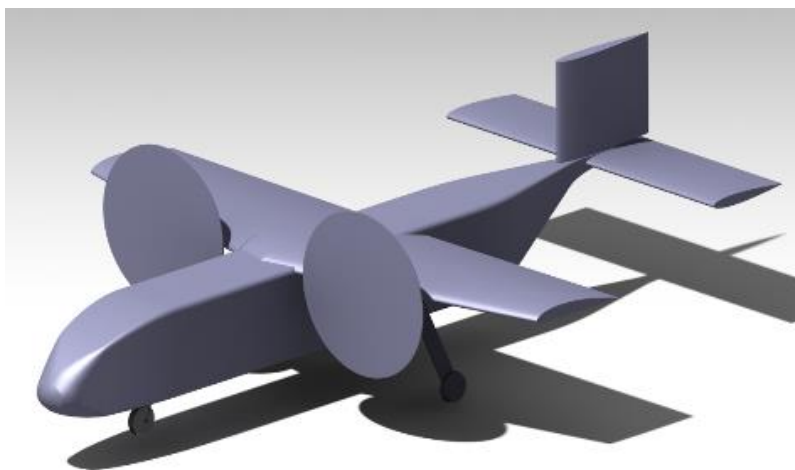


Figure 3-3: Conventional twin configuration.

The high wing configuration took advantage of the large fuselage side area in the form of dihedral effect. The dihedral effect in a high-wing aircraft is a stabilizing rolling moment produced by the wing-body flow interference in a sideslip. This behavior would allow a straight wing with no dihedral to be used, simplifying manufacturing significantly and improving structural efficiency. A wing without dihedral could take full advantage of modern composite materials using a straight carbon fiber tube with no complex breaks or bends, which would increase weight and manufacturing complexity considerably.

This design's significant concern was potentially high drag from its large fuselage wetted area. The tail's large upsweep also had the potential for large pressure drag from boundary layer separation. The square cross-section maximized the internal volume while minimizing the fuselage width to improve stability. Still, the square shape had the potential to become a bluff body at high angles of attack. A significant increase in drag at high angles of attack can accelerate the onset of stall from a rapid reduction in airspeed. To resolve this, the wing incidence could be increased to reduce the fuselage's relative angle of attack.

3.3.2 Canard

Next, the canard configuration, shown in Figure 3-4, was considered. The primary advantage of this configuration was its potential for increased CG location flexibility, which is desirable for both the Mission 2 and Mission 3 payload configurations. An aerodynamics analysis showed that the configuration would remain stable at wide ranges in CG as the neutral point was located well after the leading edge. Another advantage of the canard configuration was its potential for greater aerodynamic efficiency. A higher aspect ratio, a lifting canard for trim, and a more streamlined fuselage would result in higher lift to drag ratios across all missions.

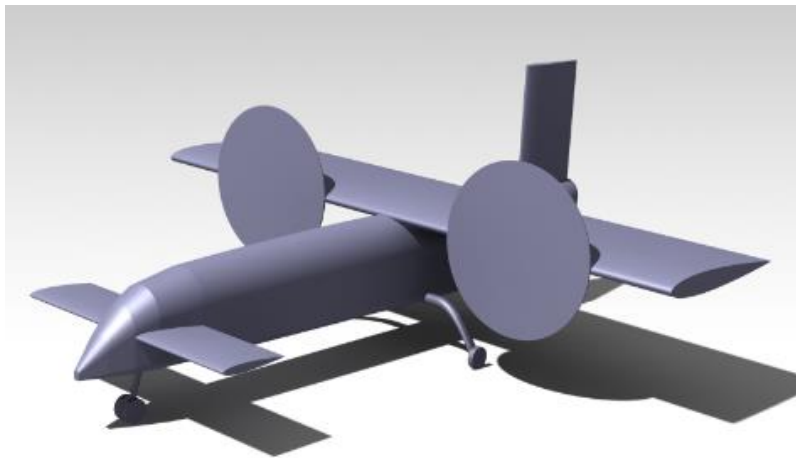


Figure 3-4: Canard configuration.

A canard configuration, however, presented multiple challenges compared to a traditional configuration. For instance, the canard must stall before the wing to make the aircraft recoverable. This challenge inherently reduces the aircraft's maneuverability because of its instabilities at high angles of attack. To solve this, the canard airfoil needed to be different from the wing airfoil with the canard having a lower stall angle

of attack. Additionally, the two horizontal surfaces needed to have different angles of incidence, which would greatly increase manufacturing complexity.

3.3.3 Twin Boom, Inverted V-Tail

The third conceptual design featured a high wing, twin-engine, twin-boom, and inverted V-tail platform, shown in Figure 3-5. The fuselage was very spacious with a square cross-section for adequate payload storage capacity, simplicity of manufacturing, and quicker ground handling for the Ground Mission. The twin-boom design allowed the fuselage to remain an independent section of the aircraft for quick disassembly and CG adjustment. The wing had no dihedral and a straight leading edge with a very shallow tapered trailing edge. The inverted V-tail design allowed the area directly behind the fuselage to be free of any obstruction, guaranteeing that the sensor could not contact any part of the tail during deployment and recovery. The inverted V-tail would also eliminate the adverse roll-yaw coupling tendency that a standard upright V-tail has.

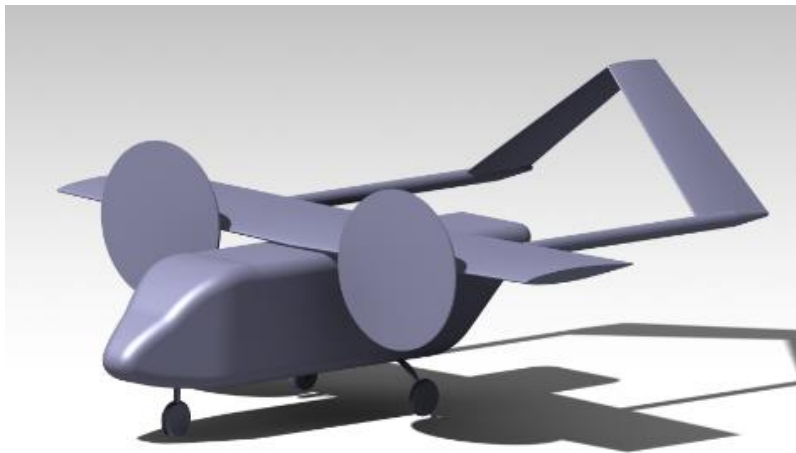


Figure 3-5: Twin boom, inverted V-tail configuration.

The greatest disadvantage of this design was the twin tail booms. From a manufacturing standpoint, there would be increased complexity in requiring a specially designed wing spar-to-tail boom intersection to carry tail moments and allow for easy disassembly.

3.4 Configuration Selection Process

The selection process consisted of a decision matrix, which weighed various aspects of the designs and determined their viability to meet the established criteria including flight characteristics, drag considerations, payload volume, manufacturability, and transportability. The process consisted of collectively ranking each parameter with a weighting that determined the importance of criteria on a scale of 1 to 10. The configuration score was then calculated using Equation 5. Table 3-6 below shows the decision matrix used to aid the configuration selection process.

$$\text{Configuration score} = \sum_{i=1}^8 \left(\frac{\text{Category weight}_i}{\text{Total weight}} \right) \times \text{Category Score}_i \quad (5)$$



Table 3-6: Design matrix with final scores.

Parameter	Weight	Conventional	Canard	Twin Boom
Aspect Ratio	4	4	6	4
Wing Area	5	6	5	6
Wetted Area	4	4	8	5
Payload Volume	5	7	4	5
CG Flexibility	3	6	7	5
Maneuverability	5	7	4	6
Manufacturability	7	7	4	6
Transportability	4	6	5	4
Final Score		8.92	7.6	7.76

Ultimately, the conventional configuration was chosen largely because of its simplicity, maneuverability, and mission capabilities. A large fuselage volume would allow Mission 2 and Mission 3 scores to be increased by adding additional containers and increasing the sensor length. Additionally, it would be spacious to allow for flexibility in the design of the SDRM. The square cross-sectional shape and large surface area also simplified the implementation of powered cargo and bomb bay doors for payload loading and sensor deployment and recovery.

A maneuverable aircraft was desired because of its ability to reduce lap times without the energy expense of increasing cruise airspeed. The large surface area of the horizontal tail of the conventional twin configuration allowed the use of a large elevator control surface to significantly increase pitch control authority during increased load factors. Additionally, the large wing area coupled with high powered twin motors allowed for increased load factors with a low wing loading and a high thrust to weight ratio.

The manufacturability was weighted as the highest importance. The manufacturing team has limited time, resources, and abilities, so a configuration that could be manufactured in a timely manner with these resources was highly desired. A simple aircraft that could be manufactured over the course of two weeks would have the potential to go through twice as many build iterations as a complex aircraft that could take up to a month to build. The ability to go through more iterations in a competition season is highly desired, because with each new iteration, issues are discovered, and the aircraft is refined to become more and more competitive. Although large, the conventional twin configuration struck a balance between size and manufacturability, with few complex curves and a simplified wing structure.

4 Preliminary Design

Following the conceptual design phase during which the conventional twin configuration was selected, the preliminary design phase aimed to maximum the mission scores through detailed sizing analyses.

4.1 Design Methodology

The design team used an iterative design approach that focused on the performance of the aircraft at maximum flying weight for Mission 2 and sensor towing conditions for Mission 3. An initial thrust-to-weight

and power constraint analysis was conducted to determine thrust and power requirements for the optimal wing loading that would satisfy all mission requirements. Based on these constraints, the design team conducted the initial sizing of the aircraft geometry and propulsion system, while also analyzing the aerodynamic characteristics of the aircraft and the towed sensor. The stability characteristics of the aircraft were examined using a vortex lattice method solver called SURFACES. The drag of the aircraft and sensor were estimated using a standard build-up method. The iterative process, which integrated flight test data for both the aircraft and the sensor, allowed the design to be refined after each analysis and test. The aircraft, as designed, was the culmination of several iterations, with each iteration improving progressively on team requirements and mission scores.

4.2 Design Trade Studies

4.2.1 Wing Constraint Sizing

Initial weight estimations were based on historical data of past competition airplanes of similar size. Based on this approach, a maximum payload fraction of 40% for Mission 2 was selected. From the scoring analysis presented in Section 3.2, a target payload of eight sensor containers was selected for Mission 2. Therefore, a maximum payload of 8 lb was set with each container projected to weigh 1 lb. With the payload fraction, the maximum gross weight was then calculated to be 20 lb.

The constraint analysis was used to determine the thrust-to-weight ratio and power required as a function of wing loading (W/S). Turn load factor, T/W , cruise velocity, rate of climb, and take-off distance were calculated as a function of W/S using Raymer's method [3]. The power required was obtained as a function of W/S using the calculated T/W and initial estimated values of velocity and propeller efficiency during each maneuver and a gross weight of 20 lb. The T/W and power required plots in Figure 4-1 indicate an optimal wing loading between 3.3 and 3.5 $\text{lb}\cdot\text{ft}^{-2}$. The lighter wing loading of 3.3 $\text{lb}\cdot\text{ft}^{-2}$ was selected as the conservative choice. With a target gross weight of 20 lb, the wing area of was calculated to be 6 ft^2 .

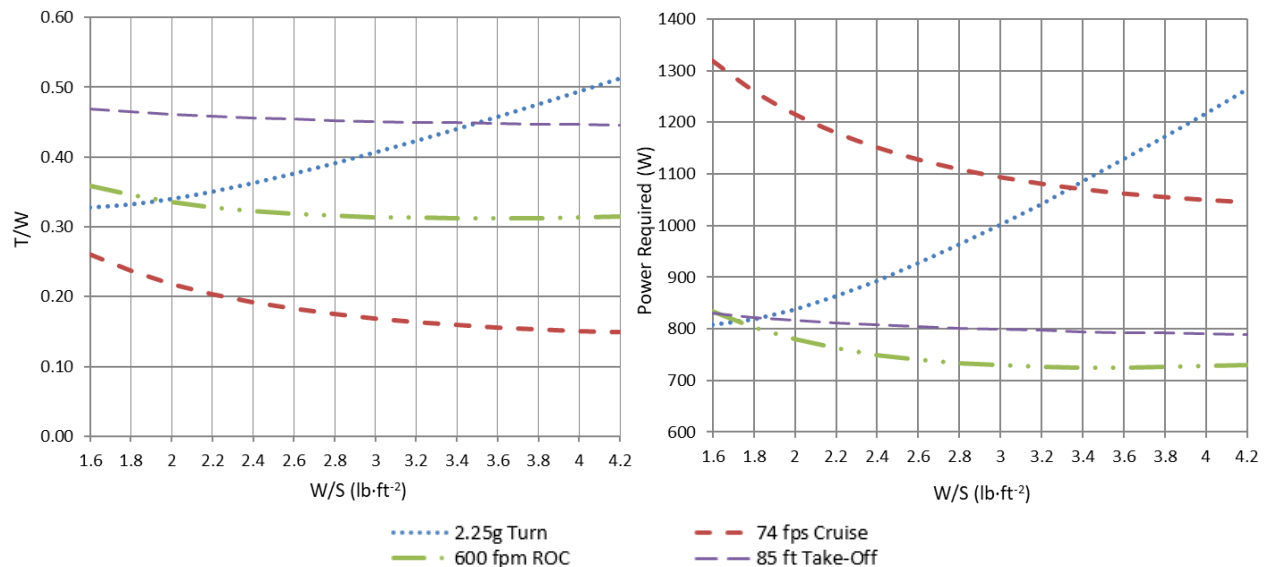


Figure 4-1: Thrust to weight (left) and power required (right) versus wing loading.



With the wingspan limited to 5 ft, the aspect ratio remained purely a function of the wing area. Since the wing area was constrained, improvements in induced drag had to be made elsewhere. Therefore, wing taper ratio was carefully considered and a taper ratio of 0.6 to was selected to maximize the Oswald's span efficiency factor using McCormick's numerical method [4].

4.2.2 Propulsion System Sizing

The propulsion system for the aircraft consisted of commercially available electric motors and electronics in accordance with the competition rules. A trade between supplying enough power and capacity to the system while minimizing gross weight had to be achieved to maximize the payload that the aircraft could carry. The components that comprised the propulsion system included the electric motor, batteries, ESCs, fuses, and propellers.

The batteries are the limiting factor of the propulsion system. The motors can only operate at peak performance if the batteries can supply enough power to them. Additionally, the rules dictate a maximum size per pack of 100 Wh and a maximum of 200 Wh on the aircraft. The batteries chosen to power the aircraft were two Admiral 6S 4500 mAh 40C LiPo batteries connected in parallel, providing a total capacity of 9000 mAh and 199.8 Wh. It was assumed that the batteries were discharged to 85% so as not to damage the batteries or the aircraft. This means the useful power available was 85% of 199.8 Wh, which was 169.8 Wh. Endurance times of 5 minutes and 11 minutes were targeted for Mission 2 and Mission 3, respectively, to allow ample time for landing and takeoff. This goal yielded average discharge rates of 2,038 W for Mission 2 and 926.3 W for Mission 3. Table 4-1 summarizes the performance of the selected battery.

Table 4-1: Performance of two Admiral 6S 4500 mAh 40C LiPo batteries.

Parameter	Value	Parameter	Value
Useful Capacity (Wh)	169.8	Mission 2 Endurance (min)	5
Voltage (V)	22.2	Mission 2 Endurance Power (W)	2038
Series / Parallel	6 / 2	Mission 3 Endurance (min)	11
Max Continuous Discharge	360 A / 7992 W	Mission 3 Endurance Power (W)	926.3

The motors were selected to operate at the targeted discharge rate for Mission 2 in a twin configuration. Table 4-2 summarizes the three different motors that were considered.

Table 4-2: Motor performance summary.

Parameter	Scorpion SII-4020-420	KDE 3520XF-400	Eflite Power 60
kV (rpm/V)	420	400	400
Maximum Constant Power (W)	1500	1335	1200
Maximum Cont. Current (A)	80	45	40
Weight (oz)	10.2	10	13

The KDE 3520XF-400 motor was selected because of its ability to provide the targeted power for Mission 2 at the lightest weight. However, the Scorpion motor with its high power to weight ratio, was a strong second choice should additional rpm have been required to reach target power levels in flight.

4.2.3 Propeller Selection

The propeller pitch and diameter were initially sized using Gudmundsson's estimation method [5]. The results showed that a 15 in diameter propeller with a pitch of about 11 in would be a good candidate based on the cruise power and the estimated cruise airspeed of the aircraft. Using this initial estimate, six propellers were selected for further analysis. To determine the propeller that would be the most efficient under cruise conditions, the propeller efficiency was plotted against the airspeed for multiple rpm values. The efficiency data was obtained from the manufacturer's website [6]. The goal was to ensure that the propeller selected could operate at or close to its optimal propulsive efficiency in cruise.

Preliminary estimations for the rpm achieved by the motor under load were made using eCalc, an online electric propulsion simulation software package [7]. It was found that at a cruise velocity of $74 \text{ ft}\cdot\text{s}^{-1}$ for Mission 1 and Mission 3, the motor achieved about 6,000 rpm. Figure 4-2 (left) shows the propeller efficiencies versus airspeed at this condition. Here, it is shown that at speeds below the targeted velocity of $74 \text{ ft}\cdot\text{s}^{-1}$, the lower pitch propellers were more efficient. However, as speeds increased above this point, the efficiency quickly diminished, and the propellers with a pitch of 10 in were more efficient. For the Mission 2 target cruise velocity of $92 \text{ ft}\cdot\text{s}^{-1}$, eCalc estimated 7,000 rpm at full power. Figure 4-2 (right) shows the propeller efficiencies versus airspeed at this condition. Once again, at the target airspeed, all the propellers had about the same efficiency, but the higher pitched propellers maintain this efficiency though higher airspeeds, while the efficiency of the lower pitched propeller quickly decreases. Regardless of drag, the lower pitched propellers effectively placed a limit on the maximum achievable airspeed. For this reason, the lower pitch props were eliminated as candidates.

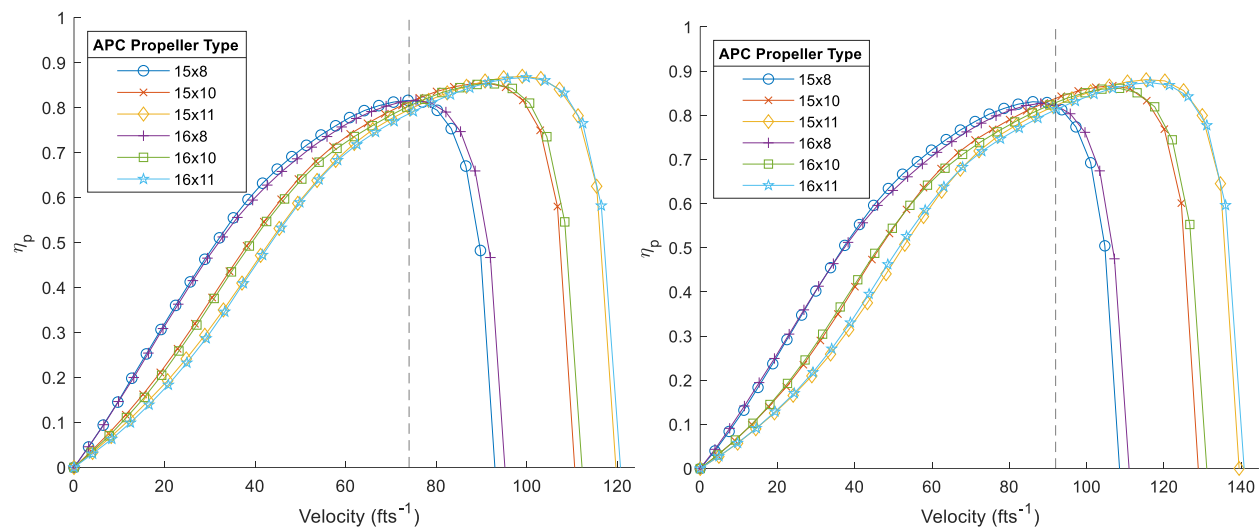


Figure 4-2: Propeller efficiency versus airspeed at 6,000 rpm (left) and 7,000 rpm (right).

Further analysis of the higher pitched propellers involved eCalc simulations for the power draw and endurance for each propeller. Initial estimates for parasitic drag were used to estimate the power required for the propulsion system. Figure 4-3 shows that the best propeller in terms of minimizing power draw and maximizing endurance was the 15x11 propeller. Although the 15x11 propeller provided the greatest efficiency, it was not available from APC in both CW and CCW configurations. For this reason, the 15x10 propeller was ultimately chosen as it was available in both CW and CCW configurations. This approach allowed for the elimination of adverse lateral stability effects, such as P-factor, produced by the propeller at high angles of attack.

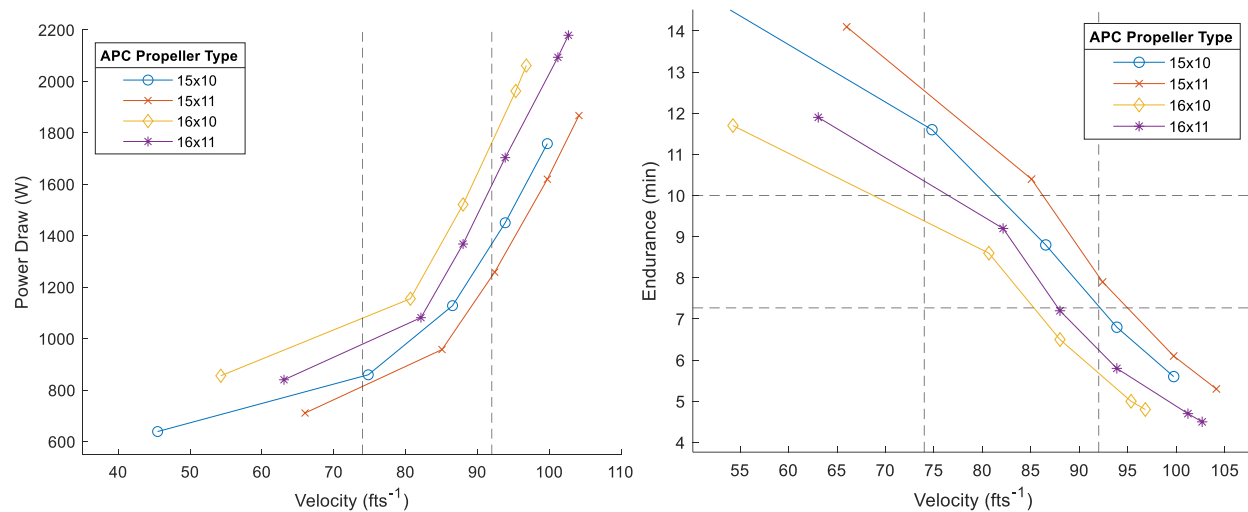


Figure 4-3: Power draw (left) and endurance (right) versus airspeed.

4.2.4 Uncertainties

The methods used in the design all contain limitations to their accuracies. All mission performance estimates assumed that the pilot was flying a constant airspeed and holding a perfect course. The calculations also neglected the effects of a tailwind or headwind. Other uncertainties included the true value of the aircraft's parasitic drag and the electrical and mechanical efficiencies between the motor and the batteries. Margins were included in the design to allow for confirmation of performance during flight tests.

4.3 Lift and Drag

4.3.1 Airfoil

Airfoil selection was performed by investigating a series of different airfoils that could meet the design requirements, the first being a thickness to chord ratio of about 12% to accommodate internal structure and servos. Additionally, each airfoil had to be easily manufactured, which necessitated a flat bottom and a linear trailing edge. Finally, a high maximum lift coefficient was desired to achieve Mission 2 payload goals. Assuming a mean aerodynamic chord length of 14.7 in and an airspeed of 74 ft/s, the chord Reynolds number was approximately 414,000. Data provided by Airfoil Tools [8] for a Reynolds number of 500,000 is plotted in Figure 4-4 for several airfoils under consideration.

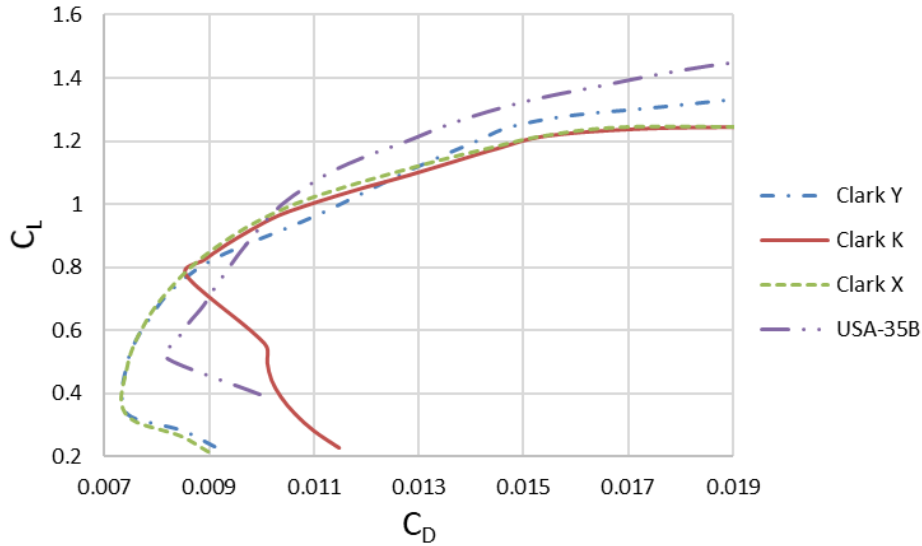


Figure 4-4: Airfoil drag polar comparison.

Table 4-3 summarizes the aerodynamic characteristics of each airfoil. The first item of interest was the drag bucket range of each airfoil. A wide drag bucket was desired as the airfoil can produce a range of lift coefficients close to its minimum drag. It was also important that the cruise lift coefficient was within this drag bucket to minimize induced drag. The design cruise lift coefficient was 0.63 for Mission 2 and 0.47 for Mission 3. The Clark Y and Clark X airfoils had the widest drag buckets that accommodated this range in lift coefficients, as shown by the drag polar plots in Figure 4-4. The Clark X had the lowest minimum drag, but the Clark Y achieved greater maximum lift. The USA-35B offered more maximum lifting capability at the expense of higher minimum drag and its narrow drag bucket did not include the design lift coefficient for Mission 2. The Clark-Y was ultimately selected because of its wide drag bucket that covers cruise lift coefficients for all mission segments. A NACA 0012 was selected for the empennage to provide ample thickness to house the servos.

Table 4-3: Airfoil comparison.

Airfoil	Drag Bucket Width	$C_{l_{max}}$	$C_{d_{min}}$
Clark Y	0.3-0.75	1.416	0.00733
Clark X	0.3-0.75	1.327	0.00731
Clark K	0.75-0.85	1.339	0.00856
USA-35B	0.45-0.55	1.505	0.00819

4.3.2 Aircraft Drag

A drag build-up method was performed according to Gudmundsson [5], which assumes that total drag is a summation of pressure drag, skin friction drag, induced drag, and miscellaneous drag. Equation 6 shows the mathematical model used to calculate the minimum drag. Skin friction and pressure drag are accounted for in one term, where C_{fi} is a skin friction coefficient, FF is a form factor, IF is an interference factor, and S_{wet} is the wetted area for different parts of the aircraft.

$$C_{D,\min} = \left(\left(\frac{1}{S_{\text{ref}}} \right) \sum_{i=1}^N C_{fi} \times FF_i \times IF_i \times S_{\text{wet},i} + C_{D,\text{misc}} + C_{D,L\&P} + C_{D,\text{Base}} \right) \left(1 + \frac{\text{CRUD}}{100} \right) \quad (6)$$

Skin friction coefficients, C_f , were first calculated as prescribed by Young [5], then form factors, FF , were applied based on general geometry. An XFOIL analysis was used to determine the turbulent transition points of primary components. The empennage and the wing used Torenbeek's model [5] for a form factor, which applies for airfoils with maximum thicknesses below 21% chord. Suggested interference factors for the main components were applied. Extra components such as the landing gear and sensor were accounted for in the $C_{D,\text{misc}}$ term. An 8% margin, as recommended by Raymer [3], was added to account for leak and protuberance drag, $C_{D,L\&P}$. Finally, base drag was considered to account for the drag created from flow separation on the upswept aft fuselage. Lastly, because drag is often underestimated, a "CRUD" factor of 25% was applied to account for errors in the various models used.

4.3.3 Sensor and Tow Cable Drag

The total drag of the sensor was estimated using a vortex lattice solver, VSPAERO at Mission 3 flying conditions of 74 fts^{-1} . This analysis resulted in a drag coefficient of about 0.0018 with the aircraft's wing planform area used as the reference area in accordance with the drag build-up. Figure 4-5 shows the paneling used for the numerical method. The sensor dimensions for this simulation assumed a length of 20 in and a diameter of 1.5 in based on preliminary dimensions of the internal width and length of the payload.

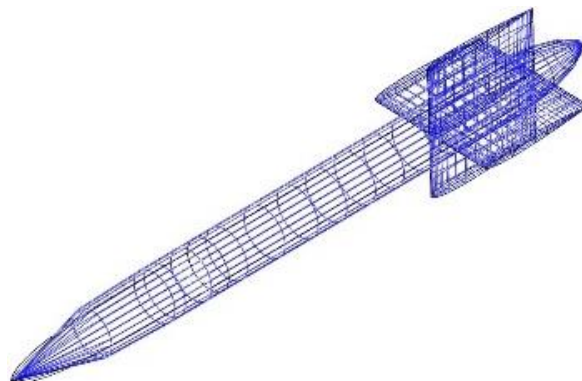


Figure 4-5 VSPAERO sensor model.

Next, the drag on the tow cable was considered. After preliminary sensor drag estimates and flight tests, it was discovered that the tow cable flew almost perpendicular to the flight velocity because of the high weight to drag ratio of the sensor. The analysis model of the tow cable initially assumed a circular cylinder placed perpendicular to the airflow. The Reynolds number for the proposed cable and flight conditions was calculated to be about 11,000, far under the desired critical Reynolds number of 400,000 as suggested by McCormick [4]. This yielded a two-dimensional drag coefficient of about 1.1 referenced to the frontal area of the cable. Therefore, at the target Mission 3 cruise airspeed, the cable produced 0.23 pounds of drag which equated to a coefficient of 0.00644 for the drag build up. These preliminary estimates showed that the tow cable is a significant source of drag, equating to as much as three times the drag of the sensor itself.

It was then discussed that using two twisted cables rather than a single cylindrical, coaxial signal transmission cable could potentially reduce the drag on the tow cable. The twisted cables could trigger turbulent boundary layers earlier than the single cable, potentially delaying separation and decreasing profile drag. McCormick's experimental data shows that when this is accomplished, the two-dimensional drag coefficient could be reduced to 0.3. Even after assuming a worst-case 100% increase in the equivalent diameter, the build-up drag coefficient of the cable could still be reduced by 45% to 0.0035.

4.3.4 Complete Parasite Drag Build-Up

Once the parasitic drag of each component was calculated, the drag build-up yielded a total minimum drag coefficient of 0.071 for Mission 3. Figure 4-6 presents a component breakdown.

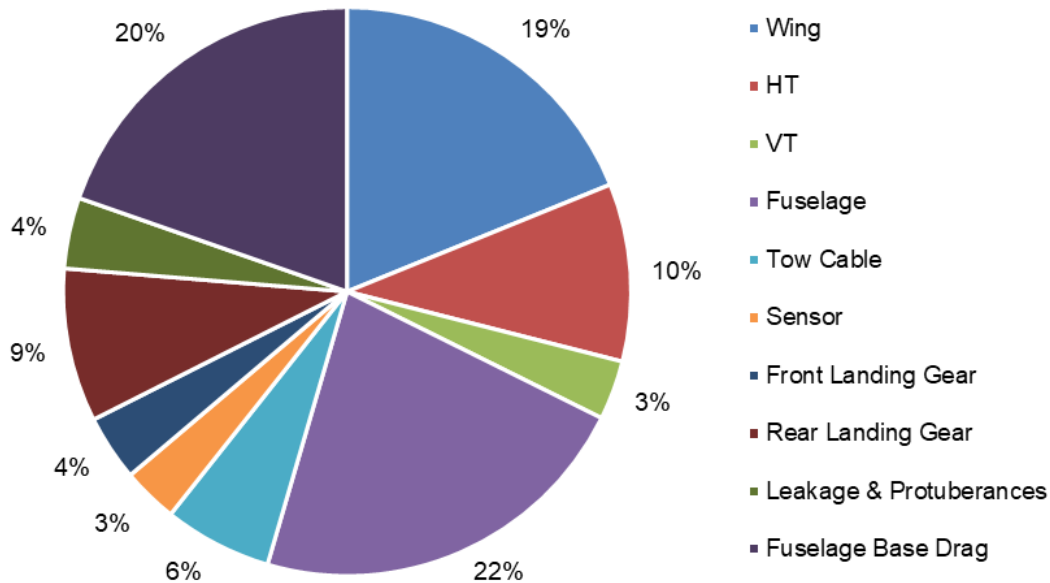


Figure 4-6: Mission 3 parasitic drag breakdown.

As expected, the fuselage was the largest contributor of parasitic drag. Therefore, it remained a focus for future drag reduction efforts, specifically in the reduction of base drag by reducing the upsweep angle.

4.4 Stability and Control Analysis

The aircraft was first analyzed using SURFACES at cruise airspeed for all three missions: 74 fts^{-1} for Missions 1 and 3 and 92 fts^{-1} for Mission 2. The analysis was performed for a Tucson, Arizona field elevation of 2,200 feet MSL at standard temperature. The stability of the aircraft was analyzed assuming no sideslip and level, trimmed conditions. Standard stability axis system sign conventions were used for all derivatives and control surface parameters.

4.4.1 Static Stability Analysis

Power effects as well as weight distribution of the surfaces were considered in the analysis. For Mission 3, the analysis was performed with the sensor deployed to better understand its effect on the stability characteristics. The sensor drag and weight were considered a single load acting at the bottom of the fuselage, which is shown in Figure 4-7 below.

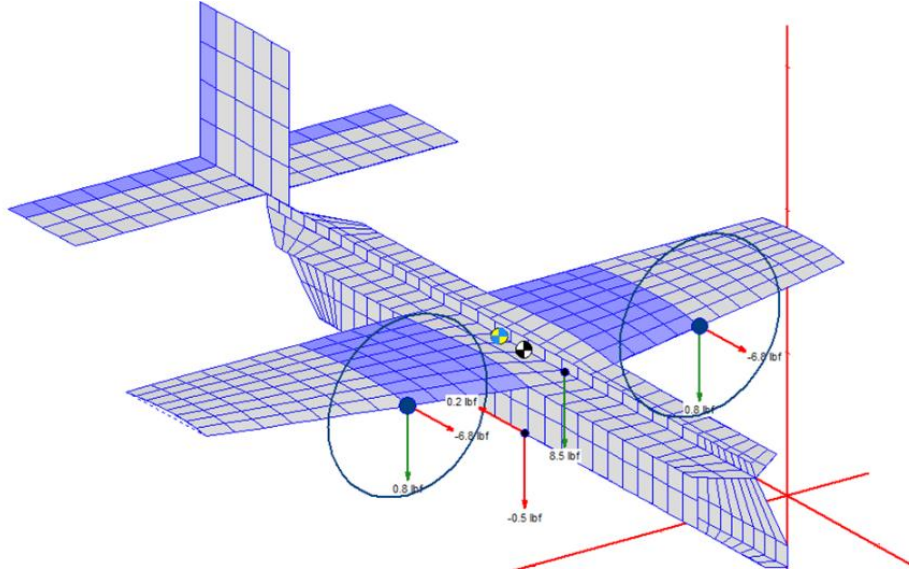


Figure 4-7: SURFACES Mission 3 configuration with deployed sensor.

The primary static stability derivatives for each mission are shown in Table 4-4. The CG of the airplane remains at approximately 30% MAC for all missions, resulting in only slight changes in static stability coefficients between missions. The aircraft was found to be sufficiently stable for all three missions based on previous ERAU DB DBF aircraft.

Table 4-4: SURFACES static stability derivatives.

Derivative	$C_{m\alpha}$ (Longitudinal)	C_{mC_L} (Longitudinal)	$C_{l\beta}$ (Lateral)	$C_{n\beta}$ (Directional)
Mission 1	-0.01578 deg ⁻¹	-0.1973	-0.00069 deg ⁻¹	0.00428 deg ⁻¹
Mission 2	-0.01577 deg ⁻¹	-0.1971	-0.00069 deg ⁻¹	0.00428 deg ⁻¹
Mission 3	-0.01797 deg ⁻¹	-0.2246	-0.00069 deg ⁻¹	0.00435 deg ⁻¹

4.4.2 Control Surface Analysis

Aileron and flap spans were determined based on structural requirements and the capability of placing the motors in a location such that half of the propeller's slipstream will improve flap effectiveness and the other half would improve aileron effectiveness at low airspeeds and high throttle settings. Values retrieved from SURFACES do not account for such "prop-wash" effects, which would theoretically improve the coefficients once those effects are accounted for [2]. Roll rates were determined based on Raymer's method [3] while assuming a maximum aileron deflection of 30 degrees at cruise conditions. The rolling rates for all three primary flight modes in Mission 3 are shown in Table 4-5.

Table 4-5: Roll determinations for flight conditions within Mission 3.

Flight Condition	V_∞	$C_{l\delta_a}$	C_{l_p}	$p_{\delta_a=30^\circ}$
Takeoff/Landing	45.7 fts ⁻¹	0.00444 deg ⁻¹	-0.00679 s·deg ⁻¹	19.6 deg·s ⁻¹
Cruise	74.0 fts ⁻¹	0.00445 deg ⁻¹	-0.00682 s·deg ⁻¹	19.5 deg·s ⁻¹

4.4.3 Dynamic Stability Analysis

The longitudinal and lateral dynamic stability behavior was analyzed using SURFACES. Longitudinal dynamic stability was characterized by the short period and phugoid (long period) dynamic modes. Short period analysis yielded a satisfactory damping ratio of 0.701. The long period (phugoid) mode shown in Figure 4-8 was found to be unstable, but the time to reach doubled amplitude is approximately 128 seconds, which is well above the time the pilot would need to correct the flight pattern.

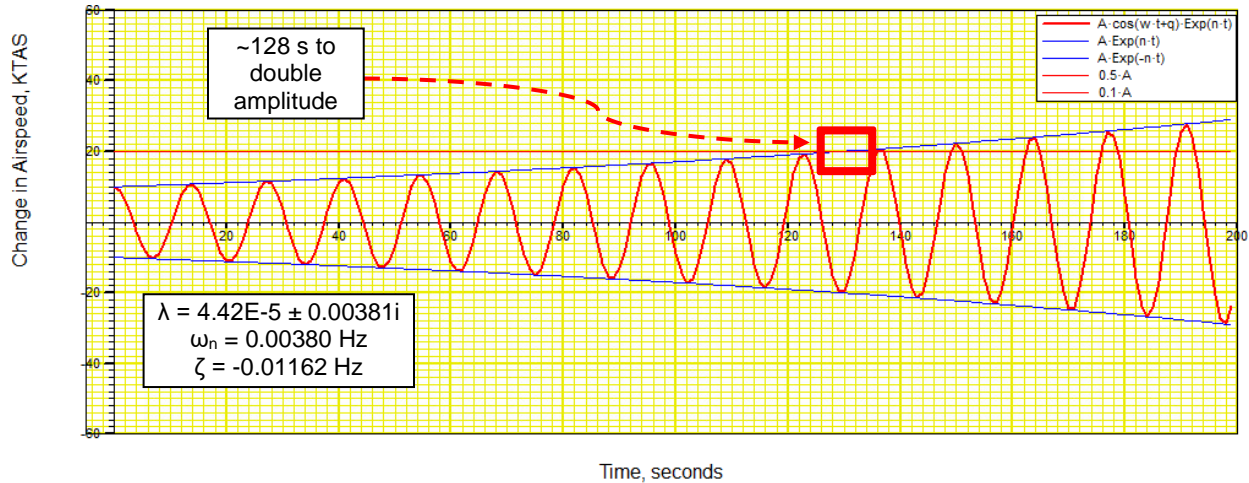


Figure 4-8: Mission 3 phugoid (long period) longitudinal dynamic mode.

Lateral and directional dynamic stability is characterized by the rolling, Dutch roll, and spiral modes. Rolling convergence analysis showed no oscillations and reached 1/10 amplitude in approximately 0.20 seconds. The Dutch roll mode analysis yielded satisfactory results with convergence in just three seconds, as shown in Figure 4-9.

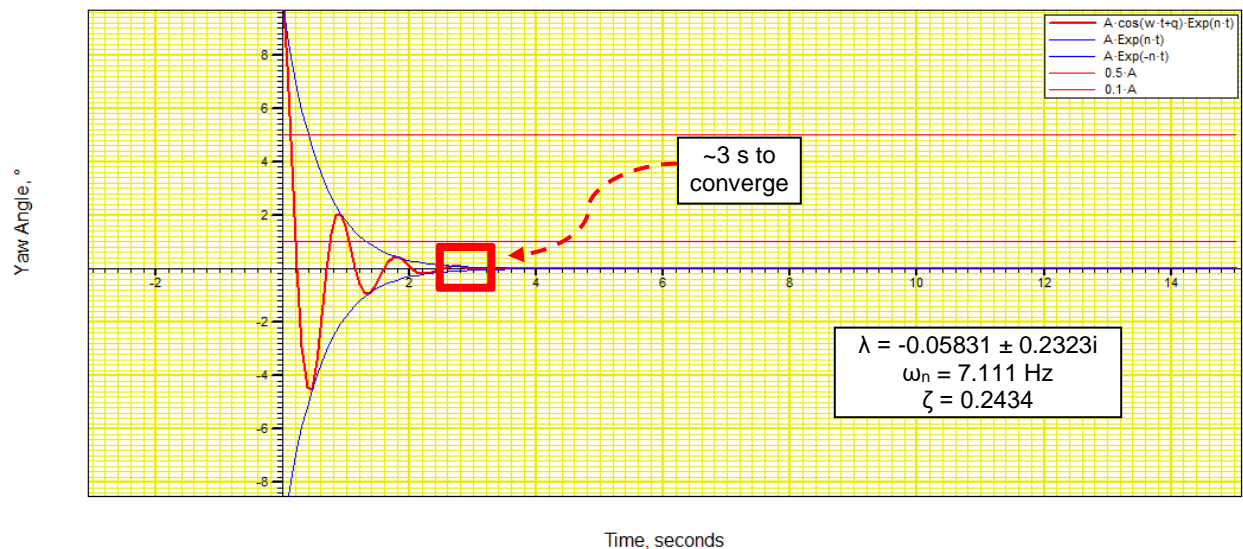


Figure 4-9: Mission 3 Dutch roll dynamic mode.

Spiral stability analysis was crucial because the aircraft features no wing dihedral. Therefore, the fuselage dihedral effect and vertical tail alone must provide most of the stability. Figure 4-10 shows that the spiral

mode was found to be unstable; however, the time to double was found to be 10 seconds. Based on the team's previous experience, this is sufficient time for the pilot to take corrective action.

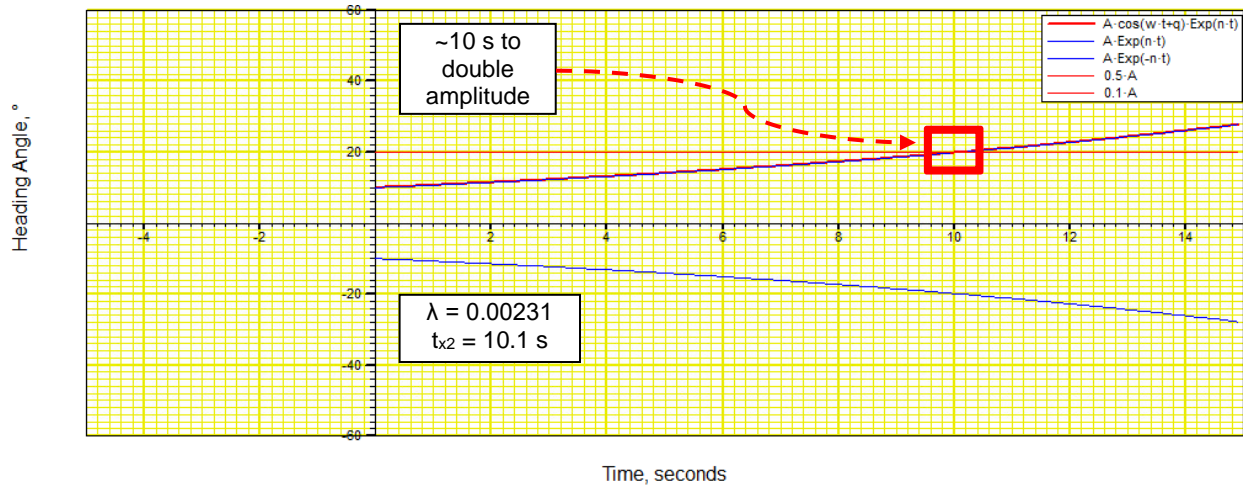


Figure 4-10: Mission 3 spiral dynamic mode.

4.5 Estimated Mission Performance

Based on the preliminary design, performance estimates could be made for each of the flight missions. The predictions were based on drag calculations and the expected performance of the propulsion system. Takeoff performance was analyzed using Gudmundsson's method [5] to iteratively calculate the takeoff distance based on the drag, rolling resistance, and thrust of the aircraft in the takeoff configuration. Figure 4-11 shows that at the maximum takeoff weight of 20 lb for Mission 2, the aircraft takes off in just 54 ft.

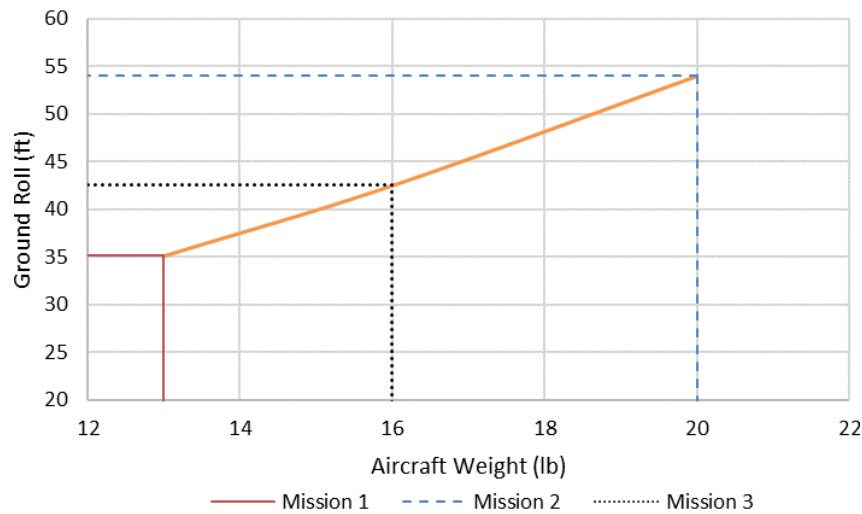


Figure 4-11: Mission takeoff performance.

Next, lift and drag coefficients were calculated for each mission configuration. From these, the lift to drag ratio was calculated and plotted against airspeed as a measure of the aerodynamic efficiency. Figure 4-12 shows that for all missions, aerodynamic efficiency is traded for higher cruise airspeeds. Although the Mission 3 configuration achieved the lowest maximum L/D because of the addition of the sensor and tow cable, it cruised at the highest L/D to meet the Mission 3 endurance requirement.

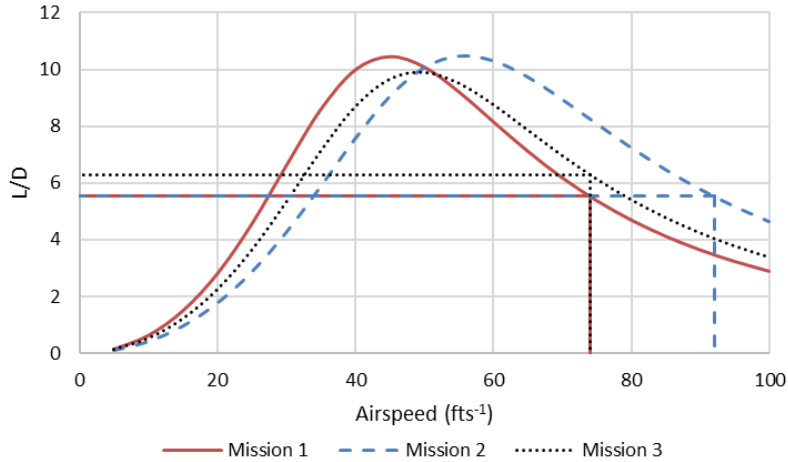


Figure 4-12: Lift over drag versus airspeed.

A power required and power available analysis was conducted to verify the targeted speed envelope for each mission configuration. Power required was obtained by multiplying the drag by the airspeed across each flight envelope. Power available was obtained from the propeller manufacturer’s measurements of thrust over a range of airspeeds at 6,000 rpm. An equivalent thrust power was calculated by multiplying the thrust by the airspeed at each data point; the results shown in Figure 4-13 verify that a Mission 2 cruise speed of 92 fts⁻¹ could be achieved. An important limitation of this result was the assumption of a constant 6,000 rpm propeller speed. Actual propeller speed would likely increase above 6,000 rpm as the airspeed approaches the top speed and the load on the propeller is reduced. This effect would theoretically increase the thrust power output, providing more power margin leading up to a greater top airspeed.

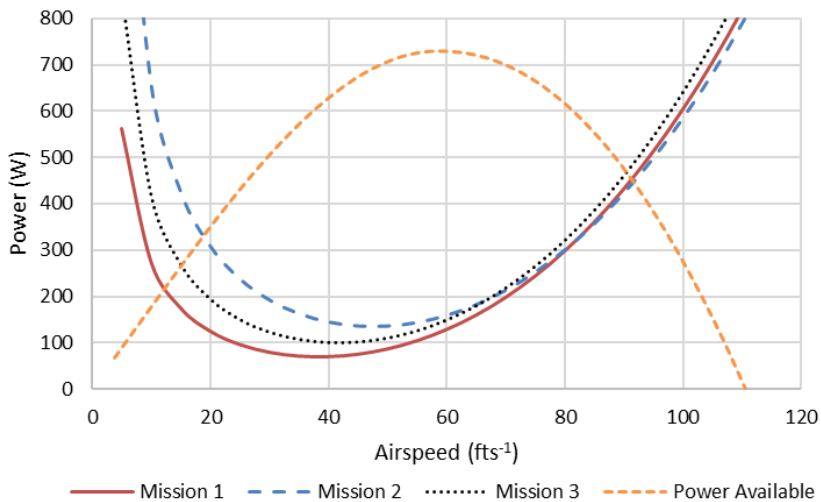


Figure 4-13: Thrust power available versus power required at 6,000 rpm.

To estimate mission lap times, the performance model attempted to estimate turn radius and turn airspeed for each mission. The model assumes a load factor of 2.25 at maximum gross weight and equivalent load factors of 2.92 and 2.56 for Mission 1 and Mission 3 weights, respectively. Turns were assumed to be flown at the maximum L/D airspeed for each configuration. With turn radius and airspeed known, lap times could

be predicted at the targeted cruise airspeeds over the 2,000 ft course. Table 4-6 summarizes the predicted performance of the aircraft for each of the flight missions. Table 4-7 summarizes the projected team scores.

Table 4-6: Mission performance predictions.

	Mission 1	Mission 2	Mission 3
Gross Weight (lb)	13	20	16
Payload Weight (lb)	-	7	3
Wing Loading (lb-ft⁻²)	2.17	3.33	2.67
Ground Roll (ft)	35.1	54.0	42.5
Cruise Airspeed (fts⁻¹)	74	92	74
$C_{L, \text{cruise}}$	0.366	0.367	0.450
$C_{D, \text{cruise}}$	0.066	0.066	0.071
L/D_{cruise}	5.55	5.53	6.30
Turn Radius (ft)	33	75	50
Number of Laps	3	3	15
Lap Time (s)	36.2	38.9	39.5
Mission Time (min)	1.7	1.9	10

Table 4-7: Predicted non-normalized team scores.

	Team Score
Mission 1	1.0
Mission 2	4.11 containers/min
Mission 3	297.5 laps*in*lb

5 Detail Design

After extensive conceptual design, preliminary design, and flight test analyses, the external geometry of the aircraft was finalized under the terms of the DBF competition and team requirements.

5.1 Final Dimensional Parameters

The final aircraft configuration is shown in Figure 5-1. Table 5-1 summarizes the overall aircraft dimensions.



Figure 5-1: Finalized design of the aircraft.

Table 5-1: Basic dimensions of the aircraft.

Overall Aircraft		Horizontal Tail	
Length	79.0 in	Mean Chord	9 in
CG Mission 1	32.8 in (from nose)	Span	36 in
CG Mission 2	33.2 in (from nose)	Planform Area	324 in ²
CG Mission 3	32.8 in (from nose)	Aspect Ratio	4
Wing		Vertical Tail	
Mean Chord	14.7 in	Mean Chord	12 in
Span	60 in	Span	14 in
Planform Area	864 in ²	Planform Area	168 in ²
Aspect Ratio	4.17	Aspect Ratio	1.17

5.2 Structural Design Methodology and Characteristics

The structural design methodology used by the team attempted to balance structural integrity, weight, and ease of manufacturing with the materials and processes available to the team. An increased design load factor of 2.5 from 2.25 was selected in accordance with the design-specified turn load factor and wingtip loading test. A semi-monocoque structure was utilized to accomplish these goals, containing wooden stringers, formers, ribs, spars, and skins. Carbon fiber spars, longerons, and main landing gear were used to transmit the loads into a central wing box, as shown by the load paths in Figure 5-2. The following subsections detail the structural design and integration of the fuselage, wing, empennage, landing gear, sensor, containers, and SDRM.

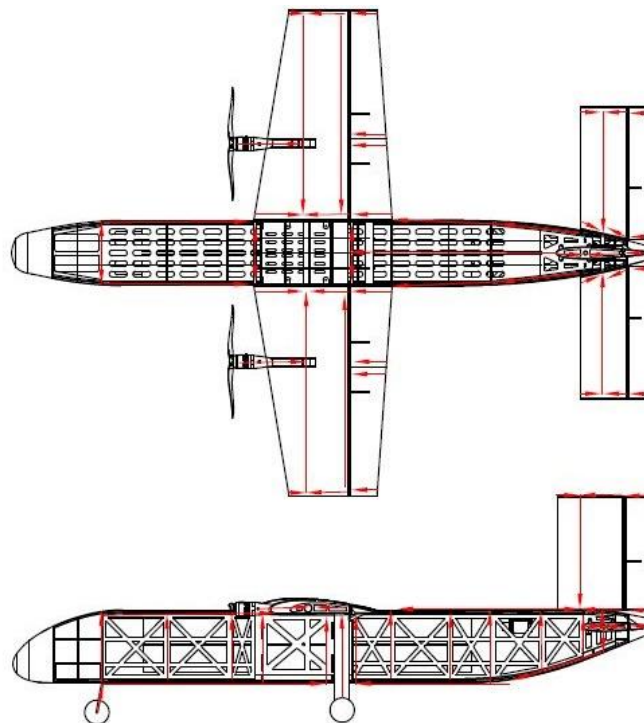


Figure 5-2: Aircraft load paths.

5.2.1 Fuselage

The built-up, semi-monocoque fuselage leverages its simple, box-like shape for ease of manufacturing and flexibility in carrying payload. Plywood formers, which made up the rectangular cross section, were joined by balsawood stringers and basswood longerons. Balsawood shear panels were located on the sides of the fuselage and on the bottom of the aft section to transfer shear loads to the upper and lower longerons. The non-load bearing 3D printed nose and tail cones, as shown in Figure 5-3, completed the geometric surfaces.



Figure 5-3: Aircraft fuselage.

5.2.2 Wing

According to the competition design rules, the wing must be able to withstand a wingtip loading test, simulating a load factor of 2.5, as well as all other expected aerodynamic loads. A factor of safety of 1.5 was applied for a total design load factor of 3.75. Schrenk's method was used to determine the wing spanwise load distribution. This method approximated the lift distribution as an average between the actual wing planform area and an elliptical planform area. Additionally, the weight distribution of the wing structure and electric motors were subtracted to account for gravity and inertial relief. The resulting load distribution is shown in Figure 5-4.

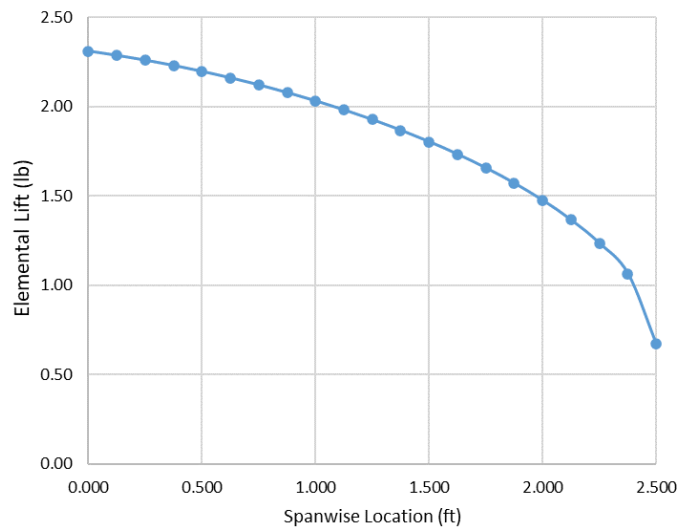


Figure 5-4: Wing load distribution.

Next, shear and bending moments were calculated along the span to determine the levels of internal stress. These diagrams are shown in Figure 5-5.

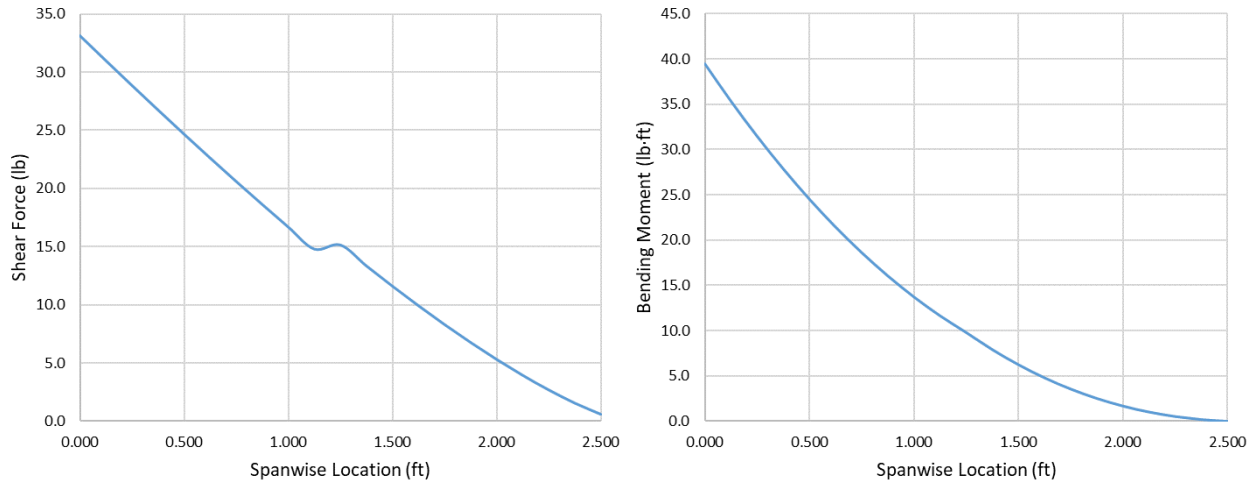


Figure 5-5: Shear and bending moment diagrams.

FEA was conducted on the selected carbon fiber spar to verify internal stress and wingtip displacement, as shown in Figure 5-6. The maximum flexural stress was found to be approximately 15,000 psi, which is just 19% of the manufacturer’s listed ultimate strength of 80,000 psi. Additionally, the wingtip deflection of 0.67 in at this loading condition was considered to be acceptable.

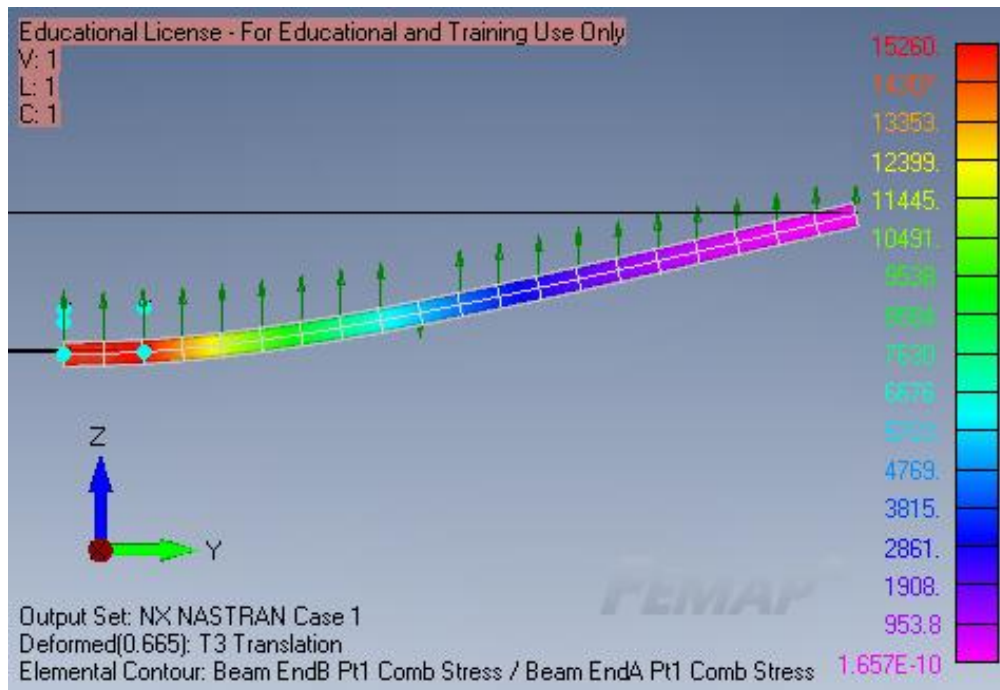


Figure 5-6: Wing spar stress FEA (deflections are not to scale).

The remainder of the wing was constructed of a monocoque balsawood skin with a foam core, as shown in Figure 5-7.

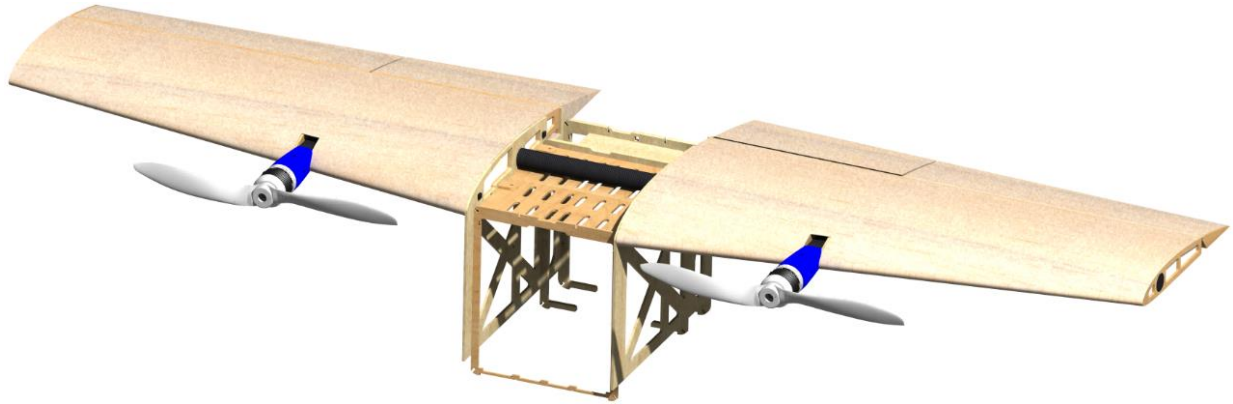


Figure 5-7: Wing and wing box structure.

The foam core provided the airfoil shape, out-of-plane compressive strength, and resistance to buckling. The skin carried the torsional shear loads and residual bending loads that were not taken by the main and trailing-edge spars. The rear basswood spar allowed for the control surface hinges to be attached securely to the main structure. The control surfaces were also made of foam core construction with plywood control horns for the servo linkages. The electric motors were attached with streamlined 3D printed mounts that were bolted to square carbon fiber booms that intersected with and transferred loads to the main spar. The removable main spar spans from wingtip to wingtip with no breaks or bends. This design allowed the spar to carry the bending stress produced by each wing through the wing box intersection. This approach greatly simplified the wing box structure because it could be idealized to support primarily shear loads. Two carbon fiber alignment pins carried torsional shear loads into the wing box structure. Two plywood screw tabs secured each wing half to the wing box.

5.2.3 Empennage

The tail structure was of similar design to the wing with its foam core surfaces and removable main spars. A wing box structure accepted the main spars and alignment screws. These screws, which pass through plywood tabs integrated into the surface root, secured the surface to the fuselage while also supporting torsional shear loads. Figure 5-8 shows a detailed view of these support tabs.

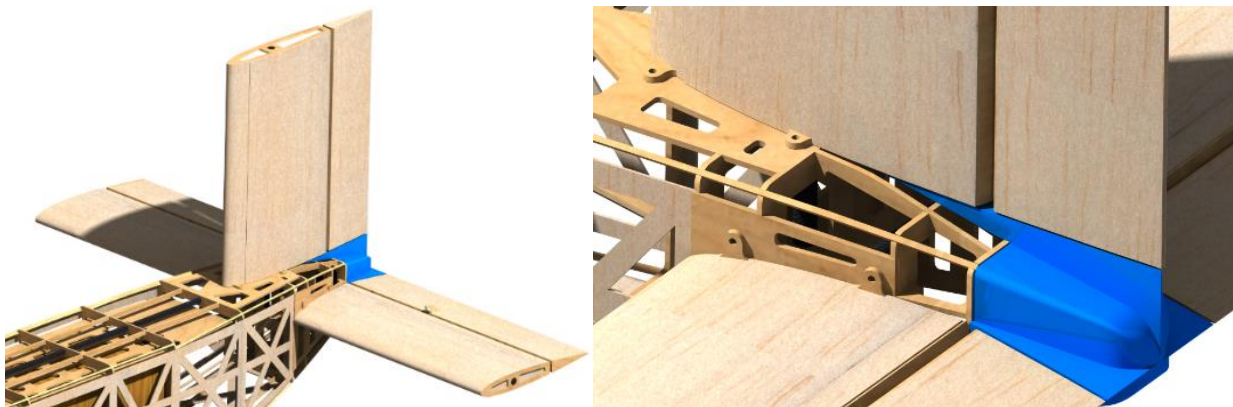


Figure 5-8: Empennage structure.

5.3 Landing Gear

The carbon fiber landing gear had to be easily removable for transport to the competition. Four bolts secured it to the upper wing box where the landing loads were transferred to the strongest part of the aircraft. FEA, as shown in Figure 5-9, was conducted to assess the stress and deflection under a landing load factor of 2. The maximum stress was found to be approximately 10,000 psi, which is only 7% of the listed ultimate strength of the plain weave carbon fiber plate at 140,000 psi. The deflection was found to be about 0.5 in, which is acceptable given the aircraft's substantial ground clearance.

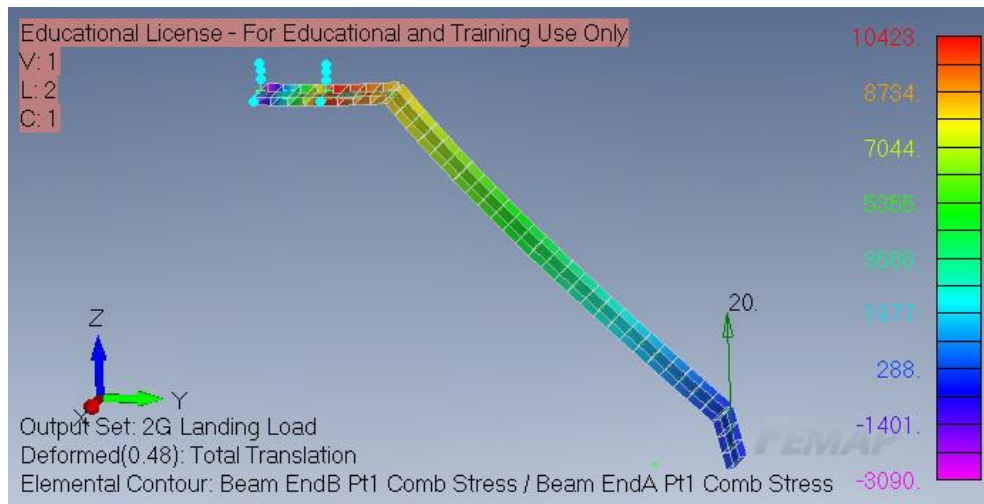


Figure 5-9: Landing gear stress FEA (deflections are not to scale).

5.3.1 Mission 2 System Integration

Cargo integration for Mission 2 and the Ground Mission was accomplished through an inverted pallet, which was easily removed through the detachable nose, as shown in Figure 5-10. Aluminum rails accepted the cargo pallet flange, and these connected to the top of fuselage formers to transfer the inertial loads to the surrounding structure. Sensor containers were attached to the pallet with Velcro straps. The SDRM was stowed on the rear of the pallet during Mission 2.



Figure 5-10: Mission 2 payload storage.

5.3.2 Mission 3 System Integration

For Mission 3, the containers were removed, and the SDRM was moved to its Mission 3 location on the cargo pallet. Three arches held the sensor during transport in Mission 3, which could be folded down into the floor to make room for Mission 2 payload. Two servo-powered bomb bay style doors on the belly of the airplane opened during deployment and recovery, as shown in Figure 5-11.

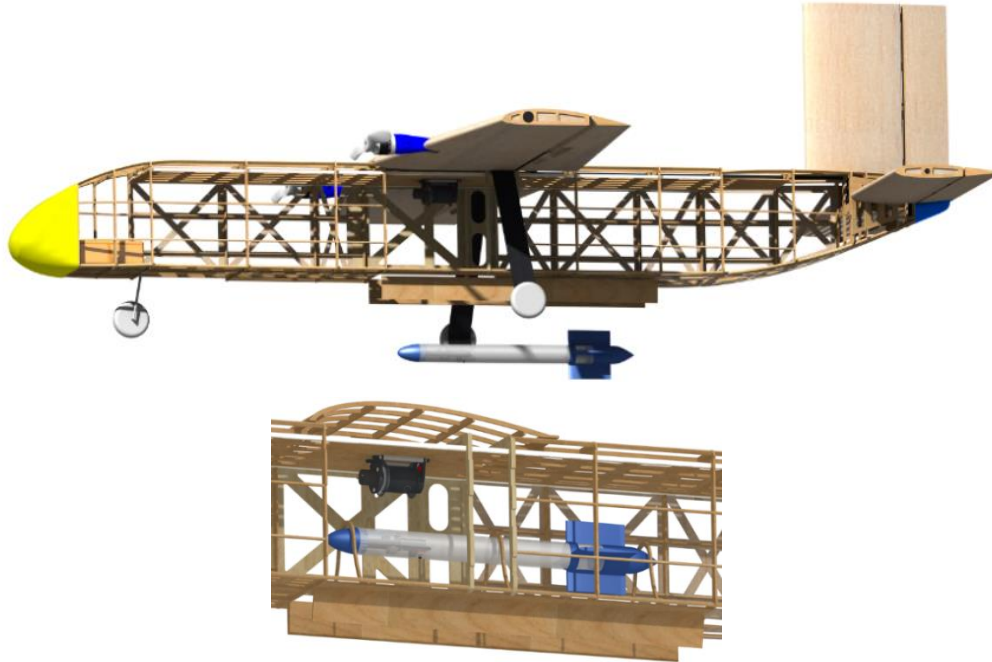


Figure 5-11: Mission 3 sensor deployment configuration.

5.3.3 Sensor

In addition to the requirements set in Section 3.1.3 for the sensor, the sensor must also operate for a minimum of 10 minutes with a minimum number of wires connecting it to the aircraft. With a focus on experience, usability, and availability, the team decided on the components shown in Table 5-2 for the sensor electronics.

Table 5-2: Selected electronic components.

Usage	Component
Microcontroller	Arduino Nano
Battery	LGMH1 18650
LEDs	Quad Row 991 Lumen/ft

While it was not necessary to have an onboard microcontroller in the sensor, the team decided that to reduce the number of wires connecting the sensor to the aircraft, an onboard microcontroller could utilize one PWM signal wire from the aircraft and output three different digital signals to the LEDs.

During the sensor validation portion of the subsystem design, the team utilized the manufacturer's specifications for each component. Because the LEDs operate at 24V while the battery supplies

approximately 3.7V, a buck converter circuit was integrated into the system. Table 5-3 shows the calculated current draw and endurance of the sensor battery.

Table 5-3: Sensor battery endurance

Current Draw	Capacity	Endurance
5.9 A	3200 mAh	32 min

In a worst-case scenario of all three LED strips operating at the same time, the sensor could operate for approximately 32 minutes, exceeding the maximum mission time of 10 minutes.

To assist in the manufacturing and assembly of the sensor, the internal electronics were carried on a “skeleton” which was attached to the nose cone of the sensor. This allowed for the electronics skeleton to be inserted and removed from the sensor without having to disconnect any wires, shown in Figure 5-12.

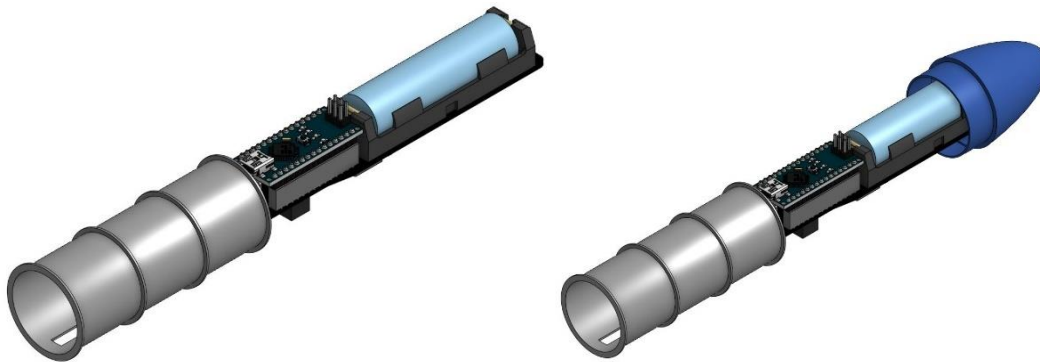


Figure 5-12: Sensor electronics skeleton (LED strips in gray).

The primary distinguishing factor of the sensor was the optically clear body; to this end the team decided to use a 1.5 in diameter clear polycarbonate tube for the sensor’s body (see Figure 5-13). This approach allowed for the LEDs to remain inside the sensor, thereby simplifying the manufacturing and assembly of the sensor while also keeping the sensor’s aerodynamic drag to a minimum.



Figure 5-13: Clear polycarbonate sensor body.

The sensor nose cone, tail cone, and fins were all 3D printed with acrylonitrile butadiene styrene (ABS) because of its complex shape and the material’s lower structural sensitivity to heat. Although the nose and

tail cones contribute greatly to the sensor's aerodynamic efficiency, their lengths did not contribute to the scored length of the sensor. Therefore, the sensor length according to the score was reduced to 19 in from 20 in.

5.3.4 Sensor Deployment and Recovery Mechanism

In addition to the requirements set in Section 3.1.4 for the SDRM, the mechanism must minimize its weight and footprint while being able to deploy and retract at least 14 oz. Additionally, because the sensor must be controlled by the aircraft, the SDRM must be capable of transmitting a signal to the sensor.

To achieve these requirements, the team developed a list of potential motors and continuous servos. From the torque, weight, and rotational speed provided by the manufacturer for each motor, the retraction time was determined for a SDRM with a 1.625 in diameter and a 200 in retraction length. From initial testing, it was determined that a retraction time of less than three seconds should be targeted. Table 5-4 summarizes the list of potential motors and their retraction times.

Table 5-4: Sensor deployment motors considered.

Potential Motor	Retraction Time (s)
REV Robotics Smart Servo	46.7
REV Robotics NEO 550	0.2
ServoCity 638101	8.7
ServoCity 638198	14.0
ServoCity 623860	3.2
ServoCity 638402	4.6
GoBilda 2000 Series	8.1

Ultimately, the REV Robotics NEO 550's (NEO550) was selected for the SDRM due to its small footprint, high-rated torque, and speed capability.

VEX Robotics [9] provided a substantial number of measurements and motor curves for the NEO550. During the motor validation portion of the subsystem design, a target efficiency of 80% was set by the team. The SDRM capabilities were calculated at the NEO550's peak power output, peak efficiency, stall condition, and at the target efficiency; see Table 5-5. The desired performance of the SDRM was well within the NEO550's capabilities and its peak load was within 5% of the target efficiency.

Table 5-5: SDRM capabilities.

Condition	Time (s)	Speed (in·s ⁻¹)	Peak Load (oz)	Current (A)	Power (W)	Efficiency (%)
Peak Power	0.40	498	62.3	56	332	49
Peak Efficiency	0.22	907	11.2	11	109	82
Stall	N/A	0.0	114.7	111	0	0
Target Efficiency	0.24	847	18.6	18	169	80

While the motor and winch would be able to deploy and retract the sensor from the aircraft, there was no method of controlling the sensor from the aircraft. To resolve this issue, the team decided to integrate a slip ring into the SDRM so that a control signal could be passed through the winch, as shown in Figure 5-14.

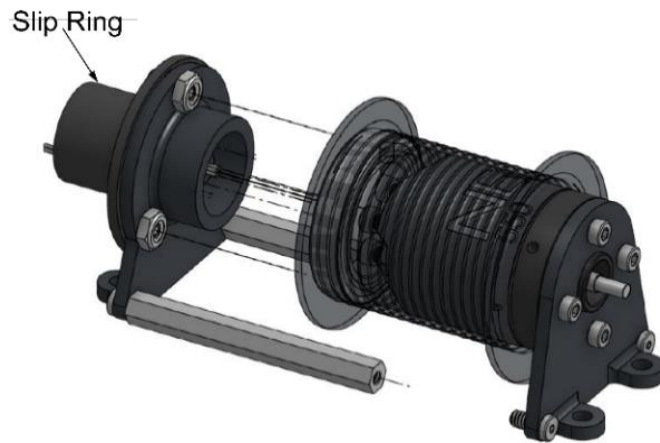


Figure 5-14: Slip ring integration into SDRM.

In Mission 2, the aircraft needed to fly with the SDRM and the sensor containers stored. To increase the amount of containers the aircraft could carry, the SDRM footprint was minimized by integrating the NEO550 into the spool, as shown in Figure 5-15. Because the SDRM does not have a separate spool tracking mechanism, often seen on fishing reels to ensure that the towline spools evenly, the team was concerned that the towline might gather on one side of the spool. To prevent this from occurring, a helical groove was integrated into the barrel of the spool; this groove provides the towline with an even path to follow along the length of the spool.



Figure 5-15: NEO550 spool Integration.

To assist in system integration, the mounting holes for the SDRM utilized a standard #8-32 screw also used throughout the aircraft. The hole pattern, as shown in Figure 5-16, is a normal 1 in by 3 in rectangle.

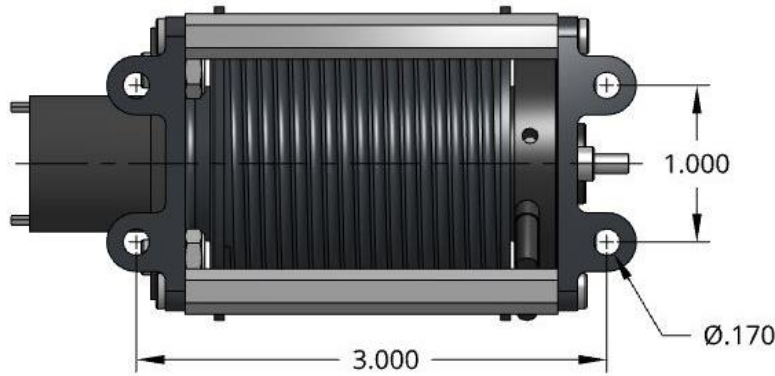


Figure 5-16: SDRM System Integration

Because of the complex shapes, the requirement to minimize the weight of the SDRM and the manufacturing capabilities of the team, the decision was made to 3D print the components for the SDRM out of ABS. Although ABS is more difficult to print compared to other common filaments such as polylactic acid (PLA), the increase in tensile strength and lower structural sensitivity to heat made ABS a better choice for the SDRM.

5.3.5 Propulsion System

The propulsion system was comprised of two Admiral 6S 4500 mAh 40C LiPo batteries connected in parallel for maximum power output and endurance needed throughout all missions. KDE 3520XF-400 motors spun counter rotating APC 15x10 propellers. Table 5-6 summarizes the selected propulsion system.

Table 5-6: Electronics and propulsion selection.

Components	Description
Motor	KDE 3520XF-400
Battery	Two Admiral 6S 4500 mAh 40C LiPo
ESC	HobbyWing FlyFun V5 Series 80A
Propeller	APC 15x10

5.4 Weight and Balance

The first structural weight analysis was conducted using estimations and data from prior designs. Approximated weights were assigned to the fuselage, wings, empennage, as well as the SDRM. The weights of the batteries, motors, propellers, and electronics were provided by the manufacturers. Fuselage stations of the major components were also assigned. As the aircraft was being built, measurements were made and cross-checked with the initial approximations. Most of the approximations for the flight surfaces were overweight, while approximations for the 3D printed parts were under weight, resulting in a significant shift forward of the CG. This issue was solved by shifting the wing forward 1.0 in for the second design iteration. The final weights and fuselage stations are given in Table 5-7.



Table 5-7: Component weights and their respective fuselage stations.

Component	Weight (lb)	FS (in)
Wing	1.18	33.0
Horizontal Tail	0.57	72.5
Vertical Tail	0.26	73.0
Fuselage	4.75	38.0
Motors	1.55	24.0
Main Landing Gear	0.80	38.8
Nose Landing Gear	0.30	11.5
Various Electronics	0.60	31.3

The layout of key components within the fuselage shifts between each mission to maintain a desired CG of 30% MAC. Table 5-8 shows the weights and CG locations of these key components for each mission.

Table 5-8: Weight and fuselage stations for each mission.

	Component	Weight (lb)	FS (in)
Mission 1	Batteries	2.8	20.6
	Total	13	32.8
Mission 2	Batteries	2.8	5
	Containers	8	36.5
	SDRM	0.5	60
	Total	22	32.8
Mission 3	Batteries	2.8	18.5
	SDRM	0.5	36
	Sensor	1	36
	Total	15	32.7

5.5 Mission Performance

With the completion of the detail design phase, performance predictions were updated based on new gross weights and an increased load factor of 2.5 from 2.25. Table 5-9 gives these updated values. The most notable improvement was the increase in the number of laps completed for Mission 3 because of the increased wing loading and turn load factor. Mission 2 performance estimates remained the same because the increased load factor was negated by the increase in wing loading. Updated predictions of team scores are shown in Table 5-10.



Table 5-9: Mission performance predictions of the final design.

	Mission 1	Mission 2	Mission 3
Gross Weight (lb)	13	21.5	14.5
Payload Weight (lb)	-	8.5	1.5
Wing Loading (lb-ft⁻²)	2.17	3.58	2.42
Ground Roll (ft)	35.1	58	38.5
Cruise Airspeed (fts⁻¹)	74	92	74
$C_{L, \text{cruise}}$	0.366	0.39108	0.40772
$C_{D, \text{cruise}}$	0.0658	0.0657	0.0711
L/D_{cruise}	5.562	5.9525	6.303
Turn Radius (ft)	25.4	74.2	28.3
Number of Laps	3	3	17
Lap Time (s)	34.1	37.3	34.9
Mission Time (min)	1.7	1.9	10

Table 5-10: Updated non-normalized team scores.

	Team Score
Mission 1	1.0
Mission 2	4.29 containers/min
Mission 3	282.6 laps*in*lb

5.6 Drawing Package

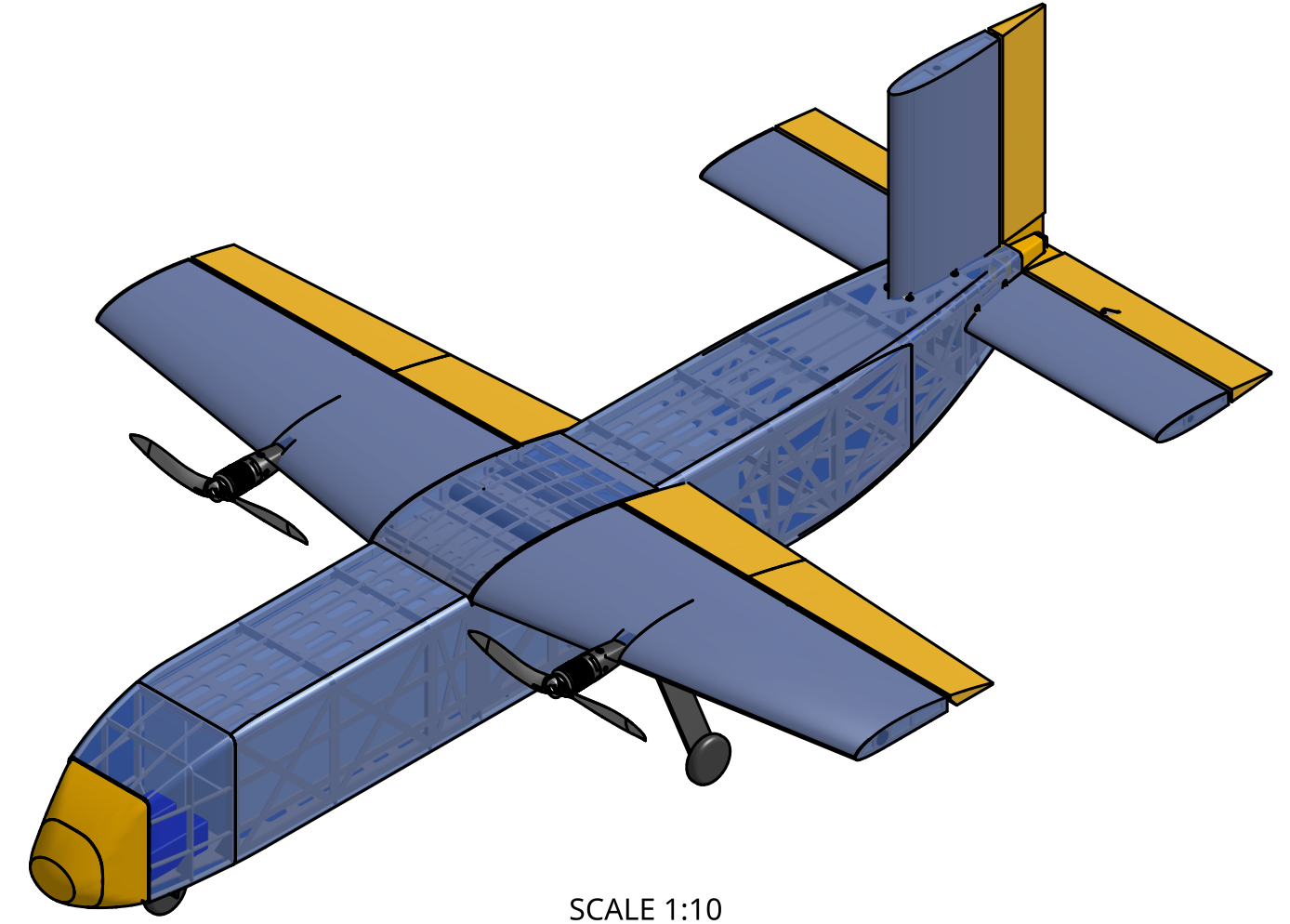
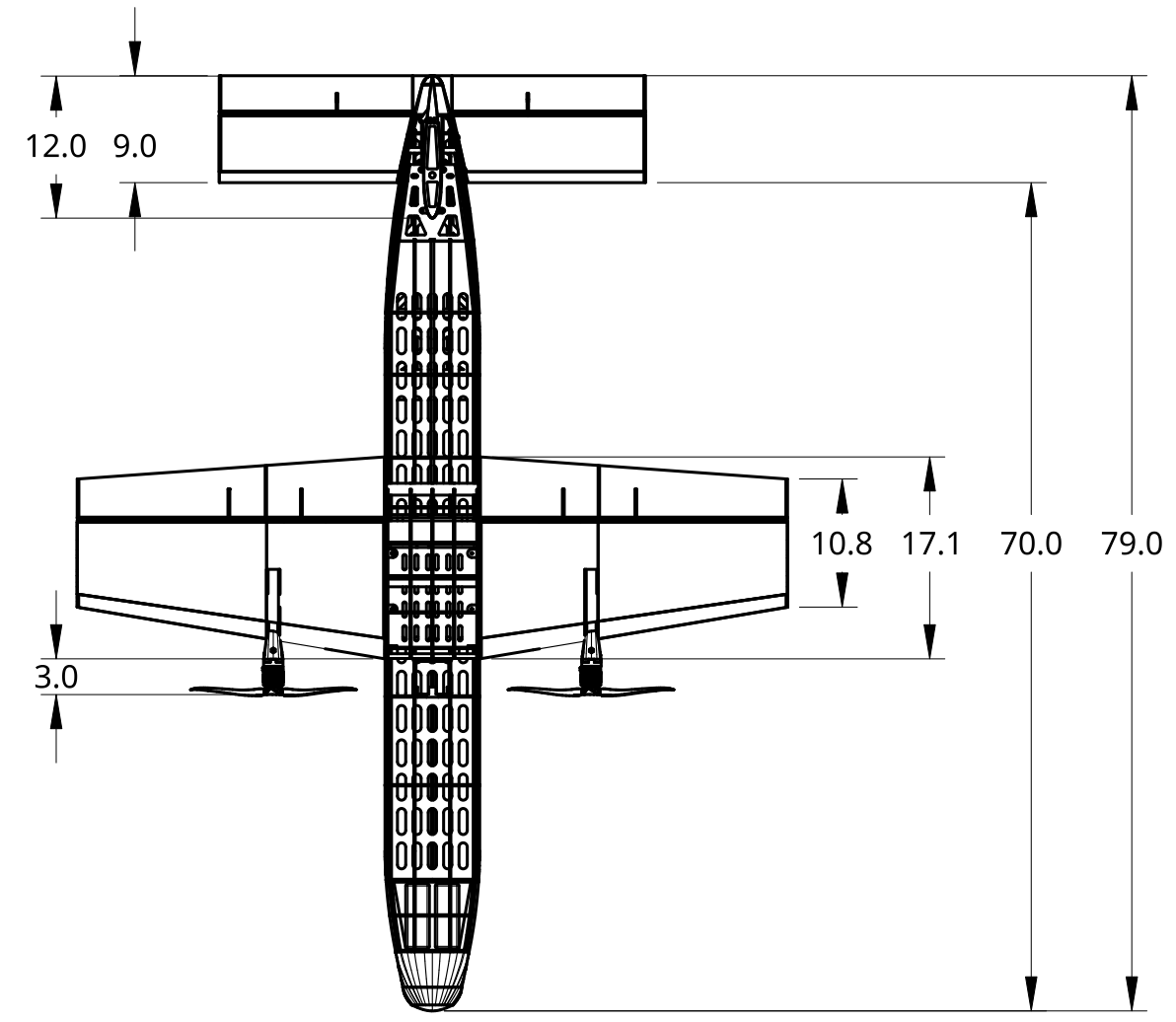
The next section provides detailed drawings of the STAT and its subsystems, including the sensor, container, and SDRM. All drawings were made with Onshape.

4

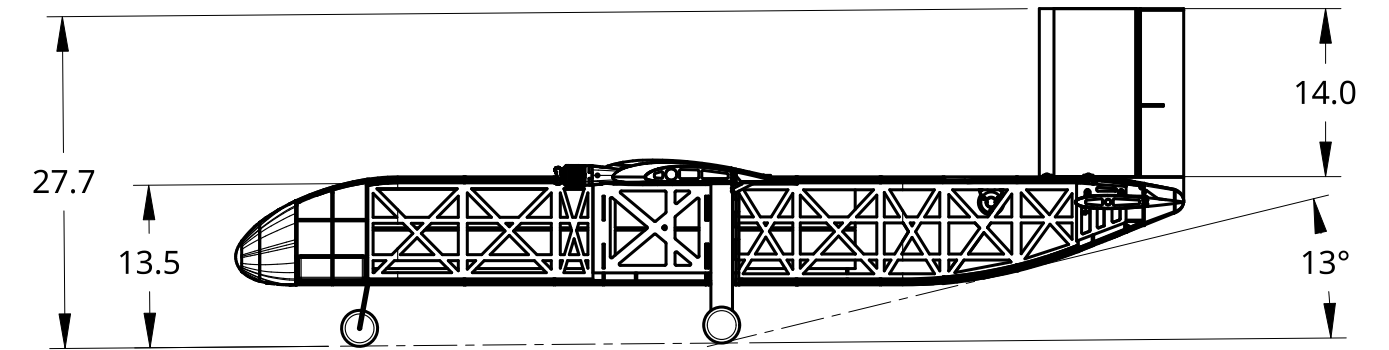
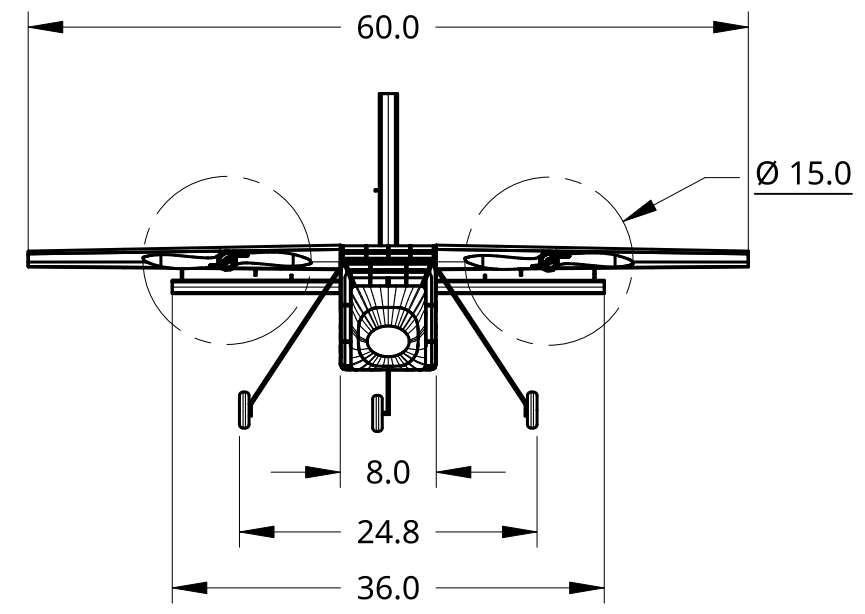
3

2

1



SCALE 1:10



UNLESS OTHERWISE SPECIFIED,
DIMENSIONS ARE IN INCHES
.XX = ±.0-
.XXX = ±.00-
.XXXX = ±.000-
SURFACE FINISH

ANGULAR = ± °
FRACTIONAL = ±

DO NOT SCALE DRAWING
BREAK ALL SHARP EDGES AND
REMOVE BURRS
THIRD ANGLE PROJECTION

	NAME	DATE
DRAWN	VICTOR CHANG	02/10/2021
CHECKED	CALEB REEVES	02/12/2021
APPROVED	CALEB REEVES	02/12/2021
MATERIAL	FINISH	



TITLE
**2020-21 ERAU DB DBF
SENSOR TOWING AIR TRACTOR**

SIZE B	DWG NO. AIRCRAFT 3-VIEW	REV. 1
SCALE 1:16	WEIGHT	SHEET 1 of 4

REV NOTES:
1. REV 0: FIRST RELEASE
2. REV 1: CORRECTED DIMENSIONING AND HORIZONTAL TAIL CLIPPING

4

3

2

1

D

D

C

C

B

B

A

A

4

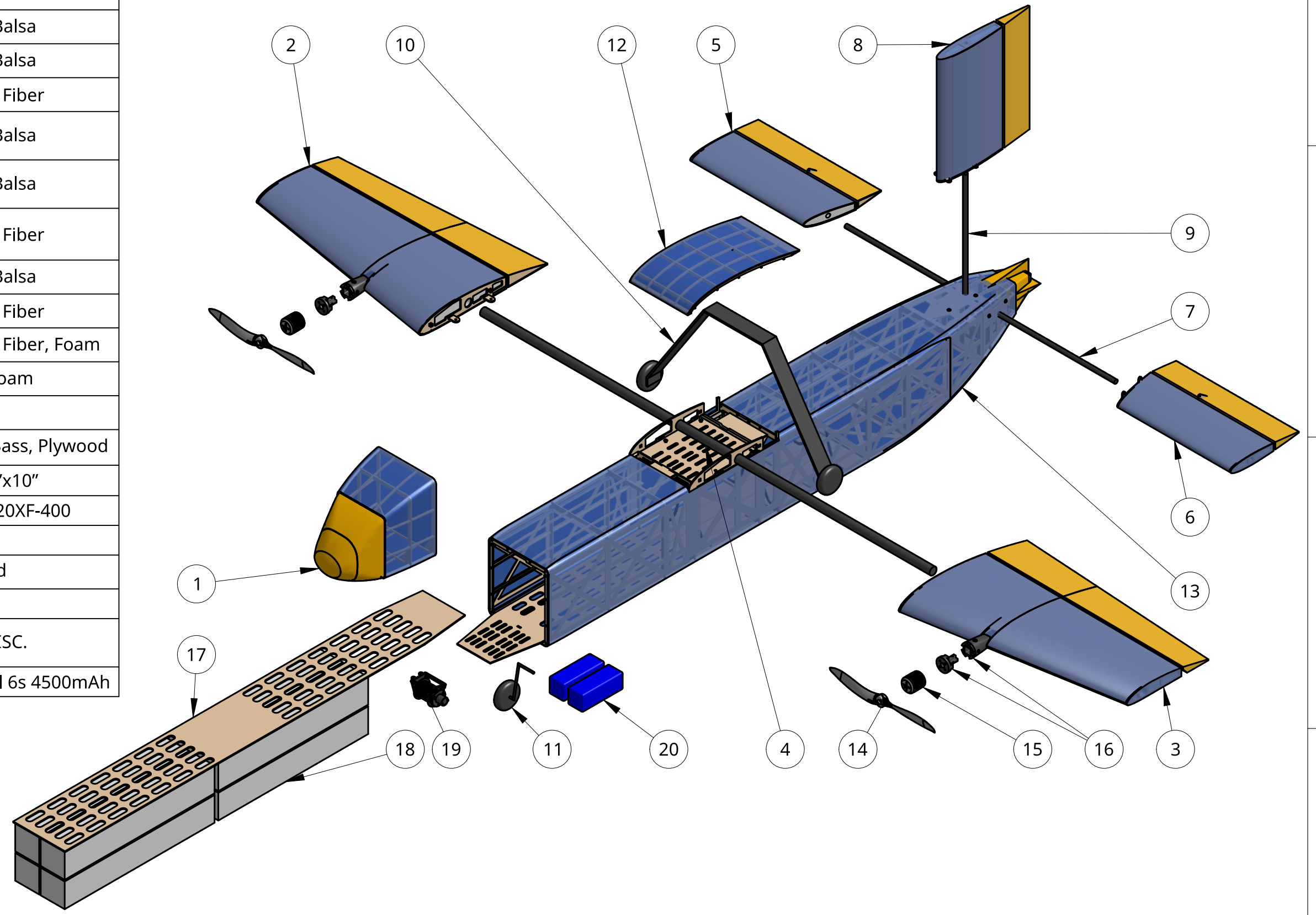
3

2

1

SYSTEM LIST

#	QTY.	ITEM NAME	DESCRIPTION
1	1	Nose Cone	ABS, Balsa
2	1	Right Wing	Foam, Balsa
3	1	Left Wing	Foam, Balsa
4	1	Wing Spar	Carbon Fiber
5	1	Right Horizontal Stabilizer	Foam, Balsa
6	1	Left Horizontal Stabilizer	Foam, Balsa
7	1	Horizontal Stabilizer Spar	Carbon Fiber
8	1	Vertical Stabilizer	Foam, Balsa
9	1	Vertical Stabilizer Spar	Carbon Fiber
10	1	Main Landing Gear	Carbon Fiber, Foam
11	1	Forward Landing Gear	Steel, Foam
12	1	Canopy	Balsa
13	1	Fuselage	Balsa, Bass, Plywood
14	2	Propeller	APC 15"x10"
15	2	Motor	KDE 3520XF-400
16	2	Motor Mount	ABS
17	1	Cargo Sled	Plywood
18	8	Sensor Crate	Foam
19	1	Sensor Deployment and Retraction Mechanism	ABS, MISC.
20	2	Battery	Admiral 6s 4500mAh



REV NOTES:
 1. REV 0: FIRST RELEASE
 2. REV 1: CORRECTED CALLOUT AND SYSTEMS LIST

4

3

2

1

D

D

C

C

B

B

A

A

4

3

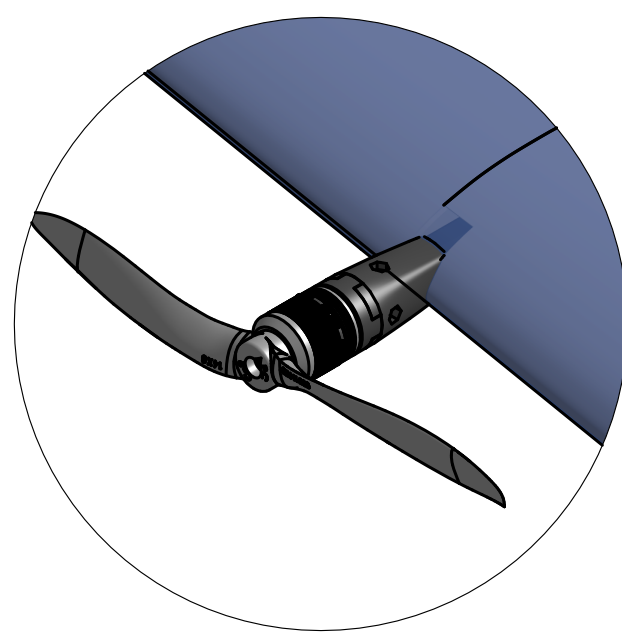
2

1

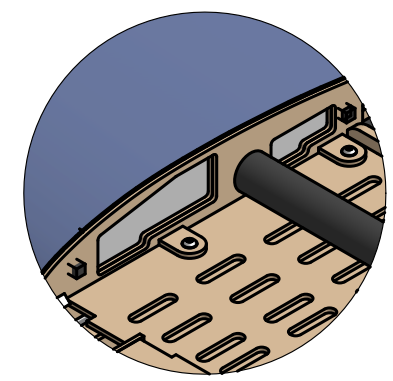
MOTOR MOUNT ASSEMBLY

WING ANTI-ROTATION AND ATTACHEMENT

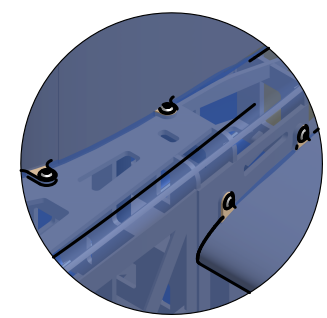
TAIL ATTACHEMENT



DETAIL D
SCALE 1:4

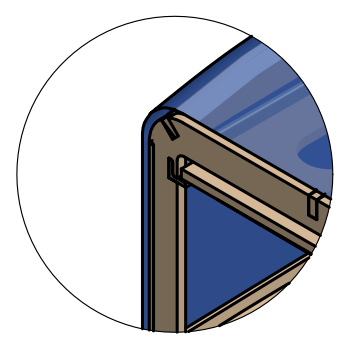


DETAIL B
SCALE 1:4



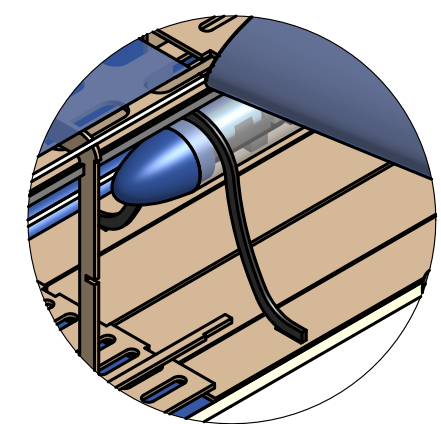
DETAIL C
SCALE 1:4

ALUMINIUM CARGO SLED RAIL

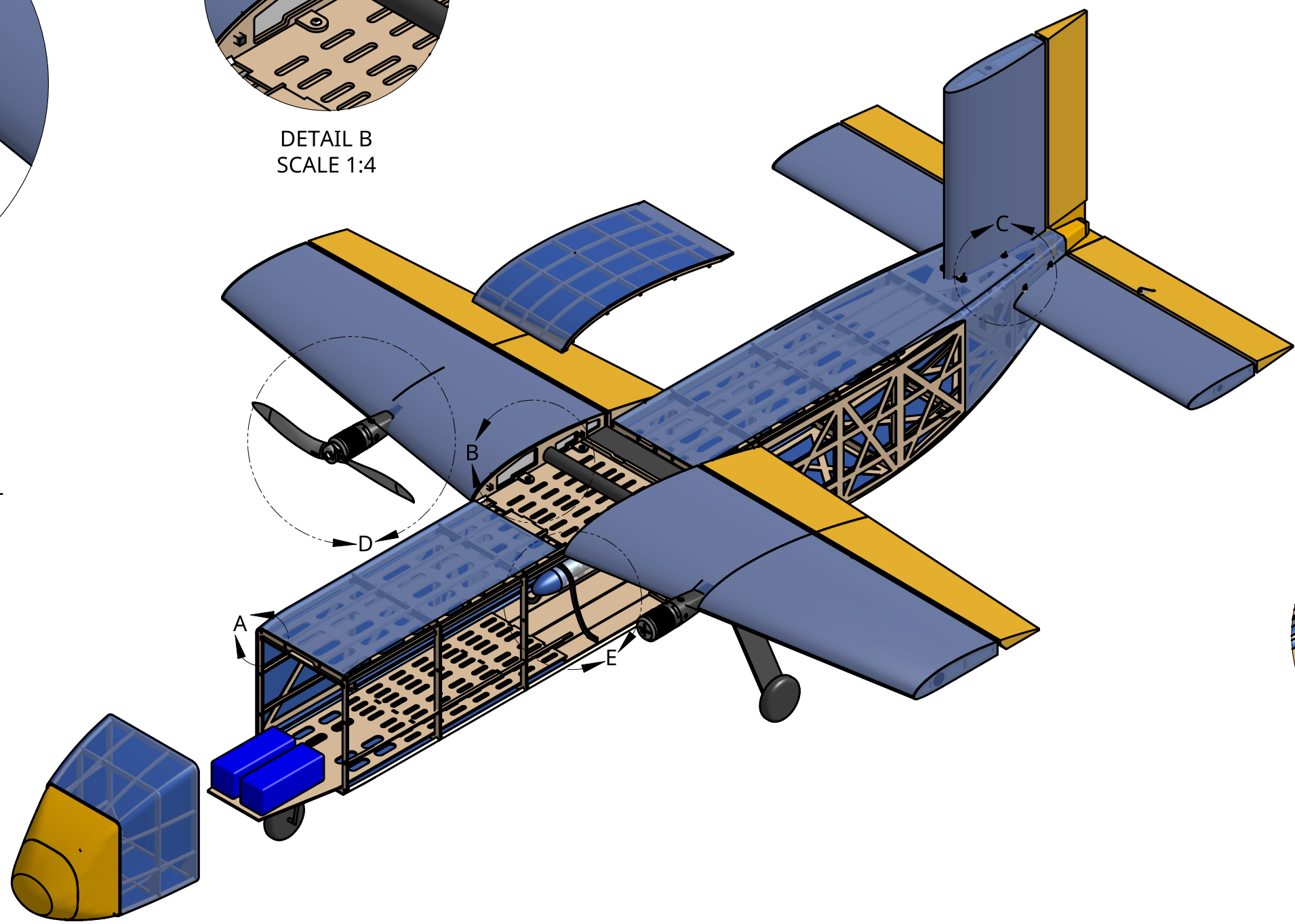


DETAIL A
SCALE 1:2

SENSOR BOMB-BAY



DETAIL E
SCALE 1:4



NOTE: PORTIONS OF THE AIRCRAFT HAVE BEEN HIDDEN TO BETTER SHOW THE INTERNAL SYSTEMS

DWG. NO.	AIRCRAFT DETAIL	SIZE	B	SCALE	1:8	SHEET	3 of 4	REV.	0
----------	-----------------	------	---	-------	-----	-------	--------	------	---

4

3

2

1

D

D

C

C

B

B

A

A

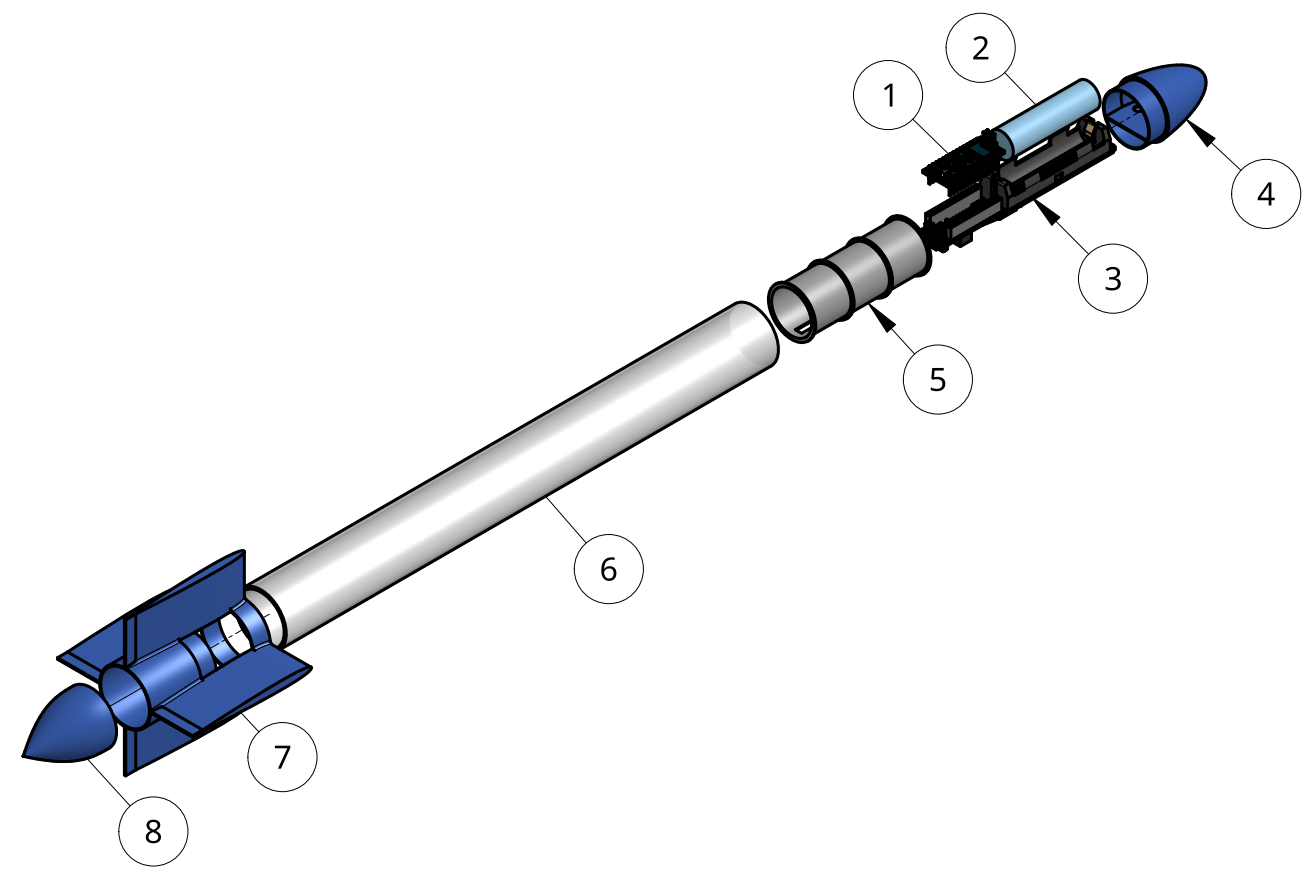
4

3

2

1

SENSOR



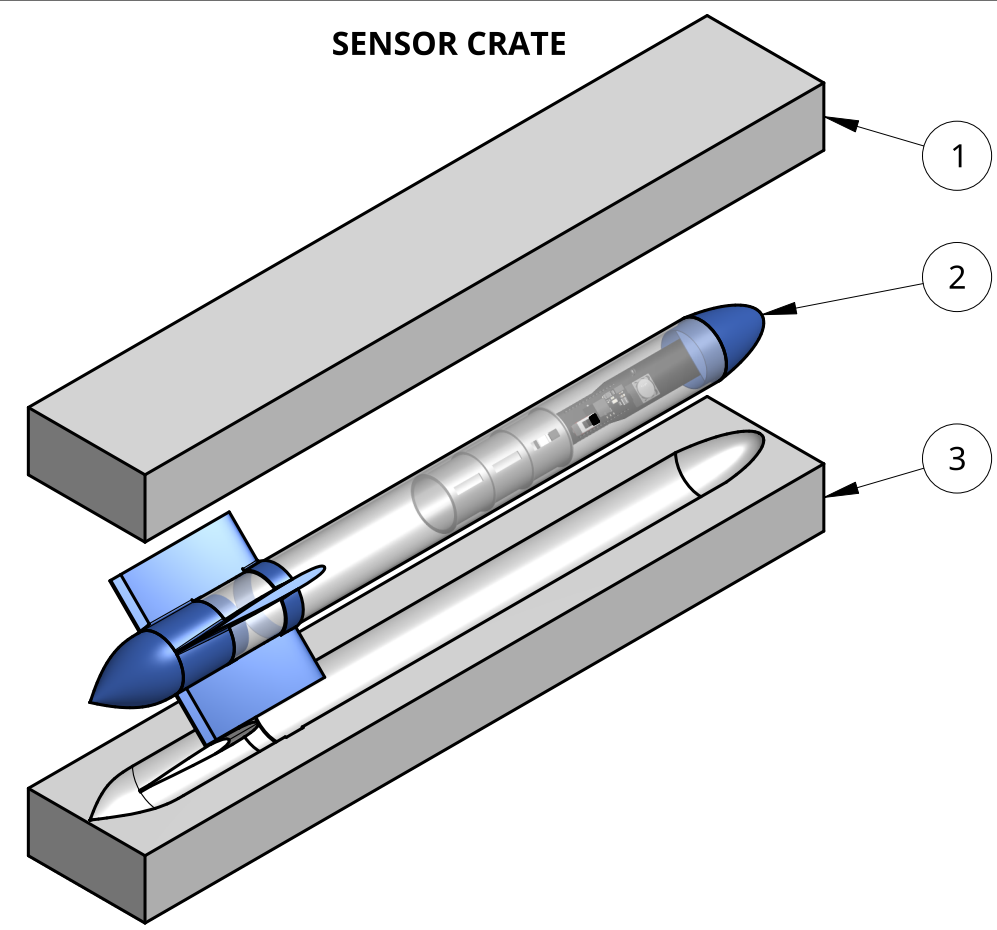
BILL OF MATERIALS		
PART	QTY	#
Arduino Nano	1	1
LGMH1 18650	1	2
Custom PCB	1	3
Nose Cone	1	4
LED Skeleton	1	5
Sensor Body	1	6
Sensor Fin	1	7
Tail Cone	1	8

SENSOR DEPLOYMENT AND RETRACTION MECHANISM



BILL OF MATERIALS		
PART	QTY	#
NEO 550 BRUSHLESS MOTOR	1	1
18-8 Hex Socket M3 x 0.5 mm, 5 mm Long	10	2
18-8 Hex Drive, 6-32 Thread Size, 5/16" Long	7	3
18-8 Thin Nylon-Insert Locknut, 6-32 Thread	3	4
Female Standoff Aluminum, 2.5" Long, 6-32 Thread	2	5
Ball Bearing, Shielded, Trade No. 6805-2Z	1	6
Slip Ring with Flange 22mm diameter	1	7
Motor Mount	1	8
Spool	1	9
Slip Ring Mount	1	10

SENSOR CRATE



BILL OF MATERIALS		
PART	QTY	#
Foam Crate Top	1	1
Foam Crate Bottom	1	2
Sensor	1	3

4

3

2

1

D

D

C

C

B

B

A

A



6 Manufacturing

Numerous manufacturing processes were identified and evaluated for each component of the aircraft and its subsystems. The selection method and manufacturing processes are discussed in the following sections.

6.1 Manufacturing Processes

6.1.1 Foam Construction

Foam construction benefits from ease of manufacturing and low cost. This method is utilized in many kit aircraft that are not subjected to high loads. Although foam construction is very cost-effective, it is relatively heavy. Furthermore, it is not a durable structural material without a composite or balsa skin to act as an exoskeleton.

6.1.2 Balsa Construction

Balsa wood construction allows for airframe material allocation to be optimized from the selection of wood species based on their material properties, such as tensile strength and density. The ability to utilize a high-precision laser cutter to quickly manufacture components can ensure that the airframe precisely meets design specifications.

6.1.3 3D Printing

The use of additive manufacturing techniques allows for efficient part fabrication and the ability to create complex parts. While 3D printing is still in development, the current technology allows for an efficient and precise manufacturing process. However, many parts cannot be 3D printed because of the increased production time compared to other methods and the limited filament materials available.

6.1.4 Composites

Composite materials can possess high strength-to-weight ratios, allowing for the airframe weight to be minimized while maintaining its strength. The downside of composites is their relatively high cost and the added complexity, as well as some safety concerns during the manufacturing process.

6.2 Manufacturing Processes Selection

6.2.1 Wing and Tail Structure

The wing and tail surfaces were constructed by sheeting the surface of an inner foam core with 1/32 in balsa wood skin. The inner foam core was fabricated out of an expanded polystyrene sheet with a CNC hotwire cutting machine. All channels for servos and wires were cut out of the foam with a handheld router. 1/8 in basswood trailing-edge plates were added to attach the control surface hinges in addition to end ribs to protect the wing tips of the foam core from damage. Removable carbon fiber spars were installed using a through-hole cut in each surface by the hotwire cutter. 1 in square carbon fiber tube was used to fabricate pylons from the main wing spar to the 3D printed motor mounts. Two anti-rotation pins constructed of 1/4 in square carbon tube were added to each main wing to prevent rotation about the main circular spar. These anti-rotation pins were keyed into square holes in the main fuselage structure. All surfaces were covered in Monokote, which is an adhesive-backed heat shrink film.

6.2.2 Fuselage Structure

The fuselage of the aircraft was constructed using a combination of wooden and 3D printed components. Along the length of the fuselage, aluminum L-channels were epoxied in the top left and right corners to provide a smooth rail for Mission 2 cargo sled. The tail of the aircraft was reinforced with a 1/4 in square carbon fiber longeron running along the top of the fuselage into the wing box. The wing box consisted of two 1/4 in thick and two 1/8 in thick plywood bulkheads with a 1/8 in plywood roof and sides. Along the nose and tail of the aircraft, 1/16 in balsa shear panels were added to the 1/8 in plywood bulkheads and a combination of balsa stringers and bass longerons. The bomb bay was constructed from 1/8 in basswood starting at the front of the wing box floor and ending in the forward portion of the tail structure. To secure the removable wings, horizontal tail, and vertical tail, twelve #8-32 stainless steel T-nuts were installed in the fuselage. The nose and tail fairings were 3D printed from PLA filament and glued to the fuselage using cyanoacrylate (CA) glue to maintain an aerodynamic shape. The nose fairing was made removable for easy access to the interior fuselage of the aircraft. The remaining wooden structure was covered with Monokote.

6.2.3 Sensor Deployment and Release Mechanism

The SDRM was 3D printed using ABS filament because of its complex shape. A brushless motor was attached to the inner barrel of the spool, which had a helical groove to assist with the even spooling of the towline and wire. A slip ring was attached to the left bracket of the winch and routed inside the spool. The winch is shown in Figure 6-1 (left).

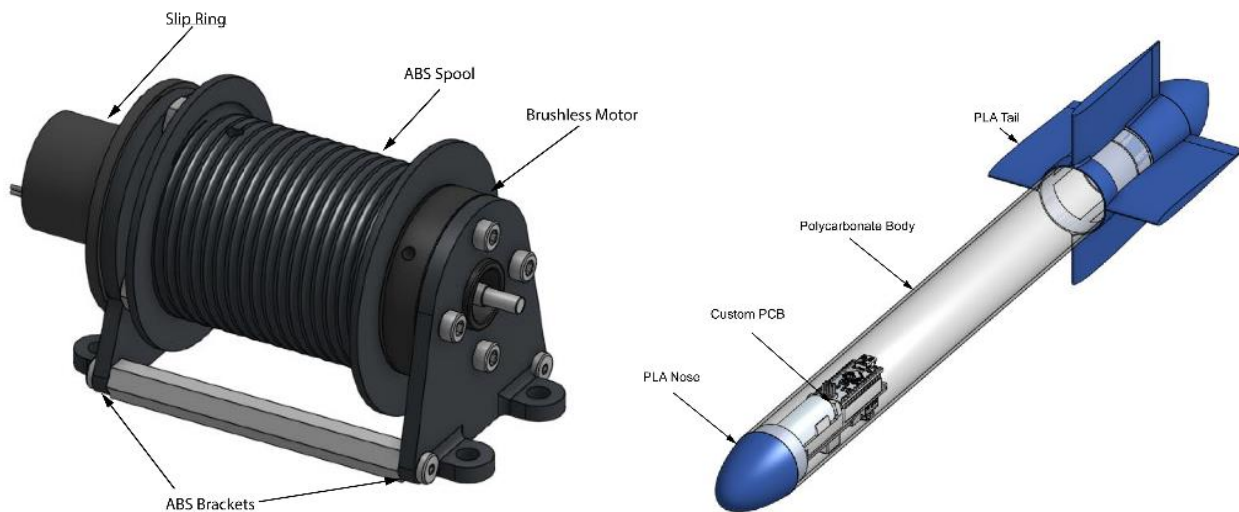


Figure 6-1: Models of the SDRM (left) and sensor (right).

6.2.4 Sensor

The sensor body was fabricated from a 1/8 in thick, 1.5 in diameter polycarbonate tube selected for its transparent properties. The tail fins and nose were 3D printed using PLA. The fin assembly was glued to the sensor body with hot glue. A custom printed circuit board (PCB) was designed and outsourced to house the battery, microcontroller, and transistors. The PCB was attached to the removable nose for easy access to all the electronics. The sensor is shown in Figure 6-1 (right).

6.3 Manufacturing Milestones

A Gantt chart was utilized to track the manufacturing progress throughout each aircraft iteration. Although the chart in Figure 6-2 only depicts the schedule for Iteration 2, similar scheduling was implemented for the manufacturing of other aircraft iterations.

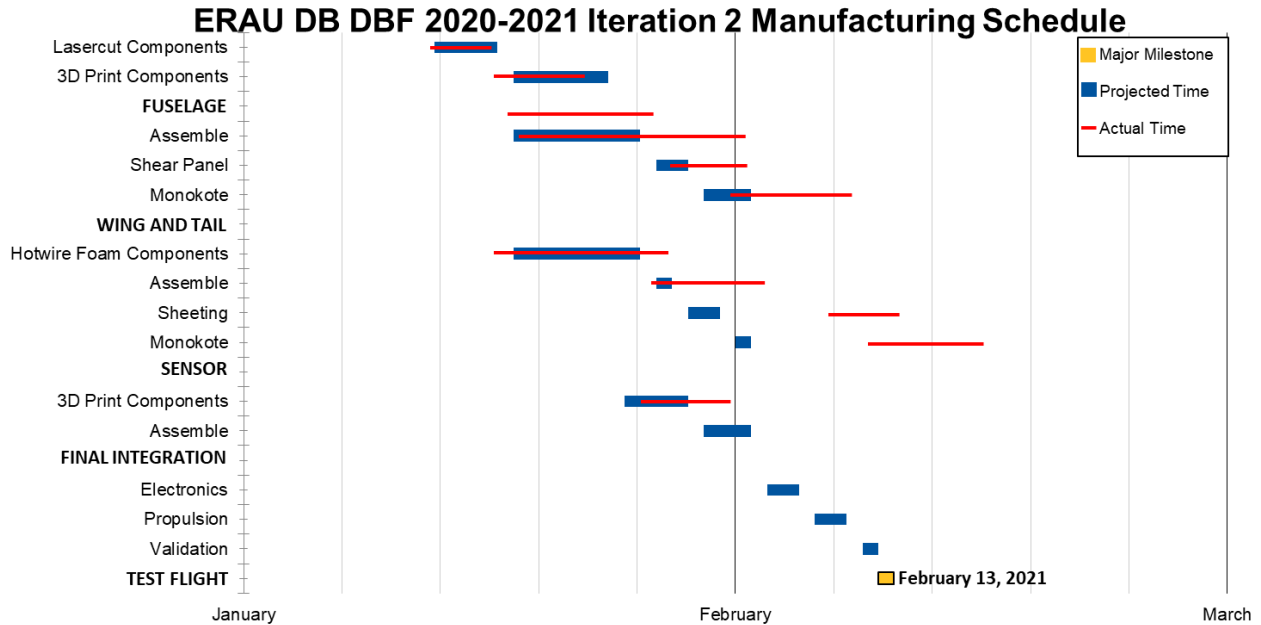


Figure 6-2: Aircraft Iteration 2 Gantt Chart. Note that planned and actual timing is shown.

New manufacturing methods, including hotwire cut-foam and sheeted wings, led to unexpected delays as the team learned the new skills required of these methods. However, such delays should not cause issues with upcoming competition deadlines.

7 Testing Plan

Complete aircraft and subsystem testing was performed to validate the design and to improve upon functionality, reliability, and performance. A Pixhawk flight computer was used to record telemetry data including airspeed, groundspeed, altitude, GPS coordinates, pilot inputs, and power consumption.

7.1 Test Objectives

Using the preliminary requirements set by the design team, the following test objectives in Table 7-1 were established to ensure all design requirements would be met.



Table 7-1: Test objectives by aircraft system.

System	Objectives
Propulsion	Collect throttle, power, and airspeed data during ground and flight tests to validate the propulsion system
Structures	Conduct wingtip loading tests at maximum takeoff weight to validate the aircraft structure and locate potential weak areas
	Evaluate the efficacy of shear paneling through fuselage loading/deflection tests
	Perform ground tests of the landing gear to validate design and record landings to monitor gear deflection
Sensor	Record video of sensor testing to select the best tail configuration
	Systematically optimize sensor stability and drag through iterative testing of different tail configurations
	Obtain pilot feedback of aircraft and sensor stability during flight tests with deployed sensor
Sensor Deployment	Validate reliability of bomb bay and SDRM during ground tests
	Verify SDRM motor can support maximum retraction loads and perform well in flight
Payload	Perform ground tests to verify shipping containers pass the Ground Mission
	Obtain pilot feedback of aircraft stability and control at maximum weight for Mission 2
Performance	Record all Pixhawk data for post-flight analysis to verify design requirements have been met

7.2 Subsystems Testing

7.2.1 Propulsion Testing

Once the propulsion requirements had been set by the design team, a mock propulsion system was assembled using the selected batteries, motors, and ESCs. Motors were run to planned flight speeds while the team ensured that current draw was below safe levels for each part of the system. Next, with Iteration 1 nearing completion, ground run-up tests were conducted to again verify safe current draw and thrust production. Then, using Pixhawk telemetry, the battery current and voltage was closely monitored during initial flight tests. Post-flight analysis was used to obtain power and airspeed data to confirm the selection of the propeller, motor, and battery.

7.2.2 Structural Testing

To validate the aircraft structure, tests were first conducted on the carbon fiber spars prior to being installed in the aircraft; design loads were applied while spar deflections were carefully monitored. Second, a fuselage deflection test was performed to study the added strength provided by the shear panels. Third, prior to the maiden flight and all subsequent flights, a wingtip loading test was conducted to validate the structure; more extensive testing was conducted at the maximum weight. Finally, in-flight video was used to monitor the wing flex at maximum weight under the design load factor of 2.5.

7.2.3 Sensor Testing

A prototype sensor was built from a preliminary design concept, which was subsequently validated by tow testing using a ground vehicle. Promising results from the prototype led to further testing at various sensor weights, towline attachment locations, center of gravity locations, and tail sizes. Sensor drag was approximated by applying the principles of statics to the images acquired during testing, shown in Figure 7-1 (left). After a final configuration was selected, the prototype was updated and tested in the wind tunnel, as shown in Figure 7-1 (right). Next, the sensor was tested on the aircraft to study its stability at full towline length and near the aircraft (simulating the period during deployment and retraction).

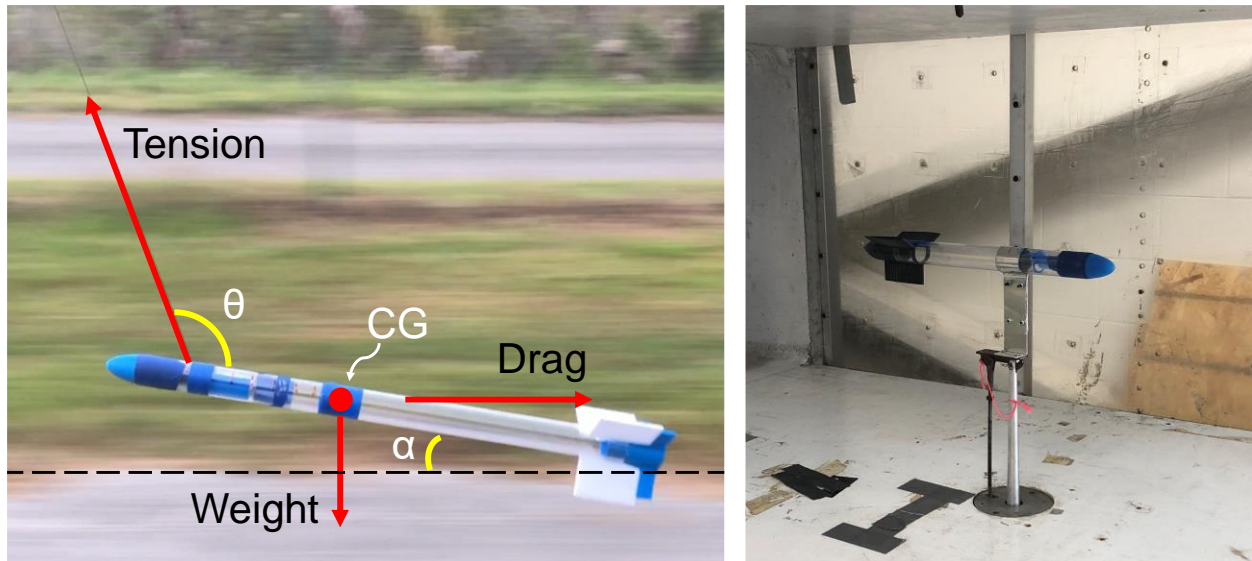


Figure 7-1: Road vehicle and wind tunnel testing setups for sensor.

7.2.4 Sensor Deployment and Recovery Testing

Before installing the SDRM in the aircraft, the design was tested for performance and reliability on the ground by performing multiple manual deployments and retractions. Then, the motor was tested under maximum expected loads. The SDRM and bomb bay were subsequently installed on the aircraft; both were tested repeatedly for reliability. Finally, the two designs were tested together in flight to validate performance of the entire sensor deployment system.

7.2.5 Payload Testing

Payload was primarily tested on the ground by verifying the fit of the sensor in the designed shipping container and the fit of each shipping container in the aircraft. Prior to completion of the design, flights at maximum weight were conducted to ensure that the aircraft could handle the proposed number containers by weight. With each successful test, the payload weight was increased while remaining within the factor of safety of 1.5 set by the design team.

7.2.6 Performance Testing

A total flight time of 1.6 hours was accrued during 14 flights across five flight days. The performance was continually monitored with the collection of 84.7 million data points recorded by the Pixhawk flight computer.

Telemetry data and pilot feedback were used to validate each competition and design requirement. After each flight, detailed debriefings were held between the pilot, flight crew, and team leadership to discuss aircraft performance. Post-flight data analysis was used to provide comprehensive feedback to the design and manufacturing teams regarding any necessary design changes. Figure 7-2 shows a sample set of telemetry data from a flight test that was used for analysis.

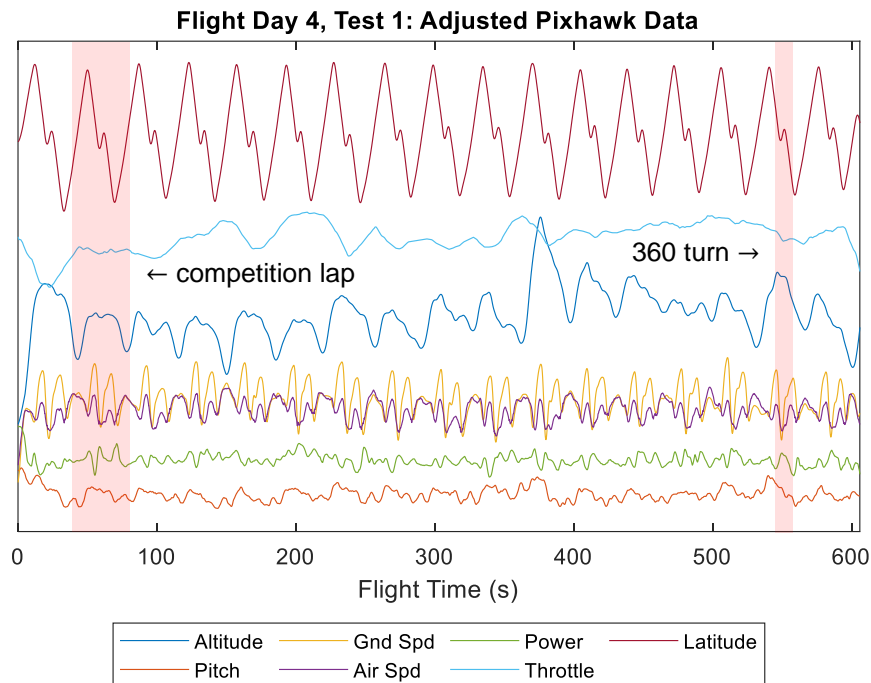


Figure 7-2: Sample Pixhawk telemetry data with a competition lap and 360 deg turn highlighted; units have been omitted and adjusted to fit on the plot.

7.3 Test Schedule

Table 7-2 summarizes completed tests and Table 7-3 summarizes planned tests through April.

Table 7-2: Completed ground and flight test schedule.

Date	Type	System	Objectives
10-07-2020	Ground	Sensor	Test prototype design
10-09-2020	Ground	Sensor	Iterate weight, towline attachment point, CG, tail size
10-14-2020	Ground	Propulsion	Initial propulsion layout/run
10-29-2020	Ground	Propulsion	Full aircraft run-up
10-31-2020	Flight	All (Iter. 1)	Proof of concept, aircraft trim, stability and control
11-04-2020	Ground	Sensor	Test alternative tail configurations
11-10-2020	Ground	Sensor	Obtain drag from wind tunnel
11-14-2020	Flight	Sens., Payl.	Observe sensor stability, test maximum weight
11-20-2020	Flight	Deployment	Test prototype designs
02-03-2021	Flight	Performance	Evaluate performance
02-06-2021	Flight	Performance	Evaluate performance



Table 7-3: Planned ground and flight test schedule.

Date	Type	System	Objectives
02-20-2021	Flight	All (Iter. 2)	Test competition readiness, sensor/payload/deploy.
02-27-2021	Flight	Sens., Perf.	Pilot practice, locate final improvements to be made
03-13-2021	Flight	All (Iter. 3)	Test competition readiness, sensor/payload/deploy.
03-20-2021	Flight	Sens., Perf.	Perfect deploy/retract, & maneuvers with sensor
Thru 04-10	Flight	All	Practice, detail modifications
04-10-2021	Flight	All	Final aircraft certification

7.4 Test Checklists

The following checklists in Table 7-4 were implemented and utilized, which are specific to this year's competition requirements and aircraft design. These checklists ensured safety and redundancy during all tests.

Table 7-4: Test checklists.

Ground Inspection	Flight Crew Inspections
Fuselage	Pre-flight
Visual inspection Pass	Propulsion batteries Install
Aircraft skin tear-free.....Check	Receiver batteries Install
Servos, linkages, horns..... Secure	CG location..... Check
Wings, ailerons, flaps..... Secure	Wingtip test.....Pass
Tail, elevators, rudder Secure	Receiver On
Landing gear Secure	Control surface directions Correct
Motors	Gyro stability Correct
Motors & mounts Secure	Range check Pass
Propellers damage-free Check	Radio failsafe Correct
Prop. nuts & direction..... Correct	Propulsion run-up.....Pass
Interior	Wind direction & runway Chosen
Battery voltage Check	Throttle down and safe..... Check
Antennas Correct	Mission Planner disarm Check
Servo, receiver plugs Secure	Arming plug Install
Payload (if req'd)	External hatches Secure
Containers..... Secure	Pilot ready to fly?..... Go/No-Go
Pallet Install	Mission Planner arm Fly!
SDRM..... Secure	Post-flight
Payload not free to move Check	Throttle down and safe..... Check
Sensor (if req'd)	Mission Planner disarm Check
Sensor damage-free Check	Arming plug Remove
SDRM prepped Check	Propulsion batteries Unplug
Sensor..... Install	Receiver batteries Unplug
Bomb bay Secure	Debrief Complete

8 Performance Results

The previous testing plan was used to obtain data to evaluate and compare design with actual performance. The following section outlines the results of all ground and flight tests.

8.1 Components and Subsystems

8.1.1 Propulsion

The propulsion system proved adequate to meet design requirements using two Admiral 6S 4500 mAh 40C LiPo batteries connected in parallel. Endurance was proven during two flights with at least 10 minutes of continuous, high-performance flight time to complete Mission 3, and a maximum airspeed of $100 \text{ ft}\cdot\text{s}^{-1}$ was achieved to remain competitive at the maximum weight for Mission 2. Mission 3 target battery power consumption was about 900 W, at which $85 \text{ ft}\cdot\text{s}^{-1}$ was achieved. Battery power consumption at the maximum speed for Mission 3 was 975 W. Figure 8-1 compares measured thrust power required versus airspeed with calculated design curves, as well as curves adjusted to fit the experimental data. The thrust power required curve was adjusted by lowering propeller rpm from 7,000 to 6,500, the average value measured during testing. The thrust power required curves were adjusted by changing the drag “CRUD” factor to match the experimental data more closely.

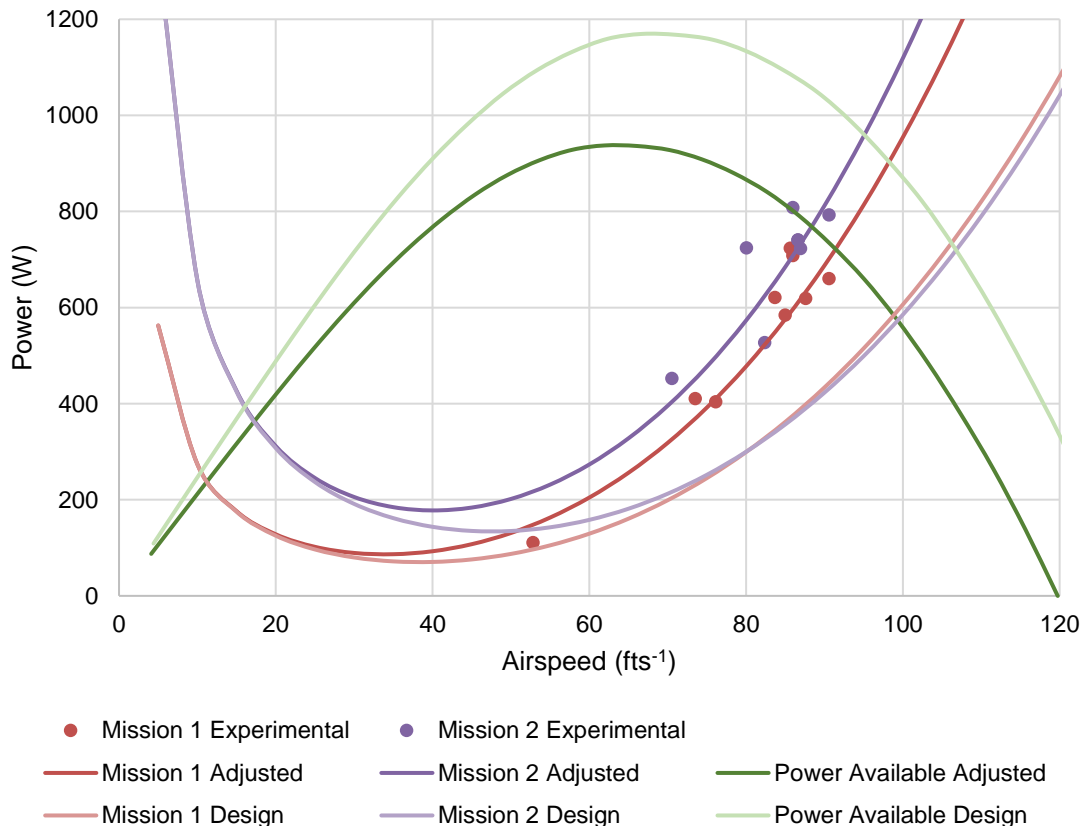


Figure 8-1: Experimental thrust power versus airspeed data plotted against design and adjusted curves.

First, initial testing of the wing spar revealed that the selected spar was strong enough for flight, but a stiffer spar would be purchased for Iteration 2 to reduce wingtip deflection. Second, the fuselage deflection test validated that shear paneling added significant resistance to flex and torsion, as seen in Figure 8-2.

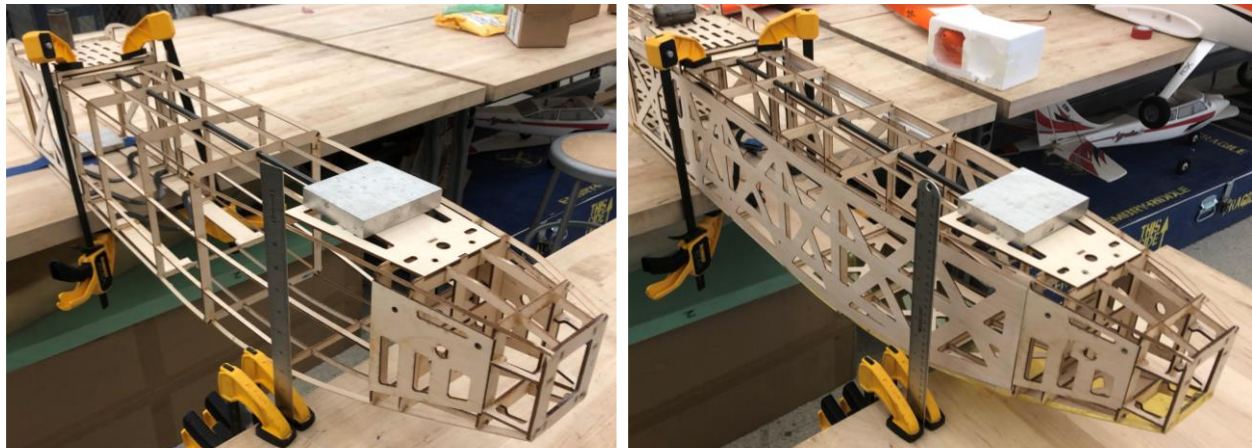


Figure 8-2: Fuselage deflection test comparing before and after shear panel installation.

Prior to shear panel installation, the fuselage tail deflected $5/8$ in under a 1-lb load; after installation, deflection was limited to $1/64$ in (a 98% improvement). Third, the wingtip loading test confirmed that the structure could handle a load factor of at least 2.5 at maximum payload weight. Finally, wing flex at maximum payload weight was found to be acceptable, as shown in Figure 8-3.

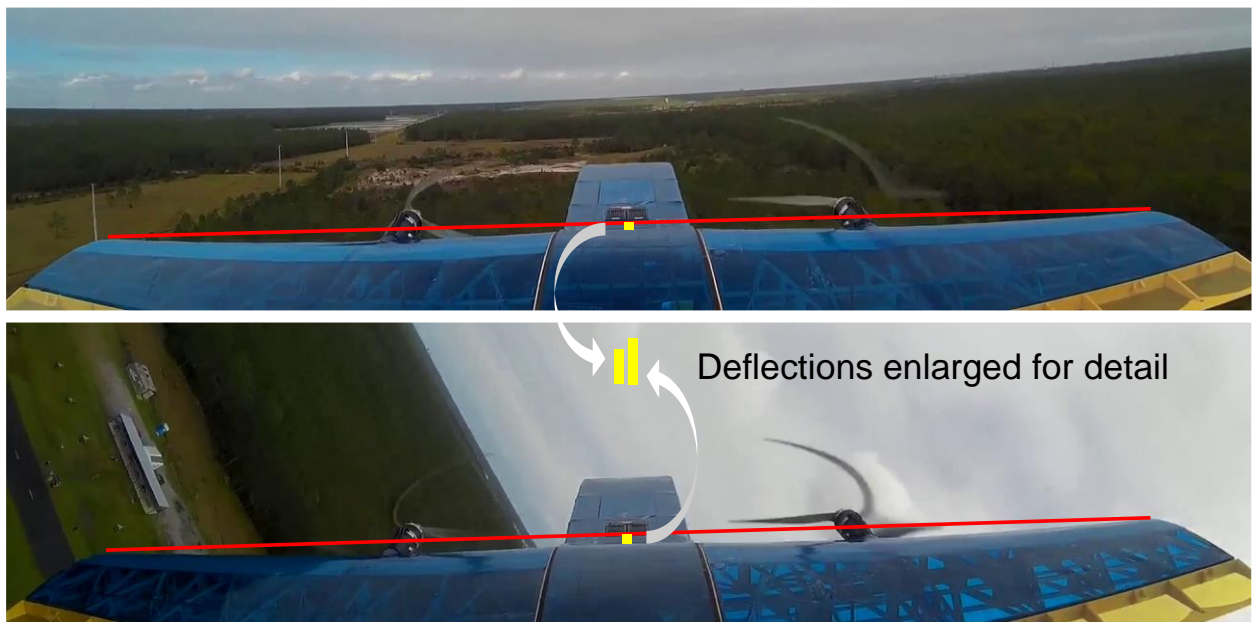


Figure 8-3: Maximum weight wing flex for level (top) and 60-degree bank (bottom).

8.1.2 Sensor

The initial sensor prototype was estimated to have a drag coefficient of 0.0057 from statics. An important limitation of this method is that it assumed zero lift from the sensor to isolate forces in the vertical direction. Additionally, it did not account for the drag on the tow cable used. A shorter, updated design of the sensor

was found to have a drag coefficient of 0.0018 using VSPAERO. This value was verified through wind tunnel testing. Figure 7-1 shows the set up for both sensor tests.

Flight tests with the sensor, performed at both full towline length and close proximity to the fuselage, confirmed its overall stability in all directions; however, a “pendulum” type motion was discovered to form following turns. Further pilot practice is planned to mitigate this issue. Figure 8-4 shows the sensor being tested at both towline lengths.



Figure 8-4: Sensor in flight at different tow lengths: 200 in (left) and 6 in (right).

In addition, the sensor’s lights were clearly visible from the ground during all periods of flight; the blue light is shown operating in Figure 8-5 (left), as viewed from the aircraft during deployment. Sensor controls from the aircraft have been successful during ground tests but are still being validated in flight.

While Mission 3 has not been simulated in full with the sensor deployed, a 17-lap, 10-minute flight was completed to prove endurance and record lap times. The team is confident in the ability to complete 15 laps with the sensor deployed during Mission 3.

8.1.3 Sensor Deployment

The SDRM, including the winch and bomb bay, were both successful in the prototype stage. Changes were made to the design and installation, leading to improved performance and reliability. Table 8-1 compares design and actual performance parameters of the SDRM.

Table 8-1: Sensor deployment and retraction design versus actual performance.

Task	Design	Actual	Difference
Sensor Deployment Time (s)	1	2	+ 100%
Sensor Retraction Time (s)	1	3	+ 200%

Figure 8-5 shows operation of the prototype system in flight. While the actual performance values are outside of the design range, the team plans to improve the times with further pilot and co-pilot practice.



Figure 8-5: Sensor and bomb bay prototypes during deployment (left) and retraction (right), with blue sensor light visible (left).

8.1.4 Payload

Through ground testing of storage configurations and flight testing of payload weights, the ability to carry eight sensors was confirmed. The payload capacity allowed for sensors to weigh 14 oz and containers to weigh 2 oz. Further ground tests were conducted to verify an 18-sensor concept; this required the sensor tail configuration to change to four fins, instead of three, and for the sensor weight to be reduced. Even with a reduced sensor weight, the aircraft would increase by 4.5 lb to a gross weight of 24.5 lb. To validate this change, the aircraft was flown at a gross weight of 28 lb, which proved that the 18-sensor concept was possible. Therefore, the current configuration is 18 sensors, weighing 9 oz each. Upcoming flight tests will validate the new sensor tail variation. However, the mentioned ground vehicle tests of the sensor and in-flight wing flex tests indicate promising outcomes to make this change. In addition, Ground Mission times for loading sensors and containers are currently considered to be reasonable and will be improved prior to competition.

There is one more storage configuration being conceptualized that would increase the number of sensors to 26, as shown in Figure 8-6. By utilizing the space already available in the fuselage and relocating storage of the SDRM, this layout is practical. At the currently validated gross weight of 28 lb, the sensor weight would need to be reduced by 1 oz to stay within weight constraints. Performance at this weight was tested to study its effect on the overall score. The 40% increase in weight caused a 112% increase in takeoff distance (to 125 ft) and a 29% increase in lap time (to 45 seconds). While further testing and analysis is needed to meet competition requirements, the team is confident in its ability to select a configuration that optimizes the available performance of the aircraft with its maximum possible score.

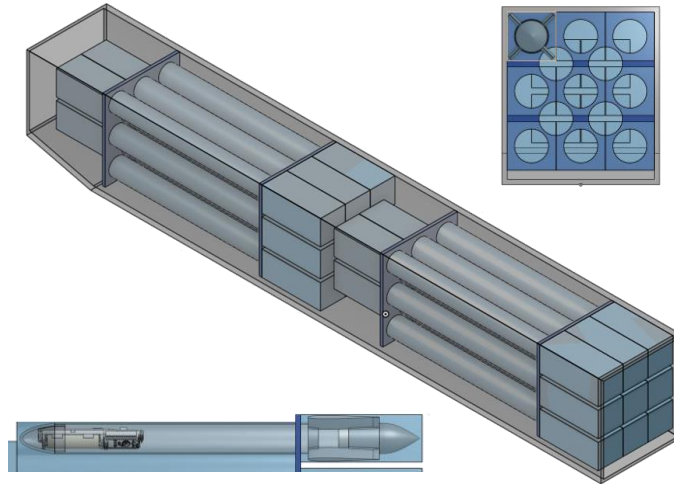


Figure 8-6: 26-container storage concept: sensor in container, containers in fuselage, container grid view (left to right).

8.2 Complete Aircraft Performance

This year, the ERAU DB team has consistently designed, built, and flown well ahead of schedule. This made time for detailed analysis of components and subsystems, leading to earlier success in evaluating the performance of the complete aircraft. Successful results have presented the opportunity to continue advancing the design and working towards achieving the maximum possible score. Performance results at the time of writing have been compiled in the following tables. Table 8-2 summarizes the outcomes of completed ground and flight tests, Table 8-3 details specific aircraft performance regarding scoring parameters and competition requirements, and Table 8-4 summarizes final team scores. In addition, Figures 8-7 and 8-8 show Iteration 1 of the aircraft in flight.

Table 8-2: Outcomes of completed ground and flight tests.

Date	Type	System	Outcome
10-07-2020	Ground	Sensor	Sensor prototype successful
10-09-2020	Ground	Sensor	16 iterative tests conducted, optimal sensor configuration selected
10-14-2020	Ground	Propulsion	Propulsion system concept successful
10-29-2020	Ground	Propulsion	Propulsion system fully successful
10-31-2020	Flight	All (Iter. 1)	Aircraft design successful, trimmed, design/manufacturing feedback provided
11-04-2020	Ground	Sensor	Sensor tail configuration confirmed
11-10-2020	Ground	Sensor	Sensor drag obtained
11-14-2020	Flight	Sensor and Payload	Sensor mostly stable, aircraft maximum weight successful
11-20-2020	Flight	Deployment	SDRM prototypes successful
02-03-2021	Flight	Performance	Lap times and endurance validated, motor mount issue concluded test early
02-06-2021	Flight	Performance	Performance data recorded

Table 8-3: Complete aircraft design versus actual performance.

Task	Design	Actual	Difference
Mission 1 Lap Time (s)	34.1	35	- 3%
Mission 2 Lap Time (s)	37.3	35	- 6%
Mission 2 # Containers	8	18	+ 125%
Max Gross Weight (lb)	21.5	28	+ 30%
Sensor Length (in)	20	19	- 5%
Sensor Weight (oz)	14	9	- 36%
No Payload # Laps	17	17	+ 0%
Mission 3 # Laps	17	15 (est)	- 12%
Mission 3 Endurance (min)	11:00	10:32	- 4%
Takeoff Distance No Payload (ft)	35	25	- 29%
Takeoff Distance @ 21.5 lb (ft)	58	59	+ 2%

Table 8-4: Final non-normalized team scores.

	Team Score
Mission 1	1.0
Mission 2	10.29 containers/min
Mission 3	160.3 laps*in*lb



Figure 8-7: Takeoff at 20 lb gross weight.



Figure 8-8: Aircraft completing a 360-degree turn with sensor deployed.



Bibliography

- [1] "2020-21 Design, Build, Fly Rules," *Competition Information*, AIAA, retrieved 20 January 2021.
<https://www.aiaa.org/dbf/competition-information/rules-resources>
- [2] U.S. Army, "Effects of Propeller Slipstream on V/STOL Aircraft Performance and Stability," Transportation Research Command Technical Report 64-47, August 1964.
- [3] Raymer, D. P., "Aircraft design: A conceptual Approach," AIAA, Reston, VA, 2018.
- [4] McCormick, B. W., "Aerodynamics, Aeronautics, and Flight Mechanics," 2nd ed., Wiley, New York, 1995.
- [5] Gudmundsson, S. "General Aviation Aircraft Design: Applied Methods and Procedures," Amsterdam: Butterworth-Heinemann, 2016.
- [6] "APC Propeller Performance Data," Advanced Precision Composites, retrieved 15 October 2020.
<https://www.apcprop.com/technical-information/performance-data/>
- [7] "Propeller Calculator," eCalc Reliable Electric Drive Simulations, retrieved 15 October 2020.
<https://www.ecalc.ch/motorcalc.php>
- [8] "USA-35B AIRFOIL (usa35b-il)," Airfoil Tools, retrieved 30 September 2020.
<http://airfoiltools.com/airfoil/details?airfoil=usa35b-il>
- [9] "VEX Robotics Motor Data - NEO 550 (REV-21-1651)," VEX Robotics, retrieved 1 February 2021.
<https://motors.vex.com/other-motors/neo550>